UNIVERSIDADE D
COIMBRA

Guilherme Pinheiro Pereira

CONTINUOUS CALIBRATION AND MONITORING FOR LZ DARK MATTER EXPERIMENT

Tese no âmbito do Doutoramento em Engenharia Física, Instrumentação orientada pelo Doutor Vladimir Solovov e pelo Professor Doutor Cláudio Silva e apresentada Departamento de Física da Faculdade de Ciências e Tecnologia da Universidade de Coimbra

Novembro de 2022

FACULDADE DE
CIÊNCIAS E TECNOLOGIA
UNIVERSIDADE D
COIMBRA

Guilherme Pinheiro Pereira

Continuous calibration and monitoring for LZ Dark matter experiment

Tese no âmbito do Doutoramento em Engenharia Física, orientada pelo Doutor Vladimir Solovov, pelo Doutor Claúdio Silva e apresentada ao departamento de Física da Faculdade de Ciências e Tecnologia da Universidade de Coimbra.

Novembro 2022

Continuous calibration and monitoring for

LZ Dark matter experiment

Abstract

The LZ (LUX-ZEPLIN) experiment is a dark matter detector located at the Sanford Underground Research Facility (SURF) in the United States. Its main scientific objective is the direct detection of Weakly Interacting Massive Particles (WIMPs). The detector features a dual-phase TPC with the active volume containing 7 tonnes of liquid xenon, observed by 494 photomultiplier tubes (PMT). This thesis presents the methods used by the LZ experiment to reconstruct the position and energy of interactions occurring in the liquid xenon from the signals measured by the PMTs. The main focus is on the calibration techniques that permit in-situ reconstruction of the PMT light response as a function of event position, determination of their dynamic range and saturation profiles and monitoring of their gain. This work demonstrates that all these calibrations can be performed using only background events in the detector, permitting to continuously monitor the important detector parameters without interruptions to the acquisition of the science data as in the case of the regular calibrations. Using these techniques, a record energy resolution of (0.67±0.01)% at 2614 keV was measured for the whole LZ fiducial volume of 5.6 tonnes of liquid xenon. The unbiased position reconstruction with a resolution of better than 1.35±0.13 mm for 164 keV internal conversion electrons from decays of ^{131m}Xe isotope is also demonstrated.

The Slow Control, one of the most vital systems of the experiment, performs a supervisory control

and monitoring of the critical systems of the detector to maintain the stability of the detector operation parameters and guarantee the safety of the detector and the xenon supply. Development and commissioning of the Slow Control was an important part of this work program. The most important tasks performed in this context encompassed the integration of various detector sub-systems with the experiment control, development of the user interface, alarm propagation system and automation procedures to be executed during operations.

Given the complexity of the LZ experiment, the operations involving data acquisition are accompanied by a real-time analysis. This task, to be executed by the Underground Processing Monitor, permits to monitor the state of the detector and the quality of the data trhough a graphical user interface. The development of such an interface was also achieved within the framework of this thesis.

Continuous calibration and monitoring for

LZ Dark matter experiment

Resumo

A experiência LZ (LUX-ZPLIN) é um detetor de matéria escura com o objetivo de detetar os recuos nucleares induzido por interações de WIMP (*Weakly Interacting Massive Particles*).

O detetor, situado na *Davis Cavern* do laboratório SURF (*Sanford Underground Research Facility*) nos Estados Unidos, a uma profundidade de 1478 m, consiste numa câmara de projeção temporal de duas fases com 7 toneladas de xénon liquido equipada com 494 fotomultiplicadores. Esta tecnologia permite reconstruir a posição e a energia de interações que ocorrem no xénon liquido através dos sinais luminosos medidos pelos fotomultiplicadores.

Nesta tese apresentam-se métodos utilizados pela experiência LZ para a reconstrução da posição e da energia depositada pelas partículas ao interagir com o detetor. No trabalho desenvolvido aperfeiçoou-se o procedimento para gerar um modelo de resposta à cintilação e desenvolveram-se novos métodos para uniformizar esta resposta, permitindo melhorar significativamente a prestação dos algoritmos existentes. Além disso, com uma abordagem baseada no conceito de calibração contínua com dados de fundo, foi possível medir o perfil de saturação dos fotomultiplicadores e monitorizar o seu ganho utilizando apenas dados de fundo do detetor sem a necessidade de recorrer a fontes de calibração dedicadas. Estas técnicas permitem obter uma resolução de energia de

(0,67±0.01)% para uma energia de 2611 keV, próxima da linha de energia do decaimento duplo beta sem neutrinos do ^{136}Xe (2458 keV). Em relação à reconstrução da posição, obteve-se uma resolução de, no máximo, 1.35±0.13 mm para uma energia depositada de 164 keV correspondente ao decaimento do ^{131m}Xe.

O desenvolvimento do sistema de controlo de LZ (*slow control*) foi outra das tarefas alcançadas neste trabalho. Neste contexto foram desenvolvidos várias interfaces gráficas, o sistema de alarmes e vários *scripts* de automação. Estes contribuíram para a realização das principais funções do sistema que são assegurar o funcionamento do *hardware* e o fornecimento de xénon no detetor, e garantir a segurança do detetor.

A complexidade da experiência LZ requer que as operações relacionadas com aquisição de dados sejam acompanhadas por uma análise efetuada em tempo real para possibilitar a monitorização do estado do detetor e da qualidade dos dados adquiridos. Neste trabalho desenvolveu-se uma interface gráfica que permite efetuar uma análise preliminar dos dados adquiridos pelo detetor.

Acknowledgements

Before anyone else, I believe the first word of appreciation should be directed to my parents, grandparents and sister, for they always provided unconditional support, and it is thanks to them that I was able to embark in this adventure. It is to them to whom I dedicate this thesis. I also want to express my eternal gratitude to my wife, for being a never ending source of support, for providing a good dosage of laughter and distraction whenever I felt frustrated. For listening to my complaints about conflicting results or my broken code, and also for taking care of me, especially during these last months.

Secondly, I want to thank my supervisors: Cláudio and Vladimir. Their guidance and most importantly, hours of discussion, provided me some of the most rewarding lessons in the course of this PhD. Apart from an extra dose of patience to indulge a stream of questions, I hope that they also gained new insights. A big thanks to the remaining members of the LIP Dark Matter group for their ongoing support, and for the granted opportunity to be part of this adventure in the "hunt" for Dark Matter.

I also want to extend my thanks to the LZ collaboration and its members. They truly go above and beyond to express the concept of a scientific collaboration. This work would not be possible without them.

Finally, I want to thank you, the reader. Without you, the knowledge gathered in this document would

be gaining dust in a bookshelf somewhere. Hopefully whatever page, section, paragraph, you read here, will contribute to a better understanding of the Universe and of the described methods.

This work is supported by a Ph.D. scholarship within the DAEPHYS doctoral programme and funded by the Fundação para a Ciência e Tecnologia (FCT), with the reference PD/BD/142788/2018 and COVID/BD/152669/2022.

Cofinanciado por:

Contents

Symbols and Abbreviations

CoG	Center of Gravity
CMB	Cosmic Microwave Background
DM	Dark Matter
D-D	Deuterium–deuterium
EL	Electron Lifetime
ER	Electron Recoil
FWHM	Full width at half maximum
GdLS	Gadolinium-loaded Liquid Scintillator
GUI	Graphical User Interface
GXe	Gaseous Xenon
HG	High Gain
JSON	JavaScript Object Notation
ICV	Inner Cryostat Vessel
IoT	Internet of things

LDAP Lightweight Directory Access Protocol

LIP Laboratório de Instrumentação e Física Experimental de Partículas

LG Low Gain

LN Liquid Nitrogen

LRF Light Response Function

LRM Light Response Model

LUX Large Underground Xenon

LXe Liquid Xenon

LZap LZ Analysis Programme

LZ LUX-ZEPLIN

MFC Mass Flow Controller

ML Maximum Likelihood

MDC Mock Data Challenge

MOND Modified Newtonian Dynamics

NERSC National Energy Research Scientific Computing Center

NN Neural Network

NR Nuclear Recoil

OCV Outer Cryostat Vessel

OD Outer Detector

PHE Photoelectron

PHD Photons detected

PLC	Programmable logic controller
PMT	Photomultiplier Tube
PTFE	Polytetrafluoroethylene
QA	Quality Assurance
QE	Quantum Efficiency
RGA	Residual Gas Analyzer
RQ	Reduced Quantity
SCADA	Supervisory Control and Data Acquisition
SD	Spin-dependent
SI	Spin-independent
SURF	Sanford Underground Research Facility
TPC	Time Projection Chamber
TCP	Transmission Control Protocol
UPS	Uninterruptible power supply
UPM	Underground Processing Monitor
WIMP	Weakly Interactive Massive Particle
ZEPLIN	ZonEd Proportional scintillation in LIquid Noble gases

Chapter 1

Overview

Nowadays, our knowledge of the Universe is expanding at an ever-accelerating speed, just like the Universe itself. With excellent certainty, we can "look" billions of years into the past and reconstruct its transformation into the present form. We can map how planets, solar systems, and galaxies agglomerate to form cosmic structures, and we have observed extraordinary astronomical objects, such as comets, black holes and neutron stars. Yet, we do not know what most of the Universe is made of. Several pieces of evidence, originating from the analysis of the Cosmic Microwave Background fluctuations, the study of galactic rotation curves and the observation of large cosmic structures such as the ones produced by Baryonic Acoustic Oscillation (BAO), converge to the same result: the baryonic matter, or colloquially, "normal" matter, represents 5% of the Universe, where the remaining 95% are attributed to dark matter and dark energy (20% and 75%, respectively) [1]. However, the true nature of these dark components is still unknown. Currently, one of the most favored explanations for dark matter involves a new class of elementary particles, or WIMPs [2].

The technological advances made in various fields over the past century allowed us to develop different methodologies to build various detectors to probe the elusive WIMP, but, so far, no experiment has made an irrefutable discovery. Among various methods to search for dark matter, the

most straightforward is direct detection, where we look, in an Earth-bound experiment, for their postulated interactions with a target material [3]. This approach can be accomplished using various technologies and target materials. Examples of detectors include: solid state employing semiconductors or crystals, such as the ones developed by CDMS [4], CRESST [5] and DAMA [6] groups; bubble chambers using superheated liquids, developed by the PICO collaboration [7]; and gaseous time projection chamber, such as the DRIFT detector [8], which aim to measure a daily variation in the WIMP recoils caused by the rotation of the Earth. Currently, the only experiment that claims a positive result is the DAMA/LIBRA that reports an annual variation of the signal observed with ultra-radiopure NaI(Tl) scintillation counters [6]. However, these results contradict the null results obtained by the remaining detectors. Besides, in an attempt to validate the DAMA results, the ANAIS group developed a detector of a similar design using the same target materials, yet, no annual variation was observed [9].

This illustrates how challenging is the task of direct DM search. Indeed, direct detection dark matter detectors strive to measure any distinct signal which stands out from the expected interactions composing the background. To this end, these experiments exploit several techniques to minimize the presence of radioactive isotopes in the detector, such as comprehensive selection of the materials, extensive cleanliness protocol and the development of high-efficiency purification/fabrication methods. Moreover, they are often placed deep underground to reduce the contributions of particle from cosmic-ray.

Currently, the most sensitive dark matter detectors (XENON [10], PANDA [11], LZ [12]) are all based on the common technology, namely noble gas dual-phase time projection chamber (TPC) [13]. In this approach, particle interactions with the active medium of a detector (liquid xenon or argon) produce both scintillation photons and ionization electrons. While the photons are promptly registered by photosensors, forming the S1 signal, the electrons drift in the uniform electric field in the vertical direction at constant speed toward the surface and into the gas phase where they produce a secondary scintillation registered by the photosensors as the S2 signal. The event position in the horizontal plane can be reconstructed from the spatial distribution of the secondary scintillation light and the event depth from the time it takes the electrons to get to the surface, i.e., the delay between S1 and S2 signals. The integrals of the S1 and S2 signals are proportional to the energy transferred

by the interacting particle to the medium and their ratio depends on the type of the interaction, i.e., if it involved an atomic electron or a nucleus. The ability to simultaneously reconstruct the energy and position and identify the nature of the interactions occurring in the target material, allows obtaining an excellent background discrimination. Moreover, the outermost volume of the target material provides a natural shield against the ionizing radiation coming from the materials surrounding the detector, resulting in an inner region with an extremely low radioactive background.

The LUX-ZEPLIN (LZ) detector, one of the most sensitive experiments to date, is a dual-phase TPC featuring a sensitive volume that contains 7 tonnes of liquid xenon viewed by 476 photomultipler tubes (PMT) installed in two arrays, to observe the interactions formed within [12]. Currently, the LZ detector has ended its inaugural science run demonstrating a world-leading sensitivity in the search of WIMP with the limit on the WIMP-nucleon cross-section of 6.5×10^{-48} cm^2 for spin-independent scatterings at 30 GeV/c^2 [14]. Although the primary goal of the LZ experiment is the dark matter search, given its large target mass and low backgrounds, the scientific program also includes the detection of rare decays such as, for example, neutrinoless double beta decay of ^{136}Xe [12]. Such observation would constitute the first evidence that the neutrinos are Majorana particles, that is, they are their own antiparticle [15].

Similar to the other TPCs, precise knowledge of event position is essential for background suppression in LZ. To reconstruct the horizontal position, LZ analysis employs the Mercury algorithm successfully used in the past by ZEPLIN-III [16] and LUX [17] collaborations.

In the scope of the presented PhD work, the algorithm was enhanced, by implementing the versatile parameterization scheme for light response functions first proposed in [18]. Moreover, the Mercury algorithm was upgraded to enable the usage of a dynamic subset of PMTs during the reconstruction. This permits to improve the signal-to-noise ratio, by excluding, on a per-event basis, PMTs with signals failing to satisfy signal cutoffs. Moreover, the utilization of a dynamic list permits to exclude malfunctioning or disabled PMTs and even improve the position resolution for high energy events as PMTs operating in a non-linear regime can be excluded.

Originally, the Mercury had to be calibrated with a uniformly distributed monoenergetic radioactive source. In the LUX experiment, this was easily accomplished by injecting a short-lived gamma-ray

source ^{83m}Kr (41.5 keV) into the circulation system in order to bypass the detector's self-shielding capabilities [19]. However, in a tonne scale detector such as LZ, obtaining a uniformly distributed calibration source in the entire volume is difficult. Therefore, we have explored the possibility of using background sources present in the liquid xenon as a standard candle to calibrate the xy reconstruction algorithm. On this subject, we identified two suitable sources for this purpose: ^{222}Rn α-particle (5.5 MeV) and internal conversion electrons from ^{131m}Xe (164 keV).

Mercury light response model allows to predict the signal of a given PMT from the signals of its neighbors, as long as they are all in the linear mode. Based on this fact, this thesis presents a technique to characterize the linearity of the PMTs using only background data acquired during the science run. This technique permits to improve the position reconstruction for high-energy events, resulting in a better identification of particle interactions originating from the TPC wall, and consequently an improvement of the detector sensitivity in this energy region.

Even as the LZ PMTs are kept at very stable conditions, the response of the PMTs is expected to drift with time [20], meaning that periodic calibrations of each individual device are required to obtain a good energy resolution. In the LZ experiment, the PMT gains are monitored by a dedicated LED calibration system, however, these calibrations are typically time-consuming and interfere with normal data taking. Also, during the periods between the calibrations, the gains are found by interpolation and may deviate from the actual values. In this thesis, we present a framework monitor the PMT gain using the S2 signals produced by extracted single electrons, acquired during the science run. This approach, that we called "continuous calibration", greatly improves the granularity of the PMTs calibrations and does not interfere with the regular data acquisition operations.

The walls of the TPC, while made from a highly reflective material, still absorb scintillation light, therefore, interactions occurring closer to the wall, have a smaller light collection efficiency than interactions occurring at the center of the center of the detector. Moreover, the fact that the quantum efficiency of PMTs in the same array can vary, and that some of these devices might not be operating during the long acquisition periods, leads to local abrupt variations of the light collection efficiency of the array. Besides, the amount of S2 light produced by the same charge can depend on the position in the horizontal plane due to slight deviations of the applied electric field from uniformity. These

phenomena lead to position-dependent variations of the measured signals. Therefore, to obtain a good energy resolution, the S1 and S2 signals require the introduction of position-dependent corrections, with the goal of improving the detector energy resolution, background discrimination, and consequently, its overall sensitivity. To this end, we developed position-dependent corrections maps using background data of ^{222}Rn and ^{118}Po α-particles acquired during the science run. Furthermore, the S1 and S2 signals are calculated by summing the output of the PMTs for pulses identified in the same time window. However, for the purpose of energy reconstruction and background discrimination, this summation needs to account for different light collection response of each PMT. In this regard, we present a novel method to produce a light collection correction of the S2 signal, based on individual LRFs.

Achieving a good energy resolution is paramount to obtain an accurate background estimation in the WIMP search region, as it will enable a better identification and quantification of the radioactive sources constituting the background. Therefore, with the objective of demonstrating the excellent capabilities of the LZ detector, and as a means to assert the techniques developed in this work, the energy spectrum of electron recoils in the range of [0.1, 3] MeV was reconstructed from the data acquired during 60 live days of the first LZ science run. The energy resolution of (0.67±0.1)% at 2.614 MeV for the full fiducial of 5.6 tonnes of liquid xenon was achieved. To our best knowledge, this is so far the best energy resolution reported for a liquid xenon particle detector.

One of the main requirements of the LZ detector is the need to operate under stable conditions, as abrupt changes in the liquid xenon conditions lead to variations of the S1 and S2 yields and, consequently, worse resolution for the reconstructed position and energy. Stabilization of the liquid condition is partially accomplished by equipping the detector with a large number (about 100) of temperature sensors installed at various locations to monitor the liquid xenon and provide feedback information to a cryogenic system holding 1800 liters of liquid nitrogen. Moreover, the detector also features a state-of-the-art circulation system, which, through a hot zirconium getter, removes outgassing impurities from the liquid xenon as a measure to improve the quality of the S1 and S2 signals [12].

The operation of a large-scale detector such as LZ requires a sophisticated system to perform

supervisory control and monitoring of the experiment. This task is accomplished by the LZ Slow Control system. One of the tasks performed in the framework of this PhD work was development of various components, namely user interface, alarm system, scripting and automation, access control and historical trend visualizer of the Supervisory control and data acquisition (SCADA) system used by the LZ experiment. Furthermore, to accommodate the stringent data acquisition and calibration operations, the LZ detector performs real-time analysis of the data acquired by the optical sensors. Such analysis, performed by the Underground Processing Monitor (UMP), permits the monitoring of the state of the detector and the quality of the acquired data itself. An additional task accomplished during this PhD work was the development of a web-based graphical user interface to consult the data generated by the UPM analysis.

The main concepts behind the dark matter search are introduced in Chapter 2, which entails a brief overview on some dark matter evidence and its leading candidates. This chapter also describes the technologies used in the direct detection approach, by presenting some of the most prominent experiments in that field in the past 20 years. Chapters 3 and 4 present a detailed overview of the liquid xenon dual-phase TPC technology and of LZ detector technical aspects, respectively. Chapter 5 presents the position reconstruction algorithm used by the LZ detector and new methodologies to produce the corrections of the signals from background data. In this context, the study of energy resolution for high-energy electronic recoils is also presented. Chapter 6 described the techniques to characterize and calibrate the array of PMTs of the LZ TPC. Chapter 7 briefly describes the framework of the UPM analysis and describes with more detail its data structure and the web-based graphical user interface used to consult the data. Finally, Chapter 8 describes the Slow Control system and the SCADA system developed in the scope of this thesis.

Chapter 2

Dark Matter Evidence and Direct Detection

Dark matter! The mention of these words makes most people's eyes shine with curiosity and wonder. What is it? Where is it? How does it affect us? Though its impact and interest only recently captured the attention of the general audience, the scientific community has been working to find its nature for the past century.

In 1933, the Swiss astrophysicist Fritz Zwicky was the first to propose the existence of an excess of non-luminous matter, named dark matter. By studying the redshift of the galaxies in the Coma Cluster (Abell 1656 catalog), Zwicky noticed that their velocity dispersion exceeds 2000 km/s. This result did not agree with the value of 80 km/s obtained when applying the virial theorem[1]. He stated that "In order to obtain, as observed... the average density in the Coma system would have to be at least 400 times greater" [22, 23]. In 1937, Zwicky applied the virial theorem to calculate the mass

[1] This theorem establishes a relation between the kinetic and potential energies of a non-relativistic system composed by discrete particles, and permits to calculate the mass of a large scale system by measuring its size and the velocity distribution of the individual bodies [21]

of the Coma cluster [24]. The difference between the virial theorem mass (4.5×10^{13} $\mathrm{M}_{\odot}$[2]) and the luminous mass (8.5×10^{10} $\mathrm{M}_{\odot}$) was so large that only an excess of mass could explain such discrepancy. With more recent techniques, such as gravitational lensing, the Coma cluster mass is reported to have 1.8×10^{15} $\mathrm{M}_{\odot}$, which differs from the luminous mass of 1.45×10^{13} $\mathrm{L}_{\odot}$, by more than a factor of 100 [25–27].

Decades after the Zwicky studies, the nature of dark matter still remains a subject of heated scientific discussion. However, due to advances in CMB monitoring, by the WMAP and Plank satellites, we now know with amazing precision how much it contributes to the total density of the Universe. Currently, it is accepted that the Universe, in terms of mass density, is made of 75% dark energy, 20% dark matter and 5% hadronic matter, with minor contributions from photons and neutrinos [1, 28].

2.1 Cosmological evidences for Dark Matter

Modern cosmology offers a series of observations that can be explained by the presence of dark at various scales. In the following section, a brief description is provided for a few selected evidences which lay out the foundations for dark matter studies.

2.1.1 Galactic Rotation Curves

One of the most cited pieces of evidence for the existence of dark matter is the study of the velocity of stars versus their radial distribution, called Galaxy rotation curves [29]. By measuring this distribution, it is possible to infer the total mass of a Galaxy. Assuming that most of the Galaxy's mass lies in the central bulge, Newton's orbital mechanics predicts that the velocity of stellar bodies revolving around the Galaxy in the luminous disk should be inversely proportional to the distance from the galactic center. However, stellar bodies revolving at great distances from the Galaxy center do not follow this rule, and instead, their velocity remains constant or can even increase. This can be observed in figure 2.1, where the inner part of the Milky Way Galaxy (R < 5 kpc) seems to be dominated by visible matter and agrees well with Newton's predictions, but for distances beyond this Galactic disk the experimental data cannot be explained, and suggest the presence of a ring-like

[2] Denotes the solar mass

dark matter structure surrounding the Galaxy [29].

This experimental disagreement can be explained with a modification of the law of gravity called MOND (Modified Newtonian Dynamics). In this hypothesis, the gravity acceleration felt by a star can be split into two regimes: a strong field governed by the traditional Newton's equation and a weak field where the acceleration has a linear dependency on the distance [29,30]. This modification does require a dark matter component to explain the revolution of the galaxies, but it fails to explain other evidences such as the Bullet Cluster collision (see section 2.1.4).

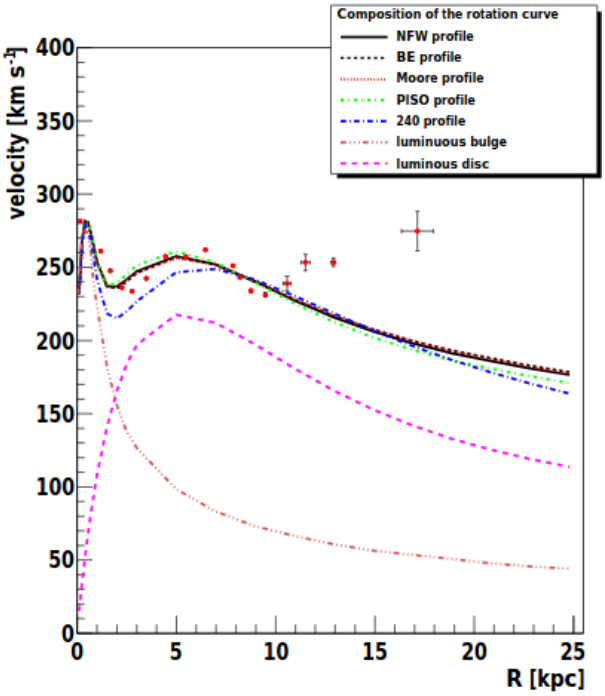

Figure 2.1: The rotational velocity of stellar bodies within the Milky Way versus their distance. For distances greater than 10 kpc the various dark matter density profiles predict a slow decrease in the rotational velocity, but the experimental data (orange dots), acquired using the Doppler shift tuned to the 21 cm line of neutral hydrogen, does not follow the same tendency. The experimental data represents averaged data with 17 radial bins (image from [29]).

2.1.2 Cosmic Microwave Background

Initially, the Universe was a hot and dense plasma where protons and electrons could not bind to form atoms. Due to this high electronic density, photons were frequently scattered, and the Universe was opaque to photons. With its adiabatic expansion, the Universe cooled down, and the first hydrogen atoms were formed as electrons could bind to protons. With this recombination process,

which occurred about 380 thousand years after the Big Bang, the Universe diminished electronic density allowed for the photons to decouple from the plasma and travel unperturbed. This originated to an isotropic and roughly uniformly distributed form of radiation in thermal equilibrium with its environment and with a temperature governed by the Planck's Law for the black body radiation emission. The wavelength of this radiation increased with the Universe's expansion, and today it is observed in the low-energy microwave region, corresponding to a mean temperature of 2.7 K [31]. These photons constitute the Cosmic Microwave Background (CMB), and their angular distribution encodes, so to say, a snapshot of our infant Universe at the end of the recombination.

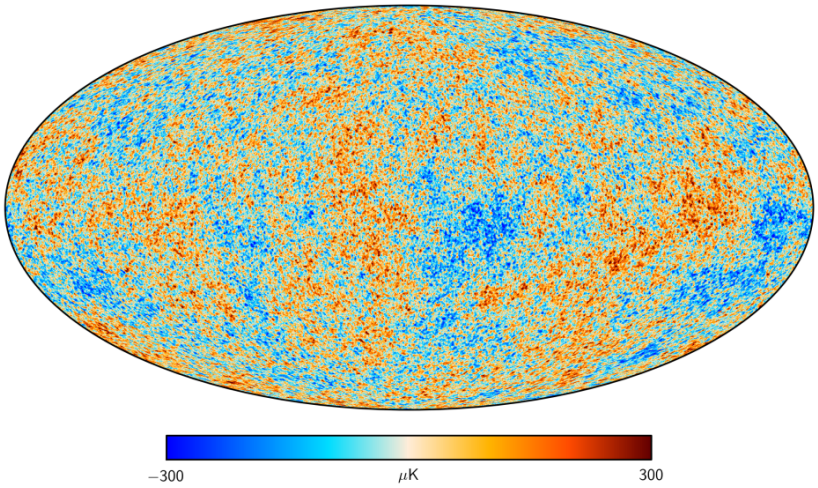

Figure 2.2: Mollweide projection of CMB dispersion measured by the PLANCK satellite in 2015 [28].

As shown in figure 2.2, the CMB is not entirely isotropic, as it contains microscopic fluctuations at the μK scale. These are correlated with quantum fluctuations in the distribution of the primordial plasma that attained galactic dimensions with the Universe inflation.

At the same time, the fluctuations also lead, through gravity, to the formation of regions with a higher concentration of "regular" and dark matter. Consequently, the overall dark matter density in the Universe would directly affect the primordial plasma fluctuations and, indirectly, the distribution of the CMB.

A detailed CMB fluctuations mapping, like the one presented in figure 2.2, provides information about the state of the Universe at the time of the plasma decoupling, with higher temperature corresponding to a higher density of baryonic matter. By studying the CMB temperature fluctuations, it is

possible to calculate the relative densities of baryonic and dark matter, which currently are expected to be 5% and 26%, respectively, to the total mass of the Universe [32]. These measurements are accomplished by producing a power spectrum that characterizes the fluctuations as a function of the angular scale, where the position of the peaks of the spectrum is sensitive to the initial conditions of the Universe [31].

2.1.3 Baryonic Acoustic Oscillations

The early Universe, before the recombination, was an almost homogeneous hot and dense plasma opaque to photons that scatter frequently. Through gravity, baryons and dark matter began to aggregate, originating high-density regions [33]. With the increasing density of these regions, the photons exert an outward force (radiation pressure) that counteracts gravity. As the two forces attempt to find an equilibrium, oscillations in the plasma fluid push spherical waves composed of baryons and photons. The dark matter remained at the origin of the wave since it did not interact with radiation. As the temperature of the Universe decreased, the photons scattered less frequently, which allowed them to decouple from the wave, reducing the photon pressure and leaving behind an almost static shell formed only by baryons (see figure 2.3 for a representation of this phenomenon).

This massive shell, whose radius — the sound horizon — is highly related to the dark matter's initial density, is nowadays the housing for the cosmic structures of galaxies that we can observe in the Universe [34]. Within the observable Universe (measured radius of 150 Mpc), the Baryonic Acoustic Oscillations predict a dark matter density of $\approx$0.2 in the Universe, which is consistent with the results obtained by the CMB measurements [35].

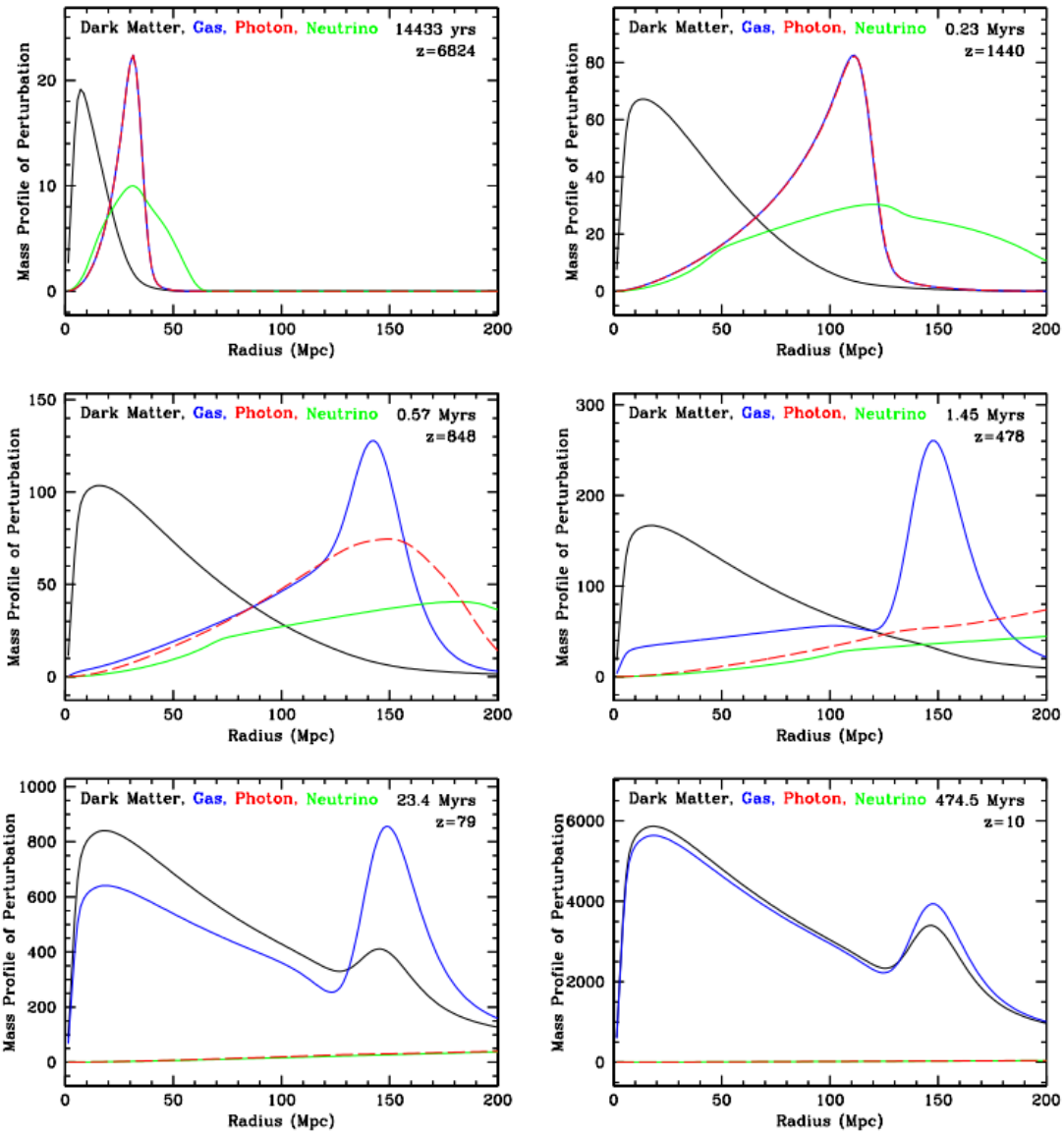

Figure 2.3: Mass profile distribution as a function of the comoving distance with respect to the spherical wave origin. Each plot illustrate the evolution and propagation of a baryonic acoustic wave. After the photonic decoupling (center left) the wave stalled and through the infinite range of gravity its protuberance became less salient [33].

2.1.4 Bullet Cluster Collision

The Bullet Cluster (1E0657–558) resulted from a frontal shock between a smaller cluster moving in the right direction and the main cluster located in the left (figure 2.4). During this shock, the increasing pressure caused the intergalactic gas to heat and produce X-rays. This is represented in the form of a heatmap of figure 2.4, obtained from the Chandra X-ray space telescope, and

represents the luminous mass of the respective clusters.

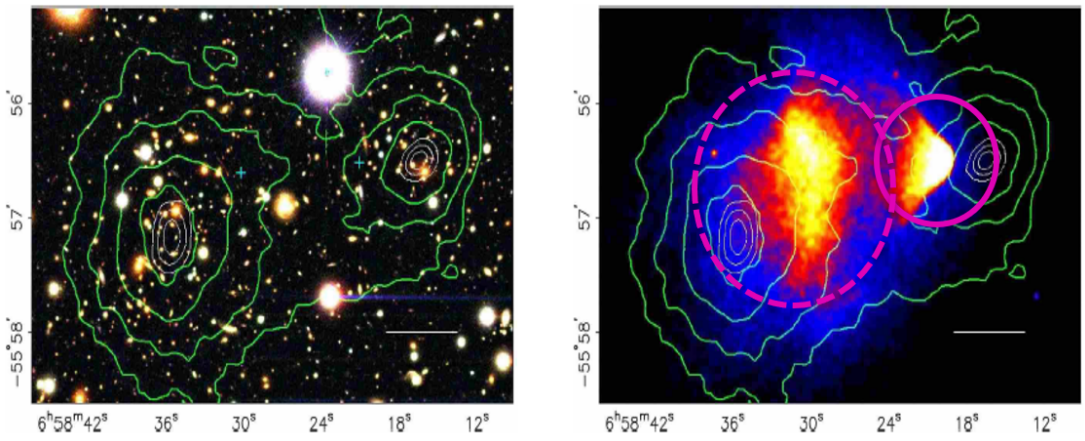

Figure 2.4: Images of the bullet cluster formed as a result of the merging of two clusters, currently separated by 0.72 Mpc, both highlighted in the right image: the less massive is represented by a dashed circular pink and the heavier is represented by a solid pink circular line. The left picture was taken by the Magellan telescope, and the right picture is an X-ray map acquired by the Chandra telescope. The heatmap shows the X-rays emitted by the intergalactic gas during this collision and represents the "ordinary" matter of both clusters. The potential lines reveal, by weak lensing, the non-luminous matter which did not interacted during the collision. The white line is a 200 kpc scale [36].

The effect of Gravitational lensing, which occurs when the light observed from stellar bodies is distorted by a massive object present in the same line of sight, offers an independent method of mapping the mass distribution in the cluster. With this method, it is possible to measure a significant amount of matter (represented by the iso-lines in figure 2.4) that did not interact during this collision. Without the presence of dark matter, the shape of the iso-lines would follow the shape of the heatmap. However, this is not what is observed, and instead, the luminous mass is clearly displaced from the iso-lines of the mass distribution inferred from gravitational lensing [36].

2.2 Dark Matter Candidates

Although there is some consensus about the abundance of the dark matter in the Universe, its true nature is an open subject, as no experiment was able to perform a positive detection. Currently, the best hypothesis is that the Dark Matter consists of a new particle outside the Standard Model [37].

In the following paragraphs, some candidates for dark matter, such as axions, sterile neutrinos, light dark matter, and Weakly Interacting Massive Particles (WIMP), are briefly introduced. As shown in figure 2.5, there is a panoply of dark matter candidates covering a vast range of masses.

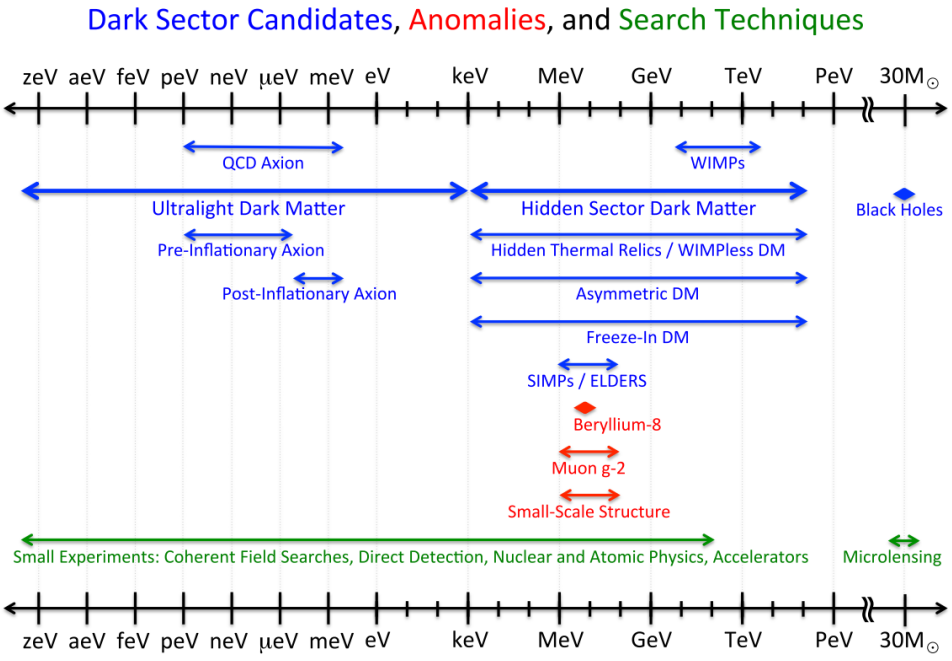

Figure 2.5: Overview of some dark matter candidates and its mass range [37].

2.2.1 WIMP

Weakly Interacting Massive Particles, or WIMPs, are perhaps the most motivated dark matter candidates. They refer to a class of non-baryonic and non-relativistic particles with a mass in the approximate range from 1 to 10^5 GeV. These candidates do not possess electromagnetic charge and interact with the baryonic matter with a very low cross-section ranging from 10^{-41} to 10^{-52} cm^2 [2,38].

In the early Universe, given its extremely high temperature, WIMPs would be produced at the same rate as they would be annihilated,

$$\chi\chi \leftrightharpoons MM, \tag{2.1}$$

where χ represents a WIMP particle, and M represents a standard model particle. With the Universe's expansion, the temperature decreased, resulting in a much lower rate of WIMP production. However, their mean free path also increased and their annihilation became less frequent, resulting in a stabilization, or *freeze-out*, of their abundance [34]. The critical aspect of WIMPs, often referred to as "the WIMP miracle," is that their abundance, naturally obtained when considering the weak force scale interaction, is mass-independent. This implies that the interaction cross-section is the main factor for the production/annihilation [2, 38].

2.2.2 Light Dark Matter

As the increasing sensitivity of dark matter experiments continues to add constraints to the dark matter most promising mass range of 10 GeV to 10 TeV, lower regions in the keV to 10 GeV region become more relevant.

Nuclear recoils-based experiments could be used to scan the light dark matter range. However, these possess a high energy threshold (>1 keV) compared with the meV-scale energy deposition expected by light dark matter candidates. In this case, better results can be achieved with semiconductor or scintillator detectors sensitive to dark matter coupling with electrons which translates into an energy threshold low enough to probe dark matter with masses in the MeV region [39].

Light dark matter is an attractive candidate, as other detectors are excluding higher mass ranges. Furthermore, the annihilation of positrons, which in this context are a product of the light dark matter self-annihilation, may explain the origin of 511 keV gamma rays that were detected in our Galaxy core by the INTEGRAL/SPI observatory [39].

2.2.3 Axions

The axion is a theorized boson that originates from Peccei–Quinn theory (PQ solution). This theory attempts to explain the nonexistent CP (charge-parity) violation in strong interactions (strong CP

problem). Despite having a low mass ($\approx 10^{-6}$ eV), the axion is a non-relativistic non-thermally produced particle, whose main long-range interactions are gravitational and may exist with the same density as that of dark matter [40].

These characteristics grant the axions the status of dark matter candidate with the added interest that it could also solve the strong CP problem.

2.2.4 Sterile neutrino

The sterile neutrino is a hypothetical particle, distinguished by the fact that it is observed with a right-handed chirality[3], as opposed to the active neutrinos [2]. Such sterile particle was theorized to fulfill the requirement that every fermion can be observed with either right-handed and left-handed chirality.

Interacting only via gravity as does not couple with weak force, the sterile neutrino would have been created in the early stages of the Universe under high temperatures, possess a neutral charge and a lifetime extending than that of the Universe. If its mass is confirmed to be in the 1-30 keV range, it can be a strong candidate for dark matter as it could be produced with the same abundance [2, 38].

2.3 Direct Detection

There is a vast range of cosmological evidence for dark matter, which together make a compelling argument favoring its existence. However, the experimental search for dark matter is complex due to its unknown nature. This can be accomplished with three main approaches: indirectly, directly or by production. As the name indicates, in the "production method," dark matter particles are created in an accelerator, and in this case, a missing transverse energy is detected. By itself, this approach cannot distinguish a dark matter candidate from any other neutral particle, as such would also be seen as missing energy. This method, however, provides the best way to characterize such a candidate. Nonetheless, collider-based experiments such as the Tetravon at Fermilab and CMS at the LHC have been constraining the limits of the dark matter mass [41, 42].

[3] Chirality of a particle is a property as abstract as the spin. Where the particle is "spinning", when in fact it is not. The chirality can be compared to the helicity (sign of the spin vector projected to the momentum vector), but this is an intrinsic property which does not vary with the observer.

The indirect methods detect the decay or annihilation products of dark matter particles in the Galaxy, in the form of gamma rays, neutrinos, cosmic rays and antiparticles [3]. These processes would generate products with well-defined energies that produce characteristic lines in the energy spectra of particles coming from the regions in the Milky Way with high dark matter density. The experiments using this method probe the galactic core or planar regions, looking for specific signature in the energy spectra of the incoming particles. This is the case with the XMM-Newton satellite or the Fermi-LAT space telescope [3, 38, 43].

The direct detection method consists of observing the signals generated when dark matter interacts with "normal" matter (henceforth referred to as the target or active material). Considering the case of elastic scattering, the rate of dark matter events, R, with a given recoil energy, E_R, in a target material with a nucleus mass of m_N, can be written as [44]:

$$\frac{\mathrm{dR}}{\mathrm{d}E_R} = \frac{\rho_{DM} M}{m_N m_\chi} \int_{v_{min}}^{v_{miax}} v f(\vec{v}, \vec{v_E}) \, \frac{\mathrm{d}\sigma_0}{\mathrm{d}E_R} \, \mathrm{d}^3 v, \tag{2.2}$$

where ρ_{DM} is the dark matter local density, M is the detector active target mass, m_χ the mass of the dark matter particle (which, to simplify the following discussion, it is considered to be the WIMP). The v_{min} is the minimum velocity required for a WIMP to cause a detectable recoil and is expressed with $\sqrt{E_{Rmin} m_N / 2\mu^2}$ where μ is the reduced mass of the target nucleus to WIMP system, and E_{Rmin} is the energy threshold of the detector. The escape velocity of the Milky Way (544 km/s [44]) is denoted by v_{max}. The velocity of the WIMP particle in the frame of the Earth is denoted by $\vec{v}$ and $\vec{v_E}$ is the Earth velocity with respect to the rest galactic frame.

In the context of direct detection, the dark matter halo is assumed to be an ideal gas with no bulk rotation and, as a consequence, the velocity distribution follows a Maxwell-Boltzmann distribution [45]:

$$f(\vec{v}, \vec{v_E}) = \frac{1}{(\pi v_0^2)^{\frac{2}{3}}} e^{-(\vec{v}+\vec{v_E})^2 / v_0^2}, \tag{2.3}$$

with v_0 representing the most probable speed of the Maxwell-Boltzmann distribution.

The Earth's velocity relative to the galactic center can be expressed by the sum of its orbital velocity

projected on the galactic plane and the tangential velocity of the Sun, as described in the following equation [6]:

$$v_e(t) = v_s + v_o \cos(\theta) \cos(\omega t_d), \quad t_d = t - t_0, \tag{2.4}$$

where v_e represents the Earth's velocity at a given day of the year t, v_s is the tangential velocity of the Sun (220 km/s), v_o and θ are the orbital speed and plane inclination of the Earth's orbit (≈30 km/s and 60º respectively), $\omega = {}^{2\pi}/_{T}$ where T is 1 year and t_0 is the time when the orbital speed of Earth is at maximum (June 2nd).

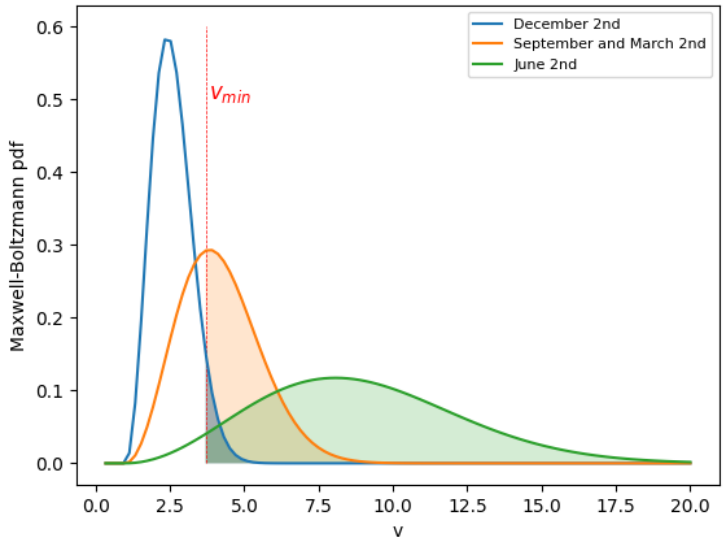

Figure 2.6: Exemplification of the annual variation mechanism: the alteration of the Maxwell-Boltzman distribution is caused by the movement of the Earth around the Sun and the relative speed regarding the population of galactic dark matter particle. The highlighted area represents the detectable population of WIMPs and v_{min} represents the velocity associated with the energy threshold.

The movement of the Earth around the Sun originates to a shift of the mean of the Maxwell-Boltzman distribution regarding the population of dark matter particles. Consequently, as expressed by equation 2.2, the rate of events, which depends on the integral of this distribution truncated by a given minimal threshold velocity, is expected to exhibit an annual variation (see figure 2.6). The measurement of this annual modulation can be used by dark matter experiments to assert the detection of dark matter candidates (see section 2.3.2.1).

Due to its high De Broglie wavelength, WIMPs interacts coherently with all nucleons of the target

nucleus with a cross-section, σ_0, given by [44]:

$$\frac{\mathrm{d}\sigma_0}{\mathrm{d}E_R} = \frac{m_N}{2v^2\mu^2}\left[\sigma_{SI}F_{SI}^2(E_R) + \sigma_{SD}F_{SD}^2(E_R)\right]. \tag{2.5}$$

Which is a combination of two terms associated with spin-independent (SI) and spin-dependent (SD) cross-sections. The components F_{SD} and F_{SI} are form factors corrections to account for the loss of coherence with high nucleus mass targets. Typically, F_{SI} is given by the so-called Helm factor. The SI cross-section is expressed by [44]:

$$\sigma_{SI} = \sigma_n \frac{\mu^2}{\mu_n^2}\frac{\left[f_p Z + f_n(A-Z)\right]^2}{f_n^2} \approx \sigma_n A^2 \frac{\mu^2}{\mu_n^2}, \tag{2.6}$$

where Z is the atomic number of the target number, σ_n is the WIMP-nucleon cross-section and μ_n is the reduced mass of the WIMP-nucleon system. The terms f_p and f_n represent the SI coupling strength with protons and neutrons, and, if $f_p \approx f_n$, the SI cross-section becomes proportional with the target mass number squared, A^2.

The differential SD cross-section for a moment transfer q, with a nucleus of total nuclear spin J, is given by [44]:

$$\frac{\mathrm{d}\sigma_{\mathrm{SD}}}{\mathrm{d}q^2} = \frac{8G_F^2}{\pi v^2}\left(a_p\left\langle S_p\right\rangle) + a_n\left\langle S_n\right\rangle\right)^2 \frac{J+1}{J}\frac{S(q)}{S(0)}, \tag{2.7}$$

with $\left\langle S_p\right\rangle$ and $\left\langle S_n\right\rangle$ representing the expected values for the protons and neutrons spins in the nucleus and $a_{(p,n)}$ expressing the SD coupling strength with protons and neutrons. The term $S(q)$ is the spin-structure function of the target nucleus and G_F the Fermi coupling constant.

As one can notice, the expected rate of WIMP events is highly sensitive to the target material. Due to the A^2 dependency of the SI cross-section, the interaction rate is expected to increase with the atomic mass of the target material. However, this would happen at the expense of a reduction in the recoil energy, making the interactions more difficult to detect, thus reducing the detector sensitivity for low WIMP masses. Also, attention must be paid to the isotope composition of the target. Isotopes with even numbers of protons and neutrons, with a null nuclear spin, have negligible contributions to SD interactions [46], which favors materials with large fractions of non-zero spin

isotopes. Moreover, the purity of the target material plays an important role in the quality of the acquired signals. Therefore, a detector would yield either a material that can be manufactured with high purification standards, such as scintillators crystals (NaI, $CaWO_4$), or semiconductor (Ge, Si), or a material that can be continuously purified on-site with a dedicated system, such as liquefied noble gases (Xe, Ar). Also, the target material must possess no long-lived radioactive isotopes, or their contribution needs to be well measured and subdominant to the background contribution of the detector materials.

Although the dark matter density distribution has not yet been directly measured, its value can be inferred from the rotation curve of the Milky Way [47]. In the vicinity of Sun, at the distance of 8 kpc from the galactic center, is it about 0.3 GeV/cm^3 [44, 47][4].

With equation 2.2 it is possible to calculate the sensitivity of a detector for various masses of a dark matter particle. Figure 2.7 provides a good overview of how various parameters related to the detector design and data acquisition program affect this sensitivity. In this figure, the black curve presents a reference value. From the left plot, a lower energy threshold results in a lower v_{min}, which, by extending the lower limit of the integral in equation 2.2, permits to probe smaller cross-sections. A small target nucleus shifts the sensitivity curve to the left due to a lower energy threshold. But it also decreased the detector sensitivity (higher cross-section) towards the high WIMP masses due to a worsening in the σ_{SI} ($\propto A^2$). An increasing of the exposure, either by increasing the detector target mass or duration of acquisition, shifts the sensitivity curve downwards. However, from the right plot in figure 2.7, the sensitivity increases asymptotically with the duration of acquisition (higher exposure for a fixed target mass). An improved discrimination between the background and the expected signal improves the overall sensitivity.

As shown in the right plot of figure 2.7, the background contribution plays a critical role in the overall sensitivity of the detector. A WIMP is assumed to induce a nuclear recoil (NR) in the target material, while a background, mainly from γ-particles and betas, produces an electronic recoil (ER). Cosmic-ray muons (inducing nuclear recoils) and radiogenic neutrons are a concerning source of background, as they produce a signal indistinguishable from the one produced by a WIMP.

[4] This means that a bottle containing 1 liter of Porto wine can have 3 WIMPs (assuming a mass of 100 GeV).

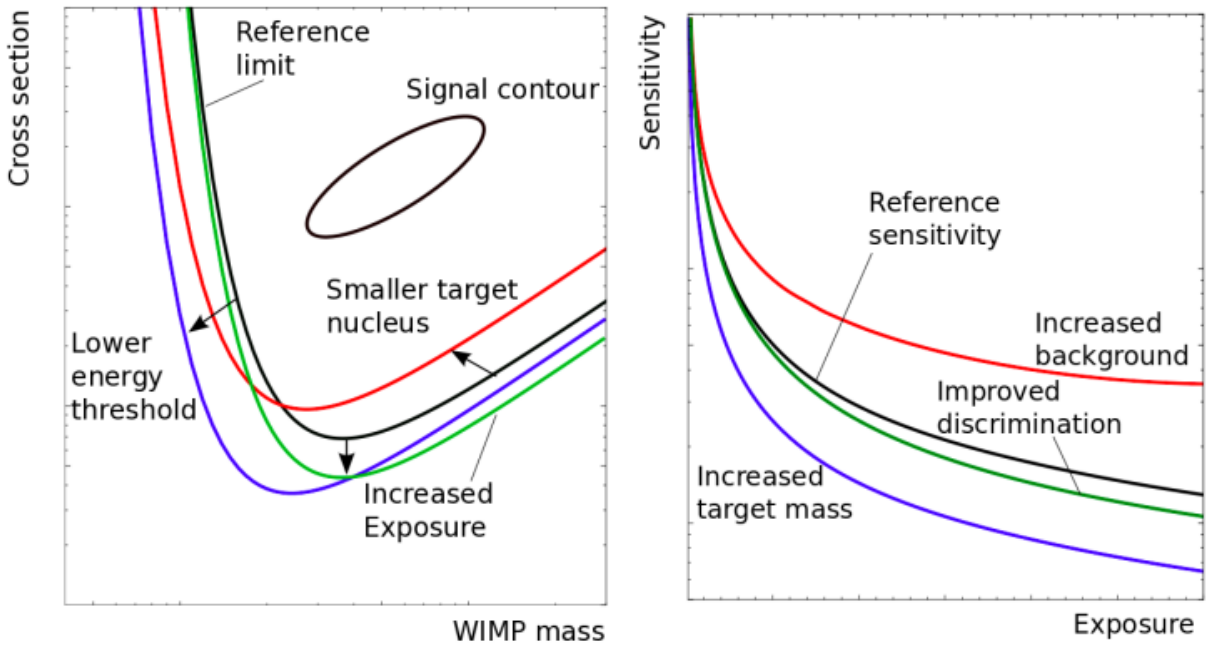

Figure 2.7: Effect of the sensitivity for different characteristics of a hypothetical detector as function of the WIMP mass (left) and the exposure time (right). The closed curve shows how a positive detection of dark matter would be displayed. The open colored curves demonstrates the alteration of the detector sensitivity with respect to the reference curve (figure from [48]).

There are various tactics to mitigate the background contribution. These include, for example, selecting appropriate materials with low and well-studied radioactivity or/and that can undergo cleaning treatments to decrease their radioactivity further. Dark matter experiments are also installed deep underground and shielded with layers of a given material (e.g., water, paraffin, lead, cadmium) to reduce the external background rates to insignificant levels. Finally, the last component consists of background rejection, which can be accomplished with a veto system to tag particle interactions that scatter in both the active volume and an additional layer of scintillating material surrounding the detector.

An additional background rejection technique is done with an event topology analysis. Such analysis develops the required algorithms to discriminate a NR from an ER. This approach takes advantage of the fact that most technological approaches detect an event from at least two of three channels: scintillation, ionization, phonons. In such cases, the topology of the event is inferred from the ratio of the used channels, as an NR and an ER would yield distinct ratios. Also, some detector resort to pulse shape discrimination techniques to distinguish NR from ER events, such as directional-based

detectors (DAMA/LIBRA, DRIFT) or Argon-based TPCs.

Within the direct detection, there is a wide range of possible methodologies and techniques capable of achieving world-leading sensitivities in dark matter searches. The following sections will present some detectors and technologies used to scan a vast range of WIMP masses:

- Semiconductor technologies capable of probing WIMPs with low mass, such as the CDMS (Cryogenic Dark Matter Search);
- Single channel scintillation, such as the DAMA experiment (Dark MAtter) which aims to detect the annual modulation of WIMP interaction rates caused by the Earth moving around the Sun;
- Phonons and photons formed in crystals operating at cryogenic temperatures, such as the ones used by the CRESST detector (Cryogenic Rare Event Search with Superconducting Thermometers);
- Bubble chambers to detect WIMP recoils in superheated liquids, such as the ones developed by the PICO group;
- Directional experiments, such as DRIFT (Directional Recoil Identification From Tracks), attempt to measure a variation in the direction of WIMP recoils caused by the rotation of the Earth;
- Additionally, under the scope of this thesis, special attention is given to liquid xenon dual-phase TPCs (Time Projection Chamber) detectors, such as XENON, PandaX, ZEPLIN and LUX (Large Xenon Underground), which measure charge and light signals generated by WIMP nuclear recoils in a chamber filled with Liquid Xenon.

2.3.1 Semiconductor

Semiconductor-based detectors, such as the CDMS represented in figure 2.8, aim to detect nuclear recoils induced by low mass WIMPs ($\leq$40 GeV), using cryogenic semiconductor detectors operating at a very low temperature ($\approx$40 mK) [4].

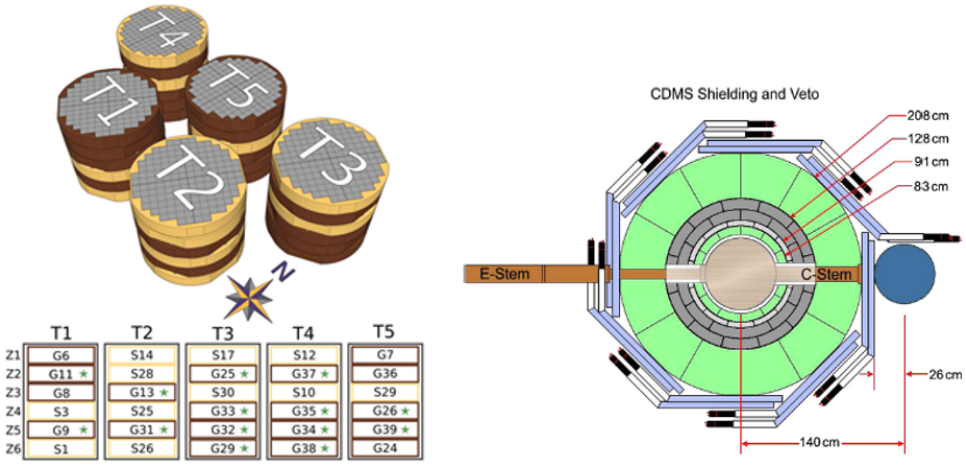

Figure 2.8: Representation of the CDMS II detector, with the left image showing the arrangement of individual silicon (S) and germanium (G) detectors, and the right image presenting the detector viewed from above: Inner polyethylene (green), inner lead (light grey), outer lead (darker grey), outer polyethylene (green), and muon-veto scintillator counters (blue) coupled with light guides and PMTs (white and black). The cooling system is represented in dark blue and the left brown tube labeled “E-stem” provides electronic connection (figures taken from [49]).

These detectors typically consist of cylindrical crystals of a semiconductor material (Ge or Si) arranged in several towers, as shown in figure 2.8. When a particle scatters a nucleus of the active material in one of the towers, the nuclear recoil energy is spent on producing electron-hole pairs and phonons. An electric field (3 V/cm for Ge and 4 V/cm for Si) drives the electrons vertically toward one of the flat faces of a crystal, where they are collected either by an inner aluminum electrode that covers 85% of the crystal face or by an outer ring. The outer ring defines a fiducial volume to exclude electronic recoils (that can originate from β emitters, photoelectrons or photons), which occur within 10 µm of the detector periphery and can be misclassified as nuclear recoils due to a reduced electronic collection [4]. The opposite flat face of the crystal has an array containing thousands of cryogenic phonon detectors, named transient-edge-sensors (TES) [4]. A TES consists of a biased superconducting device operating under cryogenic temperatures which, upon a phonon interaction, briefly shifts into a “normal” conducting regime. This produces a signal in a coupled SQUID (superconducting quantum interference), an ultrasensitive magnetometer device. Groups of TESs, defining quadrants, are connected in parallel to create a single channel, which is then connected in series with a coil. As the conducting regime shift occurs, the magnetic field pulse generated by the coil is detected by the SQUID. The event position is calculated either by measuring the relative phonon amplitude between the four quadrants, which provide the xy coordinates or by calculating the rel-

ative charge amplitude between the main electrode and the outer ring, which defines the radius at which the event occurred [50].

The energy of a recoil is calculated by measuring the energy of the phonons. The ER rejection is based the ratio between the charge and the phonon signals is higher for ER than for NR. This technology yields a high rejection efficiency (>99%) in the 10—100 keV region [49]. The SuperCDMS, which uses the semiconductor technology, reported in the year of 2020 a cross-section of 8.7×10^{-34} cm^2 for a WIMP mass range of 0.5 to 10^4 MeV/c^2 [51].

2.3.2 Scintillator crystals

Solid-state detectors taking advantage of the scintillation properties of a target crystal are, similarly to semiconductors detectors, suitable to probe dark matter low mass range due to their low energy threshold (1—10 keV). In this regard, two types of detectors will be presented: pure scintillation detectors, that attempt to detect an annual variation of the signal, and detectors measuring both photons and phonons generated in scintillation crystals operating at cryogenic temperatures.

2.3.2.1 Scintillation-only detector

A pure scintillation detector acts as a scintillation counter to observe an annual variation in the rate of events. One of the most famous detectors using this approach was developed by the DAMA/LIBRA groups and their predecessor DAMA/NaI. With 250 kg of active material, this detector is constituted by a stack of 5×5 inch NaI(Tl) highly radio-pure crystals. Each crystal is wrapped in PTFE tape to maximize the light collection and coupled to a PMT [6].

Through the NaI LIBRA experiment series, the DAMA group reported an annual modulation with a confidence level of 12.9σ, for a total exposure of 2.46 tonne x year, for single hit events in the range of 2-6 keV, as required for a dark matter positive result. The period (0.999 ± 0.001 year) and phase (145 ± 5 d, May 25) of the measured signal are compatible with the expected parameters associated with the Earth's orbital movement. The total modulation amplitude was 0.0103 ± 0.0008 cpd/kg/keV (see figure 2.9) [6].

The values reported by this group are disputed by the general scientific community due to the

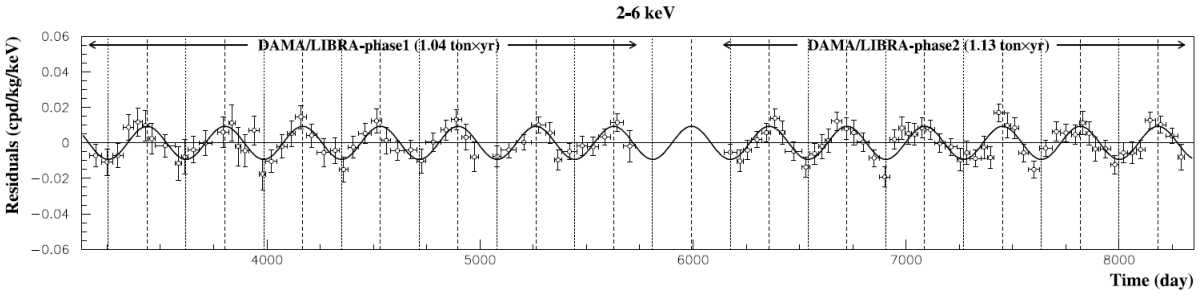

Figure 2.9: DAMA/NaI and DAMA/LIBRA results for single-hit scintillations in the 2-6 keV region, criteria for WIMP-like events. The cosine line represents the predicted modulation with the same parameters used in equation 2.4 [6].

null results obtained by other experiments with better sensitivity, such as the CDMS, XENON10, XENON100 and LUX [45]. Furthermore, a detector of a similar design, employing 112.5 kg of NaI(Tl), was developed by the ANAIS group to "shed light on the DAMA/LIBRA conundrum." This group reported an absence of an annual modulation in a run of 1.5 years [9].

2.3.2.2 Scintillation and phonons

The crystals operating at cryogenic temperatures can be employed to measure both scintillation photons and phonons generated by the WIMPs nuclear recoils [5, 52]. One of the most advanced detectors using this approach was the CRESST-II, represented in figure 2.10. It contained up to 33 cylindrical scintillation crystals of $CaWO_4$, each weighing 300 g and operating at 10 mK [5].

A thin film of tungsten, evaporated on the active material, acts as a TES, which, upon absorption of phonons, induces a signal in a SQUID. The scintillation photons are detected by a light sensor in the form of a silicon-sapphire wafer. These wafers are also equipped with a TES to measure the energy of the photons absorbed in silicon [5].

The total energy deposited by a given particle can be reconstructed only with the phonon signal due to its high sensitivity and the fact that its yield is independent of the particle type. The scintillation signal is used to improve the discrimination of electron recoil backgrounds since these have a higher relative light yield than nuclear recoils. The entire setup is placed inside a highly light reflective housing to maximize the light collection, and the detector is surrounded by layers of copper, lead and polyethylene, with an additional muon veto system in the form of several panels of scintillation

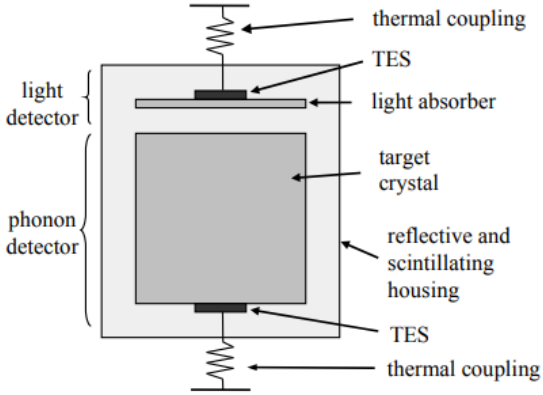

(a) Representation of the CRESST-II crystal modules.

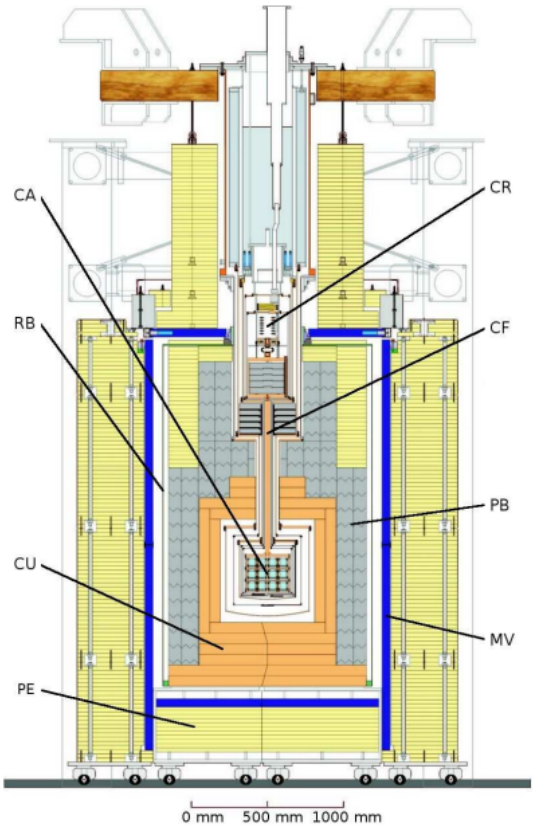

(b) Representation of the CRESST-II shielding system.

Figure 2.10: Overview of the CRESST-II detector, with a carousel (CA) to allow the installation of several modules. A 1.3 m long cooper cold finger (CF) provides the temperature transfer to the cryostat. The shielding system consists of cooper (CU), lead (PB) and polyethylene (PE). A radon box (RB) prevents the penetration of radon into the detector. In blue, the veto system (MV) tags muon events [5].

plastic [5].

The CRESST-III group reported in 2019 a cross-section in the range of 10^{-35}–10^{-38} cm^2 for a mass of 0.2 to 1 GeV/c^2 [53].

2.3.3 Superheated liquids

A sample of highly purified liquid can stay for some time in a superheated state, i.e., at a temperature above its boiling point without boiling due to a lack of nucleation centers where gas bubbles can start to grow. Under these conditions, the liquid is metastable and, when a recoil occurs, it creates a nucleation point where a microscopic vapor bubble is formed. The nucleation and continuous growth of such bubbles generate acoustic waves, and if the density of the deposited energy is above

a certain threshold, the bubble will be optically visible [7].

By taking advantage of this phenomenon, it is possible to develop an apparatus capable of detecting nuclear recoils produced by dark matter particles. The main advantage of this technology is that the bubble nucleation process is mostly insensitive to electronic recoils, making the detector impervious to most of these backgrounds. Furthermore, detectors using this technology have a low energy threshold (1.8 keV) that can be achieved with inexpensive target materials. In addition, these detectors are easily scalable due to their simple geometry, and the target material can be easily interchanged, providing the proper temperature and pressure conditions to achieve the superheated state [7].

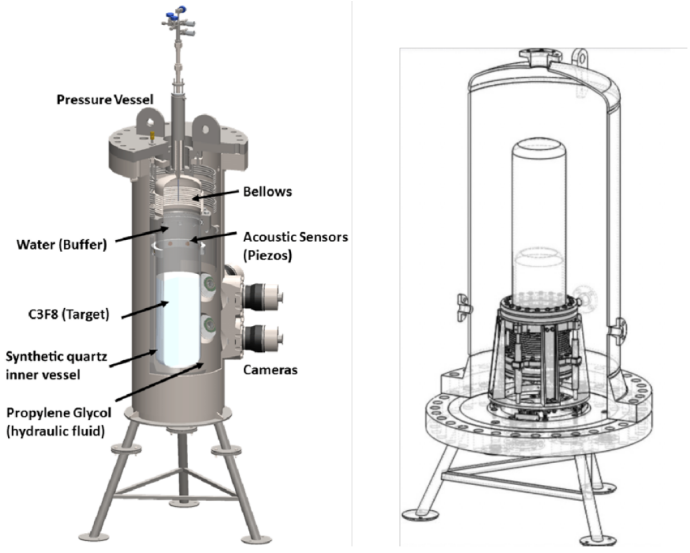

Figure 2.11: Diagrams of the PICO-60 (left) and PICO-40L (right) detectors, the “right-side-up” design of the PICO-40L permitted to remove a water buffer which had complications involving background nuclear recoils induced by water droplets present in the active volume (figures from [7]).

The PICO collaboration, which started in 2013, develops detectors operating at SNOLAB at a depth of 2 km, employing the bubble chamber technique to detect nuclear recoils in superheated liquids like C_3F_8. The presence of ^{19}F, with an odd number of nucleons, makes the detector particularly sensitive to spin-dependent WIMP-proton interactions (equation 2.7).

These detectors consist of a vertical jar-shaped quartz vessel that holds the active material. The vessel is equipped with piezo-electric acoustic sensors to measure the acoustic power generated by recoil-induced bubbles and high-speed cameras to monitor the superheated liquid continuously. The

cameras have the dual functionality of triggering the DAQ when bubbles nucleation is detected and providing the necessary information to reconstruct the position of the recoil [7]. The most concerning background is the neutrons originating from the interaction between muons and the materials surrounding the detector. Consequently, to reduce the muon flux, the detector is installed underground and placed inside a water tank as it provides shielding against external neutrons. Furthermore, a significant fraction of neutron events occurring in the active volume can be discriminated as they produce multiple nucleation sites as opposed to WIMP interactions [7].

Recently, in 2019, the PICO-60 with 52 kg of C_3F_8 achieved a WIMP-proton sensitivity of $\approx 10^{-41}$ cm^2 for a WIMP mass of 25 GeV [7]. The PICO-40L, currently in the final commissioning stage, will serve as a prototype for a ton scale detector, the PICO-500 which is in the design stage [54].

2.3.4 Directional detectors

Since the WIMP halo of the Milky Way is not expected to have a bulk rotation, the WIMPs passing through the solar system should resemble a “wind” blowing in a direction opposite to the movement of the Sun through the Galaxy. With respect to a point of reference located on Earth, there is an apparent variation of the “wind” direction caused by the Earth rotation around its axis.

A directional detector attempts to detect WIMPs by observing a correlation between the direction of nuclear recoils and the sidereal day (period of Earth’s rotation relative to positions of distant stars). With this approach, the results are less prone to misinterpretations as an external source is less likely to mimic this daily variation, and, compared with the DAMA experiment, shorter acquisition periods are required to assert the detection of the WIMP signal ($\approx$2 months) [55].

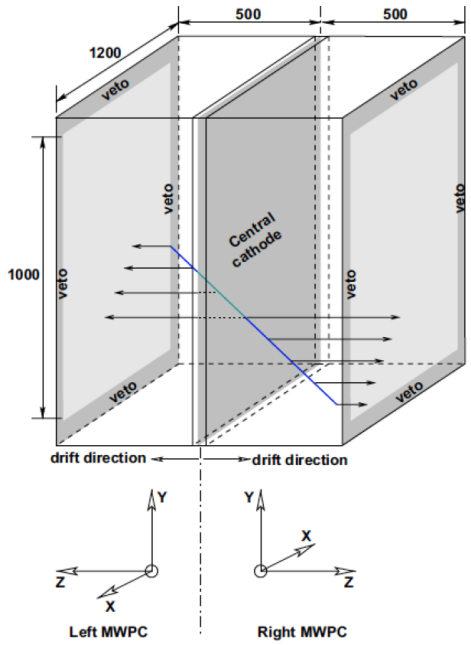

Figure 2.12: Schematic of the DRIFT detector, with a central cathode shared by two time projection chamber [8].

The DRIFT detector (figure 2.12) consists of two back-to-back ion Time Projection Chambers (TPCs) filled with CS_2 gas at low pressure (53 mbar). The two chambers share a common cathode with an applied HV of 34 kV, creating a uniform electric field in each half of the detector. A nuclear recoil, preferably caused by a WIMP interaction, ionizes the gas along its path. The ionization electrons are rapidly captured by highly electronegative CS_2 molecules, forming negatively charged ions. These ions are drifted at a speed of 26 m/s, by the electric field, towards a multiwire proportional counter (MWPC) placed at the readout face of the TPC. There, in the presence of the MWPC strong electric field, the electrons detach from the CS_2 ions and form electron avalanches, amplifying the original charge signal. Due to the low pressure in the vessel, a nuclear recoil from a WIMP is expected to form a track with a few millimeters, enabling the measurement of the recoil direction with sufficient resolution to observe daily variations.

Since there is no method to discriminate neutron recoils from WIMP recoils, the detector must be protected from neutron background. For this purpose, the TPC is surrounded by 67 cm thick polypropylene pellets and placed in the Boulby Underground Laboratory in the United Kingdom at a depth of 1100 m (2800 mass of water equivalent). This ensures a neutron background rate of 1 or

less events per year. Most of the backgrounds, which originate from the alpha decay of Rn and its daughters, are discriminated by the track length. Since these particles have low stopping power, the tracks are considerably longer than the those produced by nuclear recoils [8].

The DRIFT experiment detected no positive signal in a 54.7 days exposure spin dependent run in 2017, which reached a sensitivity of 2.8×10^{-37} cm^2 at 100 GeV/c^2 [56].

2.4 Liquefied Noble gas dual-phase TPC

Detectors of this type are currently leading WIMP searches in sensitivity, as they can be relatively easily scaled to multi-ton targets. Their typical design is a cylindrical vessel filled with the target material (liquid xenon or argon) with a layer of the corresponding gas on the top. The signal readout is done via optical sensors, typically arranged in two large arrays: one in the gas phase at the top of the detector and the other in the liquid at the bottom. See chapter 3 for a more detailed description of this technology, with a focus on the usage of liquid xenon.

A recoil in the target material produces a flash of scintillation light and a track of ionized atoms, from which the ionization electrons are extracted by the electric field applied in the vertical direction. These electrons drift to the liquid surface, where they are extracted into the gas phase and emit light through electroluminescence [13]. The first scintillation photons are promptly registered by the optical sensors to form the primary signal (S1), and the electroluminescence photons that appear after a delay associated with the drift originate a secondary signal (S2). The depth of the recoil can be calculated from the S1-to-S2 delay, and the xy position is obtained by analyzing the light distribution of the S2 signal across the top optical sensor array.

In a TPC, most of the majority of the background originates from the materials surrounding the liquid volume, which, given the high stopping power and density of the liquid Xe and Ar, deposit their energy in the most outer layers of the liquid volume. With enough resolution of the position reconstruction, it is possible to define a virtual shell where the background contribution is higher. Excluding the events occurring in this shell results in an inner fiducial volume with low background contribution. Using this technique, named *fiducialization*, an optimum solution must minimize the background levels while maximizing the fiducial volume [57–60].

Table 2.1: Sensitivities SI at 90% C.L. obtained with the detectors developed by the XENON, ZEPLIN, PandasX and LUX collaborations. The columns "Total", "TPC" and "Fiducal" refer to the mass of liquid Xenon. The difference between the total and TPC corresponds to the mass in the circulation system and other conduits.

Experiment	Year	Total	TPC	Fiducial	Exposure	Sensitivity	Ref
ZEPLIN-II	2007	-	31 kg	7.2 kg	0.61 kg×year	SI 6.6 x 10^{-43} cm^2 [65 GeV/c^2]	[61]
XENON10	2008	25 kg	14 kg	5.4 kg	0.37 kg×year	SI 4.5 x 10^{-44} cm^2 [30 GeV/c^2]	[62]
ZEPLIN-III	2012	-	12 kg	5.1 kg	3.7 kg×year	SD 2.8 x 10^{-37} cm^2 [50 GeV/c^2]	[63]
XENON100	2016	161 kg	62 kg	34 kg	48 kg×year	SI 1.1 x 10^{-45} cm^2 [50 GeV/c^2]	[64]
LUX	2017	370 kg	250 kg	102.6 kg	33.5 t×year	SI 2.2 x 10^{-46} cm^2 [50 GeV/c^2]	[65]
XENON1T	2018	3.2 t	2.0 t	1.3 t	2.0 t×year	SI 1.6 x 10^{-47} cm^2 [50 GeV/c^2]	[10]
PandaX-4T	2021	4 t	3.7 t	2.67 t	0.63 t×year	SI 3.8 x 10^{-47} cm^2 [40 GeV/c^2]	[11]

In the last decade, with this technology, several liquid xenon TPC detectors have been developed with increasing masses of the target volume, producing stronger constraints in the dark matter interaction cross-section. The following sections present the main characteristics of detectors using the dual-phase TPC technology to detect dark matter. Some results attained by these detectors are summarized in table 2.1.

2.4.1 ZEPLIN

The ZEPLIN program, founded in 2005, laid the foundations for dark matter search with liquid Xe TPC. ZEPLIN-III, consisted of a dual-phase TPC with a 38.6 cm diameter and a height of 35 cm, containing 8 kg liquid xenon fiducial volume. A polished copper plate, denominated by "anode mirror", placed on the top of the electroluminescence region, reflects photons (from both S1 and S2 signals) to a hexagonal shaped array of 31 PMTs placed directly below the fiducial volume (figure 2.13) [58].

The drift field, the liquid/gas interface extraction field, and the gaseous Xe field are accomplished by a two-electrode configuration through a grid-like cathode placed above the PMTs (directly below the fiducial volume) and the anode mirror. With this configuration, there is no need to place a gate

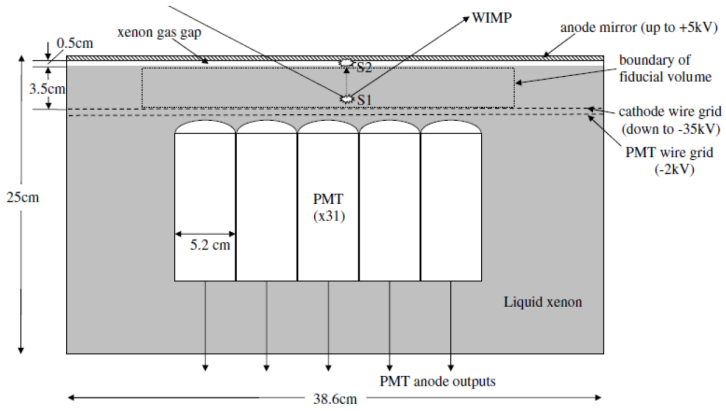

Figure 2.13: Representation of the ZEPLIN-III TPC detector [58].

electrode in the liquid, which further removes this source of background. However, it reduces the flexibility of the electric field since a higher voltage is required to accomplish a homogenous drift field [58].

This detector was also surrounded by a 30 cm thick polypropylene shield and a 20 cm thick shield of Pb, which suppressed external gamma rays and neutrons by a factor of 10^5. After the first run, in 2009, an anti-coincidence system in the form of 52 Gd-loaded polypropylene bars, each coupled with a PMT, was added to the surrounding space between TPC and the pre-existing polypropylene shield. This system demonstrated an efficiency of 60% for neutron tagging and a rejection of 28% for gamma rays [66].

2.4.2 XENON

The TPC of the XENON1T (figure 2.14), located in *Laboratori Nazionali del Gran Sasso* at a depth of 3600 m water equivalent, is a cylindrical vessel with a height of 97 cm and a diameter of 96 cm, placed into a double-wall cryostat vessel located inside a water tank. The wall of the TPC is an assembly of 24 PTFE panels to ensure a good light collection by the two arrays of optical sensors located: one with 127 PMTs at the top and the other with 121 PMTs at the bottom [10].

A homogeneous drift field is shaped by 74 copper ring electrodes stacked along the TPC height, with the negatively biased cathode installed at the bottom, a grounded gate placed directly below the liquid/gas interface, and an anode positively biased 5 mm above the gate.

To guarantee a stable pressure of the gaseous xenon layer, and thus to maintain a stable liquid/gas interface, a pressurized container – “diving bell” – enclosures the top array and keeps a tight seal with the top of TPC. This diving bell allows the entire TPC to be completely submerged in liquid xenon, providing a passive shield surrounding the TPC. A vertically adjustable exhaust tube in the diving bell allows controlling the liquid level [10].

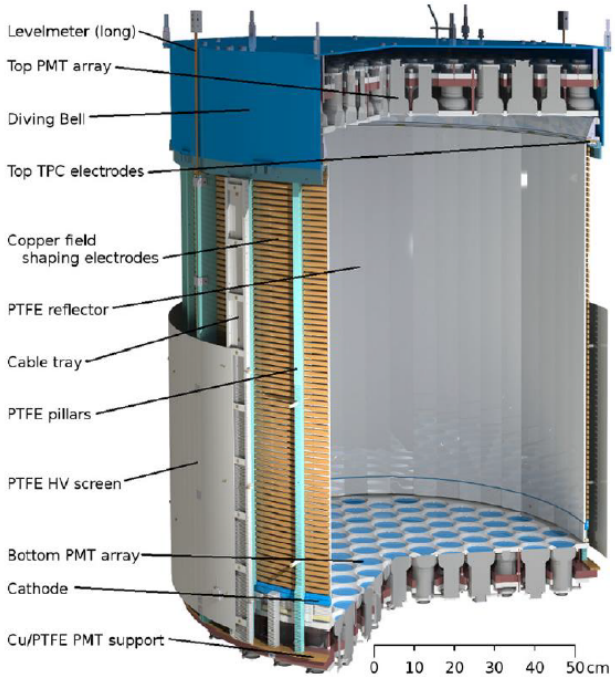

Figure 2.14: Representation of the XENON1T TPC detector [10].

The water tank is equipped with several PMTs to measure Cherenkov light produced by muon interactions, allowing to tag and veto muon-induced neutron events in the TPC.

The XENON1T is the successor of a series of detectors developed by the XENON collaboration. This group’s most notable result was the direct detection of the $2\nu ECEC$ (two-neutrino double electron capture) in ^{124}Xe. The measurement of the associated half-life presents vital information for nuclear structure models and constitutes an important step towards the search for the neutrinoless mode, which could prove the Majorana nature of the neutrino [67].

2.4.3 LUX

The LUX detector operated between 2013 and 2016 at the 1478 m level (4300 m water equivalent) of the Sanford Underground Research Facility. It has a dodecagonal shape with PFTE walls, with a maximum diameter of 48 cm (see figure 2.15). The signals of the active region, with 300 kg of liquid xenon, are observed by two arrays of 61 PMTs each, one placed below the drift field in the liquid xenon region and the other placed above the GXe layer at the top. The drift field is regulated by 2 main grids, the cathode, and gate, whilst its homogeneity is ensured by 48 cooper field rings stacked 1 cm apart along the drift height of 50 cm. An additional gate grid placed 5 mm below the liquid/gas interface creates, in conjunction with the anode grid, an extraction region. This improved the electroluminescence by increasing the extraction efficiency of the drifting electron [68].

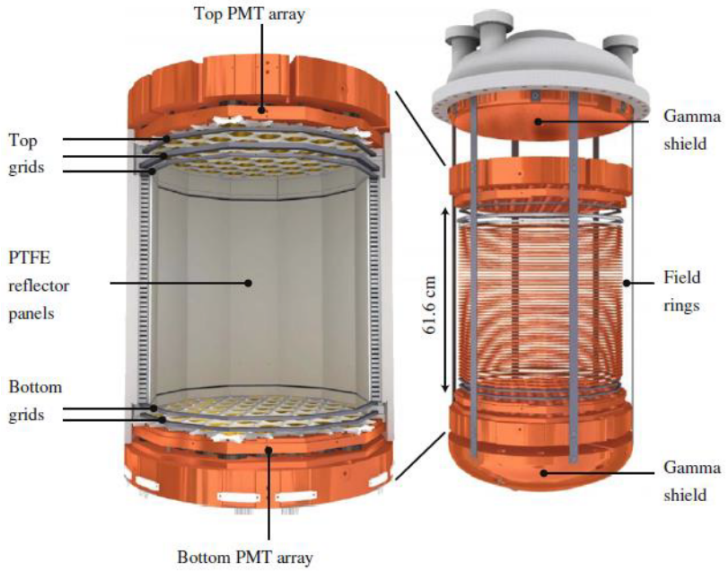

Figure 2.15: Representation of the LUX TPC detector [68].

Two thick cooper disks, installed above and below the TPC assembly, provided additional shielding against gamma rays and a thermal connection with the cryogenic system that maintains the temperature of the Xe. As in the XENON detectors, the liquid Xe in LUX is continuously recirculated through a hot getter, removing electronegative impurities that can potentially affect the light and charge yield [68].

The LUX collaboration pioneered several techniques, such as calibrations with radioactive sources

injected into the liquid volume via a circulation system [69] or calibration of NR band with neutrons from a D-D generator, which are currently used by other dark matter experiments. Moreover, the cryogenic system employing thermosyphons technology and the state-of-the-art circulation system, which allowed for energy-efficient continuous circulation, are also some technologies founded by LUX in the context of dark-matter detectors [60, 68].

2.4.4 PandaX

The PandaX collaboration, founded in 2009, operated several detectors installed at the China Jinping Underground Laboratory with a rock overburden of 2400 meters.

The first of these detectors was the PandaX-I, with the inaugural science run in 2014. It had a "pancake-shaped" TPC (60 cm diameter and 15 cm drift length) with a total of 120 kg of liquid xenon observed by two arrays of PMTs. The top array consisted of 143 30×30 mm Photomultiplier Tubes (PMTs), and the bottom consisted of 37 PMTs with 76 mm diameter [70].

The PandaX-I detector served as a prototype for the larger Panda-II detector (figure 2.16) with a TPC (height and drift length of 60 cm) containing 500 kg of liquid xenon. The top and bottom arrays of Panda-II contained 55 PMTs, each with a diameter of 76 m, plus 24 30×30 mm PMTs installed at the array periphery to act as a veto system. Another improvement was using lower activity stainless steel for the chamber vessel [70].

The latest detector developed by this group was the PandaX-4T, which, as the name indicates, contains 4 t of liquid xenon in the sensitive volume plus 2 t in the remaining conduits of the circulation system. The TPC is twice as big as the Panda-II, with a diameter of 1.2 m and a drift length of 1.3 m [11, 70].

Similarly to the other detectors of this series, the electric field was achieved by an anode, a cathode, and a gate. An additional screening electrode was installed near the PMTs as protection from the intense field. The drift field uniformity (400 V/cm) was maintained by a stack of 60 copper rings [70, 71].

The arrays of PandaX-4T consist of 169 top and 199 bottom 3-inch PMTs and an additional ring of

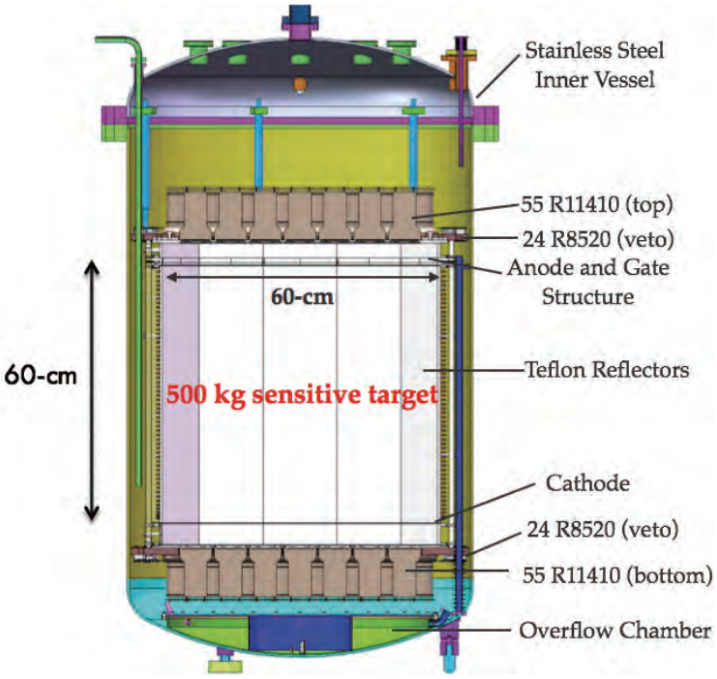

Figure 2.16: Representation of the PandaX-II TPC detector [70].

30×30 mm PMTs for each array.

2.5 Conclusion

Nowadays, the dark matter existence is a known fact, as several indirect pieces of evidence converge towards the same results. However, its true nature is still an open chapter. In the last decades, technological advances permitted the development of more sensitive experiments. Nonetheless, although a wide variety of technologies use very distinct detection approaches, no group observed an indisputable positive detection. However, as shown in figure 2.17, the increasing detection sensitivity excludes several regions of dark matter masses ranges. Current tonne scale detectors, such as LZ (LUX-ZEPLIN) and XENON-nT, can potentially be on the verge of detection.

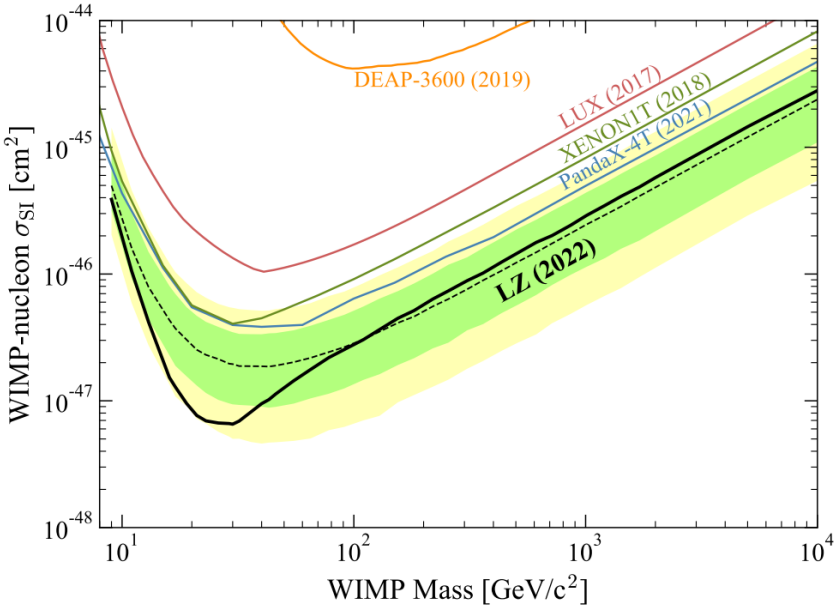

Figure 2.17: Spin-independent cross section of the LZ detector vs WIMP mass. The green and yellow bands are the 1σ and 2σ sensitivity bands. The dotted line represents the mean of the projected sensitivity. Also shown are the PandaX-4T, XENON1T, LUX and DEAP-3600 sensitivity curves [14].

Chapter 3

Liquid Xenon Time Projection Chamber

In the last two decades, the dual-phase TPC technology has been one of the main drivers pushing the limits of the dark matter direct detection sensitivity, through the improvements accomplished by the ZEPLIN, LUX and XENON groups [58–60]. Introduced in 1970, as a *method of registration of ionizing-particle tracks in condensed matter*, this technology measures the signals formed from the photons and electrons that are generated when a given particle scatters in a volume of a liquefied noble gas, such as Xe [57].

This section introduces the working principles of the dual-phase TPC, with a focus on detectors using xenon as the target material.

3.1 Introduction

The liquid xenon TPC technology has three main characteristics paramount for the detection of rare and low yields signals: *(i)* a low energy threshold[1] required to detect the weak signals from dark matter nuclear recoils; *(ii)* a good particle background discrimination; *(iii)* 3-D position reconstruction of the interaction sites, required to exclude multiple scatter events from the WIMP signal and define an inner fiducial volume with low background levels [60].

Generally, the liquid xenon TPC detectors, depicted in figure 3.1, consist of a cylindrical shaped vessel oriented in the vertical direction and filled with liquid xenon. Although other noble gases, such as argon, can be employed, xenon, with higher stopping power and density, provides better natural shielding against external radioactivity. Moreover, Xe unstable natural isotopes have an extremely long lifetime (Xe^{136}, $t_{1/2} > 10^{21}$ year [72]), whilst ^{39}Ar ($t_{1/2}$ = 269 year), a product of nuclear reactions induced by cosmic rays, and present in natural Ar in trace amounts, produces 1 decay per second per kg of natural Ar [13,34,55]. Comparatively, Xe also has a slightly higher light and charge yield for low energy events, improving the detector sensitivity near its energy threshold [34]. Finally, compared with the Ar, the Xe scintillation generates photons with a higher wavelength, which are easier to measure with commercially available photon detectors. Table 3.1 summarizes the properties of both materials [55].

The signals formed in the active material are registered by PMTs, installed in the faces of the cylinder. In simpler configurations, such as in the ZEPLIN detectors (see section 2.4.1), a single array is installed at the bottom of the detector submerged in the liquid xenon. However, all the current detectors have been equipped with an additional array above the liquid surface.

The energy deposited by a particle in liquid Xe creates photons and electrons. While the photons are promptly registered by the array of PMTs to form the S1 signal, an electric field (dubbed drift field) drives the electrons towards the liquid surface. The extraction of the electrons from the liquid, and subsequent acceleration in a gaseous region with Xe, leads to the production of a delayed scintillation to the S1 signal. The registration of such scintillation by the PMTs originates from the

[1] The minimum energy deposition producing a detectable nuclear recoil

Table 3.1: Properties of liquid Xe and Ar (adapted from [13, 14, 55]).

Properties (unit)	**Xe**	**Ar**
Atomic Number	54	18
Mean relative atomic mass	131.3	40.0
Boiling Point T_b (K)	165.0	87.3
Melting Point T_m (K)	161.4	83.8
Liquid density at T_b (g·cm^{-3})	2.94	1.40
Volume fraction in Earth's atmosphere (ppm)	0.09	9340
Cost/kg	$1000	$2
Scintillation light wavelength (nm)	175	128
Triplet lifetime (ns)	22	1700
Singlet lifetime (ns)	4.3	7
Electron mobility (cm^2 V^{-1} s^{-1})	2200	400
Scintillation yield (photons/keV)	42	40
Average energy needed per quanta, W (eV/quantum)	13.5	19.5

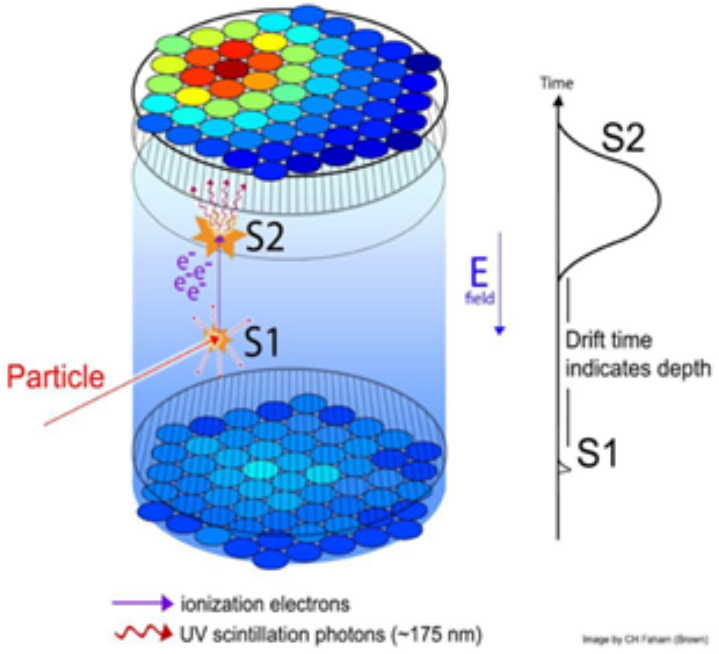

Figure 3.1: Representation of the dual-phase TPC operation principle.

S2 signal.

As shown in figure 3.1, the depth of the scatter is calculated from the delay between the S2 and S1 signal, or *drift time*, and the xy position is reconstructed by analyzing the light distribution of the S2 signal in the array. Furthermore, as discussed in further detail in the section 3.6, nuclear and electronic recoils yield different values of S2/s1. This allows the discrimination between nuclear

recoils, such as the ones expected by a WIMP interaction, from electronic recoils produced by the background. This technique offers typical values of background rejection efficiency above 99.5% near the energy threshold [73, 74].

One of the main drivers of the discrimination efficiency and the energy resolution is the maximization of the light collection, particularly of the S1 [10]. This is accomplished by covering the inner walls of the TPC and the space between the PMTs by highly reflective material. The most commonly used reflector is polytetrafluoroethylene (PTFE), as not only it exhibits a high reflectance (>97%) for the Xe scintillation light (λ=178 nm) when immersed in liquid xenon, but it is also an extremely radio-pure material with traces amount ($\approx$ppb) of radioactive contaminants, adding an insignificant contribution to the detector background ($\ll$1 mBq/kg) [75, 76]. Furthermore, PTFE has a lower outgassing rate than most other plastics, is chemically inert, and falls in the category of electric insulator [75, 76].

The outgassing of the detector materials pollutes the active material with electronegative impurities. Due to the charge attenuation of the drifting S2 electrons, the presence of these impurities creates a depth dependency of the S2 signal. This effect is mitigated by equipping these detectors with a closed-loop circulation system to improve the purity levels. The residual dependency can be corrected in offline analysis using the techniques described in section 3.5.1.

Finally, the liquid state of the active material, attained under cryogenic conditions, is achieved using a liquid nitrogen system. However, the temperature stabilization is facilitated through a vacuum jacket layer surrounding the TPC.

3.2 Signal generation process

When a particle, P, interacts with liquid xenon, its energy is deposited along a track by recoiling either electrons or nuclei. The energy is then converted into the excitation of the Xe atoms and the production of electron-ion pairs (ionization). Part of the energy also generates heat in the form of atomic motion, however, to my knowledge, currently there is no practical method of detecting it in liquid xenon [13, 77].

The excited atoms (Xe^*) can bond to neutral Xe atoms to form an excited Xe molecule (excimer),

Xe_2^{*v}. This molecule, in both electronic and vibrational excited states, relaxes to the excited electronic state (Xe_2^*) as it impacts with other Xe atoms. Although infrared emission is possible, in most cases this transition is non-radiative. Afterwards, a single photon with fixed energy is emitted as the molecule de-excites to the ground state, resulting in its dissociation. This emission can occur from two excited states: the singlet, with a decay time of 4.3 ns, or the triplet, with a decay time of 22 ns [13]. The emission line, centered at 178 nm and with FWHM of 14 nm [78], lays in the vacuum ultraviolet (VUV) region of the electromagnetic spectrum. This process is summarized in the following expressions:

$$\begin{aligned}
P + Xe &\longrightarrow Xe^* + P && \text{impact excitation}\\
Xe^* + Xe &\longrightarrow Xe_2^{*v} && \text{excimer formation}\\
Xe_2^{*v} + Xe &\longrightarrow Xe_2^* + Xe && \text{vibrational relaxation}\\
Xe_2^* &\longrightarrow Xe + Xe + h\nu && \text{VUV emission}
\end{aligned}$$

Additional VUV emission results from the recombination of the electron-ion pairs created in the initial interaction. The Xe ions form positive diatomic molecules (Xe_2^+) as they bond with the neutral Xe atoms in the vicinity. The recombination of this molecular ion with an ionization electron results in its dissociation, leaving one atom in the ground state and the other in the excited state. The latter then follow the same process as described above, resulting in the emission of more VUV photons:

$$\begin{aligned}
P + Xe &\longrightarrow Xe^+ + e^- + P && \text{ionization}\\
Xe^+ + Xe &\longrightarrow Xe_2^+ && \text{diatomic molecule formation}\\
e^- + Xe_2^+ &\longrightarrow Xe^{**} + Xe && \text{recombination and dissociation}\\
Xe^{**} + Xe &\longrightarrow Xe^* + Xe + \text{heat} && \text{relaxation}\\
Xe^* + Xe &\longrightarrow Xe_2^{*\nu} && \text{excimer formation}\\
Xe_2^{*\nu} + Xe &\longrightarrow Xe_2^* + Xe && \text{vibrational relaxation}\\
Xe_2^* &\longrightarrow Xe + Xe + h\nu && \text{VUV emission}
\end{aligned}$$

These processes lead to the formation of the S1 signal. Due to the delay of the recombination path

and the different decay times of the singlet and triplet states, liquid xenon scintillation time profile presents a sharp rising edge followed by a decay curve with different sections of varying decay constant[2]. The fraction of electrons available for the recombination depends on the nature and energy of the recoil, assuming stable temperature conditions [13,77]. As shown in figure 3.2, the drift field also affects this recombination fraction, with a stronger field resulting in decreased scintillation yields and an equivalent increase of ionization yield. This means that the ionization electrons are more rapidly extracted from the interaction site and, therefore, have a smaller probability of recombining.

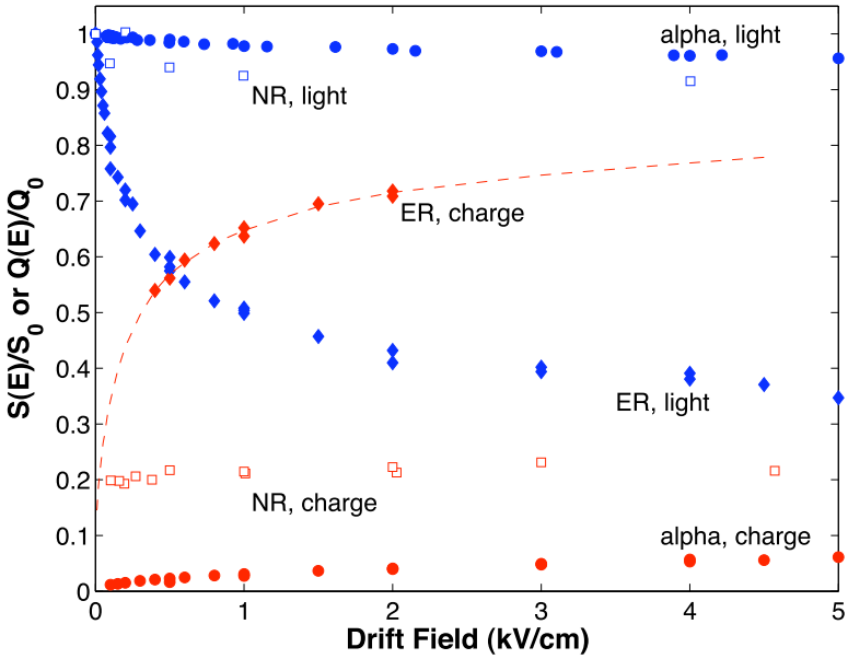

Figure 3.2: Dependence of the liquid xenon scintillation (blue) and ionization (blue) yields with the drift field. Shown are 122 keV electron recoils from γ-particles of ^{57}Co (ER); 56.6 keV nuclear recoils (NR) and 5.5 MeV alphas from ^{241}Am (figure from [79]).

The electrons that did not recombine drift in the applied electric field towards the liquid surface. The drift field must be as uniform as possible to preserve the event xy position information along the drift [13]. It also should be strong enough to ensure that a large fraction of the ionization electrons escapes recombination (typically, hundreds of V/cm, see figure 3.2).

Near the liquid surface, as the electrons need to break a potential barrier to enter the gas phase, a stronger electric field (several kV/cm) is applied to maximize the extraction efficiency. If the electric

[2]One of the main differences of Ar, with respect to Xe, is the fact that the lifetime of the triplet state is orders of magnitude higher than the singlet state. This results in faster pulse shape for nuclear recoils, since these produce fewer triplet states. In such case, with Ar, it is possible to use pulse shaping techniques as a discriminate method.

field in the gas phase is strong enough, the electrons acquire sufficient energy to excite xenon atoms. This excitation is converted (through the process described above) into VUV radiation, emitted along the electron paths in the process called electroluminescence. This photon signal is proportional to the total extracted charge and therefore is called proportional or secondary scintillation (S2). The number of photons generated by electroluminescence, N_p, per unit of distance is given by:

$$\frac{\mathrm{d}N_p}{\mathrm{d}x} = aE - bP - c, \tag{3.1}$$

where E is the electric field applied in the extraction region, P is the gas pressure, and the remaining variables are empiric parameters with values of a = 0.137 V^{-1}, b = 177 $bar^{-1}cm^{-1}$ and c = 45.7 cm^{-1} [80]. In this case, field uniformity is vital to reduce xy dependency of the electroluminescence yield, which directly affects the energy resolution. The field must be kept within sensible values to prevent the creation of sparks and hotspots [80].

Both S1 and S2 are often represented in units of *phd* (detected photons) to represent the amount of light that produced a detectable signal in the PMTs. The usage of this unit alludes to the fact that, due to the collection efficiency and quantum efficiency of the PMTs, the measured signal by the PMT does not represent the number of incident photons.

3.3 Light detection with a Photomultiplier tube

The photomultiplier tubes (PMTs) are used to convert optical S1 and S2 into electrical signals for further analysis. For this reason, their properties, presented further in this section, are extremely import for the performance of the whole detector[3]. A typical PMT consists of a tube with a vacuum seal and a transparent input window (figure 3.3). The inner face of the window contains a thin layer of semiconductor material with a low work function, denominated by the photocathode. Each photon interacting with this layer has a certain probability of ejecting a photoelectron. An electrode, represented by the letter F in figure 3.3, generates an electric field to focus the photoelectrons into an electron multiplier containing a chain of dynodes. Electrons are accelerated to energies of tens

[3] This fact is reflected in the LZ experiment slow control system, where approximately one third of the total of ≈18k channels are used to control and monitor the PMTs (see Chapter 8 for details).

to hundreds eV by the potential difference existing between the dynodes and produce secondary electrons, creating an electron cascade. The voltage differential between consecutive dynodes is selected to optimize the trajectories of the electrons in the cascade. At the end of the tube, the anode collects the amplified cascade of electrons. The output pulse of the anode current is typically converted to a voltage signal either created on an output resistor R_L or by feeding it to the input of a transimpedance amplifier.

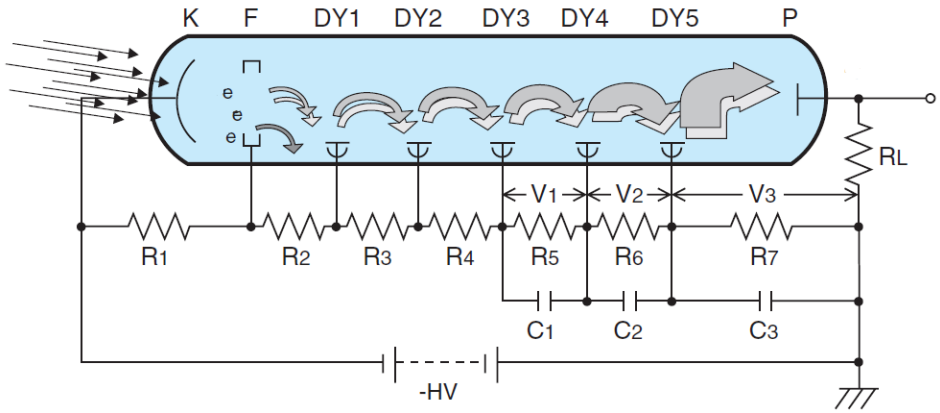

Figure 3.3: Schematic of a PMT with the principal components, where photons, represented by the left arrows, originate the emission of photoelectrons from the photocathode (K). A field F focuses, the photoelectrons to the first dynode (DY1) initiating the charge signal amplification as more secondary electrons are created in the following dynodes. A high voltage is applied between the photocathode and the anode (P) to sustain the trajectories of the electrons. The capacitors at the end stabilize the current by providing some additional charge [20].

The following list briefly describes the most important properties of a PMT:

- **Quantum efficiency**: traditionally, quantum efficiency (QE) is defined as the ratio between the number of photoelectrons emitted from the photocathode and the number of incident photons. However, due to the double photoelectron effect (DPE), a given incident photon can generate two photoelectrons. Thus, a more accurate definition of the QE, which also better describes how these values are measured in practice, is: the probability for a given incident photon to generate at least one photoelectron. Typically, a PMT has a QE of around 30%, but in some cases, it is possible to obtain values as high as 43% [20]. Furthermore, the QE of the PMT varies with the wavelength of the incident light. Therefore, the photocathode material, which directly affects the maximum QE value, must be chosen to optimize the spectral response of the PMT to its application [20, 81].

- **Gain**: the electron multiplication in a PMT is enabled by applying a differential voltage (v_t) of 1 or 2 kV between the photocathode and the collecting anode at the end of the PMT. The correct voltage distribution along the dynode chain is created by a voltage divider, such as the one in figure 3.3. The multiplication gain, typically of the order of 10^5 to 10^6, can be, in theory, calculated with the following equation:

$$G = A^n \left(\frac{\prod_i R_i}{(\sum_i R_i)^n} \right)^p V_t^{pn} \ . \tag{3.2}$$

  Where n is the total number of stages of the voltage divider, R_i is each stage resistor, A is an empiric proportionality constant, and p is a material-dependent parameter, with typical values between 0.7 and 0.8, to represent inefficiencies in the response of the dynode. Equation 3.2 represents an ideal case where the performance of the various components of the PMT is consistent between similar sensors. However, unavoidable randomness in the alteration of the manufacturing process, such as variations of the conditions during the deposition of the photocathode material, result in PMTs with different responses.

  In the scope of TPC technology, the PMTs are installed in different locations and with different orientations. Thus, given the presence of temperature gradients in the detector, the response of PMTs within the same array will vary as they are subject to different temperatures. This occurs due to alterations in the electric field geometry of each PMTs, either due to modification of the dynode configuration or due to a dependence of the dynode gains on temperature. Moreover, magnetic fields, such as the Earth's magnetic field, directly affect the trajectories of the electrons, which will cause a non-uniform response within the array if the orientation of the PMTs is not the same.

- **Photon Detection Efficiency**: the processes involved in detecting light by the PMT are not ideal because it is not guaranteed that a given incident photon produces an amplified electronic signal. The overall Photon Detection Efficiency is the product of the quantum efficiency and the collection efficiency. The latter represents the probability that a given photoelectron, ejected from the photocathode, will produce a measurable signal at the anode. In photon counting applications, the collection efficiency can also be calculated as the ratio between the number

of output pulses and the number of photoelectrons.

- **Dark Noise**: a PMT produces a certain anode current even without a light input. This is caused by the thermionic emission from the photocathode or the dynode stages. Although, only the photocathode dark count produces a similar signal to that of the single photoelectron emission, as it will trigger the complete electronic amplification. The dark count rate varies with the temperature and supply voltage of the PMT.

- **Linearity**: for more accurate light conversion into an electric signal, it is convenient that the PMT presents a linear response for a wide range of luminous flux. A PMT is said to be saturated when its response is not linear, which occurs for high-energy events. In this regard, as demonstrated in section 6.1, a PMT presents a good linearity to inputs in the order of 10^4—10^5 photons.

One important effect that can negatively affect the performance of a PMT-based detector is afterpulsing. As the name indicates, this is caused by spurious pulses observed after the principal signal. There are two different types of afterpulsing which can be distinguished by their delay regarding the main pulse. The first type, with a delay in the order of the 40 to 50 nanoseconds, is caused by the elastic scattering of the electrons from the first dynode. The second type, with a longer delay ranging from 200 nanoseconds to over 1 microsecond, occurs when residual gas in the PMT is ionized. Then, due to the electric field applied in the PMT, the ions strike the photocathode, and secondary electrons are produced, resulting in the formation of a delayed pulse.

Despite its various shortcomings, a PMT remains one of the most sensitive optical sensors available commercially. There are various commercial solutions with different materials and electric field configurations, capable of serving a vast range of applications in various fields such as Medicine, Spectrophotometry, Microscopy, and, of course, High Energy Physics.

3.4 Energy Reconstruction

As mentioned in section 3.2, the energy deposited by a particle in liquid xenon is spent in the production of electron-ion pairs, excitation of Xe atoms (excimers) and heat in the form of non-

radiative atomic relaxation, as stated by Platzman equation for rare gases [82]:

$$E = n_{ex}W_{ex} + n_iW_i + n_i\overline{\epsilon}. \tag{3.3}$$

Where E is the deposited energy, W_{ex} is the average energy to produce n_{ex} excimers, W_i is the average energy to produce n_i electron-ion pairs and $\overline{\epsilon}$ is the average kinetic energy of sub-excitation electrons. Note that the heat partition is produced in the ionization channel from the relaxation of the products created with the Xe diatomic molecule dissociation. Writing equation 3.3 to isolate the W terms, we obtain:

$$E = n_i(\alpha W_{ex} + W_i + \overline{\epsilon}), \tag{3.4}$$

where $\alpha = n_{ex}/n_i$. As stated in [83], in principle, α, the exciton-to-ion ratio, does not vary with the deposited energy and takes a theoretical value of 0.06, although it is also cited with the value of 0.2±0.13 which is consistent within the uncertainty [77]. Following the same approach of [83], a combined W-value, which also takes into account the $\overline{\epsilon}$, is written as:

$$W = \frac{\alpha W_{ex} + W_i + \overline{\epsilon}}{1 + \alpha}, \tag{3.5}$$

where W is the average energy required to produce a single excited or ionized atom, which for liquid xenon is 13.5±0.2 eV [14]. Therefore, combining equations 3.5 and 3.4, the deposited energy can be written as:

$$E = W(n_{ex} + n_i). \tag{3.6}$$

As previously discussed in section 3.2, a fraction of the produced electrons can recombine with the molecular Xe, resulting in the emission of more scintillation photons. This fraction, r, which depends on the liquid density, drift field and interaction energy, directly affects the total number of generated

photons (n_γ) and electrons (n_e), such that:

$$\begin{aligned} n_e &= (1-r)n_i \ , \\ n_\gamma &= n_{ex} + rn_i \ . \end{aligned} \tag{3.7}$$

However, as each recombination leads to the emission of a scintillation photon, the sum $n_e + n_\gamma$ remains constant:

$$n_e + n_\gamma = n_i - rn_i + n_{ex} + rn_i = n_i + n_{ex} \ . \tag{3.8}$$

So, equation 3.6 can be written as:

$$E = W(n_\gamma + n_e) \ . \tag{3.9}$$

In practice, to reconstruct n_e and n_γ from the S1 and S2 signals, calibration parameters are introduced to take into account the signal production effects. These parameters, g_1 and g_2, are called detector gains, stand for the average detector response (in phd) to a single scintillation photon and a single ionization electron, respectively:

$$\begin{aligned} n_\gamma &= \frac{S1}{g_1}, \\ n_e &= \frac{S2}{g_2}. \end{aligned} \tag{3.10}$$

The g_1 represents the average photon collection efficiency mentioned in section 3.3 and is the product between the collection efficiency and the average quantum efficiency of the PMTs. The g_2 is the product of the electron extraction efficiency from the liquid to the gas, the average single electron pulse size in phd (equation 3.1). Thus, equation 3.9 becomes:

$$E = W(\frac{S1}{g_1} + \frac{S2}{g_2}) \ . \tag{3.11}$$

Methods to calculate the g_1 and g_2 and the energy resolution will be discussed in further detail in section 5.7.

The energy resolution of liquid xenon is affected by several components described in section 5.7.

In the case of a nuclear recoil, a much smaller fraction of deposited energy is converted into excitation and ionization, while the rest dissipates as heat. This fraction is given by Lindhard theory [84] and can be used to correct the value given by equation 3.11:

$$E_{nr} = \frac{E}{f_L}, \tag{3.12}$$

where E_{nr} is the energy deposited in nuclear recoils and f_L is given by the Lindhard model, such that [77, 84, 85]:

$$f_L = \frac{kg(\epsilon)}{1 + kg(\epsilon)}\ , \tag{3.13}$$

where $k = 0.133Z^{2/3}A^{-1/2}$ is a proportionality constant between the electronic stopping power and velocity of the recoiling nucleus, and it is 0.166 for Xe [85]. The parameter $g(\epsilon)$, a function of a dimensionless quantity ϵ related to the deposited energy, is proportional to the ratio of the electronic stopping power to the nuclear stopping power [85].

However, the reconstruction of n_e and n_γ from the S1 and S2 signals is only possible if the signals are corrected for the non-uniform response of the detector. Otherwise, the energy can be degenerated, and its reconstruction is impossible. For instance, due to the charge attenuation along the electric field, a low energy event at the top of the detector will appear to have the same energy as that of a high energy event located at the bottom of the detector.

3.5 S1 and S2 position dependence

The energy reconstruction equation 3.11 was derived for an ideal detector with a completely uniform response throughout its sensitive volume. However, the response of a real detector is subject to position variations that can be divided into four main categories:

- Dependence of light collection efficiency on the position of interaction caused by VUV absorption at the walls and variability in quantum efficiency between individual PMTs[4];
- Dependence of the extracted charge on the depth of interaction due to charge attenuation via electron attachment by electronegative impurities;

[4] In the extreme case, a PMT can fail completely, resulting in a local dip in light collection

- Dependence of the charge extraction efficiency and electroluminescence light yield on the position of the extraction site in the horizontal plane;

- Effects caused by the non-uniformity of the drift field.

In other words, the gains g_1 and g_2 of a real detector are functions of the position. From the practical point of view, though, it is often more convenient to use constant gains (either averaged or fixed at some reference position in the detector) while multiplying the measured S1 and S2 signals by spatial-dependent correction factors:

$$\begin{aligned} S1_c &= S1 \cdot C_{lc}(x,y,z) \ , \\ S2_c &= S2 \cdot C_{lc}(x,y) \cdot C_{ext}(x,y) \cdot C_{elt}(x,y,z) \ , \end{aligned} \tag{3.14}$$

where C_{lc} is the position-dependent light collection correction of the S1 and S2, $C_{ext}(x,y)$ is the correction of the charge extraction efficiency and $C_{elt}(x,y,z)$ is the position-dependent charge attenuation in the liquid xenon.

3.5.1 Drift time correction

Electronegative impurities, such as O_2 and H_2O, can capture the drifting electrons, introducing a depth-dependent attenuation in the S2 signal, as more electrons can be captured along higher drift times [79]. Assuming a uniform concentration of electronegative impurities, the S2 dependence on the drift time follows an exponential decay law given by:

$$S2 = S2_0 \ exp\left(-\frac{t_d}{\tau}\right) \ , \tag{3.15}$$

where t_d is the event drift time, $S2$ is the measured signal, $S2_0$ is the signal that would be produced by the same charge without attenuation and τ is the mean lifetime of a free electron in liquid xenon before it is captured by an electronegative molecule. Since an infinite τ is impossible to achieve due to the constant outgass of the detector materials, corrections are introduced to compensate for this dependence of the $S2$ on the event depth.

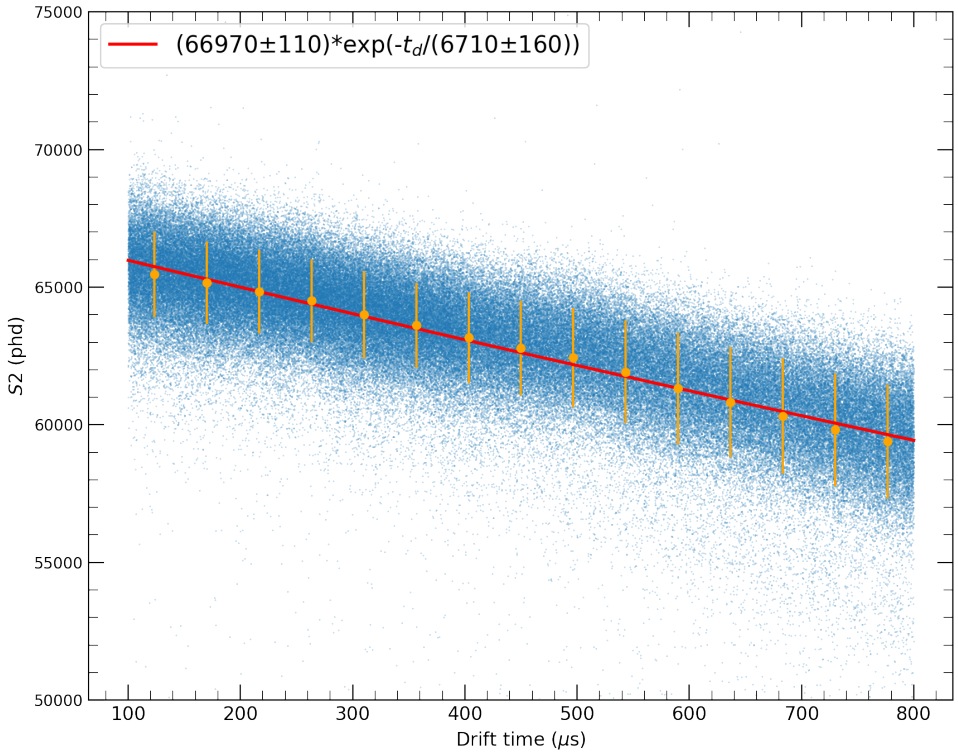

Figure 3.4: An example of the electron lifetime calculation with ^{222}Rn 5.49 MeV α-particles. The orange dots and the respective bars represent the mean a sigma for bins of the data (blue). The red line represents the fit results using equation 3.15.

The mean electron lifetime can be calculated by fitting equation 3.15 in a profile histogram[5] of $S2$ vs t_d (figure 3.4) using monoenergetic events from a well-known source. These events can be from a calibration source such as ^{83m}Kr, but the usage of background events, such as from the 164 keV line of ^{131m}Xe (conversion electrons plus X-ray) or alpha particles from the decay of ^{222}Rn and ^{118}Po, is also possible.

Note that the electron lifetime is not constant in time: it increases if the electronegative impurities are removed faster by the purification system, than they are liberated by the detector elements. Changes in xenon circulation can speed up, slow down or even temporarily reverse this trend: e.g., τ can suffer a fast decrease while circulation (and consequently purification) is stopped. Hence, constant monitoring of the electron lifetime is required to improve the quality of the data analysis by making it time-independent (see figure B.1).

[5] Similarly to a typical histogram that represents bins of a variable, the profile histogram calculates bins for the variable but along an additional dimension.

3.5.2 S2 light collection correction

The photons produced in the electroluminescence region travel throughout the detector until they are detected by one of the PMTs or absorbed. As they travel, these photons scatter on the detector materials and liquid xenon, and can be subject to a panoply of effects. Reflection or absorption by the detector materials; reflection and refraction at the liquid surface; absorption by impurities present and Rayleigh scattering in the liquid xenon, are some of the most important effects resulting in a complex light propagation model. To further complicate this model, the summed contribution of these effects is not uniform in the detector and leads to position-dependent variations of the light collection efficiency. For instance, the number of photons absorbed by the detector walls is higher for events occurring near the wall than for events occurring in the central region, as well as differences in the light detection efficiency between the PMTs within the same array result in xy variations of the light collection.

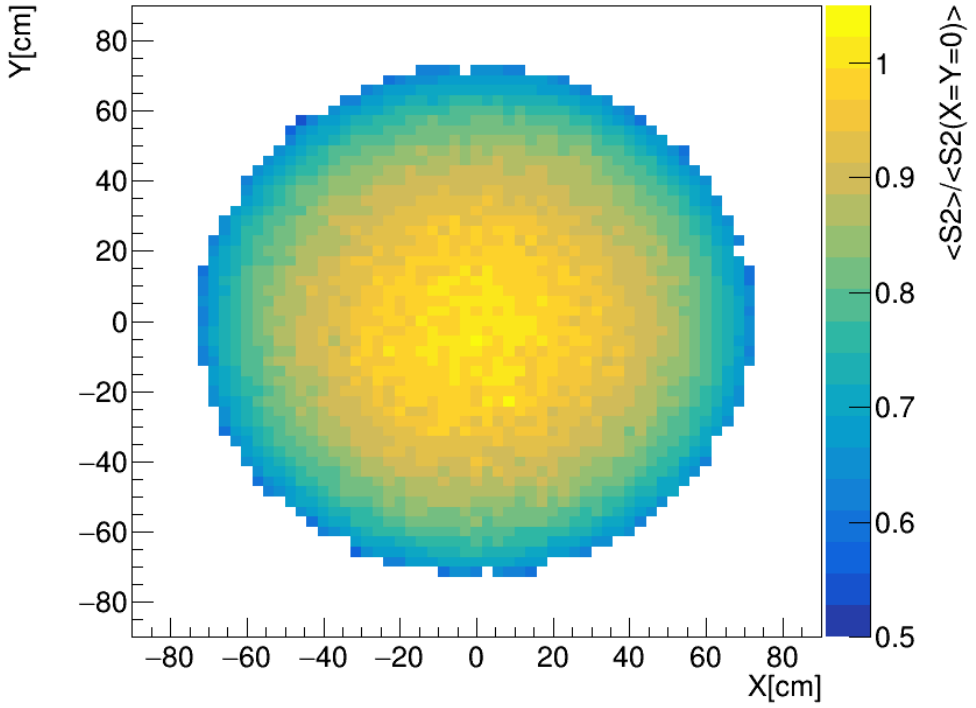

Figure 3.5: Light collection efficiency map produced for the bottom array of the LZ detector using ^{83m}Kr data. Image was kindly provided by PhD A. Stevens.

Since the vertical limits of the S2-producing region (electroluminescence gap) are fixed by the liquid surface at the bottom and the anode grid at the top, the S2 light collection efficiency depends only on

the xy position of the extraction location. Traditionally, this dependence was corrected by resorting to a look-up table called light collection map, such as the one in figure 3.5, which outputs xy-dependent correction factors. The maps are created by binning events from a specific energy source in the xy plane. The average response of the individual bins is then normalized to a reference bin, usually located at the center of the detector. The final map is then obtained from a spline interpolation to the normalized bins. The serious disadvantage of this method is that if a single PMT fails, the whole correction map becomes invalid and must be re-calculated. In the course of the work presented in this thesis, an alternative correction technique was developed that is free from this disadvantage. It is presented in section 5.6.

3.5.3 S1 correction

Liquid xenon is transparent to the characteristic wavelength of the scintillation photons, and although, compared with the S2, the S1 is less affected by the Xe purity conditions, the attenuation length of the photons is governed by absorption by impurities such as water vapor [13, 34]. Furthermore, at the liquid surface, the photons are subject to reflection and refraction effects, which, by increasing the path, indirectly affect the attenuation of the signal. These various processes contribute to a deterioration of the S1 signal and are dependent on the event position.

The S1 light collection efficiency correction is less trivial to handle than that for the S2, since, due to additional depth dependence, the generation of light collection maps in all three dimensions is required. Methods to produce such maps are described in section 5.7.

3.6 Background discrimination

In the context of dark matter search, while a WIMP interaction is expected to generate a nuclear recoil, the electronic recoils are responsible for most of the background in a liquid xenon TPC. Thus, a high discrimination factor between the two types of recoils is a mandatory requirement. Fortunately, these types of recoils yield different relative numbers of electrons and scintillation photons as part of the energy of a nuclear recoil is lost to heat as the recoiled nucleus scatters elastically with xenon atoms, resulting in a lower fraction of energy available for the excitation and ionization. Further-

more, along the denser nuclear recoils track, the ionization electrons are more prone to recombine, resulting in lower S2/S1 average ratios compared to electron recoils [13].

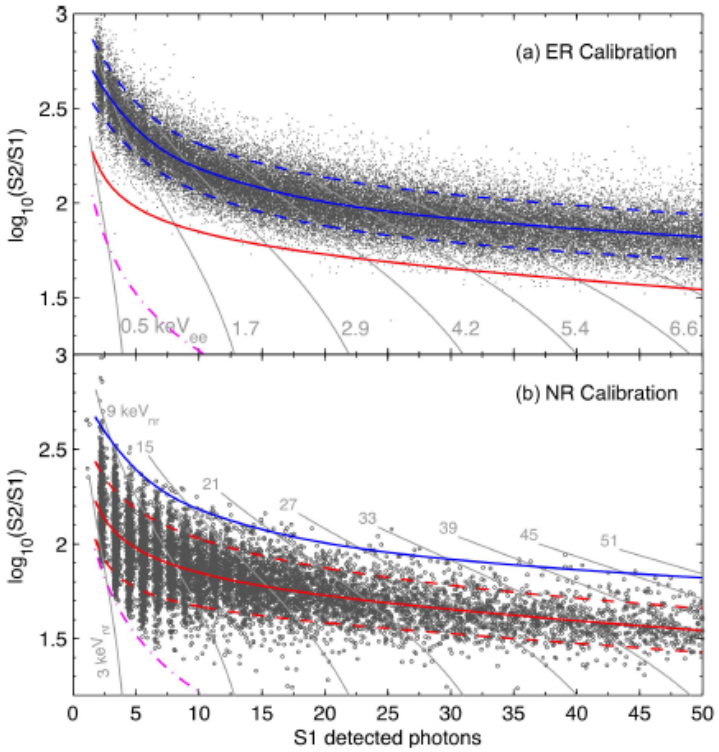

Figure 3.6: Illustration of the ER and NR bands obtained from LUX calibration operations with Tritium and D-D. The difference in ionization and scintillation yields between the two types of recoils becomes obvious by plotting the discrimination parameter log(S2/S1) as a function of the event energy, or in this case S1 (figure from [73]).

Typically, nuclear recoil and electron recoil events are distinguished by resorting to energy bands, such as the ones represented in figure 3.6, where the log(S2/S1) is plotted against the S1. The limits of each brand are obtained from calibration events producing the different types of recoils.

In dark matter detection, the main difficulty is obtaining a good discrimination efficiency at lower energy, where statistical fluctuations affect the band separation. Nonetheless, usually, it is possible to achieve a discrimination efficiency better than 99.5% above the detector energy threshold values [74].

3.7 Conclusion

In the chapter, the main aspects of the liquefied noble TPC technology were revised with a higher focus on the liquid xenon type. Due to the self-shielding capabilities of liquid Xe allied with 3D position reconstruction, this complex technology can create a fiducial volume with extreme low backgrounds. This offers the ideal conditions to detect rare and low-energy events, such as the ones expected by dark matter particles. Furthermore, this technology can detect rare decays, such as the two-neutrino double electron capture in ^{124}Xe, which was performed by the XENON1T group in 2019 [67].

Chapter 4

The LUX-ZEPLIN Experiment

The LZ detector is a dark matter direct detection experiment resulting from the merge of the former ZEPLIN and LUX groups. It consists of a liquid xenon TPC with a fiducial volume of 5.6 tonnes, surrounded by an organic scintillator to act as a veto system. The assembly is installed in the water tank of the Davis Cavern at the Sanford Underground Research Facility (SURF) in Lead, South Dakota, USA, located 1478 m (4300 m water-equivalent) underground, thus reducing the muon flux by a factor of $3{\times}10^6$ with respect to the surface [14, 73].

This chapter presents an overview of the detector's main components, focusing on the engineering and processes behind the various systems.

4.1 Scientific objectives and requirements

The primary scientific goal of the LZ experiment is to reach an unprecedented WIMP-nucleon interaction cross-section of 1.5×10^{-48} cm^2 at a mass of 40 GeV/c^2 [12]. To achieve such result, the collaboration established several requirements to fulfill the scientific objectives and guide the design and fabrication of the detector. For example, the detector needs a minimum fiducial exposure of 1000 tonnes-days for a fiducial volume of 5.6 tonnes. Moreover, detecting WIMP masses down to 5 GeV/c^2 is only feasible if the NR energy threshold is at least 6 keV with an efficiency of 50%. The WIMP sensitivity is also limited by the discrimination efficiency of ER, leading to a conservative estimation of 99.5% for a 50% NR acceptance [12].

To accomplish such goals, the TPC design requires the collection of the S1 VUV photons to be maximized in order to reduce as possible the detector energy threshold and requires the electric fields to be as uniform as possible for a good resolution of the position reconstruction. The latter is particularly important for events occurring in the detector periphery to maximize the liquid xenon fiducial mass and better characterize the detector wall background contribution [12]. Moreover, an additional consideration in a liquid xenon TPC experiment is the safety of the detector, of the Xe and monitoring of the detector parameters, entailing sophisticated engineering solutions and systems.

Although the primary goal of the LZ experiment is the detection of WIMP interactions with Xe nucleus (see chapter 2), its low background environment and signal production process, both sensitive to electronic and nuclear recoils, permits extending the LZ objectives beyond the dark matter detection. These goals involve detecting rare physical processes or particles, mainly related to neutrino physics, such as:

- **Solar neutrino detection**: The solar neutrino, or p-p neutrinos, are mainly created by the fusion of two protons into a deuteron in the Sun's core. The study of such neutrinos provides a method "...to see into the interior of a star and thus verify directly the hypothesis of nuclear energy generation in stars" [86, 87]. Due to its low sensitivity and energy threshold, LZ can potentially detect the elastic scattering of such neutrinos with the atomic electrons in Xe, providing additional information to the pp flux models pioneered by the SAGE [88] and

Borexino [89] groups.

- **Supernova neutrinos**: neutrinos produced during a supernova cause a burst of nuclear recoils (NR) well above the energy threshold, via coherent neutrino-nucleus scattering as they pass through the detector [90, 91]. The detection of such neutrinos, and the study of their profile, in terms of detection time, provides valuable insight into understanding the underlying process of a supernova. Moreover, through the coordination with other experiments around the world, it would be possible to provide an estimation of a supernova's origin, facilitating their targeting with telescopes.

- **Double beta decay**: This decay occurs in even-even nuclei when the single beta decay is energetically forbidden [15, 92]. During this decay, an isobaric transition occurs from a parent nucleus (A, Z) to a daughter nuclear (A, Z + 2), as two neutrons are converted into two protons [15]:

$$(A, Z) \longrightarrow (A, Z + 2) + 2\,e^{-} + 2\,\overline{\nu}_{e}$$

where the $Q_{\beta\beta}$ of the decay is the kinetic energy of the β-particles plus the neutrinos, ν_e. The two-neutrino double beta decay of ^{136}Xe has been observed by several groups such EXO-200, KamLAND-ZEN and by XENON1T [72, 73]. However, if neutrinos are their own anti-particle (Majorana particle) a neutrinoless double beta decay can also occur, where two betas-particles are simultaneously produced without the emission of neutrinos. The confirmation of the existence of the Majorana particle would be a significant discovery as it, by a violation of the lepton number, would provide valuable insight in leptonic asymmetries in models extending beyond the Standard Model [15].

The detection sensitivity for this decay half-life, $T_{1/2}^{0\nu}$, can be expressed as [15]:

$$T_{1/2}^{0\nu} \propto \epsilon a \sqrt{\frac{Mt}{B\Delta E}}, \tag{4.1}$$

where ϵ is the detection efficiency of the signal, a the isotope abundance of the parent isotope, M the detector active mass, t the acquisition time, B background rate and ΔE the energy resolution. Equation 4.1 provides a simple method to measure the detector sensitivity

to the neutrinoless decay by selecting a region of interest (ROI) around $Q_{\beta\beta}$ and assuming and constant background contribution. Despite its simplicity, equation 4.1 has the advantage of emphasizing the role of the essential experimental parameters. For example, the detection of the neutrinoless mode requires a good energy resolution at $Q_{\beta\beta}$ due to the dependency of the sensitivity with $1/\sqrt{\Delta E}$ in a non-free background experiment.

- **Axions**: (section 2.2.3) can be detected via the axioelectric effect (atomic electron emission by axion absorption). They are expected to produce ER events with a well-defined peak of up to tens of keV [93].

4.2 Detector Overview

The core of the LZ detector comprises a cylindrical TPC (figure 4.1) with dimensions of 1456 mm in diameter and approximately 1687 mm in height, filled with 7 tonnes of liquid xenon to act as the active material. The active region is observed by two arrays of 3" diameter PMTs (Hamamatsu R11410-22). One array with 241 PMTs facing up is located below the active region, and the other is installed above the electroluminescence region with 253 PMTs facing down [12]. The light collection is enhanced by covering the space between the PMTs with PTFE foils. The QE of these PMTs, with an average of 30.9%, was optimized for the detection of the xenon scintillation light at cryogenic temperature. To monitor the performance of the PMTs (gains, timing, afterpulsing rate etc.) a set of blue LED is installed inside the TPC, placed in a such way that each array can be illuminated by the LEDs installed in the opposite one [12].

The drift region, with a length of 146 cm, is defined by a cathode positioned 14.0 cm above the bottom array and by a gate electrode located 4 mm below the liquid surface. The uniformity and shape of the drift field in ensured by 57 ring electrodes stacked along the PFTE rings. The extraction and electroluminescence regions are formed by placing the anode grid 8 mm above the liquid level. An additional grid is installed right above the bottom array to shield the bottom PMTs from the high voltage of the cathode. This grid is kept at a potential close to that of the photocathode of the PMTs to ensure their stable operation [12].

The LZ TPC, described above, is mounted inside the inner cryostat vessel (ICV). Liquid xenon is

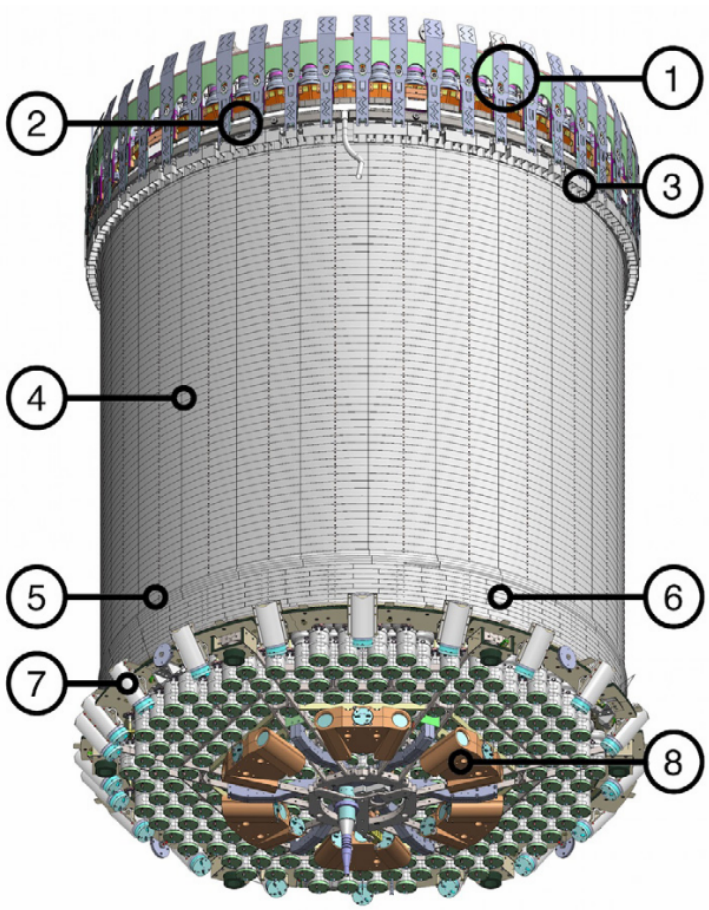

Figure 4.1: Representation of the LZ TPC. 1 – Top PMT array; 2 – Gate-anode and weir region (liquid level); 3 – Side skin PMTs (1-inch); 4 – Field cage; 5 – Cathode ring; 6 – Reverse field region; 7 – Lower side skin PMTs (2-inch); 8 – Dome skin PMTs (2-inch) [12]. The gate-to-cathode direction defines the z-axis of the detector, and the HV feedthrough presented in figure 4.4 is positioned at a 180° angle with the x-axis direction.

allowed to fill the region between the ICV and the PTFE walls to form a layer of liquid xenon around the TPC called Xe skin. The primary purpose of the skin is to provide dielectric insulation between the drift field rings and the ICV. This layer is also instrumented by an extra set of PMTs that observe interactions in this region and is used to veto the events that coincide with the TPC. Finally, the ICV is installed inside another vessel, called the outer cryostat vessel (OCV), which provides a vacuum jacket to stabilize the temperature inside the ICV. Both vessels were fabricated from low-radioactivity titanium [12].

The outer detector (OD) provides another veto-independent detector consisting of various acrylic vessels filled with a gadolinium-loaded organic liquid scintillator (GdLS) surrounding the OCV. Neu-

tron and gamma interactions occurring in the OD are tagged by 120 8' PMTs (Hamamatsu R5912) to provide a veto against multi-scatter background events interacting in both active Xe and outer region of the TPC [12].

The entire assembly, OCV and OD, is placed inside a water tank holding 250 tonnes of ultra-pure water. Although the primary purpose of the water tank is to shield the detector from external gammas or neutrons, it is also used to tag cosmic-ray muons passing through it (by using the same PMTs that observe the OD) in order to suppress the background from the neutrons produced by muon-nucleus reactions [12].

Stable conditions of the liquid Xe (175.8 K at 1.8 bar) are attained by equipping the detector with a cryogenic system, housing 1800 ℓ of liquid nitrogen (LN). By employing thermosyphon technology, first developed for LUX experiment, this system can passively remove heat from the Xe without using pumps to ensure the heat flux [12, 68].

For a detector with a considerable drift length, such as LZ, achieving a long electron lifetime is critical to accurately measure the S2 signal of events located at the bottom. Thus, the detector is equipped with a circulation system to purify the Xe and ensure the concentration reduction of impurities down to 0.4 ppb O_2 equivalent [12]. Unfortunately, the commonly used getters are unable to purify Xe from contamination by other noble gases and, consequently, their radioactive isotopes ^{222}Rn, ^{85}Kr and ^{39}Ar are an important source of background in liquid xenon dark matter detectors. ^{222}Rn, which, either directly or through its alpha-radioactive progeny, can induce (α, n) processes in the detector materials, leading to nuclear recoils similar to the ones expected by the WIMP signal. In order to mitigate contamination of the detector internals by ^{222}Rn and its progeny, in addition to monitoring its activity during the production and transportation of detector materials and limiting their exposure to Rn-rich environments, the detector circulation system features an online Rn removal system operating in parallel with the main circulation system [12, 94].

Furthermore, the commercially obtained Xe itself contains non-negligible concentrations of Kr and Ar, including radioactive, such as ^{85}Kr and ^{39}Ar isotopes. These are beta-emitters with an endpoint of 687 and 565 keV, respectively, which do not produce gamma-particles. Before its commissioning, the procured Xe was filtered, from Kr and Ar, in an independent chromatography system located at

SLAC (Stanford Linear Accelerator Center) laboratory [12].

Due to engineering and administrative complexity involving a large-scale experiment competing at an international level, the need to segment the LZ infrastructure into subsystems naturally surges. This division into subsystems also imposed a natural structure on the slow control system and shaped the interaction between the slow control developers and the respective system owners. In the following sections, a description is provided of the major subsystems directly involved in the operations of the detector.

4.2.1 TPC and Skin

The LZ TPC walls are comprised of 58 layers of PTFE, with each layer consisting of 24 segments with a height of 25 mm. This layered structure, visible in figure 4.2, minimizes the accumulation of charge in the PTFE and allows the PTFE to easily contract or expand due to of temperature variations in the TPC. Reflectivity of this PTFE material (Technetics® 8764) to the Xe scintillation light (when immersed in liquid xenon) was measured at LIP [75] and found to be 0.973.

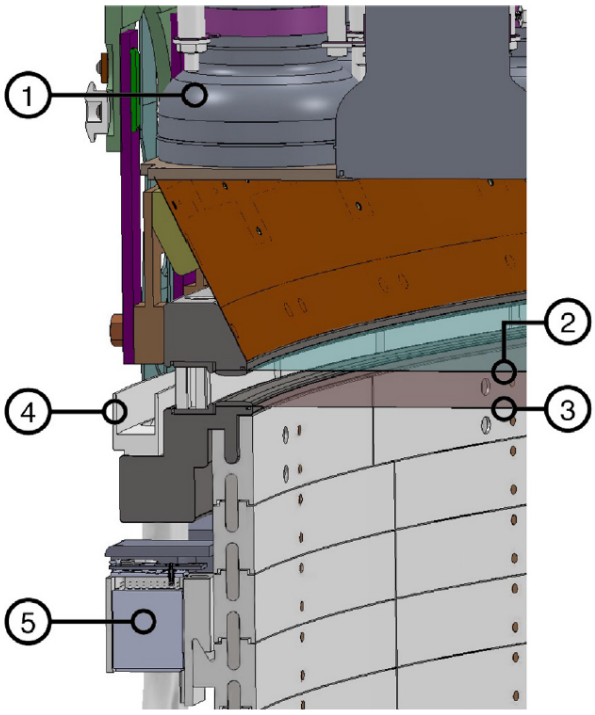

Figure 4.2: View of the LZ TPC top section: 1 — TPC PMT; 2 — Anode grid; 3 — Gate grid; 4 — Weir; 5 — Skin PMT [12].

Immediately after the electroluminescence region, the wall of the TPC presents, as shown in figure 4.2, a conical shape, with a height of 7 cm, widening from a diameter of 146 cm to 154 cm. This cone is covered by an optically absorbent material (Kapton®) to minimize the reflection effects of the S2 light, making the spatial response of the PMT as symmetric as possible, so it can be reliably reconstructed by the Mercury algorithm (see chapter 5) [12]. The geometry of the top array was obtained to optimize the S2 xy position reconstruction, resulting in a pattern with a hexagonal shape in the center transitioning to a circular format in the periphery, with the centers of the outermost top PMTs aligned with the PTFE walls [12].

The level of liquid xenon between the gate and the anode is fixed, as liquid xenon moving from the bottom to the top is allowed to spill over 3 weirs placed at the same height and equidistantly around the active volume. The liquid xenon collected by the weirs flows through 3 tubes piercing through the ICV, and returns to the circulation system as they descend in the vacuum jacket provided by the OCV [12].

The Xe skin constitutes a layer of liquid xenon filling the space between the TPC and the ICV. With a thickness of 4 cm at the top, widening to 8 cm at the cathode level, the skin contains 2 tonnes of xenon [12]. The lateral skin region is observed by 93 1' PMTs (Hamamatsu R8520-406) facing downwards installed at the top (figure 4.2) and 20 2" PMTs (Hamamatsu R8778) installed at the bottom facing upwards. The *dome* — skin region below the TPC — is also monitored by 18 2" PMTs, 12 of which are mounted radially outwards and 6 are installed radially inwards [12].

4.2.2 Grids and HV

The electric fields of the TPC are maintained by three electrically conductive electrodes, composed of the cathode, gate, and anode. These electrodes need to be optically transparent to permit the collection of the scintillation light by the PMT arrays, must allow the free passage of xenon and the gate electrode also needs to be transparent for the S2 drifting electrons. One of the best solutions that fulfill these requirements is grid-like meshes composed of hundreds of stainless steel wires with a diameter of 100 µm separated by a few mm (pitch). The parameters of these grids are a trade-off between a high optical transparency and uniformity of the local electric potential, as with increasing

distance between the wires (high pitch), the grid becomes more transparent to light, but it will also result in a less uniform electric field [80]. A similar logic is also applied to the diameter of the wires. Lower diameter values improve the grid transparency, but it also increases the density of potential lines near the wire itself, increasing the probability of spurious electron emission [80]. Also, wires with a larger diameter require more tension to be applied in the mesh without the risk of breaking wires [80]. At the same time, the wires are kept under high tension to minimize the sagging of the anode and gate grids under gravity to reduce xy non-uniformities of the electroluminescence [80].

The grids and PMTs operate under high voltage values, which must be kept as stable as possible. The values used by LZ in the first science run for the drift field were 193 V/cm along a distance of 146 cm, and 7.3 kV/cm for the extraction field [14]. This entails operating the cathode at 32 kV and the other grids at values closer to -4 kV. To polarize the cathode, a custom HV feedthrough capable of withstanding up to 150 kV was designed. This feedthrough, visible in figure 4.4, is placed outside the detector to minimize temperature effects in the liquid Xe. The final connector, linking the cabling and the cathode, was specially designed with a wide cone-like shape to mitigate sparks and discharge episodes near a critical region of the TPC [14].

The water tank and TPC arrays operate under typical voltages of 1.2 kV and the skin PMTs with voltages of 700 V. The HV system, biasing the PMTs, consists of three Wiener Mpod crates, each with 10 HV modules of 32-channels.

4.2.3 Circulation and Cryogenics

The circulation system of Xe, shown in figure 4.3, is the system responsible for maintaining the liquid Xe purity. The following explanation goes through the circulation loop, starting with liquid xenon at the top of the detector. As the liquid xenon spills through the weir, it is collected and transferred into a heat exchanger placed outside the water tank. In the heat exchanger, the liquid xenon is converted into gas, which then passes through a hot zirconium getter to remove the electronegative species from the Xe. After the purification process, the Xe is cooled again as it is recirculated through the heat exchanger, in the opposite direction, and then is liquefied by the liquid nitrogen thermosyphons of the cryogenic system. After this, to complete the circulation loop, the freshly purified liquid Xe is

slowly reintroduced from the bottom of the TPC through 7 inlet ports installed between the PMTs [12].

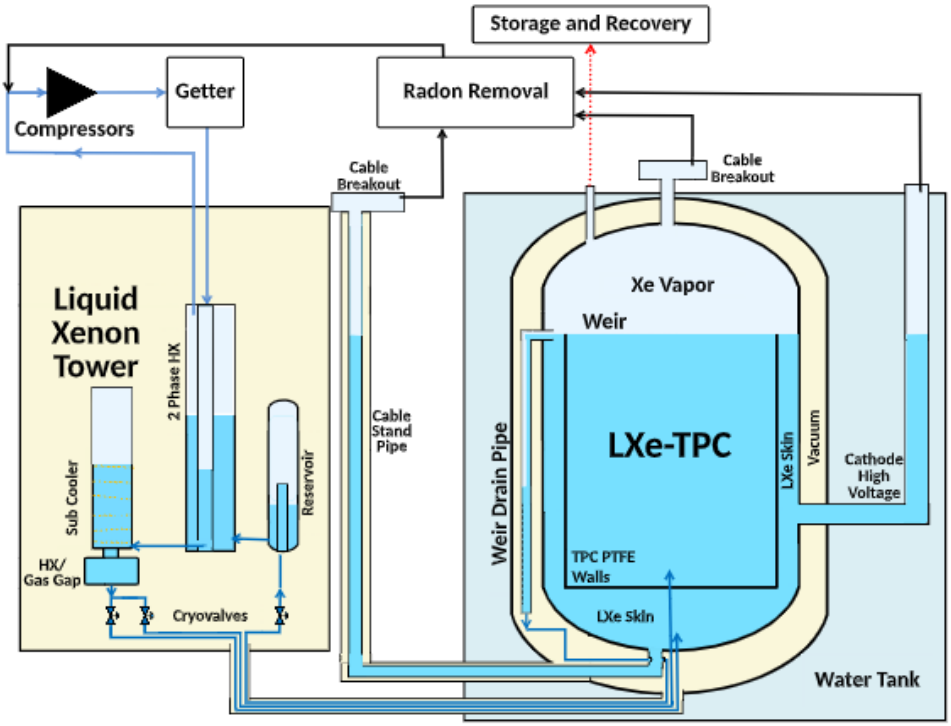

Figure 4.3: Overview of the circulation system and its major components [12].

The rate of the Xe flow is controlled and maintained by two 270 SLPM compressors (circulation compressors) and a mass flow controller [12]. During the first science run, the system, operating at 395 SLPM, was capable of maintaining the electron lifetime between 5 ms and 8 ms, significantly higher than the maximum drift in the TPC [14]. The system also features an online radon removal system with at 8.6 kg charcoal column operating in parallel to remove ^{222}Rn.

The temperature of the Xe is maintained by a nitrogen cryogenic employing thermosyphons. These are nitrogen-filled vertical tube that enables a controllable heat transfer between LN-cooled at the top and cold head at the bottom. When in operation, the nitrogen condenses at the top and then, as cold liquid descends by gravity, it evaporates, thus cooling down the cold head and, consequently, the detector parts in thermal contact with it. The heat transfer rate is controlled by adjusting the mass of nitrogen inside a thermosyphon. The main advantage of employing the thermosyphons is that this technology passively maintains the temperature of the Xe with a wide range of cooling powers that can handle both initial cooldown of the TPC and maintaining the temperature during

regular operations.

During operations that required a lot of cooling power, such as the initial Xe condensing, the cryogenic system also relied on two Stirling cycle-based cryocooler that provides an additional 1000 W of cooling power. Furthermore, four 450 liters dewars provide a backup supply of LN to the cryogenic system if the system heat load is above its nominal value (838 W) and surpasses the cryocooler capability [12]. Finally, a mobile reservoir, called COW (Cryogen On Wheels), permits to deliver additional LN to the system.

4.2.4 Xe recovery and sampling

A system as complex as LZ and using a considerable mass of liquified active material must have some contingency against critical situations. Such episodes can be a pressure surge in the TPC that could endanger the experiment; a vacuum leak resulting in a destabilization of the TPC; prolonged power outage or even an underground emergency can could jeopardize the experiment. Consequently, the LZ experiment relies on a recovery system that ensures the safety of the Xe and the ICV. In such cases, either automatically (by surpassing safety thresholds) or by operator intervention, two recovery compressors (each capable of operating at 300 SLPM) and multiple heaters are activated to store the Xe in safety containers while maintaining its purity conditions [12].

The Xenon circulation system is also equipped with an online sampling system where a small amount of gaseous Xe is retrieved and analyzed to measure the concentration of various impurities such as O_2, N_2, CH_4, Ar, He and Kr. This system operates by allowing Xe to flow, with a mass flow controller (MFC), to a residual gas analyzer (RGA) which measures, through mass-spectrometry, the partial pressure of the various species of interest. To enhance the measured concentrations and thus increase the sampling sensitivity, before entering the RGA, the sample passes through an LN cold trap where most of Xe freezes out [95].

4.2.5 Outer Detector

Neutrons with an energy between 0.5 and 5 MeV, originating from (α, n) processes in the inner detector materials, can scatter on Xe nuclei, creating nuclear recoils similar to those expected from WIMPs. If one of these neutrons scatters in the liquid xenon just once before escaping the TPC, the resulting signal would be indistinguishable from the expected WIMP signal. The main objective of the OD is to tag these neutrons after they leave the TPC and veto any event in the preceding time window.

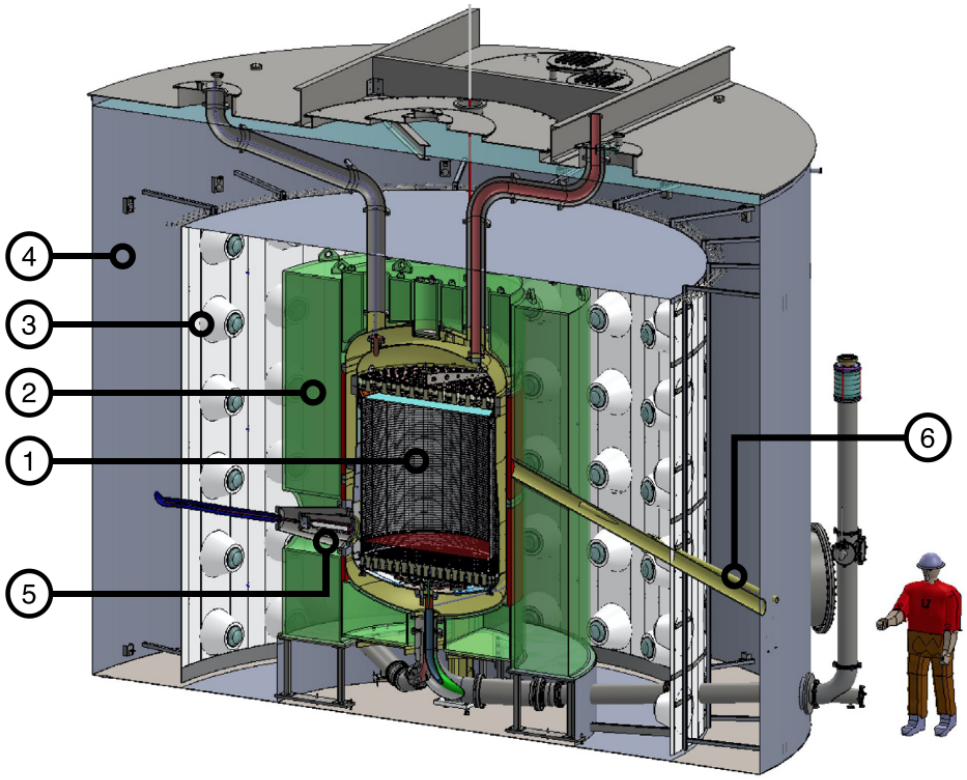

Figure 4.4: Representation of the LZ detector main components [12]: 1 — TPC; 2 — GdLS Outer detector; 3 — OD PMTs; 4 — water tank; 5 — cathode high voltage; 6 — neutron calibration conduit.

The OD consists of various acrylic vessels filled with a total of 2 tonnes of liquid scintillator loaded with 0.1% of gadolinium (GdLS) surrounding the OCV and, consequently, the liquid xenon (see figure 4.4). The GdLS consists of a solution of a linear-alkylbenzene[1] solvent, with a solute denominated by PPO (2,5-diphenyloxazole) and a wavelength shifter. When an energy deposit occurs, the solvent molecules are promoted to excited states, which, through collisions, transfer the energy to the solute

[1] hydrocarbon chain with a benzene ring

and result in the emission of fluorescent light. The wavelength shifter absorbs the fluorescent light and re-emmits lower energy photons, which better match the spectral response of the PMTs [96]. The GdLS is viewed by 120 PMTs evenly distributed in 6 ladders radially installed at the water tank wall (at a distance of 115 cm from the acrylic vessels) that are covered by Tyvek reflectors to improve the light collection efficiency. This entire assembly is submerged in 228 tonnes of ultrapure water, yielding an extra shielding layer of 84 cm against external backgrounds [12].

Systems employing this technology can veto neutrons with an efficiency above 95%, as these have a relatively small path length of a few centimeters when traveling through the GdLS [12]. Figure 4.5 presents, from simulated data, the NR background reduction attained in the TPC through the vetting system.

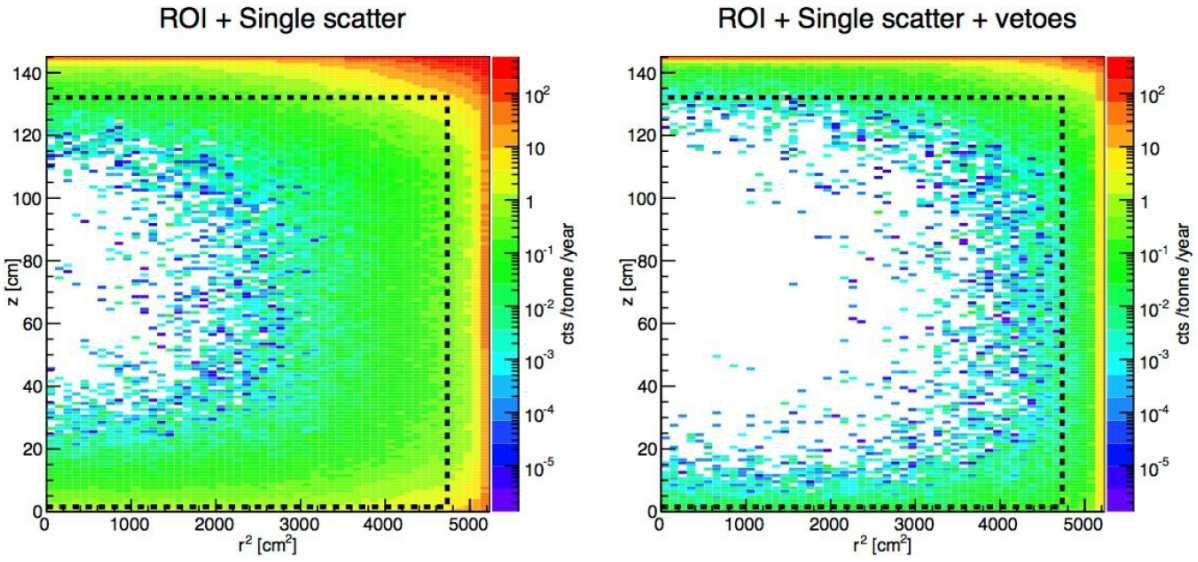

Figure 4.5: Simulation of the NR background contribution from external sources to the TPC. The right image shows the considerable improvement provided by a neutron tagging efficiency of 90% [73].

Another possible source of background is muon-induced neutrons and rock neutrons that thermalize in the water tank and are captured by the hydrogen of the water molecules, resulting in formation of deuterium nucleus and emission of gamma-rays. These, through Compton scattering, transfer energy to electrons, which, consequently, produce Cherenkov light. The detection of this light by the OD PMTs is used as an additional veto system for external backgrounds [96].

Similarly to the TPC arrays, the OD array is also equipped with an optical calibration system. Com-

prised by 30 LEDs with a wavelength of 430 nm and mounted on the supports holding the PMTs, the system is used during periodic calibrations to monitor the gain of the PMTs and optical properties of the ultrapure water and GdLS.

4.3 Calibrations

As discussed in chapter 3, the measurement of the g_1 and g_2 gains is required to correctly reconstruct the energy of an electron or a nuclear recoil with equation 3.11. The calculation of these gains is done by recording the detector response to ERs and NRs of known energies. Moreover, the non-uniform response of the S1 and S2 signals needs to be corrected with dedicated lookup maps. Although the usage of a source with known energy is not mandatory to create such maps, they require the acquisition of data under controlled conditions. Furthermore, in order to optimize ER discrimination for a WIMP search, low energy NR and ER bands must be measured so that the separation between NR and ER in the S1-S2 space can be tuned.

The LZ detector relies on several calibration sources covering a wide energy for nuclear and electronic recoils. These sources are classified as:

- Internal source – injection of a radioactive material into the xenon circulation system to calibrate the detector most inner volume, which, due to the liquid xenon self-shielding properties, is not feasible with external high energy gammas;
- External source – placement of radioactive source near the walls of the ICV;
- Neutron source – usage of the Deuterium-Deuterium generator to calibrate the detector response to NR events.

4.3.1 Internal sources

The goal of an internal source is to calibrate, as well as possible, the inner volume of the detector. As such the used materials need to be soluble in liquid xenon and have a half-life high enough (several hours), so that they can be uniformly mixed in the chamber and reach the most central region. On

the other hand, the half-life needs to be low to minimize the chances of leaving radioactive traces, prevent ADC saturation or/and needs to be filtrable by the circulation system.

One of the sources injected in the detector is ^{83m}Kr. It decays to the stable ^{83}Kr, mainly via internal conversion, through two states with a half-life of 1.83 h and 154 ns, producing two lines of 32.1 keV and 9.4 keV, observed by the detector as a mono-energetic peak of 41.5 keV (see figure 4.6). The mono-energetic and short half-life characteristics of ^{83m}Kr make it a suitable radiation source that can be diffused into the liquid xenon in the TPC, providing a method for position reconstruction calibrations of the S1 and S2 signals [19]. Unfortunately, due to the high volume of the LZ TPC, the ^{83m}Kr is not uniformly distributed before it decay presenting some regions in the z direction with a higher planar uniformity than others. As discussed in chapter 5, for the purpose of position reconstruction calibrations, spatial cuts are applied to isolate a specific slice in the z-axis with a higher uniformity.

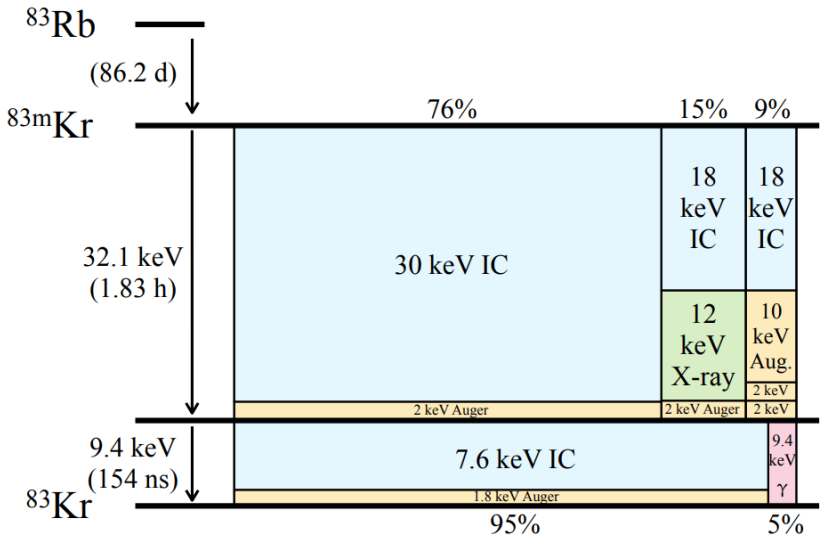

Figure 4.6: Scheme of ^{83m}Kr decay [19].

The ^{83m}Kr is injected into the detector by flowing the gaseous Xe through a radon-pure charcoal column loaded with ^{83}Rb (with a half-life of 86.2 days), where the injected dosage is controlled by the flow rate and duration of the carrier gas. The same procedure is used for calibrations with ^{131m}Xe (164 keV and half-life of 11.9 days). However, a charcoal column loaded with ^{131}I is used [12].

The other injectable source, Tritium (^{3}H), with a beta decay endpoint of 18.6 keV, is essential to

calibrate the detector response in terms of the S1 and S2 energy scale and S2/S1 discrimination efficiency for low-energy ER events. The ^{3}H is introduced into the detector by filling a pre-dosing volume with the required pressure of tritiated methane, which is then directly flushed into the Xe stream of the circulation system. The getter ensures the removal of the methane from the liquid xenon in a single pass. However, given that it takes about two days to fully purify the Xe, this calibration source cannot be used as often as the ^{83m}Kr [12].

4.3.2 External sources

External source permit asserting the detector veto and self-shielding capability and measuring the detector response to NR events [12].

4.3.2.1 Source delivery system

External sources must be placed as close as possible to the detector to increase the ratio between direct and scattered radiation entering the detector. For this reason, three vertical source delivery conduits were installed in the vacuum space between the ICV and the OCV. A source deployment system, mounted at the top of each tube, permits the placement of neutron or gamma at the required height with an accuracy of 5 mm [12, 73].

AmBe and AmLi neutron sources are used to assess the detector response to NR of energies of up to 300 keV, and 40 keV, respectively. Different types of gamma sources can also be used for different purposes. For example, ^{228}Th, emitting 2.615 MeV gammas, is used to calibrate the GdLS energy scale; the ^{57}Co, with main gamma lines at 122 keV and 136 keV, is used to assert the Xe skin energy threshold and a ^{22}Na which emits a pair of back-to-back 511 keV gamma rays from positrons annihilation, provides a method to synchronize the outer detector and skin response [12].

4.3.2.2 Photoneutron delivery system

An additional and independent source deployment system allows lowering photoneutron sources, in the form of a 20 cm diameter x 20 cm tall cylindrical tungsten pig weighting 116 kg, using a vertical conduit that traverses the water and GdLS acrylic tanks into the top of the OCV. This source uses

(γ, n) reactions to generate monoenergetic neutrons [12]. There are two such sources prepared for LZ calibration: a ^{88}Y Be source, generating 152 keV neutrons creating NR with an endpoint energy of 4.6 keV and a ^{205}BiBe, with dominant neutron energy of 88.5 keV and an NR endpoint of 2.7 keV. These sources allow calibrating the detector response to low energy NR where ^{8}B solar neutrinos might pose a source of backgrounds in LZ [12].

4.3.2.3 Deuterium–deuterium calibration system

Pioneered by the LUX collaboration, this system calibrates the detector response to low-energy NR recoils (1.1 to 74 keV) [97].

The system consists of two conduits, one crossing the water tank horizontally and piercing through the OD acrylic vessel until the OCV walls and the other, at 20° with the horizon, which, also crosses the water tank but intercepts the parallel conduit [12]. During the WIMP search these conduits are filled with water, which is replaced with nitrogen gas for the purpose of calibration. A deuterium–deuterium (D-D) neutron generator, capable of producing 2.45 MeV neutrons at the rate of up to 10^8 per second, is mounted on a lift such that neutrons can be "injected" via either of the conduits. The angled conduit permits collimating the neutron beam as the effective cross-section at the beam exit is reduced. Furthermore, the angle with the horizontal leads to a wider variation of the event depth, reducing the chances of pile-up, as events are more separated in drift time consequently facilitating the pulse matching task [12, 73].

Moreover, an additional calibration mode permits generating an almost mono-energetic beam of 272 keV backscattered neutrons, allowing to probe NR with an endpoint of 8.2 keV. This is achieved by placing the D-D generator between the horizontal conduit exit and a heavy water (D_2O) target. The D-D generator is then slightly offset so that the neutrons can only enter the conduit after being reflected by the D_2O target to the conduit entry point [12, 73].

4.4 Data readout and acquisition

Considering the large number of PMTs, the detector requires a sophisticated system to register the events. This system also needs to be versatile enough to permit the various arrays to operate

independently and to accommodate the various acquisition modes involved in the calibrations and dark matter search operations. In order to accomplish the various goals of the LZ scientific program, the acquisition system needs to cover a wide energy spectrum, from the detector threshold, at sub-keV levels, to several MeV.

Figure 4.7 presents a schematic of the main elements involved in the data readout and acquisition. The signals of the PMTs are fed into amplifiers, which output the amplified and shaped signals to the inputs of the digitizers. In order to increase the dynamic range of the system, the TPC and OD amplifiers were designed to simultaneously output two signals with a gain ratio of 10 (dual gain) [12, 98].

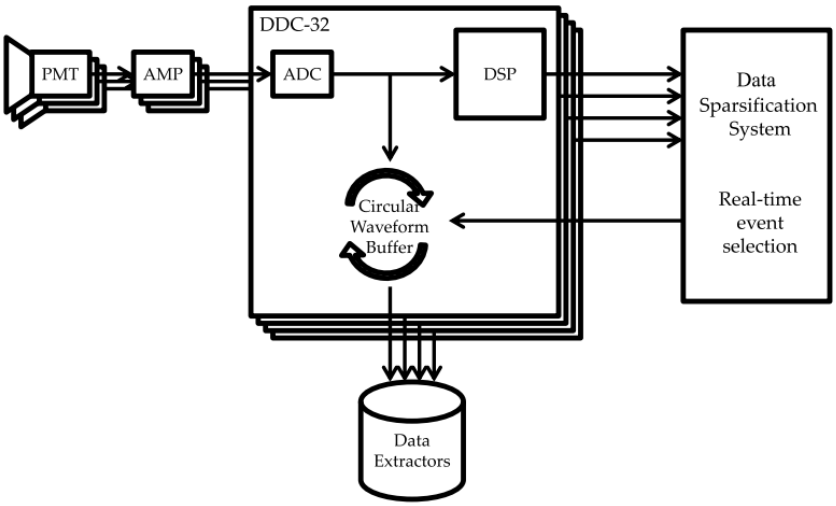

Figure 4.7: Simple representation of the acquisition system, with the amplifier boards (AMP) and the remaining DAQ chain analysing and processing the waveforms. DSP stands for Digital Signal Processing [98].

The digitizers convert, in real-time, the amplified signals into digital waveforms. Then a baseline suppression is applied, where only the pulses above a pre-defined threshold are considered for the posterior acquisition. The result is a series of pulses with the associated timestamps, denominated by PODs (Pulse Only Digitization) [98].

Various PODs acquired by a single PMT in a time window are stored in circular buffers while the Data Sparsification System executes a real-time analysis of the summed PODs waveform of a subset of PMTs (TPC, Skin and OD). This analysis looks at the outputs of digital filters tuned for the characteristic shape of S1 and S2 pulses. If pulses matching pre-defined criteria are found, the DAQ

is triggered, and the PODs are sent to the Data Extractors. Using trigger conditions restricts the volume of recorded data to a relatively small fraction containing useful information [98].

4.4.1 Electronics

The signals from the PMT are fed to amplifier boards, which re-shapes and amplifies the raw signal. To increase the dynamic range, the signals from the TPC and OD PMTs pass through two amplifier circuits with different amplification gains and shaping constants, as shown in Table 4.1. These parameters are chosen such that a 164 keV energy deposit of the ^{131m}Xe does not saturate the digitizers of any PMT.

Table 4.1: Parameters of the DAQ amplification boards [12]. FWTM represents the Full width at 10% of the maximum

	Gain	**Shaping constant (ns at FWTM**
Low Gain	4	30
High Gain	40	60

Although the dual-gain approach doubles the number of channels of both TPC and OD PMTs, it has the advantage of increasing the energy range of the detector, as high energy events causing saturation of the ADC conversion in the high gain channel can be processed and analyzed by the low gain channel [12, 98]. This design introduces the notion of mixed gain, where for a given event the pattern of PMT signals can have data from both low gain (LG) and high gain (HG) channels.

4.4.2 DAQ

The amplified signals are digitized at a rate of 100 MHz and a 14-bit resolution by 32-channel digital signal processors, or digitizers, custom-built for LZ. As the PMTs signals are processed, the digitizers create the ADC waveforms for all channels, that are stored in circular buffers [12, 73, 98].

In parallel, the Data Sparsification System receives a sum, grouped by detector (TPC, OD and Skin), of all pulses. Digital filters process this waveform by looking for pulses matching a given width and threshold criteria. This will act as the trigger condition to record the buffered waveforms into output files ready to be used by the online and offline analysis software [12, 73].

The most important trigger conditions for the WIMP search are activated by specific S1 or S2 filters. However, the DAQ can also operate with other types of triggers that are more suitable for other operations. An example is the usage of external triggers to synchronize the acquisition with the LED calibrations [73, 98]. Other examples of external triggers used during the detector commissioning are heartbeat trigger operating at a given fixed rate, and the random trigger, activated on average at a given rate.

The data generated by the DAQ is streamed to an off-site supercomputer (National Energy Research Scientific Computing - NERSC), where an offline software processes and analyses the events, outputting processed files to be used in data analysis.

4.4.3 Online System

The Online Systems comprise the components operating in real-time during the data-taking operations. As represented in figure 4.8, these are the Underground Processing Monitor (UPM), the Slow Control (SC) and the DAQ, which, for the sake of simplicity, also include the Event Builder and Data Sparsification. To ensure the quality of the acquired data, and to facilitate off-site data processing and analysis, the operations of these components require a certain degree of synchronization, which is achieved through a main central agent called Run control (RC).

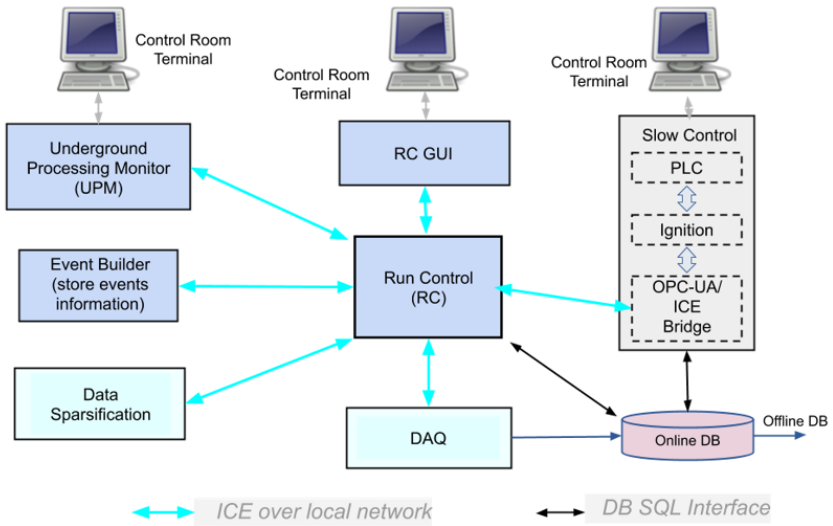

Figure 4.8: Block diagram of the online infrastructure with the main components: the Run-Control, the Slow Control, the UPM, the Event Builder and the DAQ [12].

As the DAQ generates the data, the UPM is responsible for analyzing, in real-time, the raw files to monitor the quality of the collected data and the general state of the detector. At the same time, SC provides supervisory control and monitoring of the detector subsystems and their respective hardware. Run Control coordinates the operations between these components by means of commands sent through a remote procedure framework ICE [99], while the Online database, is used for the exchange of more detailed information in the form of JSON (JavaScript Object Notation) objects.

Consider, as an example, the process of the detector calibration with a ^{83m}Kr injection. This sequential procedure is initiated by a Run Control operator via the Run Control GUI. First, a command is sent, via ICE, to the UPM to initiate specific analysis for the calibrations. Once the analysis commences successfully, the UPM reports back, through the online DB, its readiness to the RC, which will then command the SC to start Kr injection into the detector. If the operation's success is reported to the RC, the DAQ is ordered to begin the data acquisition.

This illustrative calibration ends either by the operator's action or when some termination condition is fulfilled, such as the acquisition of a predefined number of events. In the latter case, the DAQ stops its acquisition and reports this fact to Run Control, which then commands UPM and SC to complete the Kr injection operation. Upon reception of this command, the SC puts the circulation system in the original pre-injection state.

If any of these systems fail to achieve the required state along this chain, a "Failed" flag is raised and sent to RC to abort the operation. This flag is often accompanied by raising alarms, propagated by the SC, to notify the operators and provide some basic information regarding the issue encountered.

4.5 Data processing chain

The data processing chain entails all the required steps to preform the off-site processing and analysis of the files generated by the DAQ. Figure 4.9 presents an overview of the various stages of the LZ data processing chain. The raw files generated by the DAQ are initially stored underground before being sent to a 192 TB data storage array at the surface. This file transfer is ensured by two pairs of optical fibers capable of providing a rate of up to 40 Gb/s. From there, the files are sent to the primary data center located in the US at the NERSC. From NERSC, the files are copied to an

independent data center hosted by the Imperial College London in the UK [12, 73].

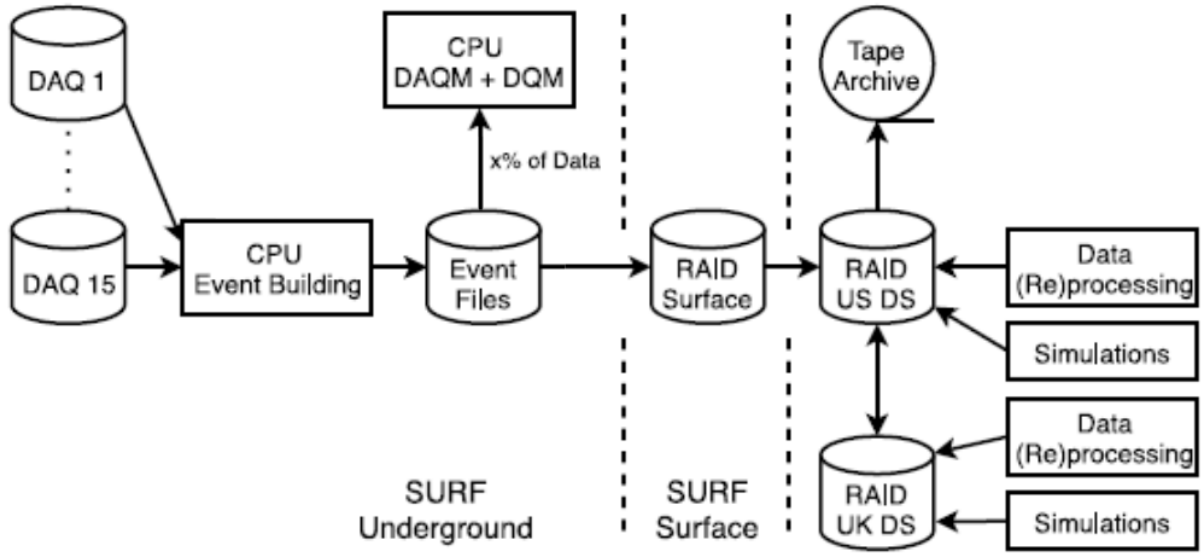

Figure 4.9: Stages of the data acquired by the LZ detector. The DQM (Data Quality Monitor) corresponds to the current UPM (adapted from [73]).

4.5.1 LZ Analysis Programme

The processing of the immense volume of data generated by the DAQ requires a dedicated and robust algorithm allocated in a dedicated infrastructure such as NERSC, as it requires a powerful CPU, but it also needs a proper framework to generate the output files with the results of the analysis regarding the acquired event. The processing of this algorithm, called LZap, is split into various sub-algorithms, starting from the most computationally expensive tasks and flowing towards the least demanding ones. This architecture approach facilitates the identification of bottlenecks in the data chain, and allows standardizing the LZap development as each stage consists of an independent module.

In the first step, LZap executes a low-level processing of the PODs to convert the raw ADC counts into a timeline of pulses (waveform), which is then analyzed to identify the boundaries of each pulse. Thereafter, the pulses are parametrized to produce variables that describe and summarize their shape. Such variables are called reduced quantities (RQs).

The next stage of the analysis chains is accomplished with the RQs calculated in the previous step. First, a classification algorithm identifies the pulses regarding their topology, such as, S1, S2, Single

Electron (SE). From the results of the classification, the analysis splits into tasks to calculate RQs specific for each pulse topology (e.g., position reconstruction of S2 pulses – see chapter 5).

The final step of the LZap processing is analyzing combinations of pulses to identify and classify physical interactions in the detector, such as single vertex interactions (single scatter) with an S1 followed by a single S2 or a multi vertex interactions (multi scatter) with a S1 followed by various S2s.

During the long acquisition periods, it is expected for the detector properties to change, introducing a time dependency of the acquired signals. This drift entails a continuous monitoring of critical detector parameters, such as electron lifetime and the single photoelectron response of the PMTs. These parameters, and the corresponding timestamps, are stored in a database dubbed *Conditions-DataModel*, which LZap queries to include corrections to minimize the non-uniformity response of the detector.

4.5.2 UPM

When one considers the many calibrations modes of the LZ detector and the associated demanding agenda to be accomplished by the underground team responsible for the data-taking operations, the need to perform a real-time monitoring of the acquired data naturally arises. Such analysis provides a method to assert the quality of the data generated by the DAQ and is used to monitor the state of the detector.

Although LZap, installed off-site at NERSC, produces a robust analysis, the underground-to-NERSC file transfer rate is the main bottleneck to, in real-time, monitor the quality of the data generated by the DAQ. One could, in theory, run a version of LZap onsite. However, its architecture requires a dedicated multicore infrastructure such as the one provided by NERSC. Moreover, to accommodate the detector's ongoing operations such "local" version of LZap would require continuous adjustments, which is not readily achievable in such complex algorithm.

The UPM is a lightweight yet robust package responsible for the real-time analysis of the acquired data. The bulk of UPM operates similarly to its offline counterpart, as most low-level algorithms are similar. However, its high-level layer performs tailored analysis suited to the various acquisition

types commanded by Run Control and, consequently, the detector operator. The consultation of the data generated by the UPM is done via a web-GUI. Moreover, the UPM can also raise alarms when it detects a deterioration of the data quality. In such cases, the alarms are sent, via a Modbus connection, to Slow Control to notify the operators.

The development of the UPM was accomplished by the LIP Dark Matter group. Details about its analysis chain, and the web-GUI developed in this thesis, can be found in chapter 7.

Chapter 5

Position and Energy Reconstruction

The reconstruction of the position of interaction is one of the essential elements of the dual-phase TPC technology, as it allows defining an inner fiducial region optimized in terms of WIMP sensitivity. Also, the study of the events formed in the detector periphery contains valuable information to estimate and model the background contribution of the TPC walls. The position reconstruction largely facilitates this study, as it permits to isolate and characterize these events [16, 17]. Furthermore, the accuracy of the position reconstruction impacts the energy resolution as well, through position-dependent corrections to the S1 and S2 signals from which the energy is reconstructed.

In the case of calibrating the detector response to nuclear recoils with mono-energetic beams of neutrons, the recoil energy can be reconstructed from the known initial neutron energy and the scattering angle of the multiple interaction sites. The accuracy with which this angle (and, consequently, the recoil energy) can be measured is defined by the accuracy of reconstructed positions of the neutron interaction vertices [16, 17].

This chapter presents the algorithm currently used by the LZ collaboration to reconstruct the xy position of the events occurring in the TPC, achieved by searching for the xy position that produces the best match between the output of the detector's position-dependent light response model and the

observed light pattern measured by the PMTs. The reconstruction technique follows the statistical position reconstruction method developed for gamma cameras by Grey and Makovsky in the mid-1970s [100]. However, this technique relied on the availability of the light response model for the detector in question in the form of spatial-dependent light response functions (LRFs) of the PMTs. These functions were typically obtained by scanning the detector with a well-collimated gamma-ray source. Implementing such scanning in a noble liquid TPC proved to be a challenging task, so an iterative technique for reconstructing the LRFs from calibration data obtained with a non-collimated source (flood irradiation) was developed by the ZEPLIN-III collaboration [16]. The statistical position reconstruction using these iteratively reconstructed LRFs received the internal name “Mercury”, which was later picked up by the LUX and the LZ collaborations [17].

This chapter also introduces a novel method to produce light collection corrections of the S2 signal within the position reconstruction framework. It presents the energy reconstruction of single scatter electronic recoil events, which produced competitive results in energy resolution in the energy region of [0.1, 3] MeV, asserting the capabilities of the new correction method.

5.1 Position reconstruction Methods

In the LZ detector, the position reconstruction of events occurring in the active region of the TPC is accomplished by analyzing the spatial distribution of the S2 light measured by the PMTs in the top array. The following section describes some position reconstruction methodologies that are most commonly used in the liquid xenon dual-phase TPC technology: the Center of Gravity (CoG) method; the usage of Neural Networks; and the statistical approach based on the statistics of the Poisson distribution. Table 5.1 provides an overview of these algorithms.

The most simple and fastest method is the Center of Gravity (CoG), and in most cases, the method only requires knowing the positions of the PMT and their relative gains (if the array is not equalized). However, this method lacks a *goodness-of-fit* parameter, which allows the identification of events with an unexpected light distribution, that can contribute to the background of the signal such as multi scatter events. Furthermore, this method has a high bias of the reconstructed position, as it does not consider the position-dependent light collection efficiency of the PMTs. On the other hand, the Neural Network (NN) algorithm is a more robust method, providing a better accuracy of the reconstructed position with a fast processing speed [101]. However, it has two main disadvantages: *(i)* it requires a training dataset, typically generated by simulated data, with the information of the *true* event position; *(ii)* an alteration on the set of PMTs used in the reconstruction entails an additional training of the NN model. Statistical-based algorithms, such as the one used by LZ, are also the most robust and complete methods. In this case, the main disadvantage lies in the complexity required for its implementation and the high processing time (see table 5.1).

Table 5.1: Criteria by which position reconstruction algorithms are compared. Processing – reconstruction speed; Training – how long it takes to calibrate the algorithm; Unsupervised Learning – if the dataset used in training requires information with the event position; Bias – systematic effects in the reconstructed position; Input validation – if the method provides a *goodness-of-fit* parameter; Failed PMT impact – bias in the reconstructed position caused by an alteration of the set of PMTs.

	Processing	**Training**	**Unsupervised training**	**Bias**	**Input validation**	**Failed PMT impact**	**Algorithm Complexity**
CoG	Very fast	Not needed	–	High	None	High	Low
NN	Fast	Slow	No	Low	Possible	High	High
Statistic	Slow	Fast	Yes	Low	Always	Low	High

5.1.1 Center of Gravity

The most popular position reconstruction method in a scintillation camera is the Center of Gravity method, or centroid, first proposed by Hal Anger in 1958 [102]. In this approach, the xy position of the event is obtained from the classical expression to calculate the center of mass of an ensemble with N particles, where the mass and the position of each "particle" are replaced with the signal, A_i, and the position (X_i, Y_i) of the i-th PMT in the array, such that:

$$x = \frac{\sum_i A_i X_i f_i}{\sum_i A_i f_i},\ y = \frac{\sum_i A_i Y_i f_i}{\sum_i A_i f_i}\ , \tag{5.1}$$

where, f_i is an additional parameter added for each PMT to compensate for the variation in their gains and quantum efficiencies. However, due to the finite geometry of the detector, the reconstructed coordinate tends to be closer to the center of the array than the true event position, especially as the event approaches the periphery of the PMT array. The resulting reconstruction bias can be partially mitigated by using a "truncated" version of equations 5.1, with the summations taken only over the PMTs above a predefined threshold and further reduced by correcting the position with a look-up table. This table can be generated either from calibration or simulated data [16, 18].

The "truncated" centroid is used in LZ as the initial starting point for the statistical reconstruction before the application of the Mercury algorithm.

5.1.2 Neural Networks

In order to obtain a more precise event position, methods with an increased level of complexity and sophistication are required. For instance, the XENON1T collaboration uses machine-learning algorithms based on Neural Networks of "multilayer perceptron" type to reach a resolution of the order of mm [101].

The task of "training" the networks consists in finding the best parameters of the hidden layer, which, for a given dataset, minimizes a loss function. The training dataset consists of records, each containing the expected signals of PMTs for a given xy coordinate. In such a case, the results obtained with experimental data will only be as good as the training dataset generated by the simulation [101, 103].

5.1.3 Statistical Methods

Consider a point-like event, producing N photons at a xy position. If p is the probability for a single photon to be detected, the probability of detecting n photons out of the initial N, is given by binomial distribution:

$$P(n) = \binom{N}{n} p^n (1-p)^{N-n}. \tag{5.2}$$

In the limit where N is large and p is low the binomial distribution approaches the Poisson distribution:

$$P(n) = \frac{\mu^n}{n!} e^{-\mu}, \tag{5.3}$$

where $\mu = pN$ is the expectation for the number of detected photons. Then the probability for a given PMT, i, to detect n_i photons is [16, 104]:

$$P_i(n_i) = \frac{\mu_i^{n_i}}{n_i!} e^{-\mu_i}, \tag{5.4}$$

with μ_i representing the position-dependent and energy-dependent expectation value for the number of photons detected by the PMT i,

$$\mu_i = N\lambda_i(x, y) \ , \tag{5.5}$$

where λ_i, is the PMT LRF, defined here as the fraction of photons emitted isotropically from a given position, that generates a detectable signal in the i-th PMT [1].

Let $\{A_i\}$ denote a vector of the measured PMT signals, and $\{a_i\}$ a vector with the expected PMT signals,

$$a_i = q_i \mu_i \ , \tag{5.6}$$

[1] This is in the limit of N $\to \infty$. Another definition of λ_i is: the probability for a photon emitted in a random direction (isotropically) from a given position, to generate a detectable signal in the i-th PMT

where q_i is the measured response of the i-th PMT to a single detected photon. The position reconstruction process, depicted in figure 5.1, can be regarded as an optimization process, where the algorithm finds the combination of (x, y, N) that provides the closest match (similarity) between the vectors $\{A_i\}$ and $\{a_i\}$.

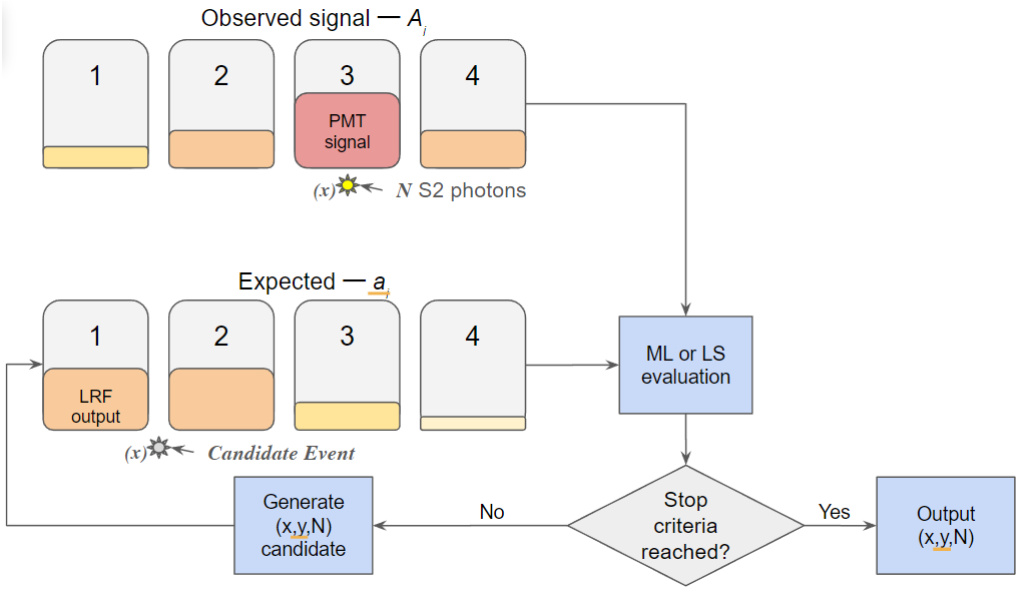

Figure 5.1: Mercury algorithm generalization with a fictional array composed by 4 PMTs. This example consists in a 1D simplification regarding the 2D case.The filled portion of each PMT represents either its own acquired signal or the Light Response Functions (LRFs) output for a "testing event" used in a given iteration.

There are several methods for estimating the similarity between $\{A_i\}$ and $\{a_i\}$, of which the most used is the maximum likelihood (ML).

5.1.3.1 Maximum likelihood

With the maximum likelihood method, as the name indicates, the likelihood function of obtaining A_i is maximized for an expected model of a_i produced by (x, y, N). If the number of detected photons, n_i, for each PMT is a known and independent variable, then the likelihood function can be expressed as [16],

$$L = \prod_i P_i(n_i, \mu_i). \tag{5.7}$$

In practice, it is more convenient to work with a log-likelihood function $\ln(L)$, as it converts a product into a sum of probabilities and helps to avoid problems with floating point precision when calculating L. This presents no impact on the maximization solution since the logarithm is a monotonically

increasing function.

In an important practical case, when n_i follows the Poisson distribution (equation 5.4), the log-likelihood can be expressed as:

$$\ln L = \sum_i \ln[P_i(n_i, \mu_i)] = \sum_i [n_i \ln(\mu_i) - \mu_i] - \sum_i \ln(n_i!). \tag{5.8}$$

Note that the last term of equation 5.8 does not depend on the event position or energy, so plugging in equation 5.5 and denoting the last term as a constant, C, we obtain:

$$\ln L(x, y, N) = \sum_i \{n_i \ln[\lambda_i(x, y)N] - \lambda_i(x, y)N\} - C. \tag{5.9}$$

Provided that we know the LRFs (λ_i), the (x, y, N) combination can be estimated by maximizing the function 5.9. Note that, for a given xy position, the log-likelihood is maximized by solving the equation $\partial \ln L / \partial \bar{N} = 0$, which gives the following closed-form solution:

$$N = \frac{\sum_i n_i}{\sum_i \lambda_i(x, y)}. \tag{5.10}$$

In this case, the reconstructed number of photons, N, is a scaling factor to match the sum of a_i at the reconstructed position xy with the sum of A_i.

From this result, the log-likelihood function can be re-written so that it only depends on the position of the event, and can be maximized analytically or by numerical methods [16].

5.1.3.2 Least squares

If the number of expected photons is high (in the order of 25 or more), then, as stated by the Central Limit Theorem, the Poisson distribution can be approximated by a Gaussian distribution with mean and variance equal to μ_i. This simplifies the position reconstruction algorithm for higher energies since, in this regime, the position reconstruction can be done by minimizing a weighted sum of residuals [16, 104]:

$$\chi^2 = \sum_i \frac{(a_i - A_i)^2}{\sigma_i^2}, \tag{5.11}$$

where, a_i, is the expected output signal for the i-th PMT and σ_i^2 is the variance of a_i.

The σ_i of equation 5.11 has several known contributions: Poisson fluctuations, given by $q_i\sqrt{\mu_i}$; fluctuations due to a non-null width of the PMT response to single photoelectrons, and electronic noise.

5.2 Light Response Functions

The shape of an LRFs is defined by the process of propagation of the electroluminescence light from the point of emission to the sensitive area of the corresponding PMT. The light can reach a PMT either directly or indirectly. Indirect paths include specular reflection at the liquid Xe surface, diffuse reflection from PTFE walls and Rayleigh scattering in the liquid Xe.

In LZ, the LRFs of the S2 light have an important role as these are used in the xy position reconstruction and also in the S2 light collection efficiency corrections. Since this light is produced in a thin horizontal layer of gaseous Xe between the liquid surface and the anode grid, the LRFs can be assumed to depend only on xy [16]. Moreover, the spread of the electron cloud due to diffusion is not expected to significantly affect the LRF shape, indeed, the value of this spread standard deviation can be calculated with [17]:

$$\sigma = \sqrt{2D_t t_d}, \tag{5.12}$$

where D_t is the transverse diffusion and t_d the drift time. Assuming a transverse diffusion constant of 60 cm^2s^{-1} [105] and a maximum drift time of 950 µs, the maximum standard deviation of this spread in LZ is approximately 3.4 mm, considerably smaller than the diameter of 3 inches (7.62 cm) of the PMT input window. Consequently, such spread of the cloud adds an insignificant uncertainty to the shape of the LRF, and S2 light source can be considered point-like.

5.2.1 LRF parameterization

The parameterization of the LRF entails defining its shape with a function. Whether this function and its parameters, have an actual physical meaning related to light propagation in the chamber or not depends on the approach and implemented solution [16, 17]. Nonetheless, the parametrization function should satisfy the following requirements [16]:

- Accurate representation of the LRF, since the LRF is the main instrument to reconstruct the event position, the more the function diverges from the *true* LRF, the worse the xy results will be;
- Minimize the number of parameters used in the function with no detriment to its accuracy, which not only reduces the number of data points required to fit the function to the shape of the LRF, but it also makes the function less prone to be overfitted;
- Fast evaluation, as the function is expected to be called several times when reconstructing the position of an event. Therefore, evaluation this function should not constitute a bottleneck to the algorithm.

In LZ, the shape of the LRFs is parameterized by a linear combination of basic splines (or B-splines) with a uniform distribution of knots (section 5.2.2) [18].

5.2.2 Top array LRFs

Due to the proximity of the electroluminescence region to the top array and the fact that the walls of the LZ gaseous region are covered by a material with a low reflectance (Kapton), the main contributions to the light collected by the top PMTs comes from the direct light and the light specularly reflected by the liquid xenon surface. In both cases, the probability of a photon to be detected depends only on the distance between the electroluminescence transversal position and the PMT center, denoted in this section by r. This implies that the corresponding LRF can be well approximated by a function of r, i.e., an axially symmetric function centered at the corresponding PMT. This fact was also confirmed by simulations of scintillation light propagation in LZ [106]. Conse-

quently, the light response of a top PMT can be parameterized as an axial LRF ensuring sufficient regularization to the convergence of the iterative LRF reconstruction described in section 5.3 [18].

When fitting a top array LRF, some additional constraints can be applied based on the physics of light collection by the top PMTs. The first and most obvious constraint is that an LRF is a non-negative function. Second, as it is mostly defined by the solid angle subtended by the PMT window from the emission point, the LRF decreases monotonically with r. Finally, the LRF consists of a smooth function of coordinates (i.e., it does not have higher spatial frequencies), as it cannot change more rapidly than a solid angle from a point in the electroluminescence gap to a small area in the PMT plane. This is important as it defines the optimal number of spline intervals.

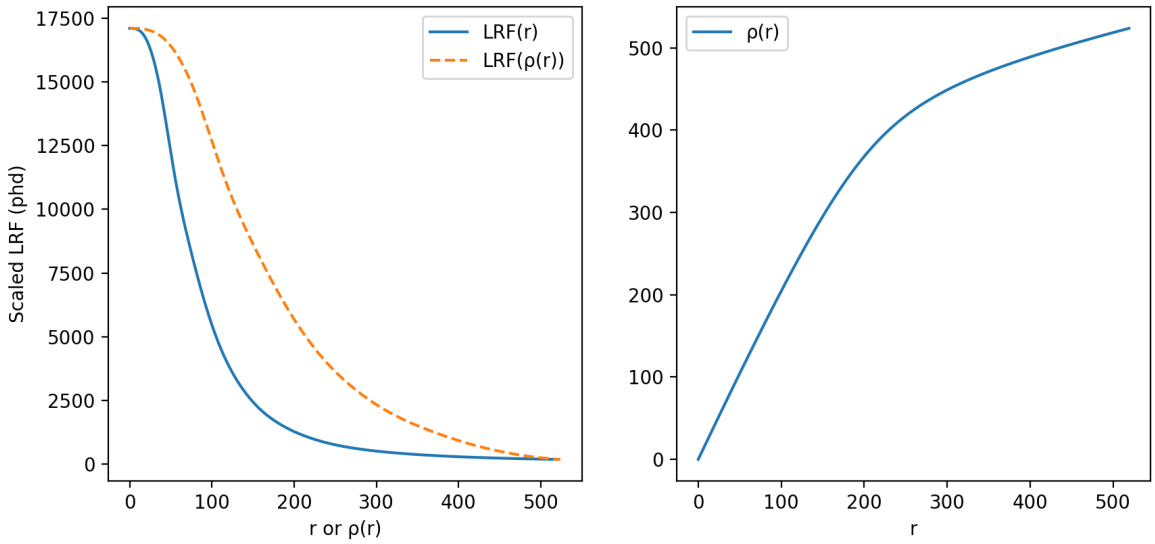

Figure 5.2: Representation of a generic axial LRF expressed as a function of r or ρ with $k = 10$, $r_0 = 200$ mm and $\lambda = 100$ mm. Right: plot of the LRF as a function of r and the $\rho(r)$ parameter (see text). Left: plot of the $\rho(r)$ parameter as a function of r.

The axial LRF, represented in figure 5.2 by the solid blue line of the left plot, has a region ($r = 100$), where its response changes rapidly with r, which complicates fitting the LRF with a uniform spline, as the number of knots needs to be well-balanced. Too few knots are not enough to accurately describe the fast-changing region, and with too many knots, the LRFs might be overfitted at higher r, creating artifacts in the reconstructed position. To overcome this problem, the LRF, instead of

being directly expressed by r, is expressed as a function of a new parameter ρ [18]:

$$\rho = b + a(r - r_0) - \sqrt{(r - r_0)^2 + \lambda^2}, \tag{5.13}$$

where $a = \frac{k+1}{k-1}$ and $b = \sqrt{r_0^2 + \lambda^2} + ar_0$. The k parameters define the overall smoothness of the LRF, r_0 and λ controls the position for the transition between the *fast* and *slow* regime. This transformation is, within the Mercury framework, denominated by *compression* [18]. The dashed orange curve in figure 5.2 exhibits much smoother behavior, allowing it to fit the LRF with the same precision using a smaller number of parameters.

In the Mercury framework, the LRF of a top PMT consists of a 1D spline with 15 uniform intervals, each expressed by a cubic function, for a maximum r of 728 mm. The coefficients of the spline are calculated from a generic Least Squares fit with experimental data.

5.2.3 Bottom array LRFs

In LZ, the S2 light measured by the bottom array is preferred to reconstruct the energy as this light is more evenly distributed in the bottom array, and consequently, these PMTs are less likely to saturate due to a smaller peak current. Although the methods indicated in section 6.1 can mitigate saturation effects of PMT, we found that the best energy resolution was obtained by considering only, in equation 3.11, the S2 signal recorded by the bottom PMTs. Therefore, knowledge of LRFs for the bottom PMTs is required to improve the accuracy of the light collection corrections. In this case, as shown in figure 5.3, the light response of these PMTs is not axially symmetric, and a smooth 2D function is required instead [18]. This function is implemented as a sum of a tensor product of uniform splines, where the smoothness is controlled by the numbers of intervals in both x and y directions. Similarly to the axial LRF, caution must be taken when selecting the number of knots to avoid overfitting.

Figure 5.3b also shows a deviation of the maximum of the LRF from the PMT center. This deviation is related to reflections of the detector wall. This effect is more pronounced for PMTs closer to the walls.

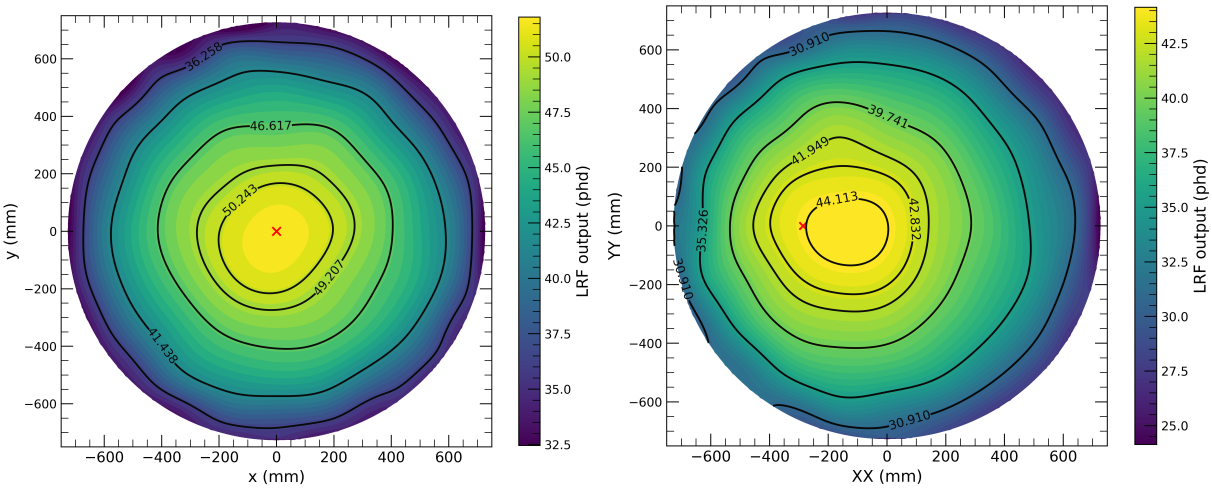

(a) PMT 0 **(b)** PMT 40

Figure 5.3: Map with the response of the bottom array LRFs created from ^{83m}Kr events. Left: response of the LRF for the central PMT. Right: response of the LRF for an off-center PMT. The red cross indicates the PMT position.

5.3 Iterative reconstruction of LRFs

In a few practical implementations of the gamma camera with statistical reconstruction, the LRFs were obtained by scanning the detector with a well-collimated gamma-ray beam and interpolating between the scan points [104]. For the cases when such a scan is difficult, the calculation of LRFs through Monte Carlo simulation of the scintillation light collection in the detector was proposed in [16]. Unfortunately, this kind of simulation tends to be computationally demanding, while its precision is limited by the uncertainty in the optical parameters available for the detector materials. While simulated LRFs show reasonably good results for gamma cameras of simple geometry [107], the attempts made so far to apply this technique to dual-phase TPCs were, to the best of our knowledge, unsuccessful [16].

Consider the S2 LRF reconstruction using the PMTs in the top array. Each single vertex event generates a vector $\{A_i\}$ of measured PMT signals, with dimensionality equal to the number of active PMTs, and encoding only three parameters: x, y and N. The excess information in $\{A_i\}$ encodes the spatial dependence of the light response of the detector. The iterative method proposed in [16] permits extracting this information (in the form of LRF spline coefficients) from a sufficiently large set of calibration events, even if the positions of these events are initially unknown. This calibration

dataset should fully cover the sensitive area of the detector (though not necessarily uniformly) and have a reasonably narrow distribution in *N*.

In this method, the shape of the LRFs is improved by fitting the position reconstruction results achieved in a previous iteration. The fitting of each LRFs consists in performing a least squares optimization between the parameters of the spline and the measured PMT pulse area for a given xy position. The first approximation of the LRFs is obtained using the event's positions reconstructed with the center of gravity method. With this first set of LRFs, it is then possible to use the ML or LS position reconstruction (sections 5.1.3.1 and 5.1.3.2, respectively) to improve the reconstructed positions with respect to the centroid. These improved position reconstruction results are then used to generate a second and improved set of LRFs.

This iterative process continues until a given stop criterion is reached. An important parameter used is the reduced chi-squared (χ^2_{red}) between $\{A_i\}$ and $\{a_i\}$ at the reconstructed xy. The better the LRFs are at describing the position-dependent light measured by the PMTs, the lower the dataset mean $\langle\chi^2_{\mathrm{red}}\rangle$ is. In this case, the $\langle\chi^2_{\mathrm{red}}\rangle$ is compared between iterations to determine if a given iteration makes a significant improvement. An additional criterion consists in analyzing a histogram of the radial position of the events. When the LRFs converge correctly, with which iteration, the spatial distribution of the reconstructed events, that were pulled towards the center by CoG reconstruction at the first iteration, becomes more uniform in the inner detector region. In that case, the outermost reconstructed events move closer to the detector walls, and the χ^2_{red} distribution shifts towards smaller values.

Between iterations, a set of event selection cuts is applied based on the output of the position reconstruction step in order to improve the precision of the LRF reconstruction and the convergence rate of the iterative process. The most important of these cuts are:

- cut of minimization status excludes those events for which the minimization did not converge;
- fiducial cut to exclude events erroneously reconstructed outside the sensitive volume;
- energy cut to exclude events with reconstructed energy, N, outside a predefined high range;
- reduced χ^2_{red} cut to remove the events that do not conform with a single scatter hypothesis

(most probably misclassified multiple-scatter events).

The convergence can also be improved using another technique proposed in [108] under the name of *blurring*. It consists of adding Gaussian noise to the reconstructed event coordinates with a progressively decreasing standard deviation. This technique can help resume the iterative process stuck in a local maximum of the global likelihood.

5.4 Event Reconstruction

A statistical position reconstruction algorithm depends on the following three components:

- A model of the detector response to scintillation events;
- A method for estimating the similarity between the two vectors $\{A_i\}$ and $\{a_i\}$;
- A method for searching the parameter space (x, y, z, N) for the optimal similarity (best match).

Below, the implementations of these three components in the Mercury position reconstruction package[2] used by LZ are briefly discussed.

5.4.1 Light Response Model

The Light Response Model contains all active sensor's positions and LRF parameterization. It receives an input of (x, y, N) and returns the expected PMT signals, i.e., the $\{a_i\}$ vector. It also contains the facility for saving and loading the complete LRM to/from a JSON file, making the maintenance, exchange, and distribution of detector models straightforward.

5.4.2 Similarity function

This similarity function receives two vectors, $\{A_i\}$ and $\{a_i\}$, and outputs a single value characterizing the similarity between them. At the time of this writing, Mercury implements two similarity functions:

[2] `https://github.com/vovasolo/pymercury`

- Maximum likelihood – it implements equation 5.9, which assumes a Poisson distribution for the detected photons.

- Least square – it implements equation 5.11, which approximates the binomial distribution to a normal distribution. However, such approximation is only valid for the events producing a high number of photons, when the distribution is less skewed, and better described by a Gaussian function.

5.4.3 Optimum similarity search

The final instrument required is an algorithm that, given a set of parametrized LRFs, finds the (x, y, N), which minimizes the similarity function. In LZ this algorithm is a gradient search (Migrad) provided by CERN Minuit2 package[3]. However, there are solutions to the light response model space parameters, led by the similarity function, which could drive the Migrad algorithm into local minima. To prevent this, the reconstruction of an event is initialized by a reasonable starting point, which results from the "truncated" center of gravity algorithm (see section 5.1.1).

5.4.4 Algorithm input tuning

One of the primary considerations to obtain a good resolution in the reconstructed position lies in the set of PMTs used.

First, in the "truncated" centroid method, PMTs are only used if their signals are above 10% of the PMT with the maximum signal. Though the value is probably dependent on the geometry of the array, the usage of a relative threshold considers the high dynamic range in PMT signals.

A PMT can malfunction or be switched off for various reasons. Fortunately, this is not a problem for statistical reconstruction since the exclusion of a sensor from the calculation of the similarity function does not affect the systematic error. The only impact is a somewhat degraded resolution in the vicinity of the excluded sensor. This degradation would pose a problem only when a cluster of nearby PMTs is switched off.

[3] `https://root.cern.ch/root/htmldoc/guides/minuit2/Minuit2.html`

The reconstruction expects that the enabled PMTs have a linear behavior. However, a PMT response can become non-linear (saturate) above a certain threshold (section 6.1.1), leading to a systematic error in the reconstructed position. To overcome this problem, PMTs with a signal above a given threshold are excluded from the computation of the similarity function. Consequently, apart from the $\{A_i\}$ vector, an additional input to the algorithm is a list of boolean flags which determines the saturated PMTs. Furthermore, it is possible to configure a radial cutoff, where only the PMTs within a given distance from the center of gravity reconstruction are considered for the minimization process. This not only makes the reconstruction less demanding for the CPU, but also improves the signal-to-noise ratio and makes the reconstruction more tolerant to random signals such as after-pulsing or single electrons. For LZ, with a maximum radius of 728 mm, a radial cutoff of 600 mm was used, which depending on the position of the event, excludes 20% to 60% PMTs of the top array.

5.5 LRF reconstruction in LZ

In LZ LRFs of the top array was obtained with different sources: ^{131m}Xe (164 keV), ^{83m}Kr (41.5 keV), and ^{222}Rn α-particles (5.49 MeV). Both ^{131m}Xe and ^{222}Rn are background sources present in the detector and ^{83m}Kr is a calibration source injected into the detector circulation system (section 4.3.1).

The data was acquired during the first science run, with the detector operating with a drift field of 193 V/cm and an extraction field of 7.3 kV/cm. The datasets of each source were filtered to contain only single-vertex events, i.e., a single S1 pulse followed by a single S2 pulse[4]. For each event, the filtered datasets contain per-PMT S2 pulse area, drift time, as well as other RQs required for the quality cuts (S1 area, event timestamp, etc.). An overview of the datasets is presented in table 5.2.

Regarding the advantages or disadvantages of each source, neither presents a silver-bullet solution for calibrating the LZ xy position reconstruction algorithm. Technically, the preferred source is ^{83m}Kr as it can be frequently used, and its injection parameters can be controlled to generate a high amount of events in a short period. Moreover, at this energy range, there is no saturation of the HG (see section 4.4.1) which facilitates the calibration process and, most importantly, prevents the inclusion

[4] Usually, events with this topology are also called “single scatter” events, as opposed to “multi scatter” events, which are not considered here.

Table 5.2: Overview of the datasets used to produce the various sets of LRF, the "before" column represents the starting data, for the selected peak and from a drift time cut of [50, 900] µs. For the ^{131m}Xe and ^{222}Rn datasets, a timestamp cut also excluded a period of 3 days related with an emergency stop of the circulation system.

Source	Radial (mm)	Drift time (µs)	Events before cut	Events after cut	Cut efficiency
^{83m}Kr	<728	[120, 300]	5.6×10^5	2.3×10^5	0.39
^{131m}Xe	<728	[100, 800]	4.9×10^5	3.0×10^5	0.62
^{222}Rn	<728	[100, 800]	2.5×10^5	1.7×10^5	0.69

of an additional source of fluctuation associated with the LG calibration. However, as visible in figure 5.4, compared with the high energy α-particles, the S2 peak of ^{83m}Kr is much wider, leading to more fluctuations in the shape of the LRFs. Moreover, due to the large detector size and the relatively low half-life, ^{83m}Kr does not have enough time to be uniformly distributed within the TPC before it decays. As a result, some reconstructed LRFs have considerably more deviations from the true shape (due to statistical fluctuations) than others. In our case, the uniformity was improved by isolating a single slice in drift time in the region of [120, 300] µs.

The ^{131m}Xe source, on the other hand, is well distributed within the chamber and has a relatively high amount of events available. Furthermore, this source is produced by cosmogenic activation at the surface, which means that the LRFs can be produced once the detector enters the calibration phase and before any ^{83m}Kr acquisition. A relative disadvantage of the ^{131m}Xe source is that the PMT areas need to include low gain values due to saturation at the high gain.

The same applies to the S2 of ^{222}Rn, which has a similar S2 pulse area, but compensates, in terms of fluctuations, with much narrower peak. Compared with ^{83m}Kr, the α-particles are more uniformly distributed in the detector. The main disadvantage of this source is that, due to a low decay rate, generating a sizable dataset entails longer acquisition periods and consequently handling time dependent signal fluctuations.

The fitting process is initiated with the position reconstruction results obtained with the truncated CoG method (section 5.1.1) with a relative cut-off of 10% (excluding PMTs with a signal below 10% that of the maximum PMT signal in the given event). Although the LRFs typically converge after five iterations, a total of 15 to 20 iterations are used in combination with progressively decreasing

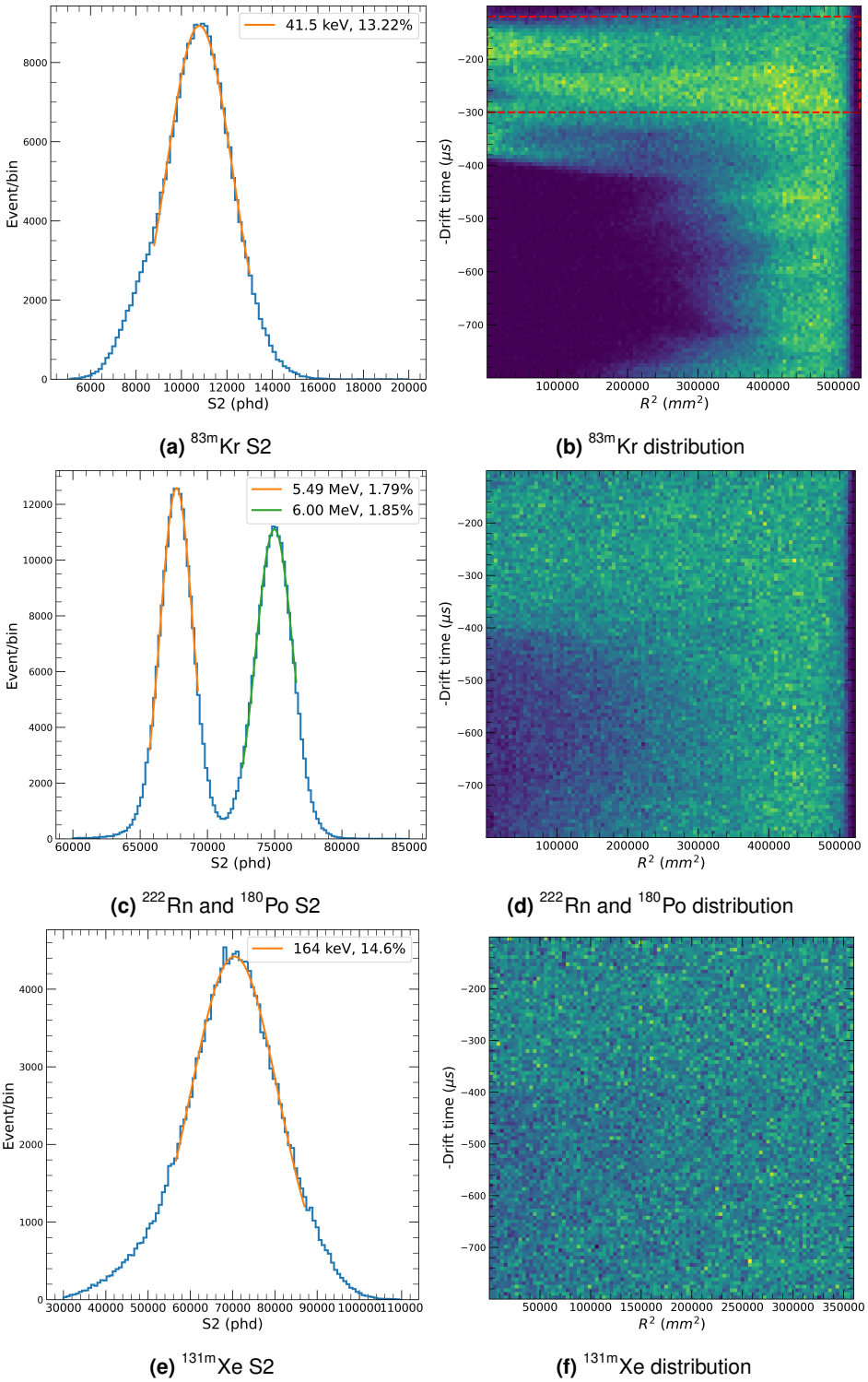

(a) ^{83m}Kr S2 **(b)** ^{83m}Kr distribution

(c) ^{222}Rn and ^{180}Po S2 **(d)** ^{222}Rn and ^{180}Po distribution

(e) ^{131m}Xe S2 **(f)** ^{131m}Xe distribution

Figure 5.4: Overview of the 3 sources used for fitting the various LRFs, the left panels present a histogram of the corrected S2 pulse as well the respective peak resolutions calculated as the standard deviation divided by its mean. The right panels plot 2D histograms with the distribution of the source within the detector. The 6 MeV ^{218}Po is shown only for reference, as it was not used in the fitting process.

Gaussian “blur” (with a standard deviation of 10–5 mm) to guarantee the complete dissipation of persistent artifacts in the shape of the reconstructed LRFs. Generic fiducial cuts in drift time of [100, 800] µs[5] and radius (<728 mm) are used to prevent possible effects at the edge of the sensitive volume. These cuts exclude regions with a non-uniform mixing of liquid xenon near the injection inlets, electric field distortions at the bottom, as well as the above-anode events and the events reconstructed outside the sensitive volume. A goodness-of-fit cut on χ^2_{red} is also included at each iteration to remove the mis-reconstructed events. Note that this cut needs to be updated with progressively smaller values to accommodate the progress of each iteration, and caution must be taken not to exclude too many events which could cause “holes” in the xy distribution.

Figure 5.5 demonstrates the improvements of the LRFs at several iterations of the fitting process for ^{83m}Kr events, presented in terms of xy distribution of the reconstruction χ^2_{red}. The fact that the regions at the periphery of the detector have higher χ^2_{red} in the first iterations (figure 5.5a) and, at later iterations, present a smaller χ^2_{red} (figure 5.5d) indicates that the axial LRF provides a good approximation to model the light response of the PMTs. Also, the region with higher χ^2_{red} in the (200 mm, -50 mm) strongly correlates with the position of the disabled PMTs of the top array (see figure A.1).

The LRFs obtained with events from three different calibration sources are shown in figure 5.6. The curves in the figure correspond to the central PMT of the top array, as an example. Note nearly identical shape of the functions reconstructed with the data from background sources (^{131m}Xe, and ^{222}Rn) and the one obtained using the data from the dedicated calibration with ^{83m}KrḞrom this we conclude that a valid light response model of the top S2 array can be reconstructed from the background data.

[5]The exception is the ^{83m}Kr LRFs which were generated from events located at the top of the chamber

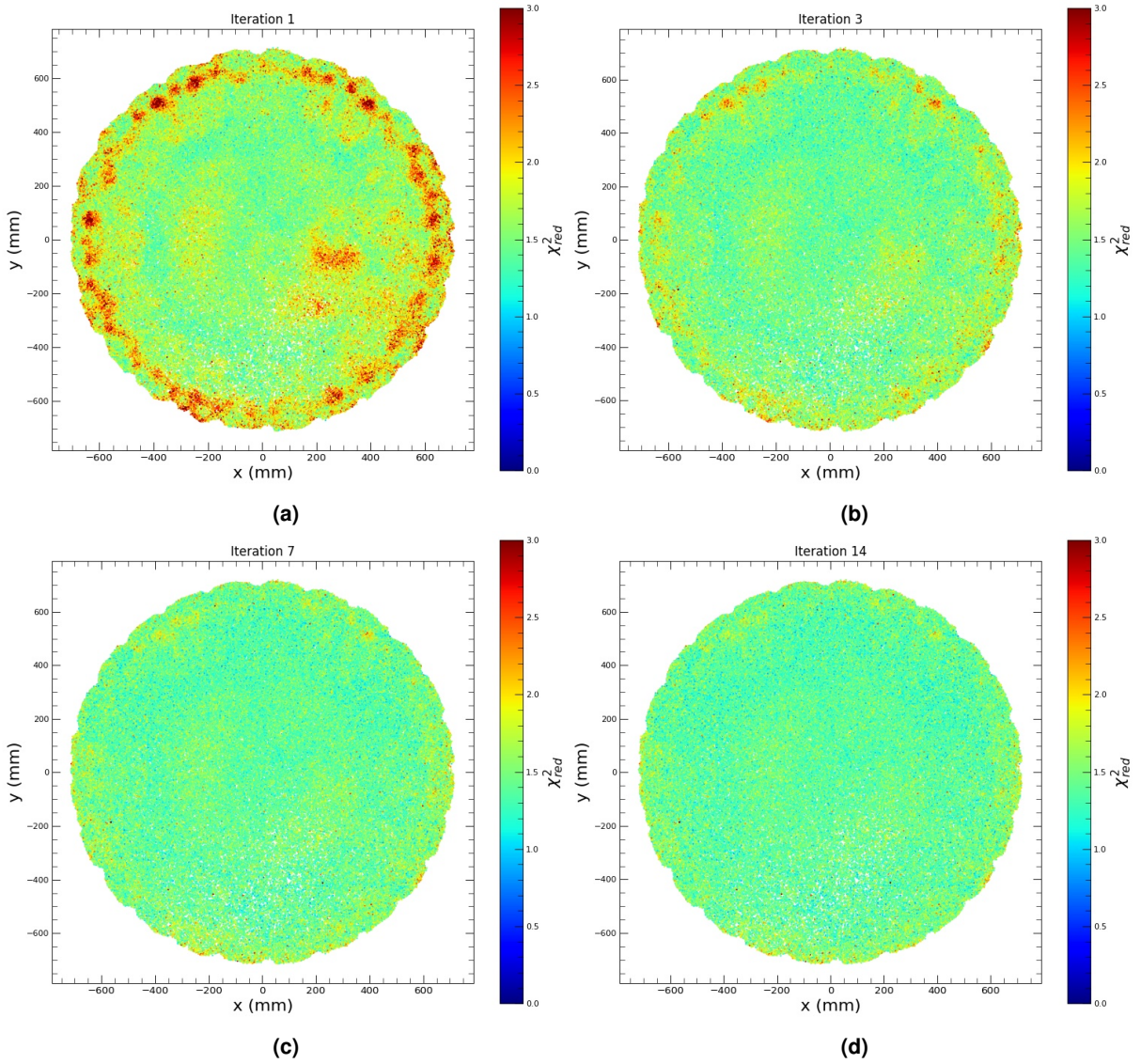

Figure 5.5: Position reconstruction results of the ^{83m}Kr LRFs. Each plot maps the spatial distribution of the reconstruction reduced χ^2 at different iterations of the fitting process.

5.5.1 Position reconstruction results and comparison between LRFs

The position reconstruction results for the ^{131m}Xe peak obtained with the Kr LRFs are shown in figure 5.7. As mentioned, this source is produced by cosmogenic activation of the liquid xenon and, consequently, is evenly distributed in the chamber. This is verified with the density parameter calculated for each event[6]. Figure 5.7 reveals interesting features in the detector. The dents spread

[6]This parameter is obtained from a 2d spline fit of a 2d histogram at the respective coordinate space (x vs y, or r vs drift time).

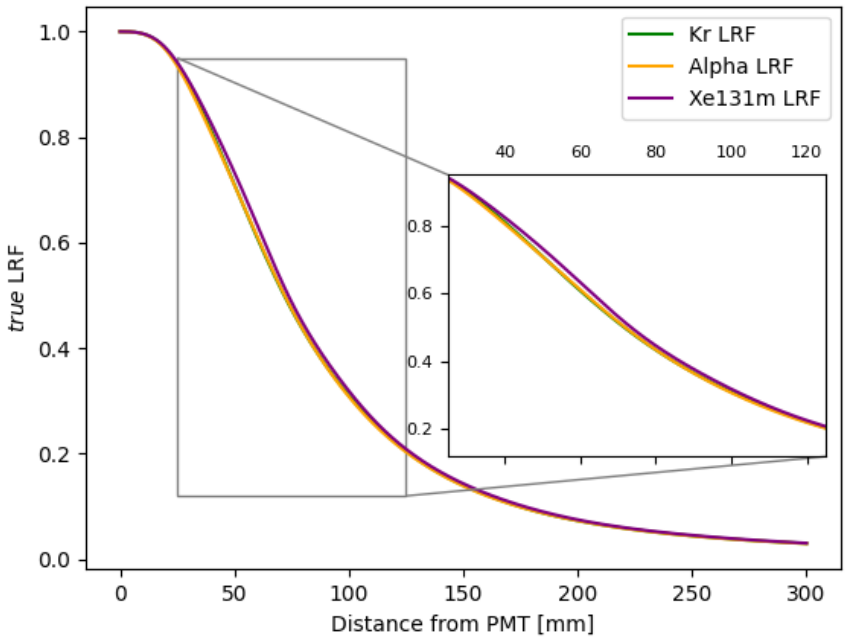

Figure 5.6: LRF of the top central PMT obtained from ^{83m}Kr, ^{131m}Xe, and ^{222}Rn alphas.

around the detector are caused by non-uniformity of the drift field. This was verified by observing a depth-dependent alteration in the shape of the dents (see figures A.2 and A.3). Another interesting feature are the two hotspots at the left. These are consistent with a ladder of field-cage resistors located at this position. The energy spectrum of these hotspots, at the 100–200 keV, is not consistent with any expected background, thus favoring the explanation of radioactivity of the resistors (see figure A.4).

A comparison between the LRFs obtained with different calibration sources is accomplished by studying the dependency of the distribution of the χ^2_{red} with the event radial position and depth in the detector. We selected the ^{131m}Xe peak for this study as it has a homogenous distribution in the chamber. The results are presented in figure 5.8 for events in r<680 mm and a drift time in [100 µs, 900 µs]. Looking at the overall results, the LRFs generated with Rn α-particles and with the ^{131m}Xe produce similar results and outperformed the ones produced with ^{83m}Kr. This is expected due to the lower fluctuation of the S2 used in the LRF fitting.

In LZ, the fluctuations of the PMTs signals have contributions that originate from the signal formation itself, as discussed in section 5.1.3.2, and from the processing of that signal. The latter is caused, for example, by the DAQ, in the estimation of the baseline of the pulse area leading to fluctuation

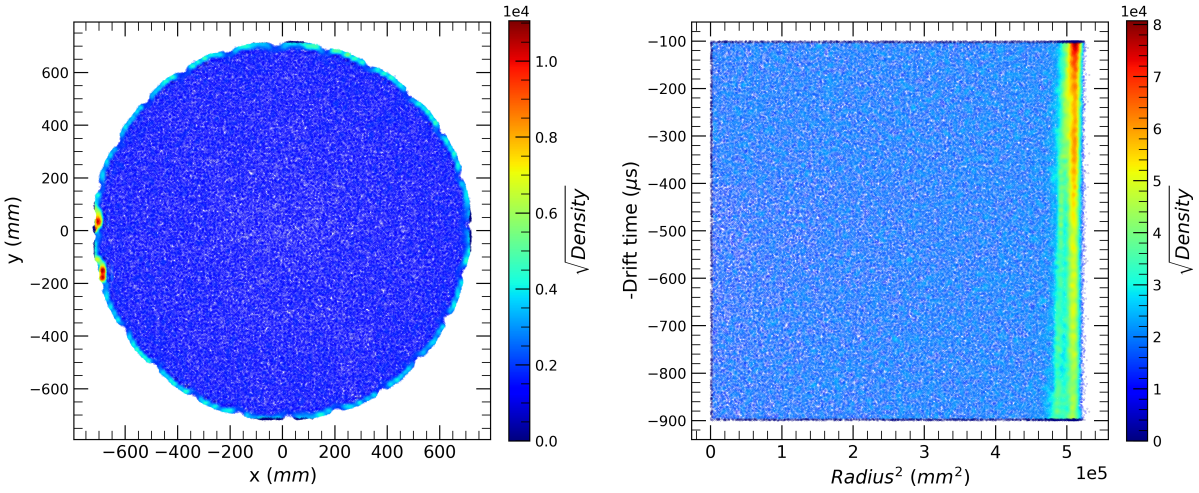

Figure 5.7: Position reconstruction of the ^{131m}Xe peak for the ^{83m}Kr LRFs, the peak, with 164 keV, was selected from the reconstructed energy at an interval of [152, 176] keV. A quality of the reconstructed xy χ^2_{red} of <12 was applied.

at the pulse parameterization level. In addition, the pulse-parametrizer algorithm also contributes to additional fluctuations associated with estimating the pulse tail. Finally, another source of fluctuations toward the high pulse area originates from the high-to-low gain scaling factor. The propagation of these fluctuations manifests in the χ^2_{red} of the reconstructed xy.

The increase of χ^2_{red} with the S2 pulse area can be explained by a systematic error of the pulse area parametrizer and an overestimating of the pulse area (section 4.5.1). For the same reason, the χ^2_{red} decreases with the event depth, as events at the bottom produce, for the same deposited energy, a smaller S2 pulse area due to electron attachment to impurities.

Moreover, as found in section 6.1.1, there is also some saturation dependency with the event depth. This is caused by the diffusion of the drifting electrons along the z-axis, associated with an electrostatic repulsion of the cloud. The result is a broadening in time of the S2 pulse and, consequently, a lower peak value at the PMT. Although small, this effect can negatively affect the position reconstruction for high-energy events closer to the liquid surface. Towards the center of the detector, there is an increase of the χ^2_{red}, most likely caused by a decrease in the resolution of the reconstructed position near the disabled PMTs, which are located at these radii. Towards the periphery, the χ^2_{red} also increases due to light reflections near the detector walls and a lower relative light collection compared with the bottom array.

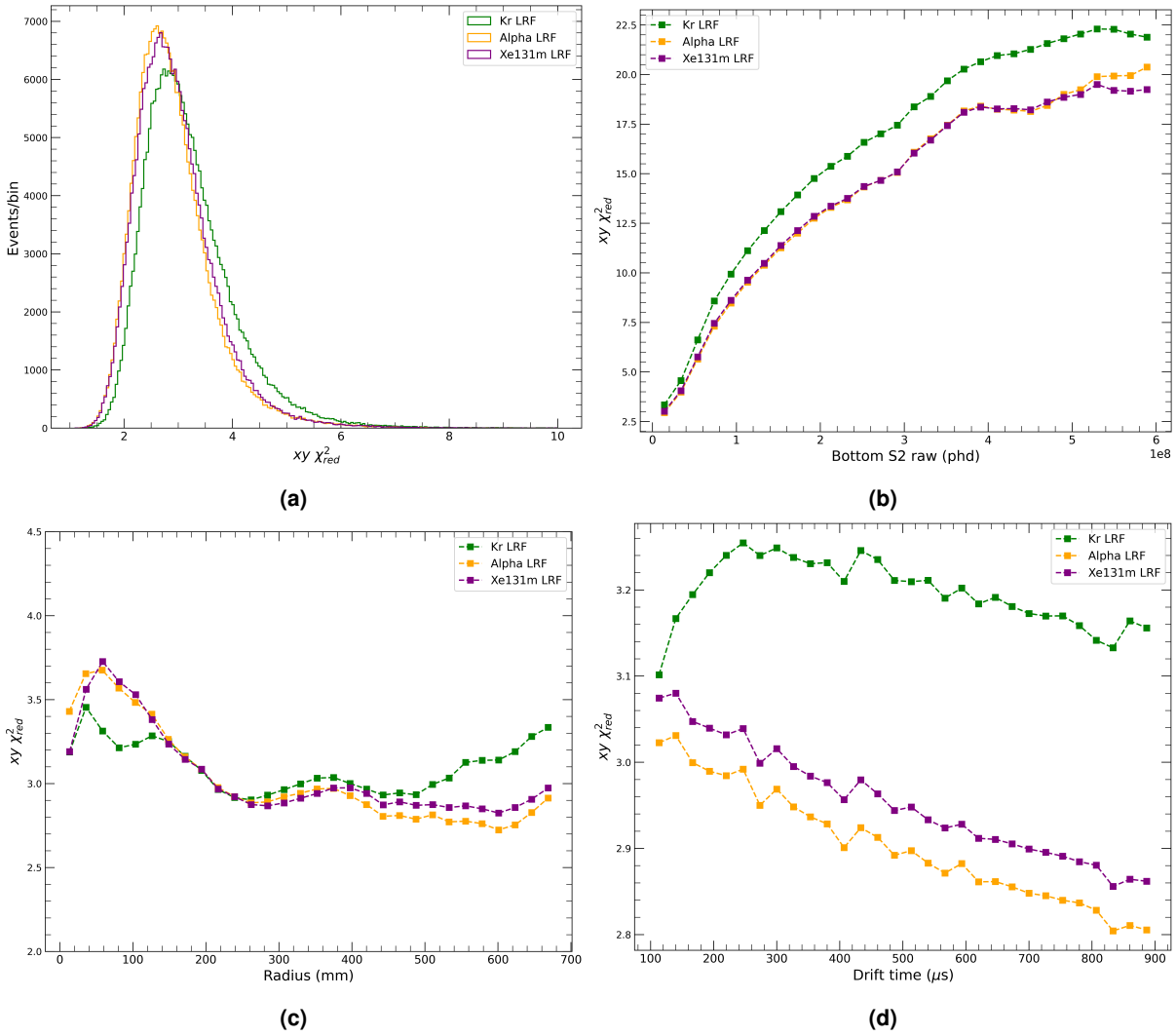

Figure 5.8: Position reconstruction results expressed in terms of bins of χ^2 for LRFs calibrated with various calibrations source. All figures present results for ^{131m}Xe events, except for figure 5.8b which presents the results for events in the [50, 500] KeV range.

Figure 5.9 also shows the dependency of the χ^2_{red} with time. This temporal profile is comparable with the profile of the mean electron lifetime shown in figure B.1, which also tends to increase and also presents an abrupt decrease towards the end of March. The dependency of χ^2_{red} with electron lifetime is justified by the same systematic effect of the pulse area estimation. Although the profile of this drift is similar between the LRFs, the lower absolute of both ^{131m}Xe and αs is a consequence of their smaller uncertainty due to the narrower S2 used in the fitting.

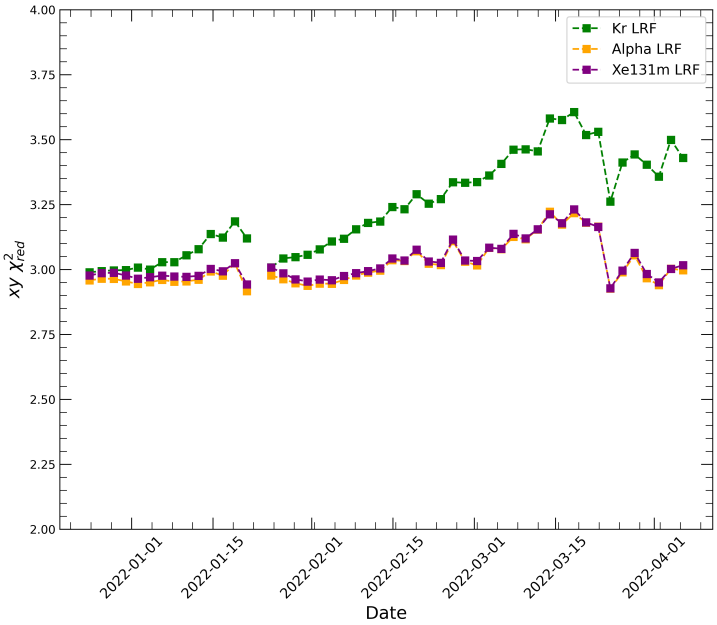

Figure 5.9: Position reconstruction results in terms of bins of χ^2_{red} expressed in time for LRFs calibrated with various calibrations source using a fiducial cut of r<680 mm and drift time of [100 µs, 900 µs].

5.5.2 Position reconstruction validation

One of the most challenging tasks of the position reconstruction in a dual-phase TPC dark matter detector consists in measuring its resolution and any bias in the reconstructed positions, as there is no obvious point of reference in the detector bulk that can be used for this purpose. One of the most straightforward methods is to study the xy distribution of events occurring near the gate of the electric field. In LZ the gate electrode is a 90° woven mesh grid with 583 wires of 75 µs diameter, placed at a pitch of 5 mm [12].

As noted in [17], and shown in figure 5.10a, due to the high difference in the drift field (193 V/cm) and the extraction field (7.3 kV/cm), the drift field lines become compressed near the gate region. This leads to focusing of the ionization electrons to the centers of the mesh elementary cells. For the majority of the events occurring in the thin layer of liquid just below the gate, this would occur to the electron cloud as a whole, as both the ionization track size, and its spread due to diffusion are well below the grid wire pitch. Therefore, with enough position resolution of the reconstructed S2, it should be possible to observe an xy distribution reproducing the mesh pattern of the gate wires.

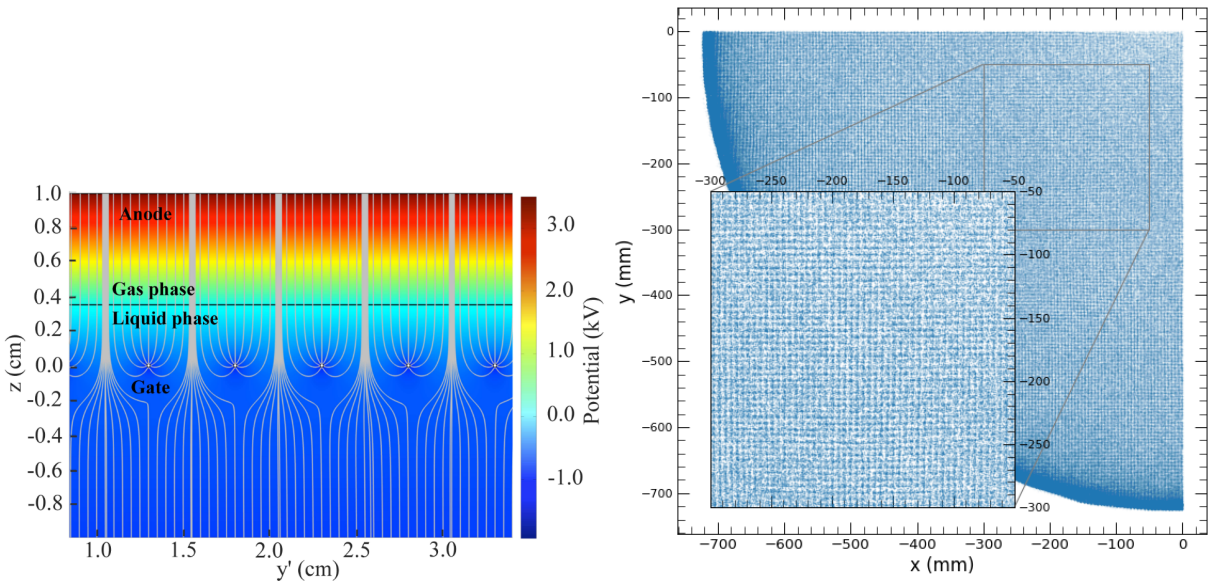

Figure 5.10: Left: simulation of the electric potential near the gate grid wires of the LUX detector, the lines illustrate the direction of the electric field, and their density has no correlation with its intensity (figure from [17]). Right: position reconstruction results for ER events in the [50, 2000] keV range located at a maximum depth of 31 cm and for a r<730 mm.

As shown in figure 5.10b, the focusing effect of the gate is evident in LZ, providing a clear validation of the position reconstruction results obtained by Mercury.

We estimated the xy resolution for ^{131m}Xe events (164 keV) selected from a region in the x-axis coordinate of [-110, -55] mm, as shown in figure 5.11. The peaks of the histogram present the space between the wires as a consequence of the focusing effect. With a fit of 11 Gaussians, we obtain an average σ = 1.35±0.13 mm which is the Mercury resolution for 164 keV. This value can be considered the upper limit for LZ position resolution at 164 keV as there is no guarantee of a perfect alignment of the wires in the grid.

Moreover, the average distance between the Gaussians means was of 5.01±0.11 mm which is within 1σ with respect with the expected gate pitch of 5 mm. The small deviation obtained is a consequence of the small bias of the reconstruction xy in the center region of the detector.

The fact that the peaks in figure 5.11 have similar intensity also provides a validation of the Mercury performance, as the ^{131m}Xe events are expected to be uniformly distributed in the detector.

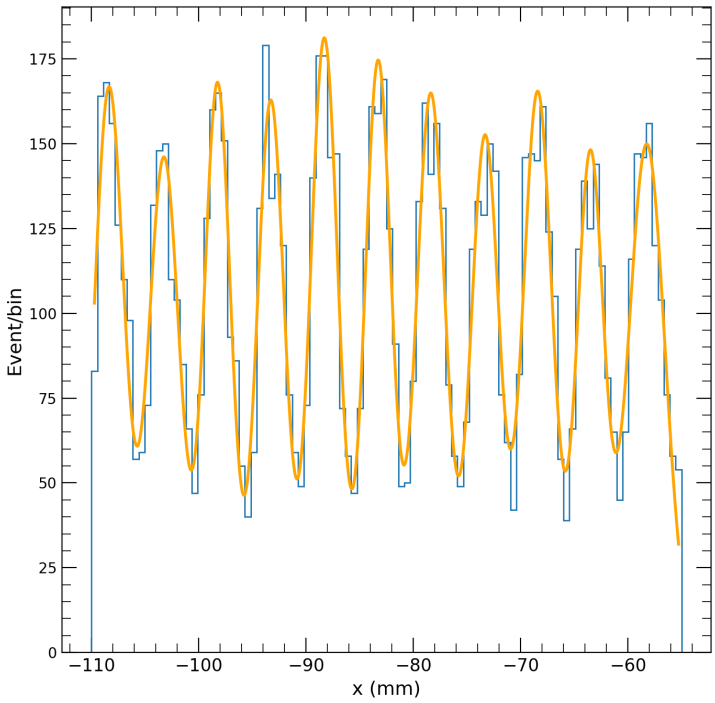

Figure 5.11: Histogram of the x coordinate for ^{131m}Xe events ([155, 170] keV) located at a maximum depth of 31 cm (drift time of 200 µs) and for r<700 mm, revealing, for the region with higher density, the space between the gate grid wires. The orange line represents a fit of 11 Gaussians summed. Fit results: $\overline{\sigma} = 1.35 \pm 0.13$ mm, $\overline{\mu} = 5.01 \pm 0.11$ mm. The bar denotes the average over the Gaussian parameters.

5.6 LZ energy reconstruction

As discussed in section 3.4, in a liquid xenon TPC, the energy of an interaction occurring in the active volume is reconstructed with the following equation:

$$E = W\left(\frac{S1_c}{g_1} + \frac{S2_c}{g_2}\right), \tag{5.14}$$

with g_1 representing the probability of detecting a single photon, and g_2 being the detection probability for an ionization electron multiplied by the gain of the electroluminescent region. The $S1_c$ and $S2_c$ are the corrected $S1$ and $S2$ signals. In the case of LZ, these corrections comprise spatial dependent-maps of the signal yield and light collection efficiency corrections to account for position-dependent variations in the collection of light by the PMTs. An additional correction is also applied to the S2 signal to consider a depth-dependent attenuation of the extracted charge caused by the finite lifetime of the free electrons in the liquid xenon due to attachment to the electronegative impurities

(see section 3.5.1).

When one considers the long acquisition periods required for a dark matter experiment (section 2.3), and the size of the detector, a utterly stable state of the liquid xenon in the detector is not easily accomplished. Such variations (e.g., temperature) alter the signal production mechanisms, which entail additional time-dependent corrections.

In this work, the energy is reconstructed by taking the S1 as the sum of the top and bottom PMTs and the S2 as the sum of the PMTs in the bottom array. The S2 light viewed by the bottom PMTs is more uniformly distributed in the array, and consequently, these PMT are less prone to saturate (section 5.2.3).

5.6.1 Light collection efficiency corrections

As discussed in section 5.2, the S2 scintillation does not depend on the event depth. Therefore, the light collection efficiency correction of the S2 signal can be generically expressed with the following equation:

$$C_{lce}(x,y) = \frac{\langle S_2(0,0)\rangle}{\langle S_2(x,y)\rangle}, \tag{5.15}$$

where C_{lce} is the correction factor, and the angular brackets represent, for a specific calibration candle, the average S2 at the event xy position and at a given reference position which, to be specific, is taken at the center of the detector.

The standard technique in LZ is dividing the xy plane in discrete rectangular bins and calculating the correction factor for each bin as the ratio between the averages of S2 sum for the events falling into some reference bin and the given bin. These correction factors are stored in a map, and the correction for an arbitrary point in xy is obtained by interpolating between the map elements. The main disadvantage of this technique is that if one of the PMTs is disabled, then the map needs to be recalculated to accommodate an alteration of the light collection. Similarly, this technique fails to consider the saturation (loss of linearity) of various PMTs for high-energy events, which creates a bias at high-area pulses.

The basis of the novel light collection efficiency corrections introduced here, lies in the result obtained in equation 5.10 from the Maximum Likelihood estimation for the number of photons (see section 5.1.3.1):

$$N = \frac{\sum_i n_i}{\sum_i \lambda_i(x,y)}, \tag{5.16}$$

where, in this case, N is the produced amount of S2 photons, n_i and $\lambda_i(x,y)$ are the observed signal and the LRF of the PMT *i*, respectively. From this result, and knowing that $\langle S2\rangle = \langle\sum_i n_i\rangle$, we obtain the S2 expressed as a function of the LRFs:

$$\langle S2(x,y)\rangle = \langle N\rangle \sum_i \lambda_i(x,y). \tag{5.17}$$

Thus, C_{lce} can be expressed as:

$$C_{lce} = \frac{\sum_i \lambda_i(0,0)}{\sum_i \lambda_i(x,y)}. \tag{5.18}$$

Note that LRFs reconstructed by the iterative method reproduce $\lambda_i(x,y)$, up to a common factor that cancels out when taking the ratio in equation 5.18.

This method can calculate the C_{lce} with any subset of PMTs, provided that the same set is used in the S2 summation to maintain consistency. This solves the aforementioned problem of a PMT disabled mid-run and mitigates the effect of PMT saturation on the energy resolution.

This work does not provide a method to produce light collection corrections of the S1 signal with dedicated LRFs due to complex variations of this signal in xyz. Instead, as described in section 5.6.2, such corrections are obtained by mapping the S1 response across the detector volume.

5.6.2 Spacial and Temporal correction of the S1 and S2 signals

Spatial corrections, produced from the events generated by ^{222}Rn 5.5 MeV and ^{218}Po 6 MeV α-particles, were applied to the S2 and S1 signals to ensure a homogeneous response in the detector. The α-particles are an undesired background in WIMP search due to (α, n) reactions but provide,

for the purpose of calibration, an almost uniformly distributed source in the detector (see figure 5.4). Moreover, recombination probability at α-particles tracks in liquid xenon is much higher compared to ERs. This is because the high energy-density track effects leads to a plasma-like behavior, in which the electron-ion cloud becomes polarized, thus attenuating the electric field inside. As a result, charge extraction from the track becomes inefficient [109]. Therefore, for a S1 with a high pulse area (>38 kphd), which entails a good relative resolution, we obtain an S2 with a comparable pulse area[7], and consequently, less prone to cause saturation of the PMTs. Last, but not least: as can be seen in figure 5.4, the relative peak width for α-particles is about 7 times less than that of the alternative calibration sources, meaning that roughly 2.6 ($\sqrt{7}$) times less statistic is required to calculate a correction map of the same precision.

The spatial corrections consist of position-dependent factors to the sum of the PMT pulse area. The corrections were obtained by fitting the position dependence of S1 and S2 signals produced by α-particles in the active TPC volume with smooth functions of all 3 coordinates. The two α-decays (^{222}Rn$\rightarrow^{218}$Po, 5.49 MeV and ^{218}Po$\rightarrow^{214}$Pb, 6.00 MeV) are used simultaneously to increase the number of events used in the fit. For this, the S1 and S2 of the 5.49 MeV line were scaled up to coincide with the 6.00 MeV line. The final correction factor to be applied for each event is found as an inverse of the value of the fit at the event position.

Figure 5.12 demonstrates the effect of the various corrections applied to the S1 signal. The first set of corrections is created from a 2D spline, with 12 bins for each coordinate, in r^2 and z space (figure 5.12b). Although satisfactory results are obtained for drift times in the [200, 700] µs interval, as the signal becomes almost flat in this region, near the edges of the detector at >700 µs and <200 µs, there is a smear caused by the disabled PMTs and variations in the QE of the enabled ones. To further remove this non-uniformity, an additional 3D correction in xyz is introduced. In this case, the binning of the spline was lower, 6 in each dimension, to avoid overfitting.

The results of the S2 signal corrections are shown in figure 5.13. Even with time-dependent lifetime corrections, the signal presented a small depth dependency in the lower region of the detector (drift time > 800 µs). The most probable explanation for this fact is spatial variation of the concentration of

[7] For instance, the ^{131m}Xe 164 keV line yields a $S2/S1$ of ≈100, while the ^{222}Rn α-particle ratio is ≈1.8

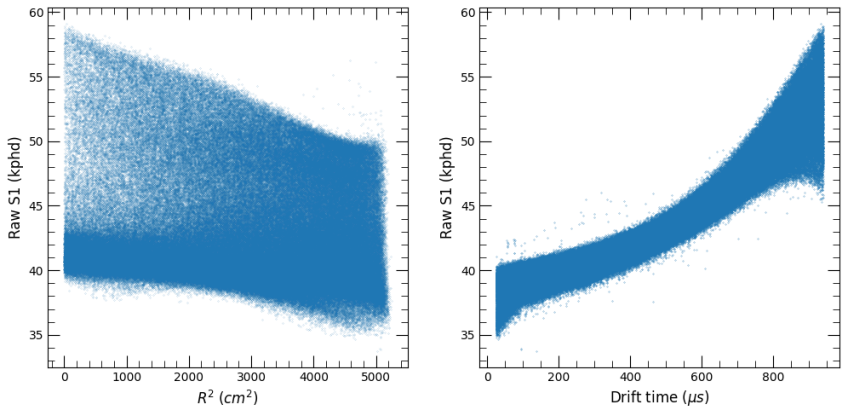

(a) S1 Raw

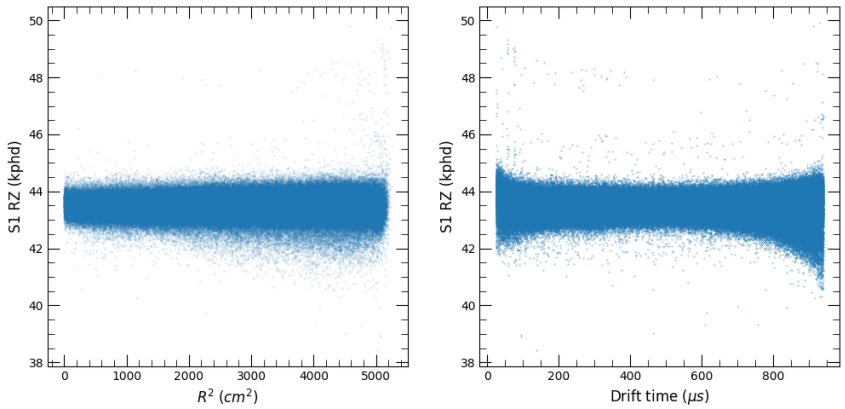

(b) S1 Radius and Z corrected

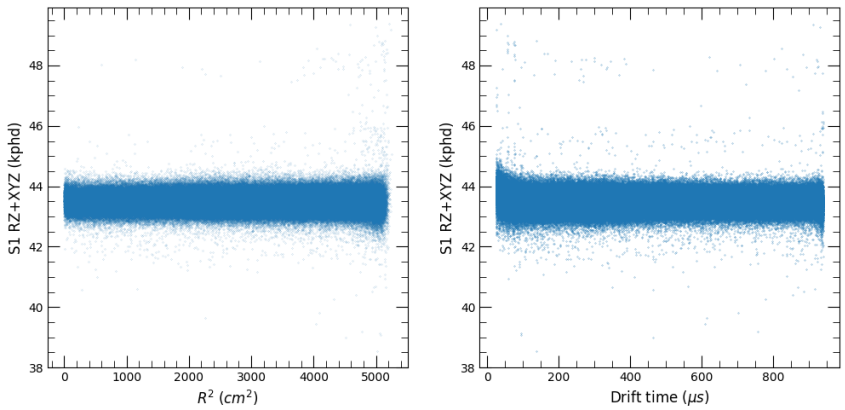

(c) S1 fully corrected (RZ+XYZ)

Figure 5.12: Effects of the S1 correction on both r^2 (left column) and z coordinates (right coordinate). Top: the measured S1 signal (raw); middle: the effects of r+z correction; bottom (final S1 corrected): results of the rz+xyz corrections. The signal is normalized to the center of the detector.

the electronegative impurities (and, consequently, electron lifetime) caused by non-uniform mixing of liquid Xe in this region of the detector. Similarly to what was done for the S1 signal, this was solved with a correction in rz space using a 2D spline with 12×12 bins. Moreover, the S2 signal

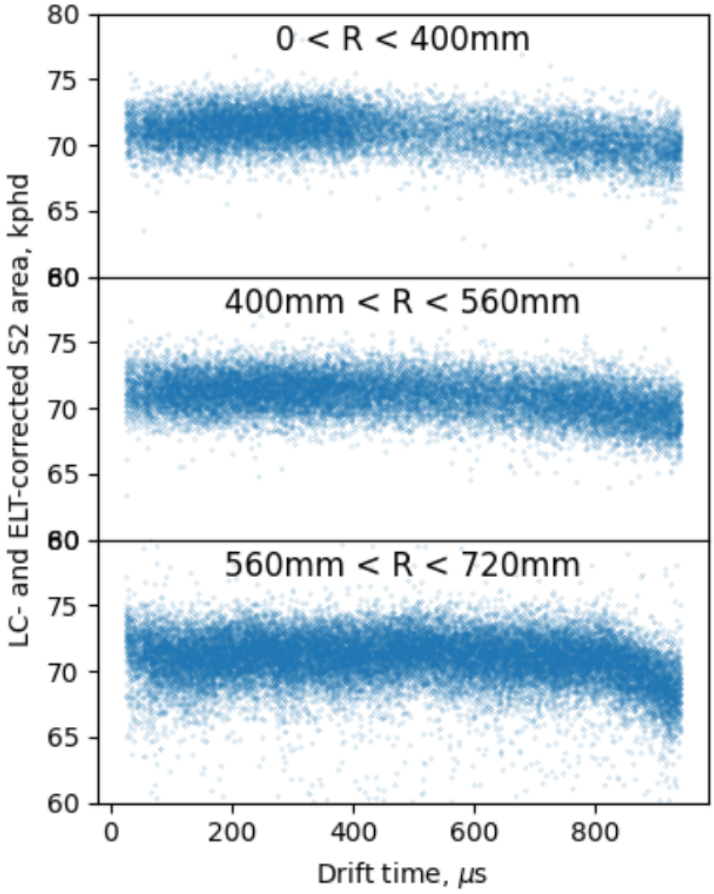

(a) S2 non-uniform mixing

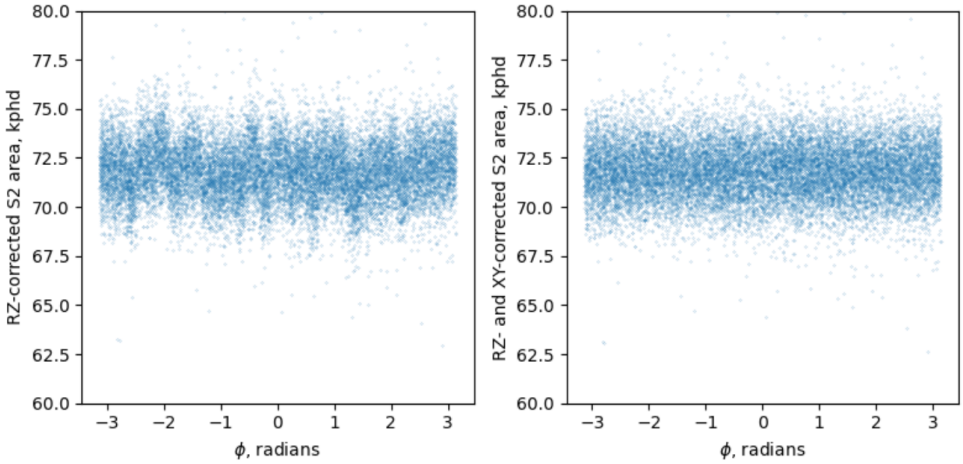

(b) S2 polar dependency

Figure 5.13: Effects of the S2 expressed over various coordinates: the top panel presents the S2 depth dependency for various sections in r of the detector (LC = light collection, ELT= electron lifetime). The bottom plot shows the polar dependency of the S2 signal and the effects of the complete set of corrections (LC+ELT+RZ+XYZ).

also presented a polar dependency (figure 5.13b), most likely caused by variations in the extraction efficiency at the electroluminescent region. This variation was corrected with an additional 2D spline in xy with 15×15 bins. Finally, time-dependent corrections of the electron lifetime were also included to accommodate variations in the purity of the liquid xenon with time (see figure B.1).

Equations 5.19 and 5.20, summarize the format of the corrections applied to the S2 and S1, normalized at the center of the detector at $(0\text{ mm}, 0\text{ mm}, 475\text{ µs})$, where the letters C_{xx} denote a correction spline for a given space parameter. The S2 light collection correction is expressed by $C_{lce}(x, y)$ and f_{el} is a time-dependent electron lifetime function. The radial position of the event is r, and x, y is the respective Cartesian coordinates. The drift time is denoted by t_d, and the event timestamp by t_s:

$$S1_c = S1\frac{C1_{rz}(0, 475)\ C1_{xyz}(0, 0, 475)}{C1_{rz}(r^2, t_d)\ C1_{xyz}(x, y, t_d)}, \tag{5.19}$$

$$S2_c = S2\ C_{lce}(x, y)\ \frac{C2_{rz}(0, 475)\ C2_{xy}(0, 0)}{C2_{rz}(r^2, t_d)\ C2_{xy}(x, y)}\ e^{t_d/f_{el}(t_s)}. \tag{5.20}$$

5.6.3 Energy calibration

Having the S1 and S2 adequately corrected for the non-uniform response of the detector, the final ingredient required to reconstruct the energy of the events is the measurement of the g_1 and g_2 gains. This is done by fitting a straight line through the points representing various ER sources of known energy in a plot[8] of scintillation yield $S1_c/E$ versus the charge yield $S2_c/E$ [79]. The gains are obtained by rearranging the original energy equation 3.11, such that,

$$E = W(\frac{S1}{g_1} + \frac{S2}{g_2}) \Leftrightarrow \frac{1}{W} = \frac{{}^{S1}/_{E}}{g_1} + \frac{{}^{S2}/_{E}}{g_2}\ . \tag{5.21}$$

Which, in turn, can be re-written to match the standard linear regression format, $u = mv + b$, where $u = {}^{S1}/_{E}$ and $v = {}^{S2}/_{E}$:

[8] Often referred to as Doke plot in literature [110]

$$\frac{S1}{E} = \frac{g_1}{g_2}\frac{S2}{E} + \frac{g_1}{W}. \tag{5.22}$$

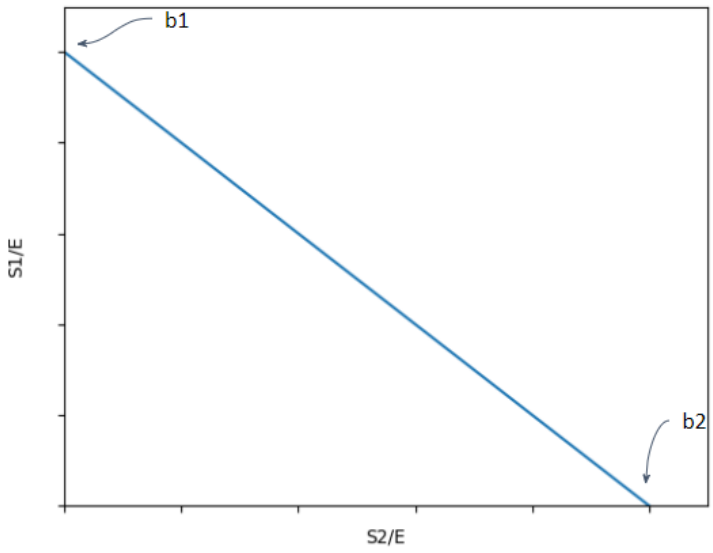

Figure 5.14: Calculating gains from a Doke plot.

As represented in figure 5.14, the g_1 and g_2 gains are calculated from the intercepts $b1$ and $b2$ of the fitted line at $v = 0$ and $u = 0$, such that:

$$\begin{cases} \frac{1}{W} = \frac{b1}{g_1} \Rightarrow g_1 = Wb1 \\ \frac{1}{W} = \frac{b2}{g_2} \Rightarrow g_2 = Wb2 \end{cases} \tag{5.23}$$

It is also possible to take g_2 as ${}^{b1W}/_{m}$, where m is the slope of the light yield vs charge yield dependency; however, calculating the associated statistical error is more complicated in this case.

To measure the light and charge yields, one first needs to measure the mean $S1_c$ and $S2_c$ for the various calibration sources. This is typically done by isolating the clusters of the events corresponding to gamma rays of different energies in $S2_c$ vs $S1_c$ space with diagonal cuts and then fitting a Gaussian to individual histograms of $S2_c$ or $S1_c$. Although this approach works quite well, the cuts proved challenging to adjust automatically for eventual variations in yields.

In this study, a new peak fitting method was developed that consists in the following procedure (also exemplified in figure 5.15):

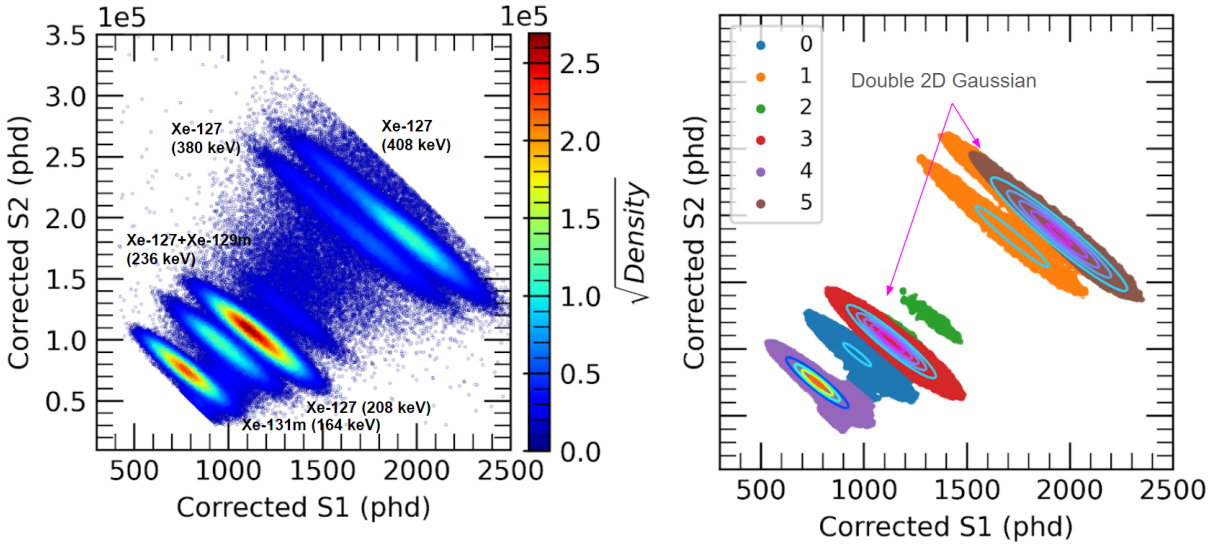

Figure 5.15: An example of 2D Gaussian fitting of the activated Xe lines in the $S2_c$ vs $S1_c$ scatter plot. The density of each event (color map of the left plot) is calculated from the interpolation of a 2D histogram with a spline. The usage of $\sqrt{Density}$ facilitates the event selection with a density cut. The plots and fits for the remaining sources can be found in appendix B.

1. **Density cut**: produce a scatter plot of $S2_c$ versus $S1_c$ with the color representing event density (left plot). A density cut removes the background events, resulting in the right scatter plot. The per-event density parameter is calculated by fitting a 2d spline in a histogram of S2 vs S1 space.

2. **Clustering**: apply a clustering algorithm to isolate the various peaks in each region. For this step, the Gaussian Mixture Model algorithm from by the sklearn python package[9] produced the best results.

3. **2D Gaussian fit**: For each cluster identified in the previous step, fit a bidimensional Gaussian function. Pairs of peaks that are not easily resolved (such as the Xe-127 380 keV and 408 keV lines) are fitted with a sum of two 2D Gaussians.

The energy spectrum was divided into three regions in order to facilitate the density cut and the posterior clustering: one for the Xe lines [164, 408] keV and two for high energies of [1, 1.6] MeV and [1.6, 2.7] MeV. Such an approach permits to adapt the fiducial volume cuts to optimize the signal-to-background ratio in each energy range. Given the high activity of the Xe lines, a smaller fiducial

[9] `https://scikit-learn.org/stable/modules/generated/sklearn.mixture.GaussianMixture.html`

volume was used at this energy range to reduce the effects caused by the non-uniform response of the detector (see table 5.3). Moreover, an additional energy-dependent cut on the goodness-of-fit of position reconstruction was applied to eliminate suspected multiple scatters. The efficiency of this cut was above 95%.

Table 5.3: Results of the fitting for various selected source for the measurement of the g_1 and g_2 gains with the Doke method. The S1 and S2 errors are calculated from the error on the mean. The true energy information was taken from [77] for energies in the range of [164, 408] keV and from [111] for energies in the range of [1.1, 3] MeV. The S2 was measure from the bottom array only.

Radial (mm)	Drift time (µs)	$xy\ \chi^2_{\mathrm{red}}$	Source	Type	Energy (keV)	$S1_c$ (phd)	$S2_c$ (phd) $\times 10^3$
<550	100-900	<10	^{131m}Xe	IC	163.9	775.4±0.1	70.51±0.01
			^{127}Xe	L shell EC + I-127 γ	208.1	968.3±0.5	90.50±0.06
			^{127}Xe	K shell EC + I-127 γ	236.1	1136.6±0.1	99.54±0.01
			^{129m}Xe	γ	236.1	1136.6±0.1	99.54±0.01
			^{127}Xe	L shell EC + I-127 γ	380.3	1704±1	176.1±0.1
			^{127}Xe	K shell EC + I-127 γ	408.2	1943.9±0.3	176.60±0.04
<700	100-900	<20	^{214}Bi	γ	1120.3	3968±2	663.0±0.2
			^{60}Co	γ	1173.2	4128±2	699.4±0.3
			^{60}Co	γ	1332.5	4617±2	804.5±0.3
			^{40}K	γ	1460.8	5056±1	882.5±0.2
<680	100-900	<40	^{214}Bi	γ	1764.5	5982±2	1080.6±0.2
			^{214}Bi	γ	2204.2	7365±4	1370.5±0.6
			^{208}Tl	γ	2614.5	8648±3	1641.0±0.4

Figure 5.16 shows the results obtained by fitting the $S1_c$, $S2_c$, and energy values of table 5.3 with equation 5.22. This figure presents an anti-correlation between the light and charge yield that depends on the event energy. This expected effect is associated with a decrease in the recombination probability for electrons that are more displaced from the initial recoil location and, consequently, more easily extracted.

The anti-correlation effect is more consistent for pure γ-particles interactions in the high energy region than for the lines of the Xe region, as the latter demonstrate a higher residual value with respect to the fitted line. As it was already shown in [112], the decay of ^{127}Xe consists in an electron-capture (EC) to an excited state of ^{127}I, resulting in the emission of a γ-ray with either 375 keV

(47.6%) or 202.9 keV (53.0%)[10]. Due to the electron vacancy left by the EC, an atomic de-excitation produces a cascade of x-rays with a total energy of 33.2 keV (83.37%), 5.2 keV (13.09%), 1.1 keV (2.88%) and 186 eV (0.66%) for a vacancy in K, L, M and N shell, respectively. The electron-capture decay lead to a disagreement in the Doke plot, which can be caused by a non-linearity of the recombination probability and energy-density effects involved in a complex multistep process [77, 112].

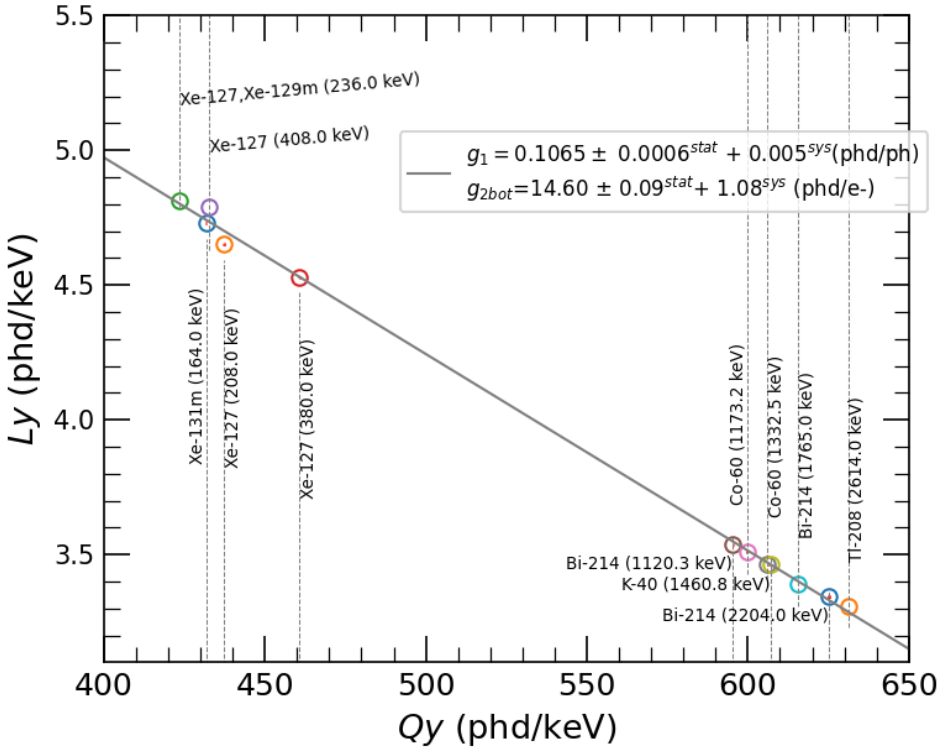

Figure 5.16: Doke plot and the respective g_1 and g_2bot gains as a result of the fits presented in table 5.3. The g2 was calculated from the bottom array. The systematic calculated by splitting the doke in low and high energies.

5.7 LZ energy resolution

The study of the energy resolution is of general interest to assert the capabilities of the detector. As mentioned in section 4.1, the detection of high-energy rare decays, such as the neutrinoless double beta decay, with a well-defined energy at $Q_{\beta\beta}$ (2.459 MeV for ^{136}Xe [15]), requires a good energy resolution, as the detector sensitivity is inversely proportional to the square root of the energy

[10] Here and below, the percentage in parentheses indicates probability of the process

(see equation 4.1). Besides, a good energy resolution, together with linearity of the energy scale, permits a better identification of the background sources and consequently an improved background estimation in the WIMP search region.

In order to estimate the energy resolution of an idealized liquid xenon detector with spatially independent S1 and S2 response, let us take the variance of the energy calculated by means of equation 3.11:

$$\mathrm{Var}(E) = \frac{W^2}{g_1^2}\mathrm{Var}(S1) + \frac{W^2}{g_2^2}\mathrm{Var}(S2). \tag{5.24}$$

Let m_γ and m_e be the numbers of photons and electrons, respectively, that contribute to the detected signal of an event producing n_γ photons and n_e electrons. Considering that m_γ and m_e are ruled by a binomial distribution [113], one can write the following:

$$\begin{aligned} m_\gamma &= n_\gamma p_\gamma, \\ m_e &= n_e p_e\ , \\ \mathrm{Var}(m_\gamma) &= n_\gamma p_\gamma (1-p_\gamma), \\ \mathrm{Var}(m_e) &= n_e p_e (1-p_e), \end{aligned} \tag{5.25}$$

where p_γ and p_e are the probabilities of detecting a photon and an ionization electron, respectively. Note that our S1 is equal m_γ and S2 is Gm_e, where G is the number of photons detected for each single electron extracted from liquid xenon. Note also that p_γ and p_e can be expressed as:

$$\begin{aligned} p_\gamma &= g1, \\ p_e &= {}^{g_2}\!/_{G}\ . \end{aligned} \tag{5.26}$$

The variance of S1 is the sum of the components associated with the signal detection, that is, the variance of the binomial distribution and the variances of the signals produced by each detected

photon (σ^2_{SPE}), such that:

$$\begin{aligned} \mathrm{Var}(S1) &= \mathrm{Var}(m_\gamma) + m_\gamma \sigma^2_{SPE} \\ &= m_\gamma(1-p_\gamma) + m_\gamma \sigma^2_{SPE} \\ &= S1(1 - g_1 + \sigma^2_{SPE})\ . \end{aligned} \tag{5.27}$$

Similarly, the variance of the S2 signal can be expressed as:

$$\begin{aligned} \mathrm{Var}(S2) &= \mathrm{Var}(Gm_e) + m_e[\mathrm{Var}(SE) + G\sigma^2_{SPE}] \\ &= G^2 m_e(1-p_e) + m_e[G(1-p_{\gamma 2}) + G\sigma^2_{SPE}] \\ &= Gm_e[G(1-g_2/G) + (1-p_{\gamma 2}) + \sigma^2_{SPE}] \\ &= S2(G - g_2 + 1 - p_{\gamma 2} + \sigma^2_{SPE}), \end{aligned} \tag{5.28}$$

where $\mathrm{Var}(SE)$ is the variance of the single electron and can be calculated from the binomial distribution as:

$$\mathrm{Var}(SE) = G(1-p_{\gamma 2}), \tag{5.29}$$

with $p_{\gamma 2}$ expressing the probability of detecting a secondary scintillation photon, such that $p_{\gamma 2} = \sum_i \lambda_i$, with λ_i representing the *true* LRF of the i-th PMT.

Plugging the equations 5.27 and 5.28 into equation 5.24, we obtain the variance of the reconstructed energy of an ideal detector:

$$\mathrm{Var}(E) = W^2 \left[\frac{S1}{g_1^2}(1 - g_1 + \sigma^2_{SPE}) + \frac{S2}{g_2^2}(1 - g_2 + G - p_{\gamma 2} + \sigma^2_{SPE}) \right]\ . \tag{5.30}$$

The result of equation 5.30 presents, for an ideal detector where there are no non-uniformities of the S1 and S2 signals, the various contribution of the energy resolution. These are caused by the variance in the single electron and photoelectron size, which are subdominant with respect to the fluctuation of m_e and m_γ.

Figure 5.17 provides an illustration of the contributions of the S1 and S2 signals to the energy res-

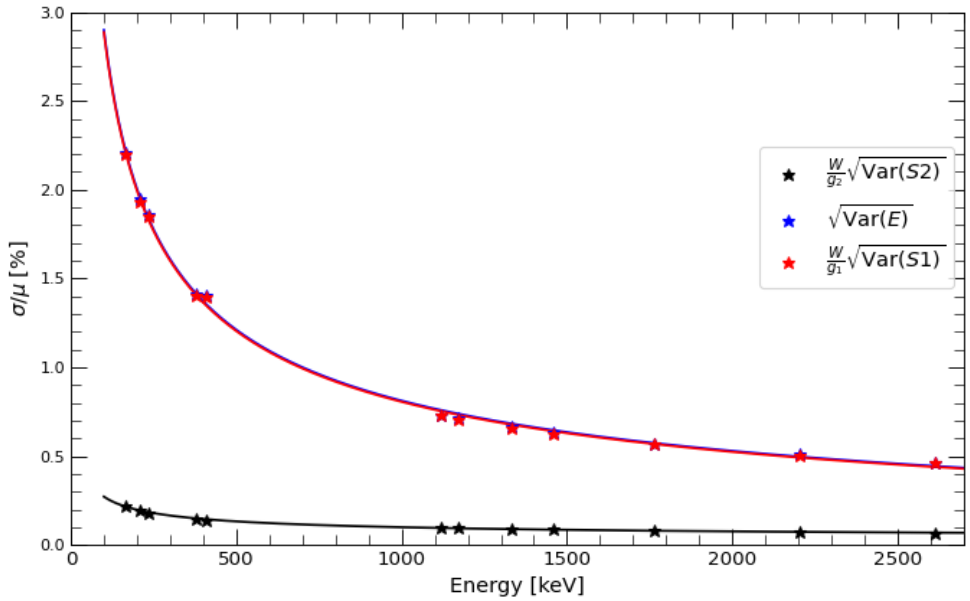

Figure 5.17: Contribution of the S1 and the S2 signals to the energy resolution. The values of S1 and S2 were taken from table 5.3 and used in the respective equations 5.27, 5.28, 5.30. The g_1 and g_2 were taken from the doke plot in figure 5.16. The G gain was of 15.7 $^{ph}/_{e^-}$ and was calculated from the mean signal produced by events classified as single electrons. As a simplification, $p_{\gamma 2}$ was assumed to be equal to g_1. As there is no official value of σ_{SPE} for the LZ detector PMTs, a value of 0.4 phe [114] was used from PMTs of similar SPE performance.

olution. This demonstrates the importance in maximizing the light collection, which is related to g_1, as the main contribution of the energy resolution comes from the S1 signal variance. Furthermore, this result also justifies the usage of the S2 signal measured by only the bottom array to reconstruct the energy, as the S2 signal variance make a negligible contribution to the energy resolution.

Moreover, in LZ, other effects can potentially contribute to worsening of the energy resolution, such as baseline fluctuation affecting the pulse area or uncertainty in the estimation of the High Gain to Low Gain conversion factor.

5.7.1 Energy resolution results

The following section presents and analyzes, the energy spectrum of the background electron recoils in the range acquired by the LZ detector during the first science run. During this period, comprising 60 live days, the detector operated with a drift field of 193 V/cm and an extraction field of 7.3 kV/cm at the center [14]. A dataset with a total of $\approx 10^7$ single-scatter events was used. The energy was reconstructed with the top+bottom S1 signal, while the S2 was only calculated with the bottom array to avoid PMT saturation effects.

The event energy is reconstructed by applying equation 5.14, with the corrections described in section 5.6, and the detector gains measured with the Doke method in section 5.6.3. Figure 5.18 presents the energy spectrum of the LZ detector for events in the [0.1, 2.8] MeV range.

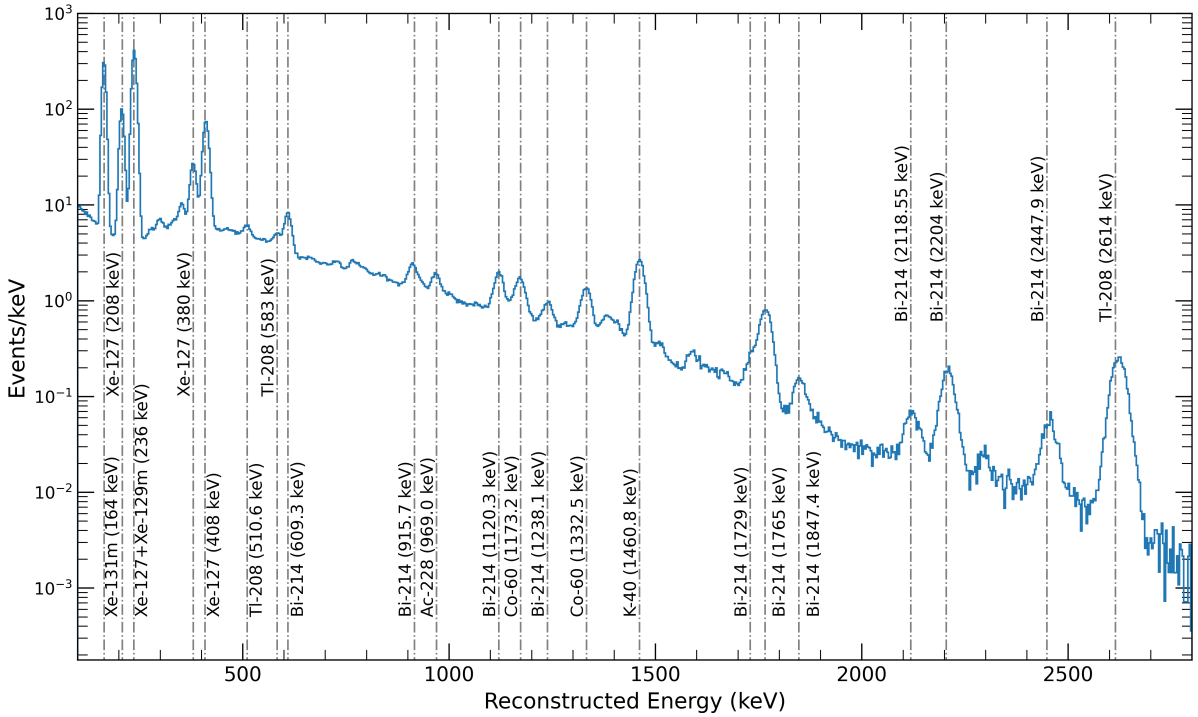

Figure 5.18: Energy spectrum for events in the [0.1, 2.8] MeV range. Fiducial cuts: r<680 mm and drift time of [100, 800] µs.

Figure 5.19 shows the fit results for various selected peaks of the energy spectrum. Well-resolved peaks were fitted with a single Gaussian curve, while a sum of two Gaussians was used for poorly resolved peaks, such as the [380, 408] keV and the [583, 609.3] keV pairs. Although not evident

in figure 5.19, the 208 keV and 380 keV ^{127}Xe L shell lines are slightly underestimated due to an unresolved contribution of the M shell. This contribution was considered by fitting each peak with a sum of two Gaussians with a fixed energy difference of 4.1 keV and a relative contribution of 22%[11] [112]. The background contribution was subtracted in the fit using an exponential curve.

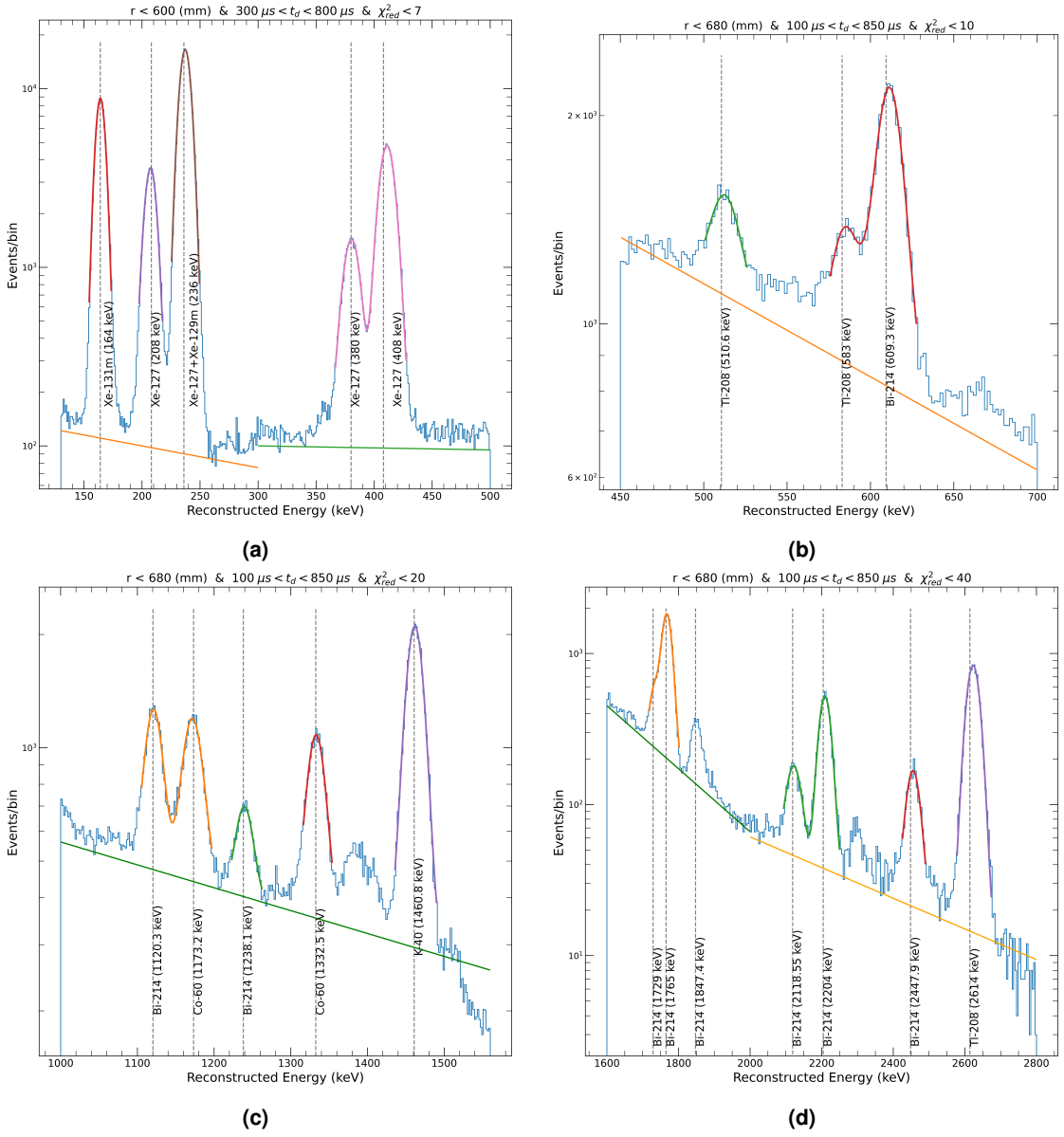

Figure 5.19: Fits of the various lines selected for the energy resolution study: most lines were fitted with a simple Gaussian. The unresolved peaks in the top plots were fitted with a sum of two Gaussians. The background was subtracted with an exponential curve.

The energy resolution results, calculated as the Gaussian standard deviation divided by its mean,

[11] The summed fit of the [380, 408] keV pair is in fact composed by a sum of 3 Gaussian, one for each K, L, M shell.

can be found in figure 5.20. To our knowledge, the energy resolution at 2614 keV of (0.67±0.01)% for the full fiducial volume of 5.6 tonnes (see table 5.4) is an unprecedented result for any liquid Xe TPC.

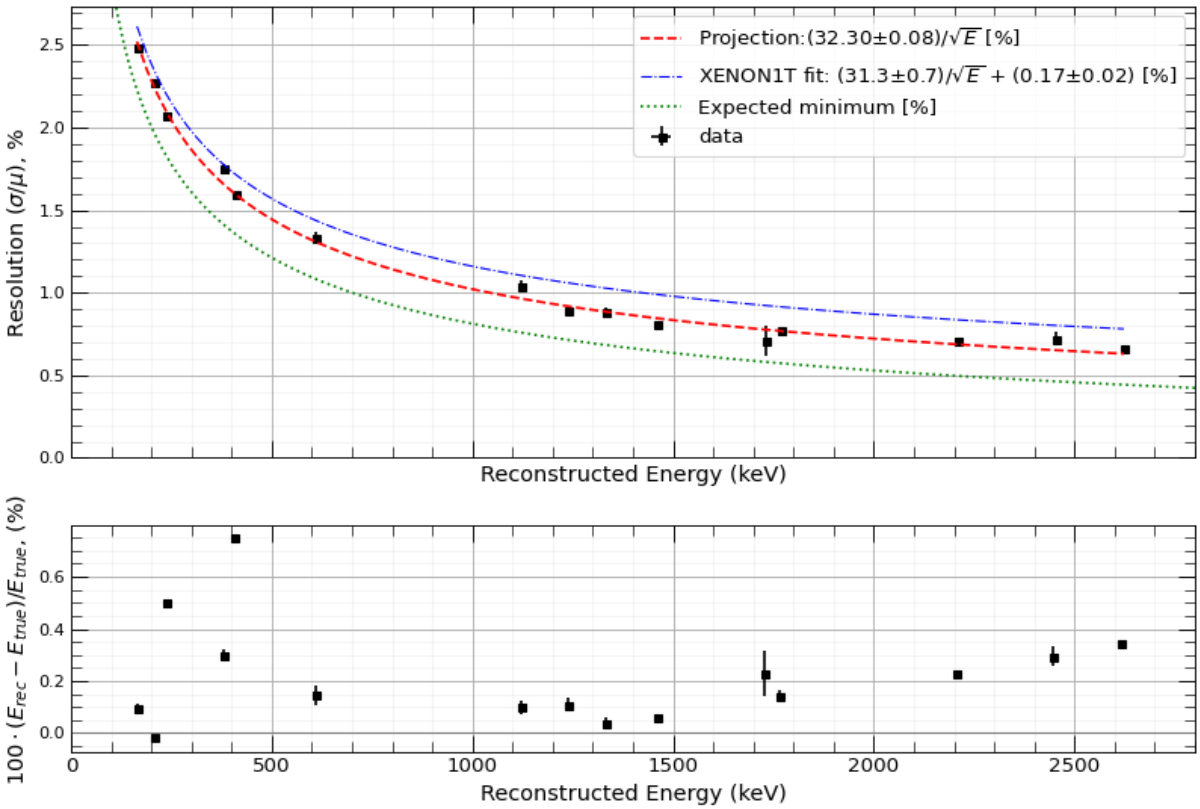

Figure 5.20: Top: Energy resolution vs energy of the LZ detector obtained in this work. As a comparison, the results obtained by the XENON1T in [115] are also shown. The expected curve represents a fit of equation 5.30 with the values of $S1_c$ and $S2_c$ from table 5.3. Bottom: deviation, in percentage, of the reconstructed energy with respect to the true energy.

Furthermore, as shown in figure 5.21, towards the bottom region of the detector in the interval of drift time between 500 and 800 µs, where the S1 light collection is improved, a resolution of (0.65±0.03)% at 2614 keV is achieved. In the region close to the bottom of the TPC (800 µs < t_d < 900 µs) the resolution is slightly worse (0.69±0.02)%, probably because of a non-uniform mixing of the purified liquid Xe and by the fact that the S1 spatial corrections do not completely compensate for the non-uniformity of S1 light collection caused by the disabled PMTs in the bottom array.

Figure 5.20 also presents the deviation of the reconstructed with respect to the true energy, which is within 1% for most cases.

Table 5.4: Results of the energy resolution for the various source presented on plot 5.20. The minimum resolution was calculated from the "Expected minimum" fit from figure 5.20 for each expected energy. The expected energy information was taken from [77] for energies in the range of [164, 408] keV and from [111] for energies in the range of [600, 3] MeV.

Source	Expected energy (keV)	Reconstructed energy (keV)	Binomial resolution (%)	Measured resolution (%)
^{131m}Xe	163.9	164.2±0.1	2.23	2.49±0.02
^{127}Xe	208.1	208.0±0.1	1.96	2.28±0.02
^{127}Xe+^{129m}Xe	236.1	237.2±0.1	1.83	2.08±0.02
^{127}Xe	380.3	381.1±0.1	1.41	1.75±0.03
^{127}Xe	408.2	411.1±0.1	1.36	1.59±0.02
^{214}Bi	609.3	610.2±0.2	1.08	1.33±0.03
^{214}Bi	1120.3	1121.4±0.3	0.76	1.04±0.03
^{214}Bi	1238.1	1239.5±0.3	0.71	0.89±0.03
^{60}Co	1332.5	1333.0±0.2	0.68	0.89±0.02
^{40}K	1460.8	1461.7±0.1	0.64	0.81±0.02
^{214}Bi	1729.6	1733.0±1.5	0.58	0.71±0.09
^{214}Bi	1764.5	1767.5±0.4	0.57	0.78±0.02
^{214}Bi	2204.2	2209.1±0.3	0.50	0.71±0.01
^{214}Bi	2447.9	2455.1±0.9	0.46	0.72±0.04
^{208}Tl	2614.5	2623.0±0.2	0.44	0.67±0.01

5.8 Summary

The position reconstruction results were presented using the LRFs produced for the first science run of the LUX-ZEPLIN (LZ) detector. With the data acquired in this period 3 sets of LRFs were generated from different energy sources —calibration injection background events from ^{131m}Xe (164 keV), events from ^{83m}Kr (41 keV) and 5.49 MeV α-particles from ^{222}Rn. The position reconstruction results obtained for these LRFs are in good agreement, and they produce similar results of xy and consistent distributions of $\chi^2_{\rm red}$. However, LRFs produced from α-particles have a better $\chi^2_{\rm red}$ due to improved resolution of the S2 signal.

In this work, the energy resolution of the LZ detector was also studied, revealing a record energy resolution for any liquid Xe detector of (0.67±0.01)% at 2614 keV for the full fiducial (5.6 tonnes) and (0.65±0.03)% at 2614 keV for the bottom region as a consequence of a better S1 light collection.

The reported value in the energy resolution of 0.67% represents a significant improvement from the initial estimate in [116] of 1% at the Q-value of the ^{136}Xe neutrinoless double beta decay. In turn, this

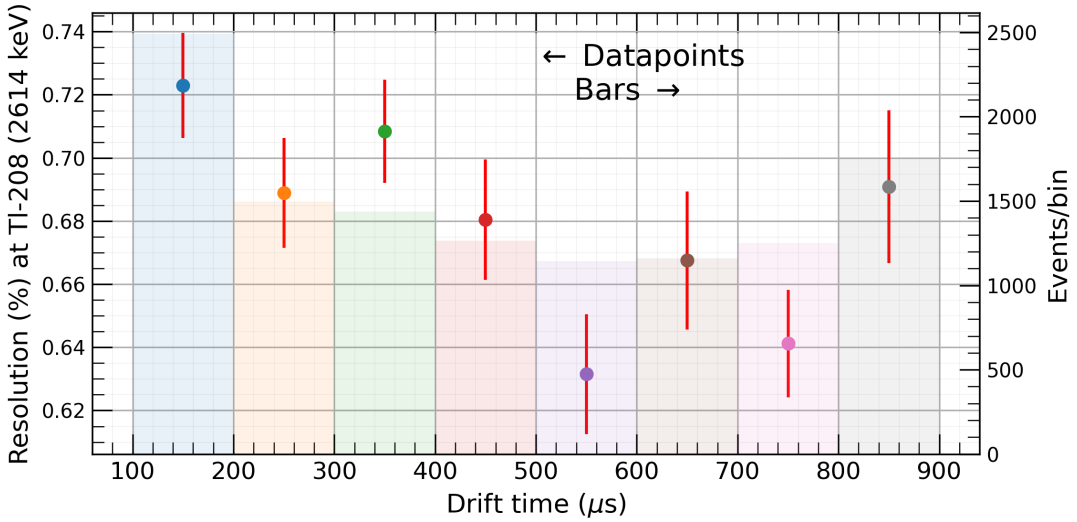

Figure 5.21: Energy resolution of the Tl-208 line at 2614 keV for various section in drift time.

entails an enhancement of the LZ detector sensitivity for this decay from 1.06×10^{26} years to 1.18×10^{26} years.

Although one of the main novel components of this study is the new method to produce light collection efficiency correction (see section 5.6), other techniques were applied to further improve the spatial uniformity of the S1 and S2 signals. In this regard, a non-invasive technique, relying on single electron events, was implemented to produce continuous time-dependent calibration of each PMT (see section 6.2). Moreover, the energy reconstruction also relied on the saturation study presented in section 6.1, which improved the position reconstruction accuracy for the high-energy events.

As a final remark, the Mercury algorithm was fully integrated into the official data processing and analysis tools developed by the LZ collaboration such as the UPM, LZAP and ALPACA.

Chapter 6

Non-invasive characterization and monitoring of PMT arrays

In a dual phase TPC, such as LZ, the precision of the reconstructed energy and position is defined, among the other things, by the quality of the signals acquired by the photosensors (PMTs) in the TPC arrays. Therefore, these devices are subject to periodic calibration in order to quantify their performance at both high and low levels of the input light signal. Two main problems are associated with periodic calibrations: *(i)* they interfere with normal data taking and *(ii)* while one can estimate the parameters of the detector in the periods between calibrations based in an educated guess about their behavior, there is no guarantee that these estimates are correct.

This chapter explores an alternative approach: monitor the PMT parameters (gain and linearity) using only the data obtained in the normal data taking process, i.e., without interfering the normal detector operation.

6.1 PMT saturation

PMT saturation occurs at high levels of incident light, in which the PMT response deviates from the expected linear behavior (see figure 6.1). This presents an added difficulty to the reconstruction of the event at high energies.

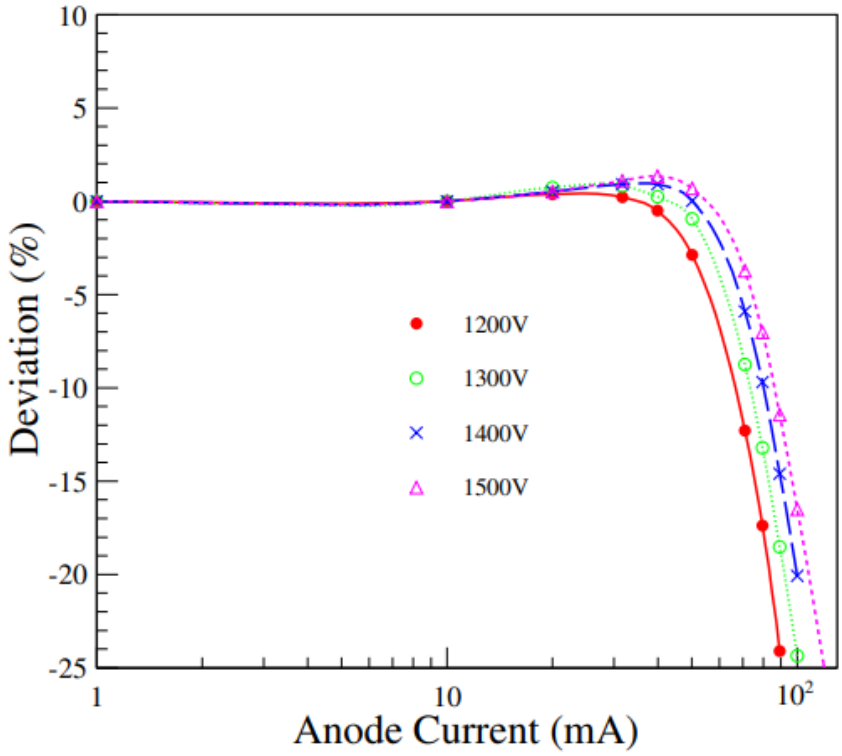

Figure 6.1: Example of the saturation effect in the response of a Hamamatsu R11410-10 PMT. Plotted is the deviation from the linear behavior versus the output anode current [117].

In the scope of LZ, for the purpose of energy reconstruction, the usage of the S2 signal measured by the bottom PMTs is preferred as this array is less prone to saturation due to a more uniform distribution of the light. This is not the case for the S2 of the top array, where most of the electroluminescence light is concentrated in just a few PMTs close to the event position in the xy plane. The loss of linearity of these PMTs, that starts for electron recoils events with energies of approximately above 200 keV, results in a bias in the reconstructed position, leading to a bias in the position-dependent corrections factors to be applied to the S2 and S1 signals. To minimize this effect, the PMTs with a signal above a given threshold need to be excluded from the position reconstruction process (see section 5.4.4). This threshold is characteristic to each individual PMT and may vary

from device to device, even for the PMTs of the same model. The objective of the work described in this section is to reliably determine these thresholds in-situ for the top array PMTs.

Depending on the underlying mechanism, saturation can be classified as [117]:

- **Cathode Saturation**: At the cryogenic temperatures, required for the operation of a liquid xenon TPC (174 K in the LZ case [14]), the photocathode, when submitted to a high photocurrent, is not capable of maintaining a uniformly distributed voltage due to an increase in its resistivity leading to a decrease in the voltage differential with the first dynode and, consequently, a decrease in the electron extraction efficiency. This form of saturation manifests itself as a drop in QE under higher illumination (e.g. during calibration) and is characterized by time constants of seconds to minutes [20].
- **Anode Saturation**: this type of saturation occurs due to space charge formation near the anode, leading to space-charge effects which prevents the current to flow from the dynodes to the anode. In the scope of LZ, this is the dominant form of saturation, as it requires a relatively small amount of time (<10 ns) for the charge build-up to occur [20].

There is also a third form of saturation occurring at the last dynodes of the PMTs due to a depletion of the associated capacitors. However, this type of saturation is not relevant for the LZ, as it requires events with an extremely high energy. Take, for instance, a pulse of 50 kphd measured by a single PMT. Assuming a PMT gain of 10^6 and taking the charge of the electron as 1.6×10^{-19} C, such a high energy pulse would result in a total charge of 8×10^{-9} C at the anode. Taking into account the resistance of the PMT voltage divider used in LZ [117] (92.5 MΩ) and the typical PMT operating voltage of 1500 V, the current passing through the divider is of 1.6×10^{-5} A. This means that a deviation of 1% of this current requires at least the equivalent of 20 pulses of 50 kphd per second, which is well below the highest load observed in LZ.

An additional form of saturation occurs at the DAQ level. The ADC of the DAQ has a limited range, and if the signal surpasses this range, the ADC is said to be saturated. In contrast to the PMT saturation, the ADC saturation is easily detected and flagged by the DAQ, and the information is stored in the data chain.

6.1.1 Saturation Detection

A typical setup to study the PMT linearity includes a calibrated adjustable light source with a wide dynamic range, the PMT to be tested and an acquisition system to record the PMT output (depending on the purpose of the study, this can be current, charge or amplitude). The dependence of the PMT output on the source intensity is studied in order to find at which level of light it starts to deviate from linearity by more than a predefined tolerance (typically, 2% or 5%). However, these measurements estimate the PMT linearity for specific and controlled conditions of temperature and supplied voltage, which are not always directly applicable in-situ.

With the knowledge of LRFs, is it possible to emulate the calibrated light source of the scheme above. Indeed, for each scintillation event, we can calculate the expected signal, a_i, as,

$$a_i = N\lambda_i(x, y) \ , \tag{6.1}$$

where λ_i is the LRF for ith PMT and x, y and N are the position and the number of photons reconstructed by Mercury with the PMT under the test excluded from reconstruction to eliminate potential bias caused by its possible saturation. The PMT is considered to be operating in a linear mode if the measured signal A_i coincides (within the measurement error) with this expected signal a_i. Conversely, deviation of A_i from a_i indicates PMT saturation.

The figure 6.2 is obtained by plotting the measured signal, A_i, versus the expected signal, a_i, for the central PMT of the top array. This presents the typical PMT response curve, with an initial linear behavior followed by a saturation plateau. The plot also reveals that saturation is less pronounced for the events with the longer drift time. This effect is related to the diffusion of the S2 electrons along the z direction, causing the pulse to be wider in time and less prone to saturate the PMT anode due to smaller peak current. This is a strong indication of anode saturation (charge-space accumulation).

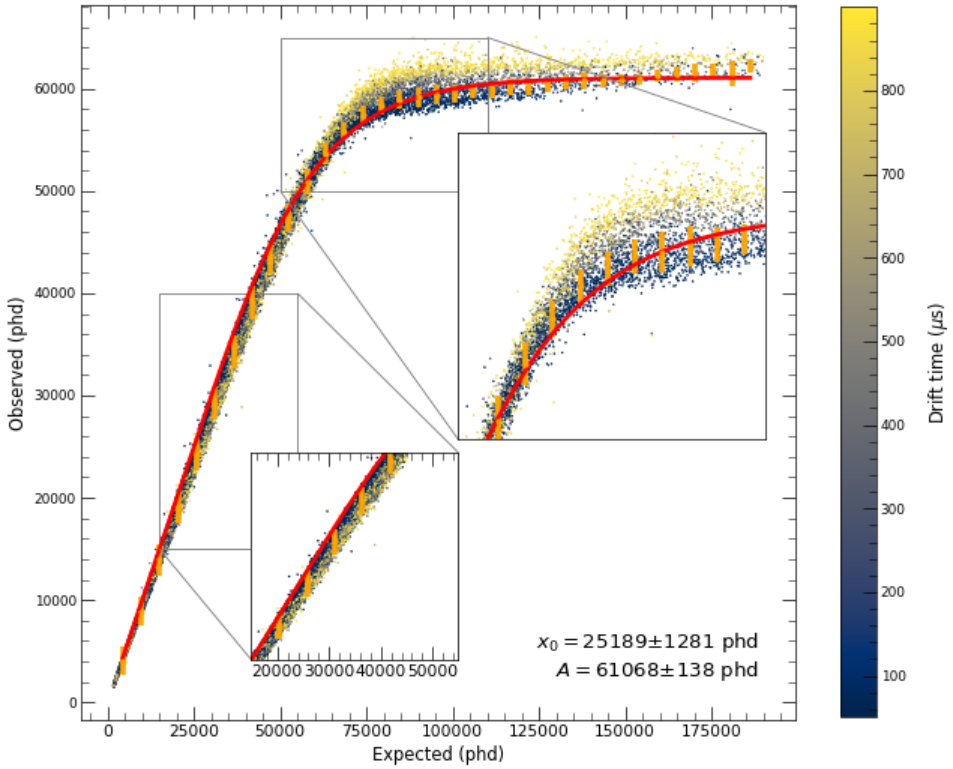

Figure 6.2: Determination of the PMT saturation using background events acquired during the first science run of LZ.

To quantify the observed curve, the data points presented in figure 6.2 were binned in a profile histogram of 40 bins of up to 1.5×10^5 phd per PMT and fitted with the following equation:

$$y(x) = \begin{cases} x & , x \leq x_0 \\ (A - x_0) \tanh\left(\frac{x - x_0}{A - x_0}\right) + x_0 & , x > x_0 \end{cases} \tag{6.2}$$

where x_0 indicates the saturation threshold, i.e., the maximum input signal that is expected to produce proportional output and A is the maximum output of the fully saturated device. This equation defines two regimes, a linear at $x < x_0$ and saturated where the output is described by a logistic function. The two parameters to be optimized are A and x_0. Note that the derivative of the logistic function is equal to 1 at x_0 to better satisfy the transition between the linear and saturated regime.

The A and x_0 parameters were estimated for all PMTs of the top array using a dataset comprising 3×10^6 background single scatter events acquired during the first science run. The dataset was filtered to include only events with a drift time between 50 μs and 900 μs and with a xy χ^2_{red} < 25 (see section 5.5.1). The PMT saturation thresholds were obtained by fitting the function 6.2 to the events at a maximum distance of 300 mm from each PMT, resulting in $\sim2\times10^5$ events per fit.

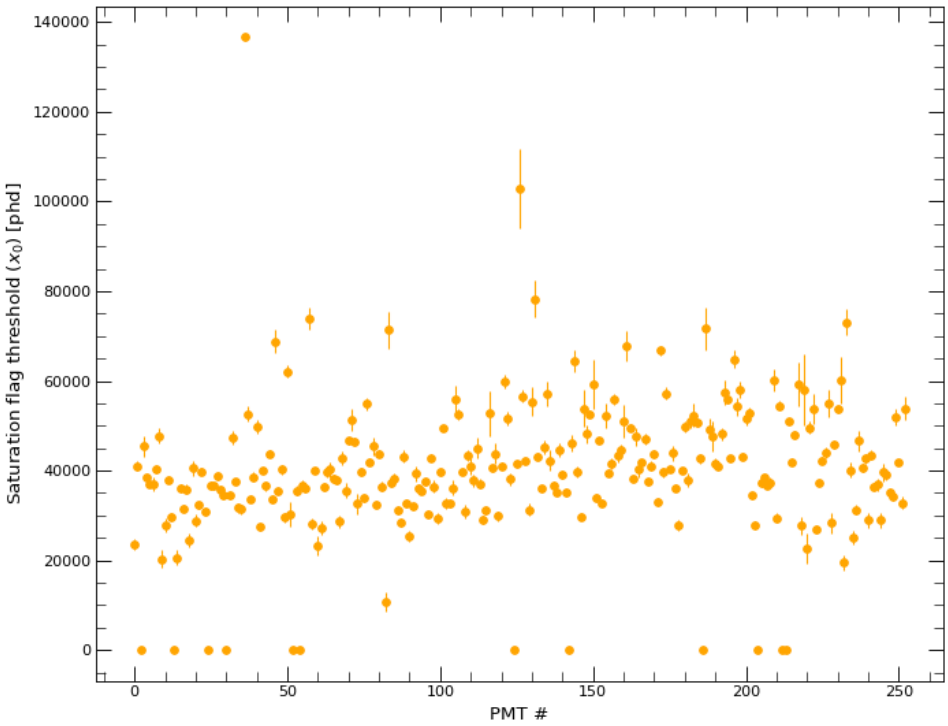

Figure 6.3: Saturation flags of the top array PMTs obtained with equation 6.2. PMTs with a value 0 were disabled during the acquisition period. PMT 36 with a x_0 above 120 kphd does not present a saturation plateau.

Figure 6.3 shows the values of saturation threshold, x_0, obtained for all active PMTs in the top array. It is possible to see that, for most of the PMTs, the linear mode ends around between $20\pm15)\times10^3$ and $40\pm15)\times10^3$. This result is in agreement with the saturation threshold of 30×10^3 phd obtained for the PMTs of the same model in [118] with a test setup[1].

No saturation of the bottom array was detected for S2 signals from electron recoils of up to 2.8 MeV. The light viewed by these PMTs is more spread in the array, and consequently, the maximum pulse area of the individual PMTs is lower than compared with the PMTs of the top array.

[1] The author reported a 5% deviation from the linearity starting at 30 mA. In their setup, 10 kph is equivalent to 10 mA.

6.2 Non-invasive PMT gain monitoring

The PMT waveforms are stored by the DAQ in units of mV at a sampling interval of 10 ns. Therefore, the pulse areas for individual PMTs are first calculated in units of mV·ns. However, before summing these individual areas to obtain S1 or S2 signals, it is necessary to scale them to the number of detected photons (phd) in order to equalize the contributions of the PMTs with different gains. This is accomplished with the following equation:

$$\mathcal{A} = \frac{\mathcal{A}_s}{\mathcal{A}_{spe} f_{dpe}} \ , \tag{6.3}$$

where, $\mathcal{A}$ is the scaled area in phd, $\mathcal{A}_s$ is the original area in mV·ns, $\mathcal{A}_{spe}$ is the average area, in mV·ns, for a single photoelectron pulse of a specific PMT and f_{dpe} is the probability for double photoelectron production, accounting for the fact that a single VUV photon has sufficient energy to simultaneously produce two photoelectrons at the photocathode.

The value of $\mathcal{A}_{spe}$, proportional to the PMT gain, is known to drift slowly with time, even when a PMT operates at stable conditions [20, 81]. This drift can be of an order of a few percent, i.e., strong enough to have a noticeable effect on the energy resolution of the detector. In the scope of the LZ calibration plan, this is mitigated by periodically measuring the $\mathcal{A}_{spe}$ as the peak of a PMT single photoelectron spectrum obtained with LED calibrations and interpolating the results between the measurements. A disadvantage of this approach is that the calibrations cannot be too frequent as they can not be run simultaneously with the science data acquisition and, therefore, reduce the live time of a science run. Between the calibrations, i.e., most of the time, we are relying on a stable behavior of the PMTs.

In this section, we propose a novel calibration technique that permits to continuous monitor $\mathcal{A}_{spe}$ without interfering with the science run. In our approach, the PMT calibration is done using S2 signals produced by single electrons extracted from the liquid xenon as a reference light source. The advantage of this technique is that it permits the measurement of the PMTs' single photoelectron response non-invasively, in parallel with the normal acquisition. To implement this technique, the event xy position must be known in order to take into account variations of the PMT light collection

efficiency.

The usual method for measuring $\mathcal{A}_{spe}$ consists in illuminating a PMT under test with light pulses of very low intensity to reduce the probability of multiple photoelectron production to the point when nearly all the observed output pulses are due to single photoelectrons. A more efficient alternative technique, suitable for periodic calibration of PMT arrays in a TPC, was proposed in [119]. It is based on the fact that the number of phd, n, measured by a given PMT i follows, with a great accuracy, a Poisson distribution,

$$P_n(\mu) = \frac{\mu^n}{n!} e^{-\mu} \ , \tag{6.4}$$

where P_n is the probability of detecting n photons from the signal with the expected value of μ.

From equation 6.4, the probability for the PMT to detect no photons is given by:

$$P_0(\mu) = e^{-\mu}. \tag{6.5}$$

If one measures the number of pulses that produce no signal in the PMT, N_0, from the total of N pulses acquired, then μ can be estimated as,

$$\mu = \ln\left(\frac{N_0}{N}\right) \ , \tag{6.6}$$

with the associated statistical error of $\sqrt{1/N_0 - 1/N}$ [119]. Once μ is known, the average single photon response of the PMT, $\mathcal{Q}_c$, can then be found as:

$$\mathcal{Q}_c = \frac{\langle \mathcal{A}_s \rangle}{\mu} \ , \tag{6.7}$$

where $\langle \mathcal{A}_s \rangle$ denotes the PMT average signal, in mV·ns, for the entire dataset, i.e., including the no-signal events. Note that since this method does not distinguish a single photoelectron from a double photoelectron the PMT calibration is defined as:

$$\mathcal{Q}_c = \mathcal{A}_{spe} f_{dpe} \ , \tag{6.8}$$

therefore, equation 6.3 can be re-written as:

$$\mathcal{A} = \frac{\mathcal{A}_s}{\mathcal{Q}_c} \, . \tag{6.9}$$

6.2.1 Method Implementation

The calibration of the PMT usually uses an LED driven by a pulse generator as the source of light pulses with a fixed amplitude [119]. In the present work, we use the light flashes produced by single extracted electrons in the electroluminescent gap for the same purpose. To select the events with the same μ, we select single electrons extracted at the same distance from the PMT to be calibrated. As these single electron pulses are always present in the science data, this type of calibration can be performed in parallel with the normal data acquisition.

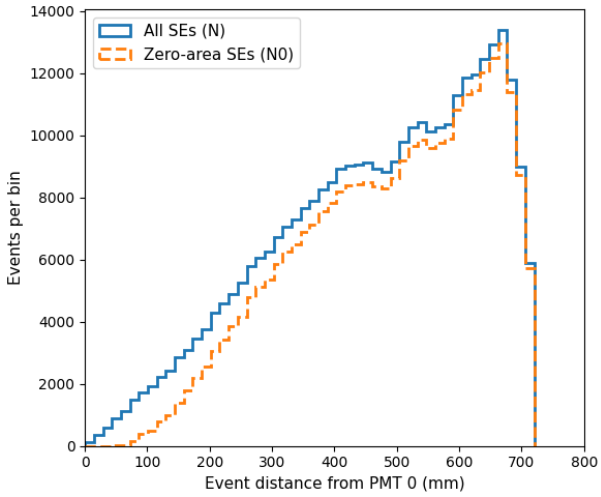

Figure 6.4: Histogram of the event distance from a PMT for the two population of N and N_0 for single electron events.

The measurement of $\mathcal{Q}_c$ needs to consider that the PMT signal varies with the distance of the event from the center of the PMT, R, thus changing the value of μ. As we know the positions of single electrons, we can arrange them in a histogram, with each bin containing the events at roughly that same R. In this manner, μ is approximately the same for the events in the same bin and can be found from the N_0/N ratio of each bin. For example, figure 6.4 shows two histograms for the same PMT: one for all events and the other for zero-area events. In this figure, it is possible to see that

towards the higher distance, the ratio between the histogram with zero areas and the histogram with all single electrons increases, hinting that μ also decreases with the event distance to the PMT.

We calculate the average signal area, $\langle \mathcal{A}_s \rangle$ for each bin of R, and using equation 6.7 obtained the value of $\mathcal{Q}_c$ for each bin. Figure 6.5, presents the μ, $\langle \mathcal{A}_s \rangle$ and the calculated $\mathcal{Q}_c$ for bins of R for the central PMT of the top array.

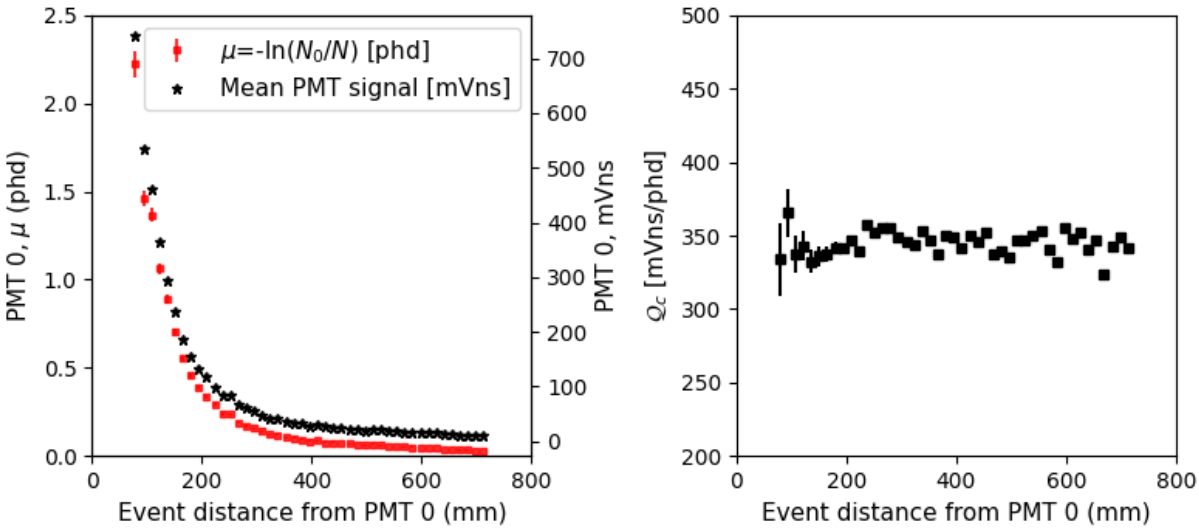

Figure 6.5: Left plot: resulting bins of μ (squares) for the left axis, $\langle \mathcal{A}_s \rangle$ (stars) for the right axis. Right plot: values of $\mathcal{Q}_c$ versus the event distance from the central PMT of the top array.

The $\mathcal{Q}_c$ of a given PMT is obtained with a linear regression of a $\langle \mathcal{A}_s \rangle$ vs μ plot, as shown in figure 6.6. Only bins with an R in the [300 mm, 700 mm] range and with $N_0 > 100$ were included, ensuring nearly constant μ among the events in each bin.

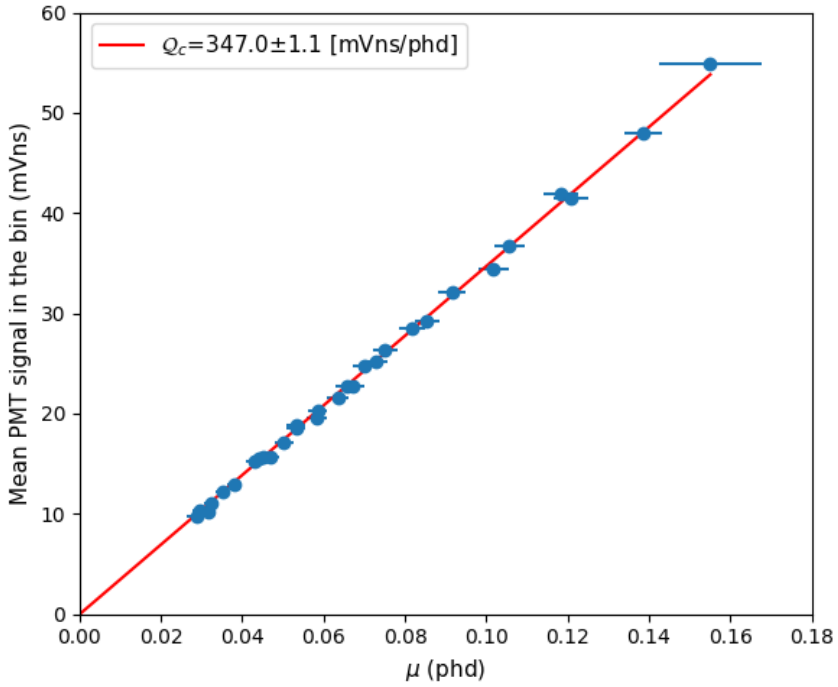

Figure 6.6: Measurement of $\mathcal{Q}_c$ using a linear fit on the binned signal in mV·ns vs μ. Only events at greater distance of 300 mm from the PMT were used.

6.2.2 Continuous calibration

To test the performance of the continuous calibration technique described above, the whole LZ science run dataset was partitioned, according to the event timestamp, into 794 2–4 hours-long segments, which then were filtered to obtain the calibration datasets, each containing 250000 single electron events. Then the $\mathcal{Q}_c$ parameters were obtained using the procedure described in the previous section for each of these datasets.

The temporal dependence of $\mathcal{Q}_c$ for each PMT was fitted by two cubic splines, one of two bins for the period preceding the data taking break and the other of 8 bins for the remaining period. The joined splines represent a period comprehended between December 24 and April 15, with each bin lasting roughly one week.

Figure 6.7 presents the results of the calibrations and the spline fits for a few PMTs of the top and bottom array. The calibrations of the LED are also presented for comparison. Most PMTs results obtained from LED calibrations and the presented method have average disagreement of less 7%.

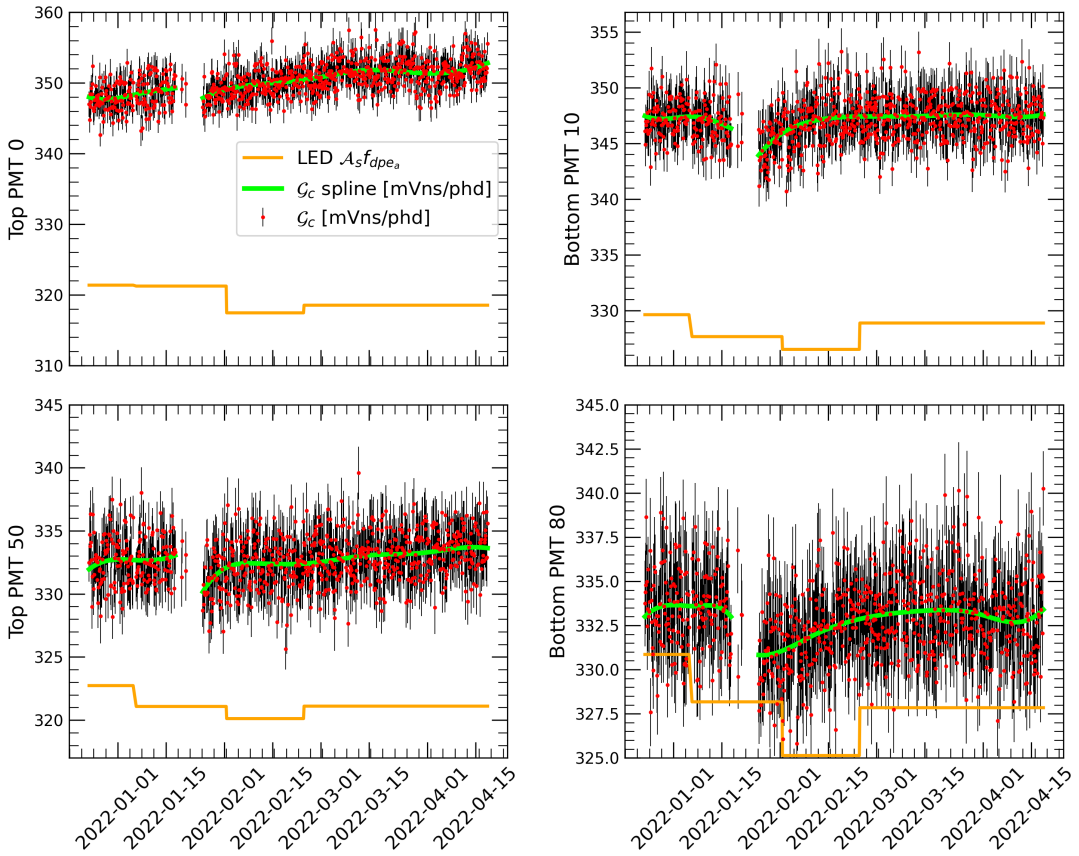

Figure 6.7: Calibration results for 2 PMTs of the top array and of the bottom array: the data points are $\mathcal{Q}_c$, and their respective error obtained from the linear fit covariance matrix. The smooth line is the spline calculated from the data points. The discrete line refers to the LED calibrations resampled in time for a better representation.

This disagreement is most likely caused by the fact that the used double photoelectron factors, estimated before the installation of the PMT in the array, changed with the new conditions imposed during the LZ acquisition.

The measurement of $\mathcal{Q}_c$ accomplished for all PMTs averages on 340$\pm$20 mV·ns/phd.

6.2.3 Results

To compare the temporal stability attained with the LED and the above technique, alpha events from the ^{218}Po$\rightarrow^{214}$Pb decay (E=6.00 MeV) were chosen as a standard candle to assert the temporal stability of the calibration method presented here for a long acquisition period due to their narrow spectra both in S1 and S2.

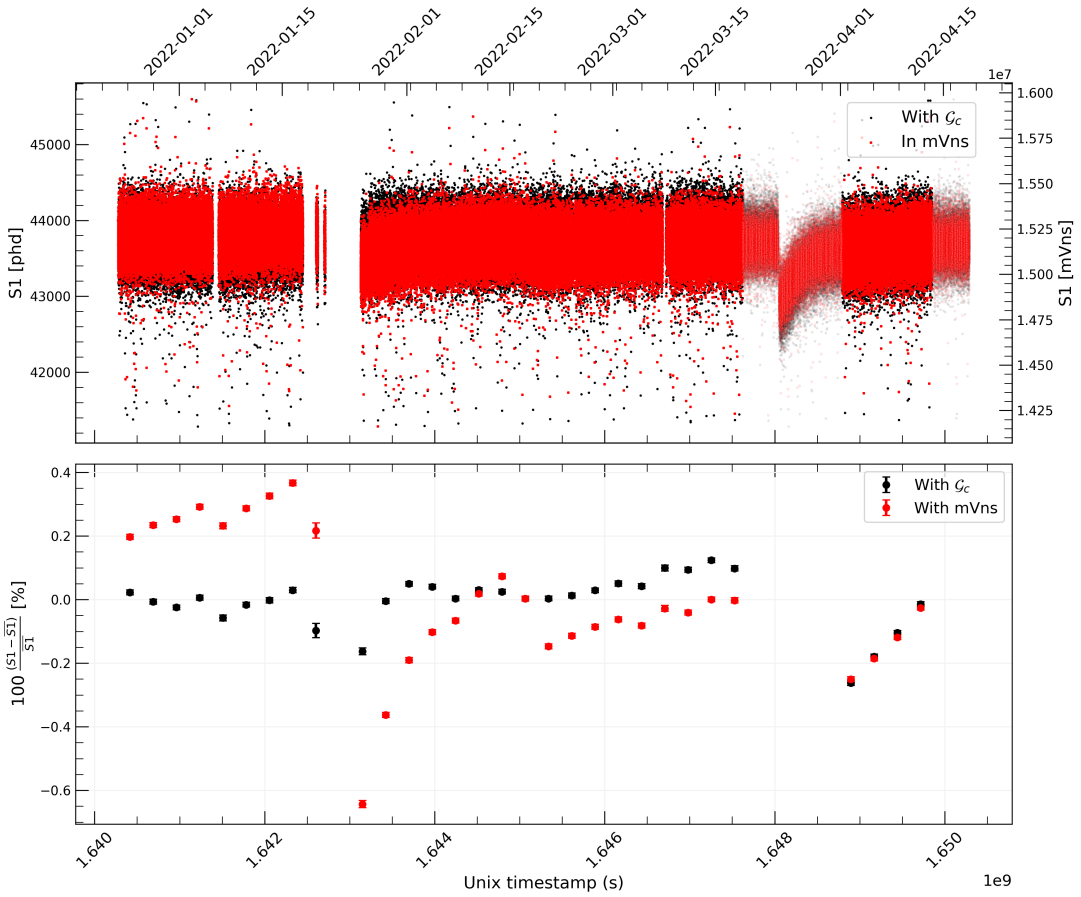

Figure 6.8: Temporal dependency of the S1 signal for 6.00 MeV alpha-particles from the ^{218}Po$\rightarrow^{214}$Pb decay. The top plot presents the S1 measured with the developed calibration method (black) and directly with mV·ns (red). The bottom plot consists of a profile histogram of the deviation, in percentage, from the average. The blurred region was not included in the histogram as it corresponds to an accidental halt of the circulation system. Additionally, a fiducial cut of [100, 900] µs in drift time and <700 mm in radius was applied.

The results obtained with the calibration methods for the total S1 (top+bottom array) of the 6.00 MeV alpha events are shown in figure 6.8. In the bottom plot, it is possible to see that, as expected, the approach with the continuous spline provides a good stability of the signal. The strong variation occurring at the end of January follows a period of calibrations with neutron events, subjecting the PMTs to high amount of light. The actual underlying cause was not identified as it requires a comparison with forthcoming calibrations. A comparison of the S2 is not included since this signal is also subjected to time dependent correction of the electron lifetime.

Figure 6.9 provides a comparison between the relative width of the S1 signal produced by 6.00 MeV alpha-particles events with and without corrections for PMT drift. The use of the PMT gain drift

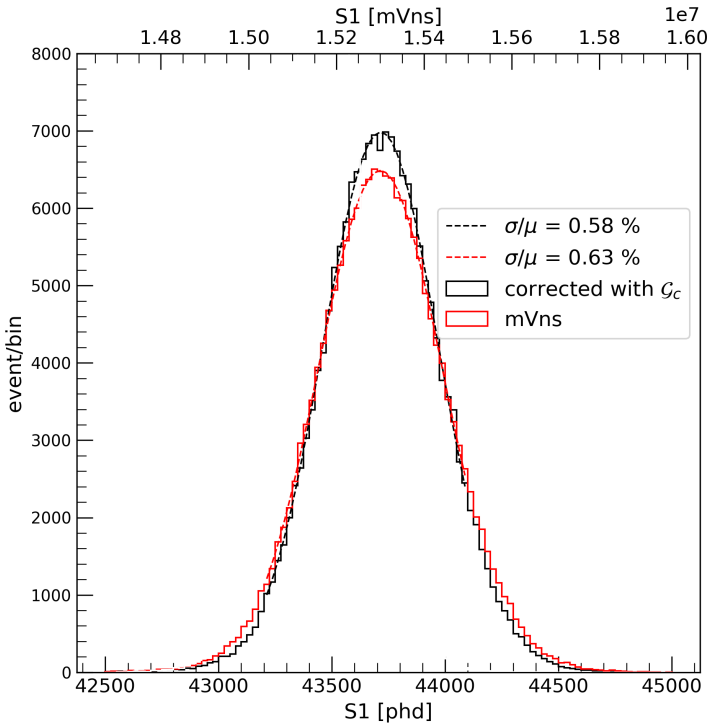

Figure 6.9: The peak from 6.00 MeV alpha-particles from ^{218}Po$\rightarrow^{214}$Pb decay. The plots represent the S1 signal measured in mV·ns (red) and corrected with $\mathcal{Q}_c$ (black).

corrections leads to a reduction of 8% in the peak width. Note that this result was achieved for a science run of only 60 live days. A significant improvement should be expected for longer acquisition periods.

6.3 Conclusions

This chapter presented novel methods to calibrate the PMTs within the scope of the LZ detector.

As a proxy for a good signal reconstruction towards higher energies, a technique was developed to characterize the saturation of the PMTs using only data acquired during the science run. With this approach, it was possible to measure a saturation threshold for each PMT of the top array, averaging 40×10^3 phd.

Finally, with the technique developed in [119], which permits the calibration of the PMTs in an array using VUV photons acquired during science data, we created a methodology to produce continuous calibrations of the PMTs using background data in the form of single electrons. As demonstrated, with this technique it was possible to obtain temporal variations of the signal within 0.2%.

Chapter 7

Underground Performance Monitor

Consider the overall data acquisition and analysis framework implemented for LZ. As the DAQ registers the signals of the PMTs, it produces several raw files holding information regarding the events that match a given trigger condition. These files, with $\approx$100 MB in size, are transferred from the underground infrastructure to a database located at the surface, from where they are placed in a queue waiting to be transferred offsite to the supercomputer National Energy Research Scientific Computing Center (NERSC). At NERSC, it is placed in a processing queue to be processed by LZap, producing the reduced quantities (RQs) to be further used in all the analyses. A fellow analyst, patiently sitting at the desk of the detector control room, detects, through his analysis, that the data generated by the DAQ is, somehow, corrupted. The data acquisition is consequently aborted. However, by then, several hours, if not days, had passed between the DAQ initialization and the abort action by the operator, rendering the acquired data useless.

The hypothetical episode described above is one of many examples which can lead to the loss of an immense volume of data and complicate even further the data-taking operations, particularly the ones required for calibrations. The primary bottleneck of this process lies in the DAQ-to-NERSC file transfer rate, which is 10 min for a single file containing roughly 250 events. Another constrain lies in

the analysis chain itself. With a processing rate of $\approx$1 $^{event}/_{s}$, it adds 5 minutes per file to the whole processing framework. Compared with the acquisition rate of, for example, ^{83m}Kr calibrations ($\approx$30 Hz), such processing rates would render the operations of the detector much more complicated to manage. Consequently, and to prevent such situations, one of the requirements set by the LZ collaboration is the ability to produce an onsite and real-time analysis of the raw files. Such analysis provides a proxy to monitor the data's quality and the detector's health.

The UPM — Underground Performance Monitor — is the part of the Online System subsystem responsible to perform this analysis and trigger alarms if a given set of undesired conditions are detected during the analysis. The alarm is sent to Slow Control and propagated through the appropriate pipelines. The results of the UPM analysis can be visualized by the on-site and remote operators through a web-based GUI, whose development is the main focus of this chapter.

7.1 Overview

The UPM, in compliance with the modern software design patterns, consists of the back-end (Core) that handles the tasks of the data transfer and analysis and the web front-end, which, henceforth, in this chapter will be referred to as GUI — Graphical User Interface.

In the general architecture of the UPM (figure 7.1), these two components are well separated from each other in the sense that the runtime state of one does not directly affect the other. If the Core analysis is interrupted, the GUI does not display new data, but in such cases, past data can still be consulted. The communication is performed on a single-way basis, from the Core to the GUI through an exchange of JSON files. This file format is well established within the software community, with libraries available for various programming languages including, Python and C++. Furthermore, JSON files are human-readable and commonly used in Internet of things applications.

The UPM Core consists of a control application that runs various services to handle specific low-level tasks, such as raw file opening, signal processing and file output. The analysis itself runs asynchronously with respect to the low-level tasks as a mean to minimize the waiting periods of the Core. In this aspect, the Analysis can be viewed as an easily replaceable add-on module. The UPM executes only one type of analysis at a time, which depends on the acquisition type defined by the

Run Control (RC) and corresponds to the ongoing operation with the detector.

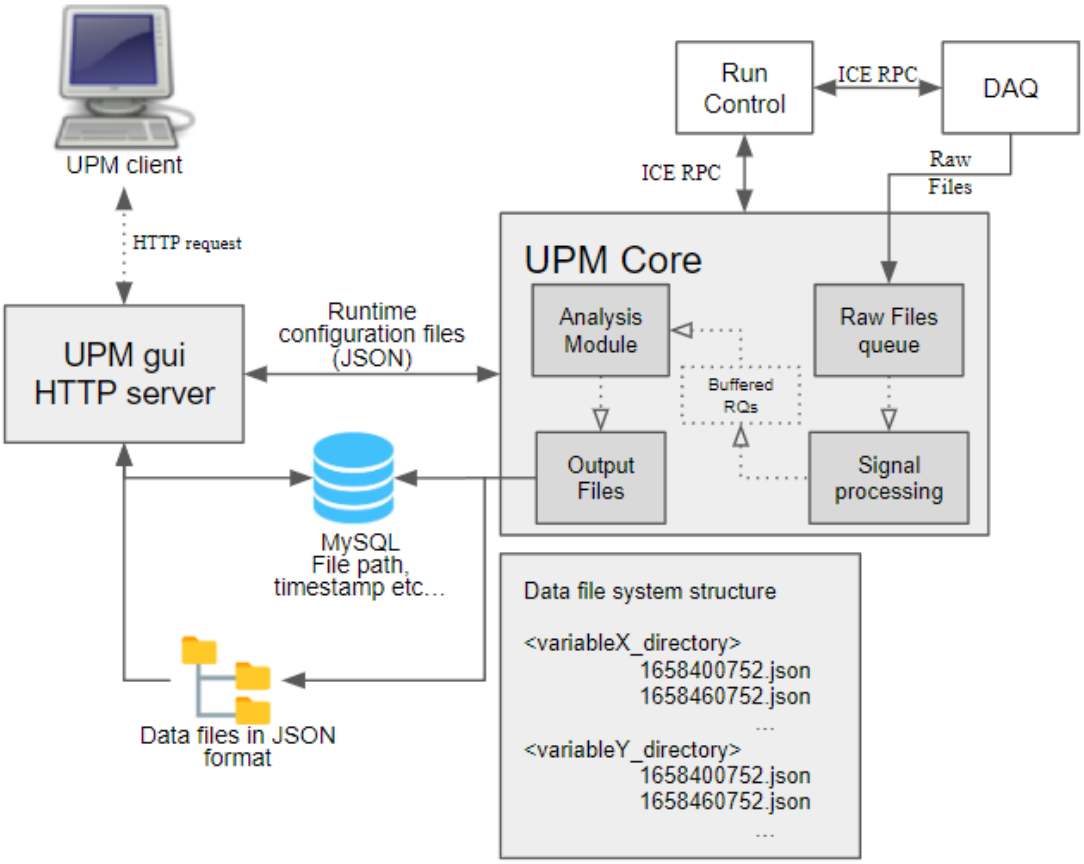

Figure 7.1: Overview of the UPM internal data structure

The interaction between the Core and the UPM client is depicted in figure 7.1. During an acquisition, the RC is continuously communicating to the UPM the location of the new raw files created by the DAQ[1]. The Core processes the raw data through its dedicated signal processing chain and generates RQs, which are stored in a buffer. These RQs include parameters required for the analysis, such as pulse classification, S1 and S2 areas, position reconstruction results and event classification.

The analysis module iterates over the events and outputs the data files. This data does not contain per-event quantities. Instead, the analysis accumulates the results over a period of 1 minute, and new files are created with predefined plots to be visualized. Two types of files are created: histogram

[1]The task of generating the raw files is executed by EB (Event Builder), a system independent to the actual DAQ. However, for the purpose of simplicity, in this chapter, EB and DAQ are treated as a single entity

files, produced by ROOT[2] through its built-in JSON mechanism, and linear trend files, consisting of a simple JSON with parameters for the mean and standard deviation of an RQ measured over a given period.

As represented in the "Data file system structure" of figure 7.1, the data files are directly written into the file system. Each plot has a dedicated directory with the various files named with the corresponding timestamp in UNIX time. In addition, the Core stores, into a MySQL database, the path, the timestamp, and the name of the corresponding variable for each plot. This database is used to speed up the search for the relevant files by the GUI.

The architecture design of storing the files in the file system is driven by the size of the histogram-like files generated by ROOT. Storing such files in the database could lead to slower queries and complicate the management of the database.

The analysis files are kept in the UPM machine for a maximum time of 15 days. After that period, the files are moved to an offsite machine located in Rochester, New York, which can be consulted by a second instance of the GUI. This instance was altered to permit the comparison of the same plot for multiple periods.

Different acquisition modes entail a different set of plots to be created by the Core analysis. Consequently, at the start of each acquisition, the Core also stores into the database the main configuration file and the acquisition starting time. The file contains the meta-data of the plots to be presented in the GUI, such as the axis type (log-log or linear), titles, legends, and other graphic-related parameters. This configuration file also holds the organizational structure of the plots, such that these are presented in a directory-like panel that represents the detector subsystem structure.

7.2 The Core

The Core of the UPM is a C++ software that comprises five asynchronous services (docks), the File Service, the Input dock, the Analysis docker, the GPU dock and the Output dock, as shown in figure 7.2. Each dock, responsible for a specific task, consists of a pool of various threads (or bots), each

[2] An object-oriented program and library developed by CERN, used mainly for the purpose of data processing and analysis.

assigned to process a given file. After a thread completes its job, it transfers the results to the next dock in the processing line before being re-initialized and given the results of the preceding dock. This data flow architecture permits maximizing the processing rate of the Core as the latency of each thread is minimized.

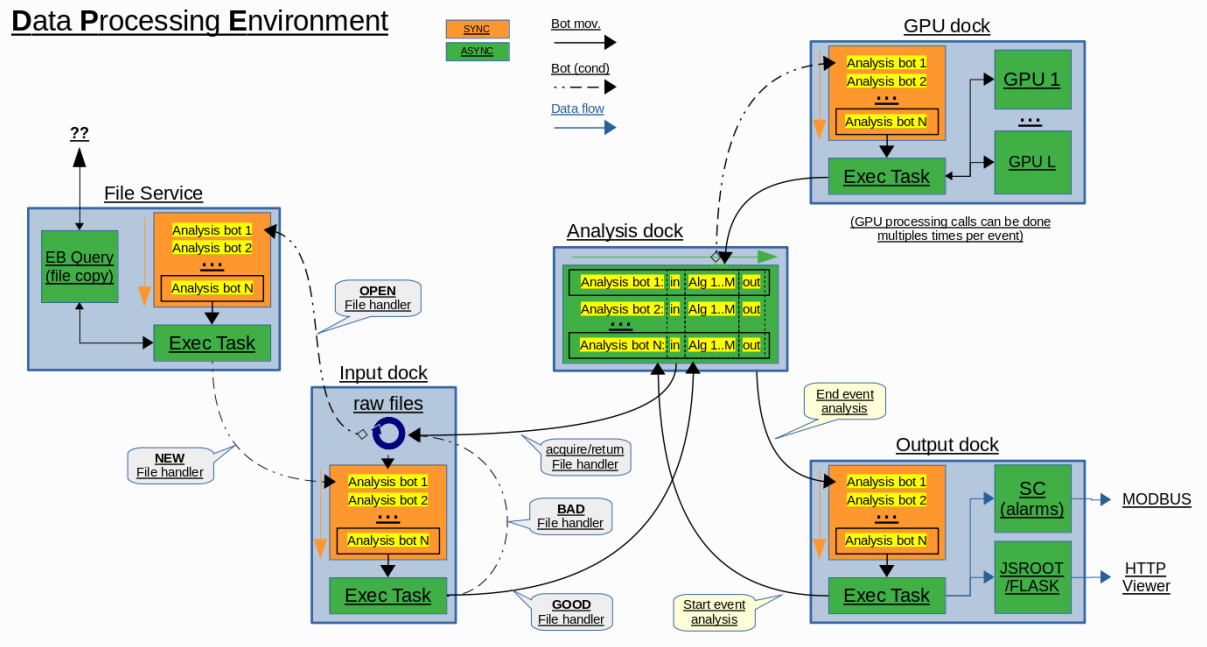

Figure 7.2: Schematic with the data flow of the UPM Core data processing (figure from [120]).

Each raw file generated by the DAQ is received by the *File Service* and its contents are stored in RAM to optimize the task of file reading to be accomplished by the *Input dock*. From there, the blocks of RAM are placed in a queue to be processed by the *Analysis dock*, where both signal processing and operation-specific analysis are accomplished. This permits that N events can be analyzed at the same time, with N representing the number of CPU threads used by the *Analysis dock*[3]. At the end of the chain, the *Output dock* writes the analysis results into the JSON files to be presented by the GUI.

[3]Note that in the figure 7.1, the *Analysis dock* was split into the Signal processing and Analysis Module blocks to better distinguish the low level signal processing, producing per event results, from a high level analysis, which returns the plot-like ROOT objects

7.2.1 Signal Processing

The task of the data processing chain, shown in figure 7.3, is to produce for each event a set of reduced quantities (section 4.5.1) to be used for further analysis and to create the plots.

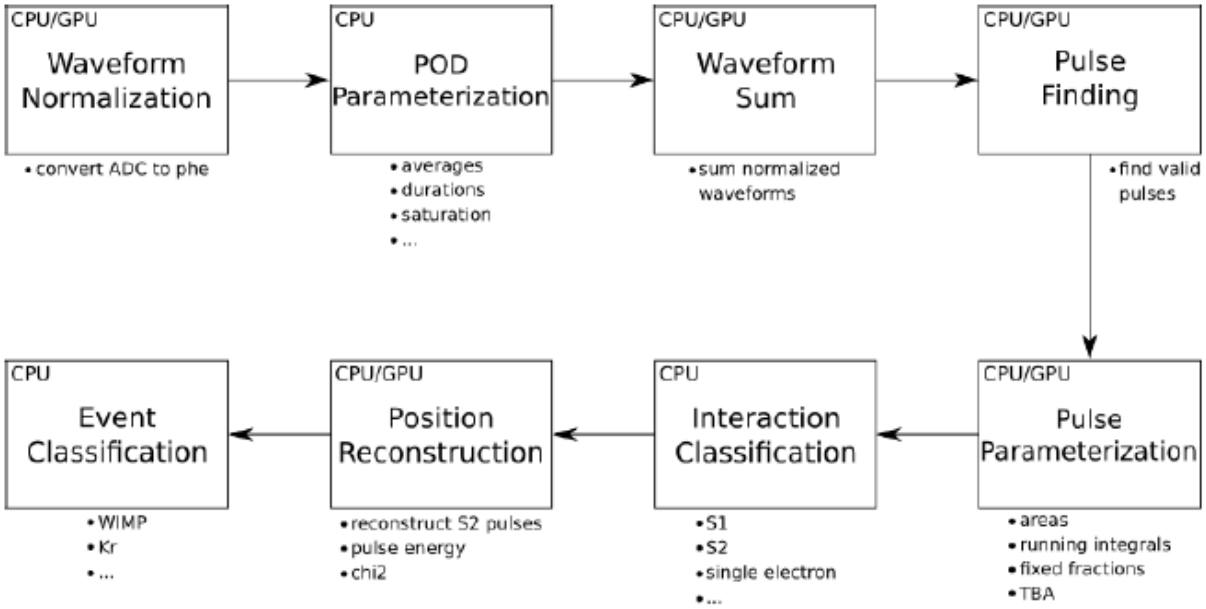

Figure 7.3: UPM Core low level data processing chain [120].

Raw files used as the UPM input consist of PODs (timestamped waveform fragments — see section 4.4 for details). The UPM Core chain begins by performing a waveform normalization, where the POD data of the individual PMTs are converted from mV·ns into photoelectrons. The PODs are then parameterized to extract parameters, such as averages, duration and saturation periods, to be used downstream. At the next processing stage, the S1 and S2 pulses are identified and parameterized for the following analysis. To do so, the normalized PODs are merged by timestamp into a common waveform representing the light detected by the whole PMT array. This is done by the Waveform Sum block. This waveform is scanned by the pulse finder algorithm, using Fast Fourier transforms filters, to mark the boundaries in time of each pulse. The Pulse Parameterization calculates low-level RQs regarding each pulse, such as area, relative area fraction[4], peak time and prompt fraction[5].

The following modules, interaction classification, position reconstruction and event classification,

[4]Time, in ns, at which the summed POD reaches a given fixed percentage of the total area

[5]Ratio between the PODs summed from the pulse start up to a given fixed period and the total pulse area.

produce the most fundamental and important, RQs for the overall detector and data quality monitoring with the UPM. This processing stage is similar to what is done by the offline analysis (see section 4.5.1), but the overhead is less significant as there are fewer RQs to calculate.

7.3 Front End

The GUI of the UPM, running in the same machine as that of the Core, permits to consult the Core generated in ROOT format. This format was chosen since it was already being used by the offline processing chain and provided a more familiar interaction with the users within the LZ collaboration. Moreover, ROOT contains a built-in graphical environment with various options, which permits the adaptation of the graphical objects to suit various needs. On top of that, the plots can be rendered by JSROOT[6], or JavaScript ROOT, to display the graphical objects in a web browser. This makes the UPM GUI compatible with most machines by users without the need to have a ROOT installation. Consequently, the GUI is supported by an HTTP server capable of handling multiple concurrent connections, thus allowing the monitoring tasks to be performed at the same time by various users located onsite or offsite.

While the GUI is sustained by the main thread responsible for the structure of the interface as a whole, a plot object, initialized by the user, encapsulates a JSROOT graphical object and a routine running asynchronously with respect to the main thread. This routine, running every minute to maintain an updated plot, handles the HTTP requests to pass the correct plotting parameters to the HTTP server and receive its response. Figure 7.4 presents an example of a plot requesting the list of files required to present the data of the S1 pulse area. The method *get_json* queries the database for the path of the files acquired in a time window delimited by *start_time* and *end_time*. If the query is successful, then a thread is created on the server side to read the content of the files, and place them in a list sorted by timestamp. This list is also accompanied by a second one with the actual timestamp in UNIX format. Both lists are encoded in a JSON-like string and returned to the HTTP request handler. The list of data files is used to generate the JSROOT object to be rendered in the web browser (see the next section 7.3.1 for more details).

[6] `https://root.cern.ch/js/`

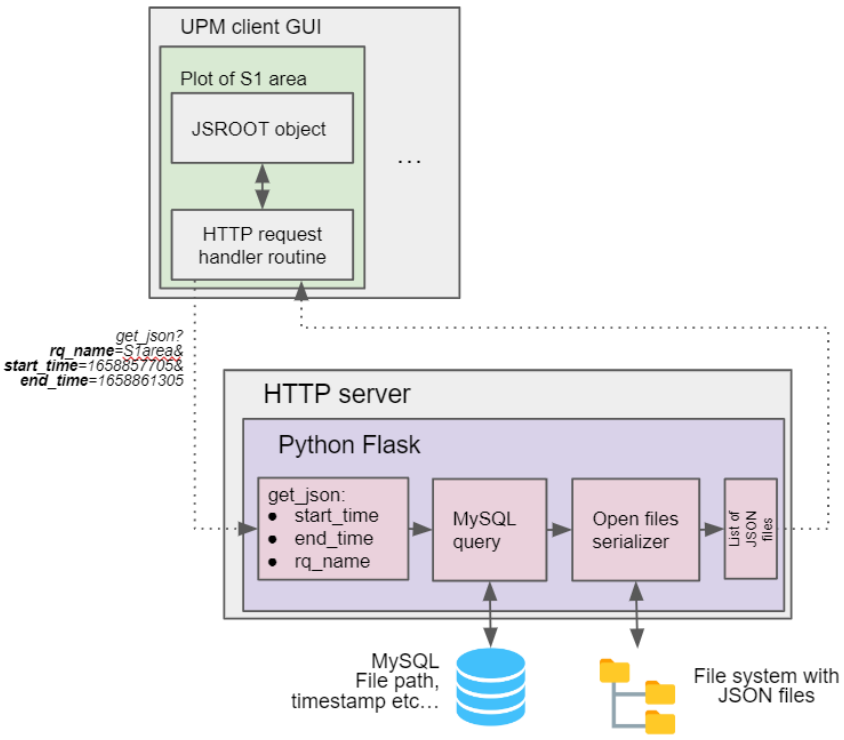

Figure 7.4: Overview of the UPM GUI request.

The HTTP server was powered by Flask[7]. This consists of a simple micro-framework to implement HTTPs requests in Python. However, the built-in server provided by Flask, suitable only for development purposes, is not the recommended gateway to distribute an application as it operates on a single-thread basis. Thus, to greatly increase the performance of the GUI, the Flask implementation is served by uWSGI[8]. This package encapsulates HTTP applications such that the concurrency of many connections is automatically processed.

The UPM GUI, shown in figure 7.5, is divided into 4 main blocks, each offering a different type of interaction with the user:

- **Header**: located at the top, the main purpose of the header is to present simple and generic information regarding the overall status of the Online System and the UPM itself. The section with LED-like components display a color-coded state of the Online System subsystem. This section is standardized throughout the various graphical interfaces of the Online System, such

[7] `https://flask.palletsprojects.com/en/2.2.x/`
[8] `https://uwsgi-docs.readthedocs.io/`

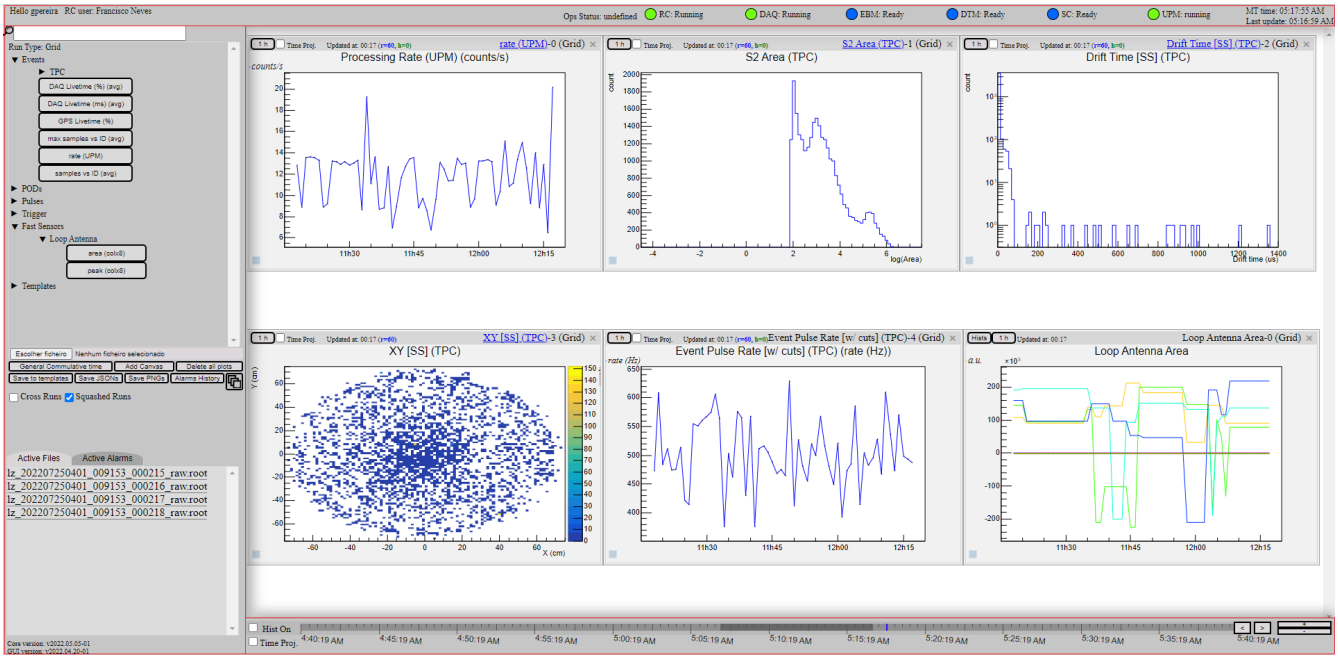

Figure 7.5: Overview of the UPM GUI. The red boxes delimit the main regions of the interface: Header, History bar, Left panel and plot area.

as the one for Slow Control and Run Control, and allows a user to assert the status of the system in a single glance. The header also indicates the current time adjusted for the detector timezone (Mountain Time) and the timestamp of the most recent data produced by the Core (Last update). The timestamp of both times is sent by the web server side. Thus, the comparison between them provides a fast and straightforward method to assert the communication involving the user side, the web server and the Core.

- **Historic bar**: located at the bottom, the GUI user can drag and resize the dark grey selector to select a specific time window. A right-click mouse action in the grey selector displays a list of the various acquisitions executed within the previous 15 days, allowing the user to navigate to a given period quickly.

- **Left panel**: this component contains the main menu with various buttons to load the plots generated by the Core. This menu is organized in a tree-based view, allowing a more user-friendly interaction. The layout of the tree view is generated by the Core and communicated to the GUI through a main configuration file generated at the start of each acquisition. A search tool is also available to quickly find the desired given plot.

The panel also contains a menu providing additional functionalities of the GUI, such as saving or erasing the rendered plots. The bottom of the panel contains a tabbed view showing a list of either the raw DAQ files being processed by the Core or a list with the active Alarms generated by the analysis.

- **Plot area**: holds the various plots in a grid layout. One of the most useful functionalities is the ability to save a given set of plots, called template. With this tool, the user can load, in a single action, the various plots required for a given type of acquisition. However, it is important to note that this tool does not save the data being visualized at a given time, as it only serves to load various plots with a single "click" action from the user.

The arrangement of these blocks maintains an organization of the information to be displayed. Minimal information of the system's state is displayed at the header, and more complex information is shown in a dedicated panel at the bottom left. The user's interaction is mainly circumscribed in the left region of the screen to reduce the number of interactions needed to use a given functionality or to display the data. The general color scheme, mainly grey based, was selected to reduce the load on the user's eye, as opposed to a color palette with vivid colors. This also makes the interface less distracting, especially since, the main operator, sitting at the desk of the control room, needs to monitor more screens with the interface of other systems, such as the Slow Control.

7.3.1 Data visualization

As mentioned above, a plot loaded into the main area is maintained by a dedicated routine that handles the data transfer between the client and the server. Depending on the type of files returned by the server, the GUI will display either a linear plot, a 1D histogram, or a 2D histogram (used only for XY position reconstruction results).

A 1D or 2D histogram is plotted as a sum of the available files over time[9]. However, for the 1D type, it is also possible to render a projection in time in a 3D object (see figure 7.6a). This functionality is one of the most preferred methods to visualize the UPM data, as it permits easy monitoring of

[9] The bins of each file are summed in time. In some cases, depending on the configuration provided by the Core, the sum of the bins is averaged over time.

complex data trends. This also solves the problem of plotting a specific property of many PMTs, such as individual rates, in a single graphical component, with a plot of *PMT ID vs time vs rate*.

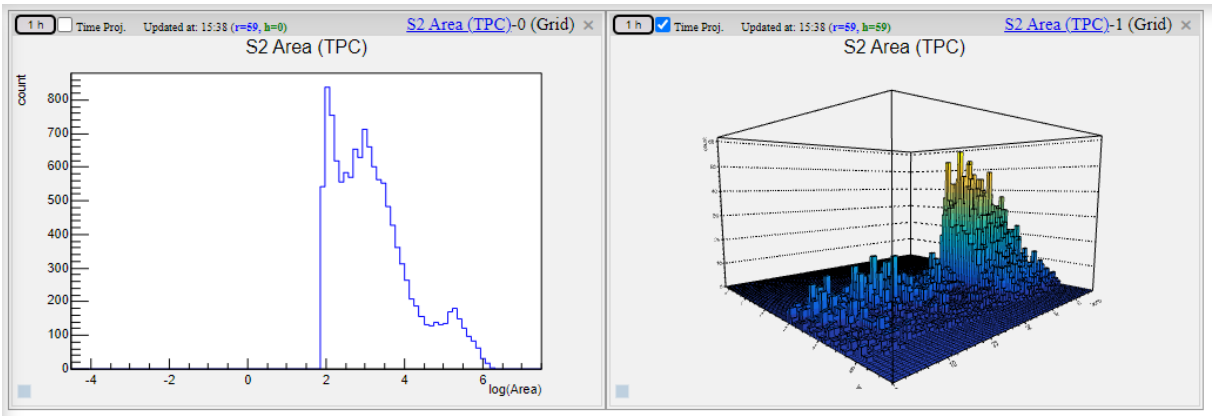

(a) 1D histogram representation

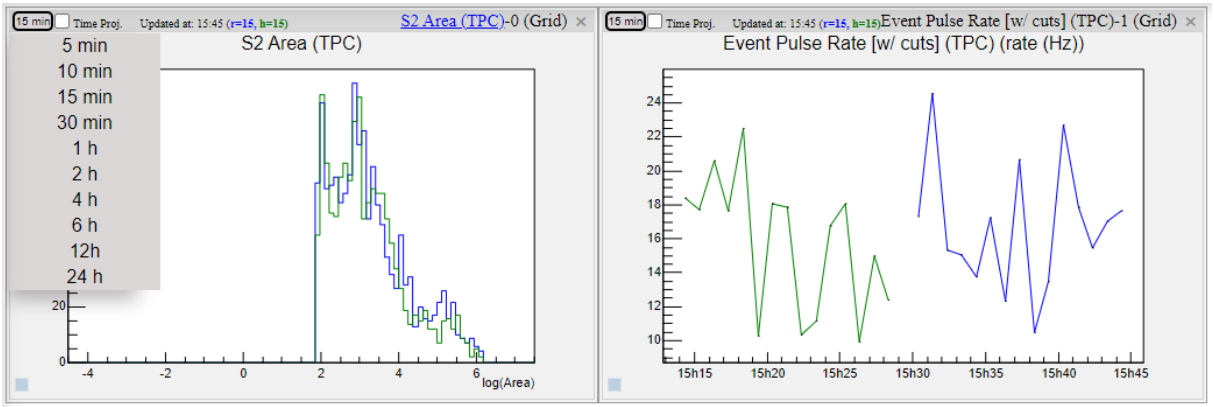

(b) Real Time vs Historic Modes

Figure 7.6: Example of the various forms of data visualization possible through the UPM GUI. The notation "(r=15,h=15)", in the header of each plot, indicates the number of files used for each mode (r= real time, h=historic). The title of the plot consists in a hyperlink guiding the user to the UPM documentation and notes about the plot.

The querying mechanism for each plot allows searching for data in two different time windows. In such cases, the data representation can be done with two simultaneous modes: historical and real-time. In the historical mode, the data is queried with the window selected with the Historic Bar at the bottom. In the real-time mode, the GUI queries the most recent data in a given range defined for each plot (see figure 7.6b). This makes it possible to, in real-time, compare the results of the ongoing acquisition to a previous one.

7.3.2 Conclusion

The UPM is responsible for a real-time processing and preliminary analysis of the events registered by the DAQ to extract RQs as a method to monitor in real-time the state of the detector and the quality of the acquired data.

In this chapter, the UPM was re-visited with a focus on its general architecture and data processing chain. Its GUI, developed within the framework of this thesis, was further presented as the only point of entry to visualize the data produced by the UPM analysis. In this regard, the implemented functionalities allowed the operators to quickly explore complex data entailed by a ton-scale detector with hundreds of photo sensors. Moreover, the web-based nature of the GUI permitted to expand the task of monitoring to off-site operators during remote shifts. Such exposure of the GUI to the "outside world" was only possible with a synergy between the UPM development team and the IT of LZ.

Furthermore, after 15 days, the data generated by the UPM is moved from the underground infrastructure to a server hosted by the University of Rochester in New York. A modified version of the GUI was also implemented to permit the consultation of this "expired" data. The modification consisted of removing functionalities related to real-time monitoring and developing a simple tool to quickly navigate to any past acquisition identified by a specific ID

Chapter 8

Experiment Control and Monitoring. of the LZ detector

The Slow Control (SC) is the LZ system responsible for performing supervisory control and monitoring of the LZ main systems, including, xenon circulation, detector temperature control, LN distribution, PMT and Grid High Voltage, Electronics and Calibrations. Its most important function is guarantee the detector's safety, prevent equipment damage and, most importantly, loss of xenon. To better guide the development of SC and to minimize the risk of xenon loss, the systems are divided into two main groups: critical and non-critical, with a given system tagged as "critical" if its malfunction can lead to loss or contamination of xenon.

The main line of defense against the malfunction of critical systems is the Programmable Logic Controller (PLC). It consists of a computer with a low-level, yet robust, logic to actuate and monitor the hardware of these systems. Given the importance of the PLC, the reliability and performance of the programmed logic is subjected to a rigorous process of Quality Assurance (QA).

An additional layer of safety of the detector arises from an alarm system to notify the operators

regarding erroneous behavior of the detector and from a user interface (UI) displaying the relevant telemetry to assess the state of the system and to provide control over its parameters. Furthermore, SC is also tasked to register several parameters of the detector by periodically reading and storing the output of various sensors in a database. Naturally, this information is displayed in the UI with plot-like graphical components to facilitate the monitoring of the detector state by the operators.

8.1 System Overview

The SC is constituted of two components: a SCADA system, in the form of the "Ignition server" — a software development platform procured from Inductive Automation — and the PLC system — Siemens SIMATIC S7-410H dual-CPU PLC — with the Master PLC and its respective I/O modules, as represented in figure 8.1 [12].

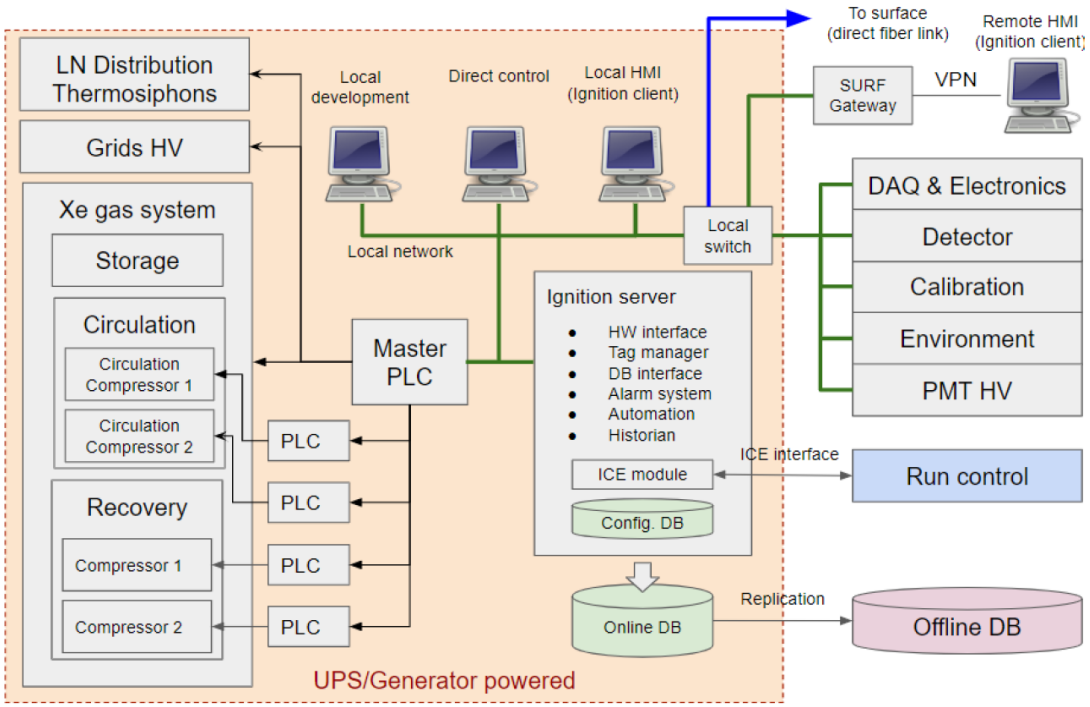

Figure 8.1: Block diagram of the Slow Control system with the main components: the PLC and the Ignition server [12].

The PLC, as mentioned above, is a low-level digital computer with I/O channels that are electrically connected to the "critical" instruments of the experiment. This computer maintains the detector in a safe state using preprogrammed interlocks. These, for example, activate the recovery compressors

and actuates the required valves to flow the Xe to a safety recovery vessel in case of a pressure surge in the TPC above a threshold deemed dangerous for the experiment. The PLC also maintains stable conditions of the detector through complex PID loops, which control the instruments from the feedback information of various sensors.

The Ignition, performing high-level tasks, is a server-based platform that centralizes the critical and non-critical systems to facilitate monitoring and controlling several parameters (i.e., channels) of the experiment. This server also records, in a MySQL database, historical data of all parameters at a rate defined by the nature of the parameter/sensor. Within the Ignition framework, the rates are configured using “Scan Classes”. Each scan class can be created from various available options, which sets a preprogrammed acquisition mechanism. The most used acquisition mode is a simple scan class executing at a specific rate. In the Ignition context, a channel requires two types of scan classes, one for requesting the data from the hardware (acquisition) and the other to store data in the Historian database. The acquisition rate is limited by the hardware’s internal rate, and by the processing power of the CPUs used by Ignition. The storage rate should be configured to prevent the duplication of values in consecutive intervals, but it also needs to accommodate unexpected sensor output variations, such as spurious pressure surges. This storage rate also needs to be balanced between the thousands of channels to reduce as much as possible the growth rate of the historian database.

Ignition is also responsible for the alarm system to propagating a notification to the operators via email, SMS, or SLACK if the value of a given sensor reaches a custom predefined threshold. In the scope of SC, there are 3 levels of severity (Alarm, Alert, Warning), each with high and low thresholds for each sensor. These levels also have configurable time-based deadbands helping to prevent false alarms relative to periods when the channel value is momentarily outside the defined thresholds. Each alarm level, when triggered, activates a specific pipeline consisting of a flowchart with a set of rules and conditions to propagate the alarm information to a specific set of operators.

A scripting framework was developed using the Python built-in Ignition engine to automate complex tasks requiring coordination between multiple systems. These operations-driven scripts behave as a state-machine algorithm, as they perform a specific action on the hardware depending on the sen-

sory information. The development of such a framework allows the creation of a standard structure of the code, thus facilitating the task of maintenance and ongoing development by various members of the SC team. A script in the framework is distinguished by the following blocks, presented in order of execution:

- **init** — initialization of the script variables and parameters with an input given by the operator;
- **requirements** — checks if the state of the hardware corresponds to a predefined state required to execute the script. The script is aborted if the requirements fail to match such state;
- **run** — the main task to be executed. Additional verifications can be performed during run-time, which could trigger an abort;
- **finalize** — the final task to be executed after the *run* block to place the system in a safe state;
- **abort** — a set of actions that can be engaged at any time, either by the operator or by the *run* block, to put the system in a safe system.

The SC system was designed as a high-availability system, with a minimal downtime, to allow uninterrupted access to the detector controls. To achieve this requirement, the main components of the system have a redundant counterpart with automatic failover. The PLC consists of a dual-CPU system, each powered by a dedicated UPS. The Ignition platform offers an out-of-the-box redundancy mechanism to mirror its software to a separate machine. A Transmission Control Protocol (TCP) link, shared between the two machines, is used to mediate the redundancy state. The Ignition failover is manually tested on a monthly basis by forcing a shutdown of its hosting machine. This switchover presents a delay in the order of 5–10 seconds. The underground-to-surface network connection is supported by two physically separated optical fibers, each capable of up to 10 Gb/s. Moreover, the Ignition database is continuously replicated to a mirror on the surface, to act as a backup and to be used by a third Ignition instance operating in read-only mode. The usage of this additional instance, mainly by remote operators during monitoring tasks, reduces the workload of the SC underground infrastructure.

8.1.1 Interfaces with Slow Control

The majority of the systems, integrated into SC, rely on a communication via PROFIBUS [121] (for PLC), MODBUS [122] or SNMP [123], which Ignition is capable of handling via its built-in drivers.

These consist of IP-based machine-to-machine communication protocols. Other systems, such as the detector RGAs, required tailored solutions by developing TCP-based drivers[1] to be integrated in Ignition.

Table 8.1 presents an overview of the channels integrated in Ignition by the subsystems of the experiment. Although the main concentration of channels lies in the PMT HV, other non-critical systems have several independent subsystems. For instance, the Calibration alone consists of the TPC optical system, the Outer Detector optical system, and the source deployment system. During the design phase of SC, the integration of these systems was facilitated by standardizing the integration by resorting to collaborative administrative tools, such as *Google Sheets* and *Trello*[2]. Moreover, a software package, named *Generic Wrapper*, was also created to standardize the channel structure of each of these subsystems and export them into SC via Modbus (see section 8.1.1.3).

Table 8.1: Channel count of the subsystems integrated into Slow Control. Critical systems are marked with *. Note that critical systems also have multiple interlocks, which does not represent an actual device.

Subsystem	Channel Count	Instruments
Detector and Xe Tower*	693	Level, Pressure, Temperature
Xe Delivery and Recovery*	594	Flow, Pressure, Temperature
Xe circulation and Purification*	594	Flow, Pressure, Temperature
Cryogenics*	335	Heaters, Level, Pressure, Temperature, Weight
Vacuum*	639	Rough and Turbo pumps, Pressure
Calibration	728	Humidity, Temperature, Pressure
Purification monitor	15	Level, Purity
PMT HV	5248	Voltage, Current
Power distribution and UPS	78	Load, Battery time
Electronics Analog+Digital	2600+1500	Voltage, Current, Air flow, Temperature
Total	13292	

[1] The author of this thesis cannot take full credit for this driver as it was mainly developed by Ricardo Cabrita, a former SC Ignition developer

[2] `https://trello.com/` — This free to use tool permits to create a dashboard with *post-it* like blocks to track the development of a given system

8.1.1.1 TPC monitoring

Ensuring the optimal and reliable collections of the S1 and S2 signals is only possible if the conditions inside the TPC are well known. Thus, a specialized effort is given to monitor critical parameters, such as liquid level, temperature, and pressure.

Monitoring of the liquid level, for instance, is done with two main types of sensors: *(i)* 3 long sensors to measure the liquid height during the filling and emptying operations of the detector and *(ii)* 6 high precision sensors ($\approx 10\ \mu m$), located in the liquid-gas interface, to measure a small range of the liquid level to assess the tilt of the detector. Furthermore, this type of sensor is sensitive to fast variations and can be used to diagnose possible perturbations in the liquid surface. Additionally, 8 acoustic sensors, installed in several locations along the TPC height, provide a rough estimate of the level as they are triggered by internal sounds of the liquid Xe [73].

Temperature increase in the detector can lead to the formation bubbles due to the boiling of liquid Xe. This is mitigated by maintaining a uniform and stable temperature of the liquid xenon, which is accomplished by measuring the thermal profile of the TPC with temperature sensors installed in 100 locations with a 4-wire configuration that provide feedback information to the cryogenic system. Furthermore, these bubbles can create electric discharges in the drift field electrodes and cause spurious light emissions. The detection of such HV breakdown episodes is performed by 6 loop antenna sensors installed near the field electrodes [73].

The detector is also equipped with position sensors to monitor the contraction and expansion of the TPC caused by temperature variations during the filling and emptying procedure. Allowing the stabilization of the TPC temperature can prevent critical displacements capable of altering the alignment of the PMTs or modifying the skin region [73].

8.1.1.2 ModBus

The preferred communication protocol used by the SC system to exchange data between the hardware is Modbus over TCP through standard Ethernet networks [122]. This protocol has been widely used in industrial applications since the 1970s, as it consists of a versatile royalty-free protocol with

a simple architecture and implementation [124]. Although Modbus does not provide any built-in authentication mechanism, making it less secure in terms of exposure in a network, the SC network is installed behind a robust firewall provided by both SURF and LZ infrastructures.

Generally, the Modbus communication is mediated between a master and a slave[3]. In the context of SC, Ignition is the master, which requests data from the hardware, that is, the slave. The blocks of data stored in the slave are referred to as *registers* representing pieces of memory with either 16 or 1 bits. Registers with 16 bits are denominated by *input register* (read-only) or *holding register* (read-write), and registers with 1 bit are denominated by *discrete input* (read-only) or *coil* (read-write). The most practical way to visualize this data is by arranging the registers in a spreadsheet with 4 columns, one for each type of register, and N rows, being N the maximum number of registers available[4] in each column. In modern implementations of Modbus, a given slave can contain various of these spreadsheets, named units.

Fields	Length	Description -	Client	Server
Transaction Identifier	2 Bytes	Identification of a MODBUS Request / Response transaction.	Initialized by the client	Recopied by the server from the received request
Protocol Identifier	2 Bytes	0 = MODBUS protocol	Initialized by the client	Recopied by the server from the received request
Length	2 Bytes	Number of following bytes	Initialized by the client (request)	Initialized by the server (Response)
Unit Identifier	1 Byte	Identification of a remote slave connected on a serial line or on other buses.	Initialized by the client	Recopied by the server from the received request

(a) Fields of the MBAP (MODBUS Application Protocol) header [125].

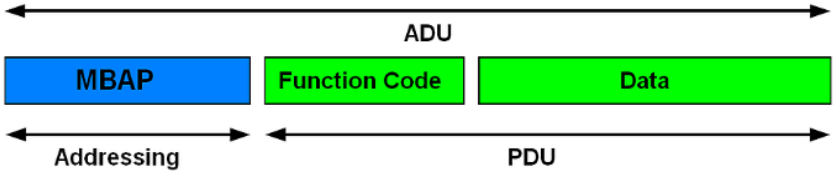

(b) Minimal overview of a Modbus request [124].

Figure 8.2: Main components of the Modbus request.

The main elements of a Modbus request are depicted in figure 8.2. The MBAP (MODBUS Applica-

[3]The master and slave terms also correspond, in a broader notion, to the client and server

[4]The value of N depends on the actual implementation. Older driver have a limitation of 9999 registers, whilst in newer implementation the range is extended to 65536 registers.

tion Protocol header) contains the necessary information to deliver the packet to the correct address (such as IP and unit identifier) and the size, in bytes, of the following portion composed by the Function Code and Data. In a given request, the master can issue a predefined command named Function Code, identified by a specific integer. Examples of these Function Codes are “Read Coil” (1); “Read Holding Registers” (3) or “Write Multiple Holding Registers” (16). The Data is the value stored in the slave requested by Ignition, such as a temperature or pressure value. Depending on the Function Code, the Data is parsed in registers of 1 or 16 bits. Also, although not represented in this figure, Modbus provides an exception error encoding an eventual problem in the processing of the request.

8.1.1.3 A universal Modbus integrator

The Generic Wrapper is a software, developed in Python, created by SC to facilitate the integration of the non-critical subsystems into Ignition. To be installed in a mini-computer such as a Raspberry or BeagleBoard, this package bridges the data to be communicated between the hardware of a subsystem and a Modbus client running in Ignition.

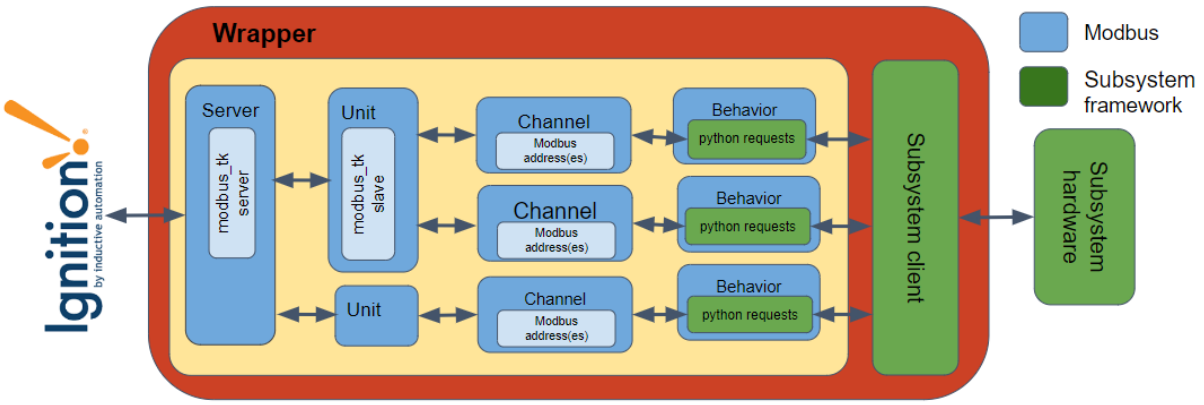

Figure 8.3: Schematic of the Modbus Generic Wrapper.

The Generic Wrapper structure is demonstrated in figure 8.3. It encapsulates the Modbus TCP implementation of the python *modbus_tk*[5] module in high level classes: the *Server*, holding a Modbus slave object which is the main server of the wrapper; the *Unit*, representing a Modbus unit; and the *Channel*, which manage the data with a set of Modbus registers. In this architecture, the Server

[5] `https://github.com/ljean/modbus-tk`

contains a list of as many Units are required, each with a list of Channel objects. Similarly to what happens in Modbus, a Channel of the Wrapper represents a set of registers, each with 16 bits. The amount and type of registers in a given channel are defined by the required data value to be communicated. However, in most cases of SC, either a Coil, for boolean data types, or a Holding register, for non-booleans, was implemented.

The key component of the Generic Wrapper is the interaction between the Channel and the associated Behavior class instance. The Behavior class has two main methods — *getValue* and *setValue* — to be coded for each implementation of the Wrapper. These methods, performing requests to the hardware, pair with the respective *Read Register* and *Write Register* of the associated Modbus Channel.

The configuration of the Wrapper is automatically generated by a table in a CSV file format, with each row representing a given channel. A row contains the necessary fields to configure the Modbus registers and to pass the required parameters of each Behavior class instance. This facilitates the task of implementing the Modbus protocol and allows the SC developers, to standardize the communication of the non-critical subsystems with Ignition.

One important use-case of the Wrapper consists in the communication with the HV Wiener crates of the PMTs. These crates communicate via SNMP, which Ignition is capable of supporting by purchasing an additional module. However, this module was not compatible with the float implementation of the Wiener crate, voiding is usability[6]. In this case the Wrapper was successfully used as a translator between SNMP, with Easy SNMP[7], and Modbus.

8.2 Ignition server

The Ignition software is a web-based platform to developed robust and complex SCADA systems, which in the LZ context, acts as gateway to centralize the subsystems of the experiment. Its architecture follows a modular approach, with various add-ons modules that can be installed to expand its functionalities. Out of the box, Inductive Automation offers modules to satisfy the most fundamental

[6] The SNMP module was still used to communicate with other important subsystems such as the UPS and the temperature monitoring system of the electronics racks.

[7] `https://easysnmp.readthedocs.io/en/latest/`

functionalities, to handle for example, SQL connections, the Historian mechanism, Alarm system, support for PROFIBUS and MODBUS communications with PLC and hardware modules, respectively, Auditing and Authentication. Ignition developers can also create custom modules to satisfy specific user-case requirements.

The access to Ignition is done through a Java applet, downloadable through the gateway, that can be launched in any personal computer. The communication between the user computer, the gateway, and the hardware is mediated by a Tag management system served. A Tag is the most basic block of data in the Ignition scope. These are essentially variables holding a given value with the standard data types (eg: bool, int, float, string). Ignition has many types of configurable tags, each with different functionalities. For example, there are “memory” tags holding a static value, SQL tags executing queries with a specific database and “expression” tags performing mathematical expressions on the values from other tags. However, the most important types of tags, denominated by OPC tags, are the ones connecting to the hardware. These are often referred to as “channels” from the SC perspective.

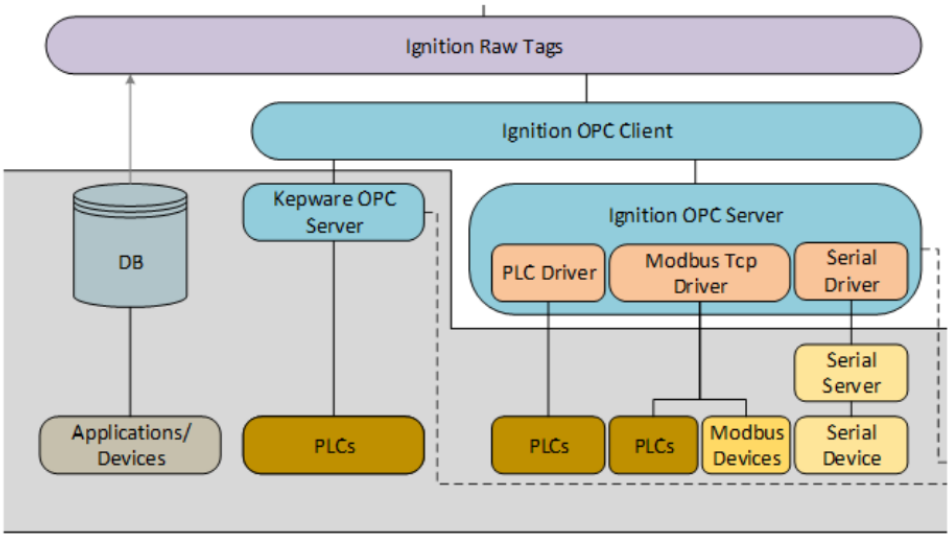

Figure 8.4: Diagram of the Ignition server architecture. Components outside the dark grey area are part of the Ignition server.

OPC is a specification for the transport and manipulation of data commonly used in the industry field. As shown in figure 8.4, the Ignition communication with the hardware is handled by an internal

connection between an OPC server and the respective client[8], with the drivers providing a bridge between the OPC and whatever protocol a given hardware handles. These internal drivers operate with asynchronous read and synchronous writes. Synchronous writable operations ensures that a command is sent to a device as soon as the communication channel is available. When an operators issues a write request to an OPC tag, it triggers a query to the channel of the hardware. The value and status of the write operation, is then returned to the OPC Client as soon as the hardware responds. The asynchronous Read operations are configured with an acquisition rate given by the scan class. A buffer in the OPC server mediates the communication between the OPC client and the hardware. When an OPC Client requests a tag value, the most recent value will be returned from the buffer. The actual tags exposed to the client UI or used internally by some kind of script/logic, such as alarms or automation scripts, are managed by an internal SQL database, represented by the "Ignition Raw Tags" block of figure 8.4.

In the Ignition implementation for the SC, an OPC Tags can be either a Sensor, that performs a read-only operation or a Control if performs read-write operations. Any given instrument, from the Ignition point of view, can be represented by a set of Sensors and Controls. For example, a solenoid valve connected to the PLC has 3 tags exposed to Ignition, two to open and close the valve and a Sensor tag to read the state.

8.2.1 UI development

The design of the Slow Control user interface was driven by the guidelines outlied in the "The High Performance HMI Handbook" [126]. Among many notions, the main philosophy is that "data is not information" in reference to display only the relevant data, as opposed to overwhelm the operators with excessive information which they would need to visually filter to assess the state of the system. Furthermore, this data should be presented without the presence of distracting elements such as unnecessary animations or 3D objects, sometimes used to represent the state of a given instrument or to represent the material of a pipeline. Visually simple components, with the historical data of a given set of variables, is enough for most cases. In addition to this, to prevent operator's visual

[8] To not be confused with a regular client notion, this OPC client only exists in the gateway and is not exposed to the "outside" world.

fatigue, the used colors should not present a high contrast unless indicating such as alarm states, where bright color should be used to attract attention.

Figure 8.5 shows, as an example, the panel used for the liquid nitrogen system. From the interface the operator can easily see the trend of important variables, such as the mass of LN in the dewars and COW[9], and the state of the solenoid valves (components with the shape of a bowtie: light grey=open, dark grey=close). The panel also contains the real time value of various sensors, such a temperature and pressures transducer, and the state of various electronic switches. When a given component triggers an alarm, it becomes hightailed with a color encoding a given priority (from low to high: yellow for Warning, orange for Alert, and red for Alert.)

The development of the panels required for a given system was guided by the expertise and input of the administrators and experts of that said system in a cycle of 3 dedicated meetings. In the first meeting the system is introduced to the SC developers to convey its requirements. The following iterations serve to present the ongoing development progress and obtain additional feedback by the experts.

After the final approval of the respective system owners, the individual panels were organized in a tree-like structure, presented in figure 8.6. This structure consists in a collection of various panels which the operator can browse through. This simplifies navigation, especially for novice users, as the complete slow control interface contains, at the moment of this writing, 50 GUI panels. These, organized in a tree view representing the subsystem LZ structure, contain the graphical components, such as buttons, plots and displays, required for a given operation.

[9] COW or Cryogen On Wheels, is a vessel that permits to supply the system with LN from the surface.

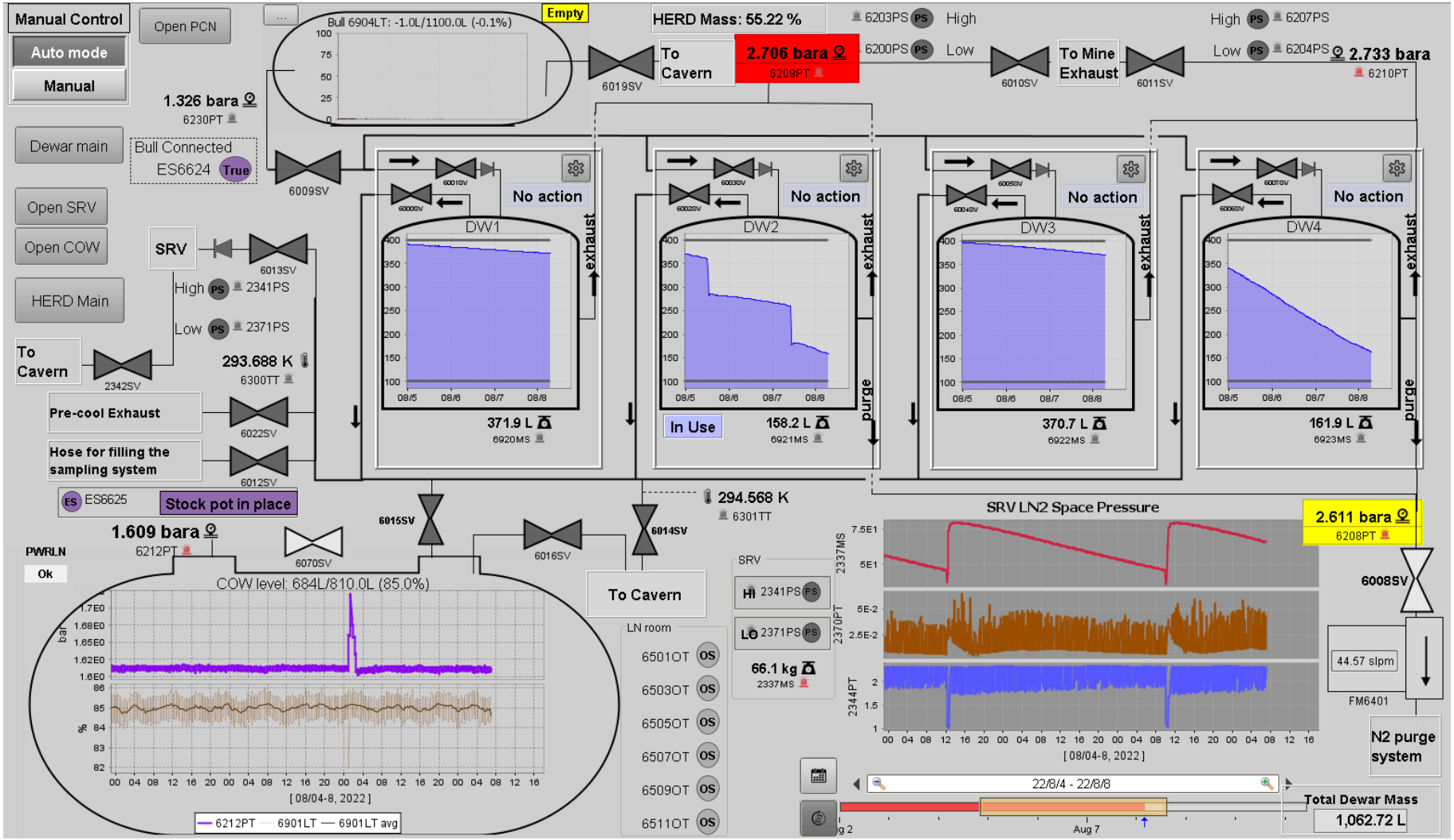

Figure 8.5: UI used to control and monitor the Liquid Nitrogen system.

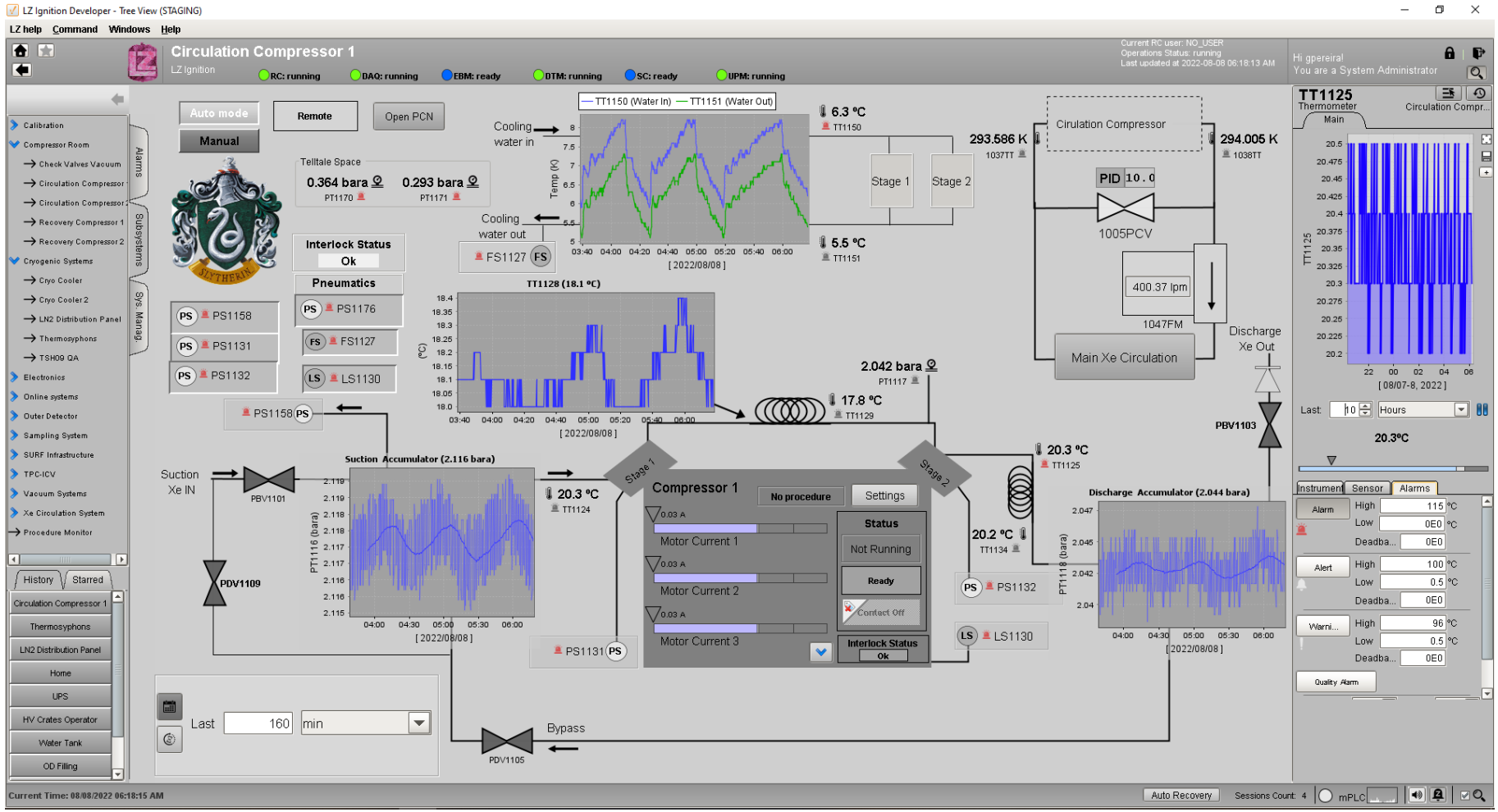

Figure 8.6: Generic structure of the SC UI. The header and the footer sections display minimal information, such as the state of the Online System and provides menus with additional functionalities of the interface like custom user settings, a tag filter browser. The left tree-view permits to navigate through the various system dedicated panels and other functionalities of the GUI to be presented in the main area. The right sidebar exhibits information for a given instrument selected by the user and provide the mean to configure the associated alarms. The main central area presents the UI panel for one of the circulation compressors.

8.3 Access Control

An important consideration in a SCADA system is security to, not only prevent the usage by unauthorized personal, but also to minimize the chances of human error. The later consideration is of most importance for a project, such as LZ, with many intricate systems. By default, every member of the LZ collaboration has read-only access to the system. Write access is only granted for the users which undergo a specific training. Since the training varies from subsystem to subsystem, the permissions structure requires a certain granularity such that a user can only access a specific set of channels associated with specific subsystems. Moreover, in terms of permissions, a subsystem has two types of users: experts, who manage the system and are, usually, more familiar with technical specifications and the operators, those responsible to use the system during an operation of the detector. This means that a user, with expert clearance on the High Voltage system, does not have control access over the LN system, for example. He or she must undergo the required training and be authorized by the respective LN system expert before being granted access. Furthermore, a system expert is only allowed to grant and revoke permissions related to his subsystem. Inevitably, this originated to the creation of an addition type of user tasked to assign and manage the permissions and configurations of the experts. Such superuser is dominated by Czar.

This role validation and user authentication is supported by Ignition through a connection with the Active Directory, powered by LDAP. However, to manage permissions of the operators, the experts of a system use a additional tool called “Role Manager”. This tool, developed by the LZ collaboration, is a web-based application that provides a layer between the interaction of the system expert and the LDAP server.

Figure 8.7 presents the UI of the Role Manager. This is connected to an HTTPS server, which in turn executes the LDAP queries. The user of the UI can select any account presented on the left list and manage its roles (or permissions) by moving the entries, with a double click action, between the “LZ Roles” and “Roles for:” tables. The alterations made to the permissions of various users are first cached in the UI so that they can be reviewed in the right panel before being committed to the Active Directory. The middle bottom table lists all users with the selected role.

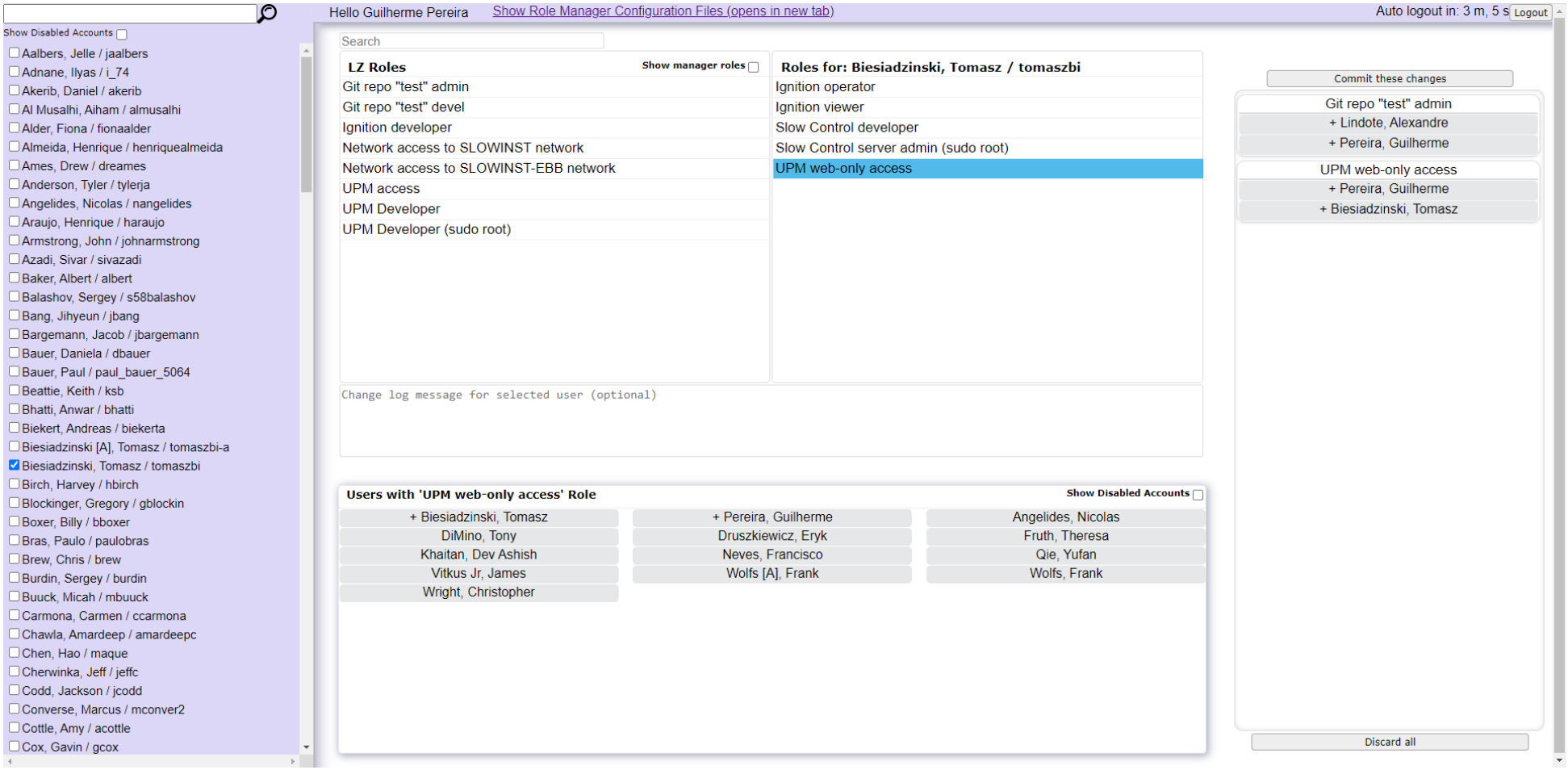

Figure 8.7: User interface of the Role Manager

8.4 Conclusions

The chapter presented an overview of the Slow Control system with an higher focus towards the SCADA system developed in the context of this thesis document. This system, embedded in the LZ network infrastructure, allows operators to control and monitor, through a user interface, the subsystems of the detector in a single centralized mainframe. At the time of this writing, the Ignition UI comprises more than 50 operations driven panels developed by the SC group. Also, in the context of this thesis, a software was developed to facilitate the integration of the subsystems without a standard communication solution.

Furthermore, in a partnership with the LZ IT group and also in the context of this thesis, the student developed a web-based UI application to facilitate the management of the security permissions of the LZ collaboration.

Chapter 9

Conclusions

The PhD work presented in this thesis, took place between March 2018 and November 2022, and was accomplished at the Laboratório de Instrumentação e Física Experimental de Partículas (LIP) at the Physics Department of the University of Coimbra within the scope of the LIP Dark Matter group participation in the LUX-ZEPLIN (LZ) Collaboration. This work presents my contributions to the design, commissioning, and the first science run of the LUX-ZEPLIN detector.

To achieve consistent analysis of the experimental data, it is very important to maintain stability of the detector output for extended periods of time. The first line of defense here is the experiment control and monitoring system that keeps the conditions within the detector stable most of the time. The unplanned periods of instabilities (due to, e.g., hardware failure) are excluded from the analysis based on the historical records of the detector parameters.

One of my responsibilities within the LZ Collaboration was development of the key elements of the experiment controls, including user interface, alarm system, scripting and automation, access control and historical trend visualizer. The user interface was implemented in compliance with the guidelines of efficient human-machine interface (HMI) design and can be roughly classified into two main groups: system control and process control. In total, more than 50 GUI panels, designed by

me or under my supervision and approved by the system experts, are currently being used in the detector operations. I was also responsible for the controls system integration with the experiment infrastructure, namely development of interfaces with run control, data acquisition system (DAQ), underground performance monitor (UPM) as well as with on-site environment and power monitoring infrastructure. Currently, the Ignition system, comprising nearly 20000 control and telemetry channels, is used as a primary user interface to control and monitor the detector and its supporting systems. As lead developer of the Slow Control group, I also participated in several critical tasks of the detector commissioning, such as testing of the circulation system, and supervision of the detector during the initial liquid xenon fill.

The consistency of the data recorded throughout the experiment lifetime is also ensured by regular calibrations. The LZ experiment extensive calibration program includes measurement of the PMT single photoelectron response with LEDs, and calibrations with external and injectable radioactive sources as well as with neutrons from a DD generator. While this is the standard technique used by many experiments, it has a couple of inherent problems:

1. the calibrations are typically time-consuming and interfere with the science data taking;
2. during an ongoing science acquisition, the detector parameters are estimated by interpolating the results of consecutive calibrations and, therefore, may deviate from the actual values.

In this PhD work I explored a concept of continuous calibration, i.e., calibrating the detector using the data acquired in the course of normal data taking. The continuous calibration does not strain to eliminate the standard calibration procedures, it rather complements them, allowing to monitor the stability of the detector parameters in the periods between the regular calibrations. Eventually, if consistency between the regular and continuous calibration is confirmed, the frequency of the periodic calibrations can be reduced leading to an improvement in the experiment duty cycle.

An additional personal responsibility within the LZ Collaboration was the development and maintenance of the data analysis chain component responsible for S2 position reconstruction. This required reconstruction of the detector light response model from the calibration data obtained with a ^{83m}Kr source. The applied techniques permit to achieve, as demonstrated, spatial resolution of 1.35±0.13

mm for 164 keV electron recoils.

In the scope of the continuous calibration, I also presented the possibility to recreate the detector light response model, to be used by position reconstruction algorithm, with background sources always present in the detector, namely ^{222}Rn α-particles and internal conversion electrons from ^{131m}Xe. We found that the usage of these background source results in an improved accuracy of the light response model of the detector due to a lower statistical fluctuation of their S1 and S2 signals compared to those of ^{83m}Kr. From this result, we realized that events produced by ^{222}Rn alpha particles and its progeny provide an excellent source to characterize the spatial dependency of the S1 and S2 signals.

In order to demonstrate the performance of the position reconstruction and the precision of the position-dependent S1 and S2 correction techniques developed in the course of this PhD work, I reconstructed the energy spectrum of the electronic recoils acquired in the range of [0.1, 2.8] MeV during the first science run of the LZ detector and studied its energy resolution. On this subject, I would like to highlight the parametrization of $\sigma/\mu = 32.1\sqrt{E}/E$ and the value of (0.67±0.01)% at 2614 keV for the full fiducial volume containing 5.6 tonnes of liquid xenon. To the best of my knowledge, this presents the best energy resolution for any liquid xenon TPC.

To further improve the reconstruction of the signal for long acquisition periods, I developed a framework to monitor the stability of the gain of the PMTs, using S2 light produced by single extracted electrons as a “standard candle”. Such an approach permits to minimize the effect of the PMTs’ gain drift on position and energy resolution of the detector without interfering with the normal data taking operations. Moreover, I designed a technique for monitoring of the PMTs linearity, namely assessment of their dynamic range and reconstruction of their saturation curve from the experimental data. This technique is paramount to improve the xy position reconstruction for high energy events.

The UPM – Underground Processing Monitor – is the primary system to monitor and analyze, in real-time, the data acquired by the PMTs of the detector. Chapter 7 describes this system with a higher focus on the web-based interface which allows the consultation of the data generated by the analysis algorithm. This interface is currently used on a daily basis during the operations of the detector.

Currently, the LZ detector has ended is first science run, producing world leading sensitivities for a dark matter search with an exposure of 330 tonnes$\times$days. The work developed in this thesis also demonstrated the excellent capabilities of the detector regarding energy and position reconstruction. Moreover, the various analysis framework and scripts already developed will also help to produce ongoing compelling results for the upcoming second science run.

References

[1] R. Caldwell and M. Kamionkowski, “Cosmology: Dark matter and dark energy,” *Nature*, vol. 458, no. 7238, pp. 587–589, 2009.

[2] A. Boyarsky, M. Drewes, T. Lasserre, S. Mertens, and O. Ruchayskiy, “Sterile neutrino Dark Matter,” *Progress in Particle and Nuclear Physics*, vol. 104, pp. 1–45, 2018.

[3] F. S. Queiroz, “Dark Matter Overview: Collider, Direct and Indirect Detection Searches,” no. i, 2016. [Online]. Available: http://arxiv.org/abs/1605.08788

[4] R. Agnese *et al.*, “Silicon detector results from the first five-tower run of CDMS II,” *Physical Review D - Particles, Fields, Gravitation and Cosmology*, vol. 88, no. 3, pp. 1–5, 2013.

[5] G. Angloher *et al.*, “Results from 730 kg days of the CRESST-II Dark Matter search,” *European Physical Journal C*, vol. 72, no. 4, pp. 1–22, 2012.

[6] R. Bernabei *et al.*, “The DAMA project: Achievements, implications and perspectives,” *Progress in Particle and Nuclear Physics*, vol. 114, 2020.

[7] G. Cao, “Electron Recoils in the PICO Direct Dark Matter Detection Experiment,” Ph.D. dissertation, Queen’s University, 2019.

[8] E. Daw *et al.*, “The DRIFT Directional Dark Matter Experiments,” *EAS Publications Series*, vol. 53, no. October, pp. 11–18, 2012.

[9] J. Amaré *et al.*, “First Results on Dark Matter Annual Modulation from the ANAIS-112 Experiment,” *Physical Review Letters*, vol. 123, no. 3, pp. 1–6, 2019.

[10] E. Aprile *et al.*, “The XENON1T dark matter experiment,” *European Physical Journal C*, vol. 77, no. 12, pp. 1–23, 2017.

[11] Y. Meng *et al.*, “Dark Matter Search Results from the PandaX-4T Commissioning Run,” *Physical Review Letters*, vol. 127, no. 26, p. 261802, 2021. [Online]. Available: https://doi.org/10.1103/PhysRevLett.127.261802

[12] D. S. Akerib *et al.*, “The LUX-ZEPLIN (LZ) experiment,” *Nuclear Instruments and Methods in Physics Research, Section A: Accelerators, Spectrometers, Detectors and Associated Equipment*, vol. 953, no. October 2019, 2020.

[13] V. Chepel and H. Araújo, “Liquid noble gas detectors for low energy particle physics,” *Journal of Instrumentation*, vol. 8, no. 4, 2013.

[14] J. Aalbers *et al.*, “First Dark Matter Search Results from the LUX-ZEPLIN (LZ) Experiment,” vol. 33, 2022. [Online]. Available: http://arxiv.org/abs/2207.03764

[15] M. J. Dolinski, A. W. P. Poon, and W. Rodejohann, “Neutrinoless Double-Beta Decay : Status and Prospects,” 2019.

[16] V. N. Solovov *et al.*, “Position Reconstruction in a Dual Phase Xenon Scintillation Detector,” *IEEE Transactions on Nuclear Science*, vol. 59, no. 6, pp. 3286–3293, Dec. 2012.

[17] D. S. Akerib *et al.*, “Position Reconstruction in LUX,” *JINST*, vol. 13, no. 02, p. P02001, 2018.

[18] V. Solovov, A. Morozov, V. Chepel, V. Domingos, and R. Martins, “B-spline parameterization of spatial response in a monolithic scintillation camera,” *Journal of Instrumentation*, vol. 11, no. 9, 2016.

[19] D. S. Akerib and other, “Kr 83 m calibration of the 2013 LUX dark matter search,” *Physical Review D*, vol. 96, no. 11, pp. 1–11, 2017.

[20] Hamamatsu Photonics K. K., *Photomultiplier Tubes: Basics and Applications*, 2015, vol. 30, no. 4. [Online]. Available: http://search.jamas.or.jp/link/ui/2015332641

[21] S. G. Fedosin, “The virial theorem and the kinetic energy of particles of a macroscopic system in the general field concept,” *Continuum Mechanics and Thermodynamics*, vol. 29, no. 2, pp. 361–371, 2017.

[22] F. Zwicky, “The redshift of extragalactic nebulae,” *Helvetica Physica Acta*, vol. 6, pp. 110–127, 1933.

[23] H. Andernach, “English and spanish translation of zwicky’s (1933) the redshift of extragalactic nebulae,” 2017. [Online]. Available: https://arxiv.org/abs/1711.01693

[24] E. ZWICKY, “On the masses of nebulae and of clusters of nebulae,” *Zhurnal Eksperimental’noi i Teoreticheskoi Fiziki*, vol. 86, no. 3, pp. 21–34, 1937.

[25] K. A. Pimbblet, S. J. Penny, and R. L. Davies, “How typical is the Coma cluster?” *Monthly Notices of the Royal Astronomical Society*, vol. 438, no. 4, pp. 3049–3057, 2014.

[26] J. M. Kubo *et al.*, “The Mass of the Coma Cluster from Weak Lensing in the Sloan Digital Sky Survey,” *The Astrophysical Journal*, vol. 671, no. 2, pp. 1466–1470, 2007.

[27] J. liang Zhao, S. nian Huang, R. shi Pan, and Y. ping dHe, “Studies on the coma cluster. iii. the virial mass and kinematics,” *Chinese Astronomy and Astrophysics*, vol. 15, no. 3, pp. 260–269, 1991. [Online]. Available: https://www.sciencedirect.com/science/article/pii/027510629190020X

[28] Planck Collaboration, Aghanim, N. *et al.*, “Planck 2018 results - i. overview and the cosmological legacy of planck,” *A&A*, vol. 641, p. A1, 2020. [Online]. Available: https://doi.org/10.1051/0004-6361/201833880

[29] M. Weber and W. De Boer, “Determination of the local dark matter density in our galaxy,” *Astronomy and Astrophysics*, vol. 509, no. 1, 2010.

[30] R. Scarpa, “Modified Newtonian dynamics, an introductory review,” *AIP Conference Proceedings*, vol. 822, pp. 253–265, 2006.

[31] G. Eric and J. Silk, “The Cosmic Microwave Background Radiation,” *Annals of the New York Academy of Sciences*, vol. 375, no. 1, pp. 188–209, 1981.

[32] N. Aghanim *et al.*, “Planck 2013 results. XVI. Cosmological parameters,” *Astronomy & Astrophysics*, vol. 16, 2014.

[33] B. Bassett and R. Hlozek, “Baryon Acoustic Oscillations,” *Astrophysics and Space Science Proceedings*, no. 202459, pp. 141–145, 2009.

[34] A. Dobi, “Measurement of the electronic recoil band of the LUX dark matter detector with a tritium calibration source,” Ph.D. dissertation, 2014.

[35] D. J. Eisenstein, H. Seo, and M. White, “On the Robustness of the Acoustic Scale in the Low-Redshift Clustering of Matter,” *The Astrophysical Journal*, vol. 664, no. 2, pp. 660–674, 2007.

[36] D. Clowe, M. Bradač, A. H. Gonzalez, M. Markevitch, S. W. Randall, C. Jones, and D. Zaritsky, “A Direct Empirical Proof of the Existence of Dark Matter,” *The Astrophysical Journal*, vol. 648, no. 2, pp. L109–L113, 2006.

[37] M. Battaglieri *et al.*, “US Cosmic Visions: New Ideas in Dark Matter 2017: Community Report,” 2017. [Online]. Available: http://arxiv.org/abs/1707.04591

[38] M. Loewenstein and A. Kusenko, “Dark matter search using XMM-newton observations of Willman 1,” *Astrophysical Journal*, vol. 751, no. 2, pp. 1–9, 2012.

[39] S. Knapen, T. Lin, and K. M. Zurek, “Light dark matter: Models and constraints,” *Physical Review D*, vol. 96, no. 11, pp. 1–26, 2017.

[40] L. D. Duffy and K. Van Bibber, “Axions as dark matter particles,” *New Journal of Physics*, vol. 11, 2009.

[41] A. M. Sirunyan *et al.*, “Search for dark matter produced in association with a single top quark or a top quark pair in proton-proton collisions at $\sqrt{s}$=13 TeV,” *Journal of High Energy Physics*, vol. 2019, no. 3, 2019.

[42] Y. Bai, P. J. Fox, and R. Harnik, “The Tevatron at the frontier of dark matter direct detection,” *Journal of High Energy Physics*, vol. 2010, no. 12, 2010.

[43] A. Albert *et al.*, “Searching for dark matter annihilation in recently discovered milky way satellites with fermi-lat,” *The Astrophysical Journal*, vol. 834, no. 2, p. 110, jan 2017. [Online]. Available: https://doi.org/10.3847/1538-4357/834/2/110

[44] M. Schumann, “Direct detection of WIMP dark matter: Concepts and status,” *Journal of Physics G: Nuclear and Particle Physics*, vol. 46, no. 10, 2019.

[45] D. Hooper, J. I. Collar, J. Hall, D. McKinsey, and C. M. Kelso, “Consistent dark matter interpretation for CoGeNT and DAMA/LIBRA,” *Physical Review D - Particles, Fields, Gravitation and Cosmology*, vol. 82, no. 12, pp. 1–8, 2010.

[46] D. S. Akerib *et al.*, “Results on the spin-dependent scattering of weakly interacting massive particles on nucleons from the run 3 data of the lux experiment,” *Phys. Rev. Lett.*, vol. 116, p. 161302, Apr 2016. [Online]. Available: https://link.aps.org/doi/10.1103/PhysRevLett.116.161302

[47] J. I. Read, “The local dark matter density,” *Journal of Physics G: Nuclear and Particle Physics*, vol. 41, no. 6, p. 063101, may 2014. [Online]. Available: https://doi.org/10.1088/0954-3899/41/6/063101

[48] T. M. Undagoitia and L. Rauch, “Dark matter direct-detection experiments,” *Journal of Physics G: Nuclear and Particle Physics*, vol. 43, no. 1, 2015.

[49] R. Agnese *et al.*, “Improved WIMP-search reach of the CDMS II germanium data,” *Physical Review D - Particles, Fields, Gravitation and Cosmology*, vol. 92, no. 7, p. 72003, 2015. [Online]. Available: https://doi.org/10.1103/PhysRevD.92.072003

[50] V. Mandic *et al.*, “Position dependence in the CDMS II ZIP detectors,” vol. 509, no. March 2002, pp. 509–512, 2003.

[51] D. Amaral, T. Aralis, T. Aramaki, I. Arnquist, E. Azadbakht, S. Banik, D. Barker, C. Bathurst, D. Bauer, L. Bezerra *et al.*, “Constraints on low-mass, relic dark matter candidates from a surface-operated supercdms single-charge sensitive detector,” *Physical Review D*, vol. 102, no. 9, p. 091101, 2020.

[52] M. Bravin *et al.*, "The CRESST dark matter search," *Astroparticle Physics*, vol. 12, no. 1-2, pp. 107–114, 1999.

[53] A. H. Abdelhameed and other, "First results from the CRESST-III low-mass dark matter program," *Physical Review D*, vol. 100, no. 10, p. 102002, 2019. [Online]. Available: https://doi.org/10.1103/PhysRevD.100.102002

[54] R. Neilson, "PICO: Current Status and Future Plans," in *APS April Meeting 2020*, 2020. [Online]. Available: https://meetings.aps.org/Meeting/APR20/Session/C13.5

[55] R. W. Schnee, *Introduction to dark matter experiments*, 2011, no. March.

[56] J. B. Battat *et al.*, "Low threshold results and limits from the DRIFT directional dark matter detector," *Astroparticle Physics*, vol. 91, pp. 65–74, 2017. [Online]. Available: http://dx.doi.org/10.1016/j.astropartphys.2017.03.007

[57] B. A. Dolgoshein, V. N. Lebedenko, and B. U. Rodionov, "New Method of Registration of Ionizing-particle Tracks in Condensed Matter," *Soviet Journal of Experimental and Theoretical Physics Letters*, vol. 11, p. 351, Jun. 1970.

[58] D. Y. Akimov *et al.*, "The ZEPLIN-III dark matter detector: Instrument design, manufacture and commissioning," *Astroparticle Physics*, vol. 27, no. 1, pp. 46–60, 2007.

[59] E. Aprile *et al.*, "The XENON100 dark matter experiment," *Astroparticle Physics*, vol. 35, no. 9, pp. 573–590, 2012.

[60] D. S. Akerib *et al.*, "First results from the LUX dark matter experiment at the sanford underground research facility," *Physical Review Letters*, vol. 112, no. 9, pp. 1–7, 2014.

[61] G. J. Alner, H. M. Araújo, A. Bewick, C. Bungau, B. Camanzi, M. J. Carson, R. J. Cashmore, H. Chagani, V. Chepel, D. Cline, D. Davidge, J. C. Davies, E. Daw, J. Dawson, T. Durkin, B. Edwards, T. Gamble, J. Gao, C. Ghag, A. S. Howard, W. G. Jones, M. Joshi, E. V. Korolkova, V. A. Kudryavtsev, T. Lawson, V. N. Lebedenko, J. D. Lewin, P. Lightfoot, A. Lindote, I. Liubarsky, M. I. Lopes, R. Lüscher, P. Majewski, K. Mavrokoridis, J. E. McMillan, B. Morgan, D. Muna, A. S. J. Murphy, F. Neves, G. G. Nicklin, W. Ooi, S. M. Paling, J. Pinto da Cunha, S. J. Plank,

R. M. Preece, J. J. Quenby, M. Robinson, G. Salinas, F. Sergiampietri, C. Silva, V. N. Solovov, N. J. Smith, P. F. Smith, N. J. Spooner, T. J. Sumner, C. Thorne, D. R. Tovey, E. Tziaferi, R. J. Walker, H. Wang, J. T. White, and F. L. Wolfs, "First limits on WIMP nuclear recoil signals in ZEPLIN-II: A two-phase xenon detector for dark matter detection," *Astroparticle Physics*, vol. 28, no. 3, pp. 287–302, 2007.

[62] J. Angle *et al.*, "First results from the XENON10 dark matter experiment at the gran sasso national laboratory," *Physical Review Letters*, vol. 100, no. 2, pp. 1–5, 2008.

[63] D. Y. Akimov *et al.*, "WIMP-nucleon cross-section results from the second science run of ZEPLIN-III," *Physics Letters, Section B: Nuclear, Elementary Particle and High-Energy Physics*, vol. 709, no. 1-2, pp. 14–20, 2012. [Online]. Available: http://dx.doi.org/10.1016/j.physletb.2012.01.064

[64] E. Aprile *et al.*, "XENON100 dark matter results from a combination of 477 live days," *Physical Review D*, vol. 94, no. 12, pp. 1–12, 2016.

[65] D. S. Akerib *et al.*, "Results from a Search for Dark Matter in the Complete LUX Exposure," *Physical Review Letters*, vol. 118, no. 2, pp. 1–8, 2017.

[66] D. Y. Akimov *et al.*, "The ZEPLIN-III anti-coincidence veto detector," *Astroparticle Physics*, vol. 34, no. 3, pp. 151–163, 2010. [Online]. Available: http://dx.doi.org/10.1016/j.astropartphys.2010.06.010

[67] E. Aprile *et al.*, "Observation of two-neutrino double electron capture in 124Xe with XENON1T," *Nature*, vol. 568, no. 7753, pp. 532–535, 2019.

[68] D. S. Akerib *et al.*, "The Large Underground Xenon (LUX) experiment," *Nuclear Instruments and Methods in Physics Research, Section A: Accelerators, Spectrometers, Detectors and Associated Equipment*, vol. 704, pp. 111–126, 2013. [Online]. Available: http://dx.doi.org/10.1016/j.nima.2012.11.135

[69] M. C. Carmona-Benitez *et al.*, "First Results of the LUX Dark Matter Experiment," *Nuclear and Particle Physics Proceedings*, vol. 273-275, pp. 309–313, 2016.

[70] K. Ni *et al.*, “PandaX Dark Matter Experiment: from PandaX-I to PandaX-II,” pp. 24–29, 2009.

[71] H. G. Zhang *et al.*, “Dark matter direct search sensitivity of the PandaX-4T experiment,” *Science China: Physics, Mechanics and Astronomy*, vol. 62, no. 3, 2019.

[72] N. Ackerman *et al.*, “Observation of two-neutrino double-beta decay in Xe136 with the EXO-200 detector,” *Physical Review Letters*, vol. 107, no. 21, pp. 1–5, 2011.

[73] B. J. Mount *et al.*, “Lux-zeplin (lz) technical design report,” 2017.

[74] D. S. Akerib *et al.*, “Projected WIMP sensitivity of the LUX-ZEPLIN dark matter experiment,” *Physical Review D*, vol. 101, no. 5, pp. 1–17, 2020.

[75] F. Neves *et al.*, “Measurement of the absolute reflectance of polytetrafluoroethylene (PTFE) immersed in liquid xenon,” *Journal of Instrumentation*, vol. 12, no. 1, 2017.

[76] E. Aprile *et al.*, “Material screening and selection for XENON100,” *Astroparticle Physics*, vol. 35, no. 2, pp. 43–49, 2011.

[77] D. Akerib *et al.*, “Signal yields, energy resolution, and recombination fluctuations in liquid xenon,” *Physical Review D*, vol. 95, no. 1, Jan 2017. [Online]. Available: http://dx.doi.org/10.1103/PhysRevD.95.012008

[78] V. Chepel, M. I. Lopes, and V. Solovov, “Primary scintillation yield and α/β ratio in liquid xenon,” *Radiation Physics and Chemistry*, vol. 74, no. 3-4, pp. 160–167, 2005.

[79] E. Aprile and T. Doke, “Liquid xenon detectors for particle physics and astrophysics,” *Reviews of Modern Physics*, vol. 82, no. 3, pp. 2053–2097, 2010.

[80] R. Linehan *et al.*, “Design and production of the high voltage electrode grids and electron extraction region for the LZ dual-phase xenon time projection chamber,” *Nuclear Instruments and Methods in Physics Research, Section A: Accelerators, Spectrometers, Detectors and Associated Equipment*, no. September, 2021.

[81] D. Carter, “Photomultiplier handbook: Theory, design, application,” *Burle Industries, Inc., Lancaster, PA*, 1980.

[82] R. L. Platzman, "Total ionization in gases by high-energy particles: An appraisal of our understanding," *The International Journal Of Applied Radiation And Isotopes*, vol. 10, no. 2-3, pp. 116–127, 1961.

[83] M. Szydagis, N. Barry, K. Kazkaz, J. Mock, D. Stolp, M. Sweany, M. Tripathi, S. Uvarov, N. Walsh, and M. Woods, "NEST: A comprehensive model for scintillation yield in liquid xenon," *Journal of Instrumentation*, vol. 6, no. 10, 2011.

[84] P. Sorensen and C. E. Dahl, "Nuclear recoil energy scale in liquid xenon with application to the direct detection of dark matter," *Physical Review D - Particles, Fields, Gravitation and Cosmology*, vol. 83, no. 6, pp. 1–6, 2011.

[85] B. Lenardo, K. Kazkaz, A. Manalaysay, J. Mock, M. Szydagis, and M. Tripathi, "A Global Analysis of Light and Charge Yields in Liquid Xenon," *IEEE Transactions on Nuclear Science*, vol. 62, no. 6, pp. 3387–3396, 2015.

[86] J. R. Wilson, "An Experimental Review of Solar Neutrinos," in *Topical Research Meeting on Prospects in Neutrino Physics*, 4 2015.

[87] J. N. Bahcall, "Solar neutrinos. i. theoretical," *Phys. Rev. Lett.*, vol. 12, pp. 300–302, Mar 1964. [Online]. Available: https://link.aps.org/doi/10.1103/PhysRevLett.12.300

[88] J. N. Abdurashitov *et al.*, "Measurement of the solar neutrino capture rate with gallium metal. III. Results for the 2002-2007 data-taking period," *Physical Review C - Nuclear Physics*, vol. 80, no. 1, pp. 1–16, 2009.

[89] G. Bellini *et al.*, "Neutrinos from the primary proton-proton fusion process in the Sun," *Nature*, vol. 512, no. 7515, pp. 383–386, 2014. [Online]. Available: http://dx.doi.org/10.1038/nature13702

[90] S. Chakraborty, P. Bhattacharjee, and K. Kar, "Observing supernova neutrino light curve in future dark matter detectors," *Physical Review D - Particles, Fields, Gravitation and Cosmology*, vol. 89, no. 1, pp. 1–8, 2014.

[91] D. Khaitan, “Supernova neutrino detection in lz,” *Journal of Instrumentation*, vol. 13, no. 02, pp. C02 024–C02 024, feb 2018. [Online]. Available: https://doi.org/10.1088/1748-0221/13/02/c02024

[92] P. Bras, “SENSITIVITY TO THE 0vbb DECAY OF Xe136 AND DEVELOPMENT OF MACHINE LEARNING TOOLS FOR PULSE CLASSIFICATION FOR THE LUX-ZEPLIN EXPERIMENT,” Ph.D. dissertation, Universidade de Coimbra, 2020.

[93] K. Arisaka, P. Beltrame, C. Ghag, J. Kaidi, K. Lung, A. Lyashenko, R. D. Peccei, P. Smith, and K. Ye, “Expected sensitivity to galactic/solar axions and bosonic super-WIMPs based on the axio-electric effect in liquid xenon dark matter detectors,” *Astroparticle Physics*, vol. 44, pp. 59–67, 2013.

[94] D. S. Akerib *et al.*, “The LUX-ZEPLIN (LZ) radioactivity and cleanliness control programs,” *European Physical Journal C*, vol. 80, no. 11, 2020.

[95] A. Dobi, C. Davis, C. Hall, T. Langford, S. Slutsky, and Y. R. Yen, “Detection of krypton in xenon for dark matter applications,” *Nuclear Instruments and Methods in Physics Research, Section A: Accelerators, Spectrometers, Detectors and Associated Equipment*, vol. 665, pp. 1–6, 2011. [Online]. Available: http://dx.doi.org/10.1016/j.nima.2011.11.043

[96] S. J. Haselschwardt *et al.*, “A liquid scintillation detector for radioassay of gadolinium-loaded liquid scintillator for the LZ Outer Detector,” *Nuclear Instruments and Methods in Physics Research, Section A: Accelerators, Spectrometers, Detectors and Associated Equipment*, vol. 937, no. November 2018, pp. 148–163, 2019. [Online]. Available: https://doi.org/10.1016/j.nima.2019.05.055

[97] LUX Collaboration, Akerib *et al.*, “Low-energy (0.7-74 keV) nuclear recoil calibration of the LUX dark matter experiment using D-D neutron scattering kinematics,” pp. 1–24, 2016. [Online]. Available: http://arxiv.org/abs/1608.05381

[98] E. Druszkiewicz, “The Data Acquisition System for LZ,” *Journal of Instrumentation*, vol. 11, no. 2, pp. 1–6, 2016.

[99] “Ice, a comprehensive rpc framework,” https://zeroc.com/, accessed: 2022-10-19.

[100] R. M. Gray and A. Macovski, “Maximum a posteriori estimation of position in scintillation cameras,” *IEEE Transactions on Nuclear Science*, vol. 23, no. 1, pp. 849–852, 1976.

[101] U. Simola, B. Pelssers, D. Barge, J. Conrad, and J. Corander, “Machine learning accelerated likelihood-free event reconstruction in dark matter direct detection,” *Journal of Instrumentation*, vol. 14, no. 03, p. P03004–P03004, Mar 2019. [Online]. Available: http://dx.doi.org/10.1088/1748-0221/14/03/P03004

[102] H. O. Anger, “Scintillation camera,” *Review of Scientific Instruments*, vol. 29, no. 1, pp. 27–33, 1958.

[103] B. Pelssers, “Position Reconstruction and Data Quality in XENON,” Ph.D. dissertation, University of Utrecht, 2015.

[104] H. H. Barrett, W. C. Hunter, B. W. Miller, S. K. Moore, Y. Chen, and L. R. Furenlid, “Maximum-likelihood methods for processing signals from gamma-ray detectors,” *IEEE transactions on nuclear science*, vol. 56, no. 3, pp. 725–735, 2009.

[105] J. B. Albert *et al.*, “Measurement of the drift velocity and transverse diffusion of electrons in liquid xenon with the EXO-200 detector,” *Physical Review C*, vol. 95, no. 2, pp. 1–8, 2017.

[106] D. S. Akerib *et al.*, “Simulations of events for the LUX-ZEPLIN (LZ) dark matter experiment,” *Astroparticle Physics*, vol. 125, 2021.

[107] J. Marcos, “Self-calibrating compact gamma camera for real-time medical imaging,” Ph.D. dissertation, Universidade de Coimbra, 2020. [Online]. Available: http://hdl.handle.net/10316/93193

[108] A. Morozov, V. Solovov, F. Alves, V. Domingos, R. Martins, F. Neves, and V. Chepel, “Iterative reconstruction of detector response of an anger gamma camera,” *Physics in Medicine and Biology*, vol. 60, no. 10, pp. 4169–4184, may 2015. [Online]. Available: https://doi.org/10.1088/0031-9155/60/10/4169

[109] E. Aprile, R. Mukherjee, and M. Suzuki, “Ionization of liquid xenon by 241am and 210po alpha particles,” *Nuclear Instruments and Methods in Physics Research Section A: Accelerators,*

Spectrometers, Detectors and Associated Equipment, vol. 307, no. 1, pp. 119–125, 1991. [Online]. Available: https://www.sciencedirect.com/science/article/pii/016890029190138G

[110] L. Baudis, P. Sanchez-Lucas, and K. Thieme, "A measurement of the mean electronic excitation energy of liquid xenon," *Eur. Phys. J. C*, vol. 81, no. 12, p. 1060, 2021.

[111] L. N. H. Becquerel, "Library for gamma and alpha emissions." [Online]. Available: http://www.nucleide.org/Laraweb/index.php

[112] D. S. Akerib *et al.*, "Ultralow energy calibration of LUX detector using Xe 127 electron capture," *Physical Review D*, vol. 96, no. 11, pp. 1–10, 2017.

[113] G. Cowan, *Statistical data analysis*. Oxford university press, 1998.

[114] C. Faham, "Prototype, Surface Commissioning and Photomultiplier Tube Characterization for the Large Underground Xenon (LUX) Direct Dark Matter Search Experiment," 2014.

[115] E. Aprile *et al.*, "Energy resolution and linearity of XENON1T in the MeV energy range," *European Physical Journal C*, vol. 80, no. 8, pp. 1–9, 2020.

[116] D. S. Akerib *et al.*, "Projected sensitivity of the LUX-ZEPLIN experiment to the $0\nu\beta\beta$ decay of ^{136}Xe," *Phys. Rev. C*, vol. 102, no. 1, p. 014602, 2020.

[117] K. Lung, K. Arisaka, A. Bargetzi, P. Beltrame, A. Cahill, T. Genma, C. Ghag, D. Gordon, J. Sainz, A. Teymourian, and Y. Yoshizawa, "Characterization of the Hamamatsu R11410-10 3-in. photomultiplier tube for liquid xenon dark matter direct detection experiments," *Nuclear Instruments and Methods in Physics Research, Section A: Accelerators, Spectrometers, Detectors and Associated Equipment*, vol. 696, pp. 32–39, 2012.

[118] M. Tan Supervisor and R. Gaitskell, "Linearity of the Hamamatsu R11410 Photomultipler Tube at Cryogenic Temperatures for the LUX-ZEPLIN Experiment," 2018.

[119] F. Neves *et al.*, "Calibration of photomultiplier arrays," *Astroparticle Physics*, vol. 33, no. 1, pp. 13–18, 2010. [Online]. Available: http://dx.doi.org/10.1016/j.astropartphys.2009.10.004

[120] J. F. M. d. Silva, "Development of the underground processing monitor for lz," Ph.D. dissertation, Universidade de Coimbra, 2020.

[121] “Profibus,” https://new.siemens.com/global/en/products/automation/industrial-communication/profibus.html, accessed: 2022-11-01.

[122] Modicon, “Modicon Modbus Protocol Reference Guide,” p. 115, 1996.

[123] J. D. Case, M. Fedor, M. L. Schoffstall, and J. Davin, “Rfc1157: Simple network management protocol (snmp),” 1990.

[124] “Modbus in a nutshell,” https://blog.gridconnect.com/topic/modbus-explained, accessed: 2022-10-05.

[125] Modbus Organization, “MODBUS Messaging on TCP/IP Implementation Guide V1.0b Modbus Organization,” pp. 1–46, 2006.

[126] B. Hollifield, “The high performance hmi,” *System*, 2012.

List of Figures

List of Tables

Attachments

Appendix A

Position reconstruction

This appendix presents additional plots regarding the position reconstruction results in LZ.

Figure A.1 shows the distribution of the TPC PMTs of the top and bottom arrays.

Figure A.2 and A.3 present 2D histograms with the xy distribution of ^{131m}Xe events acquired during the first science run. Each histogram maps a different region in the z-axis to demonstrate the dependency of peripheral dents with the event depth.

Figure A.4 shows the energy spectrum of regions in the TPC isolated with a circular cut in xy. The spectrum in blue presents events of the hotspot centered at (-700 mm, 40 mm) and the spectrum in orange provides a reference using a different region of the detctor.

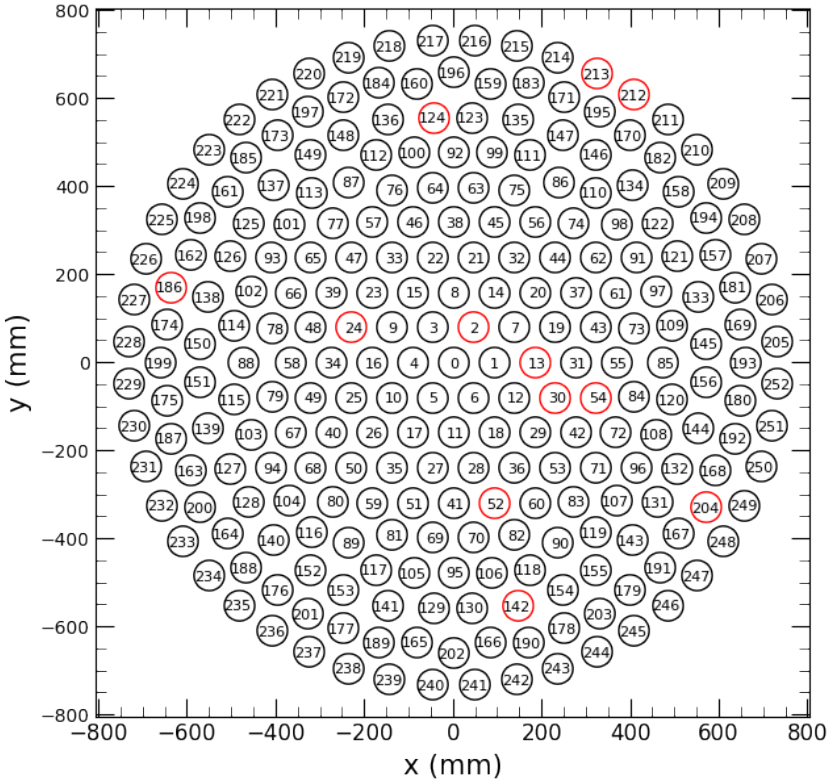

(a) Top

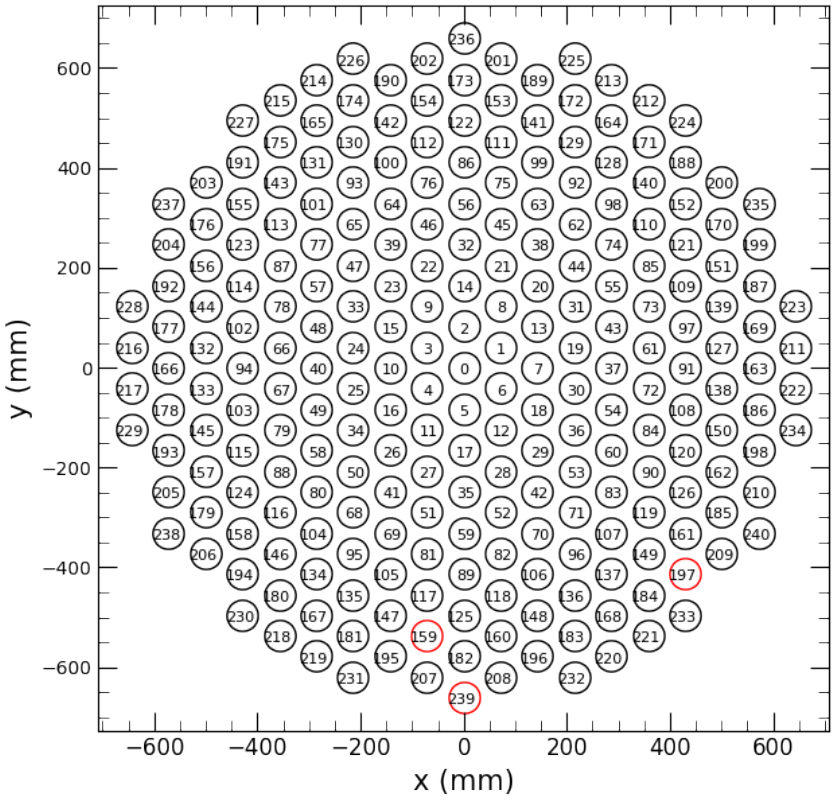

(b) Bottom

Figure A.1: Distribution of the PMT in the top and bottom array of the LZ detector. The PMTs represented by a red circle were disabled during the first science run.

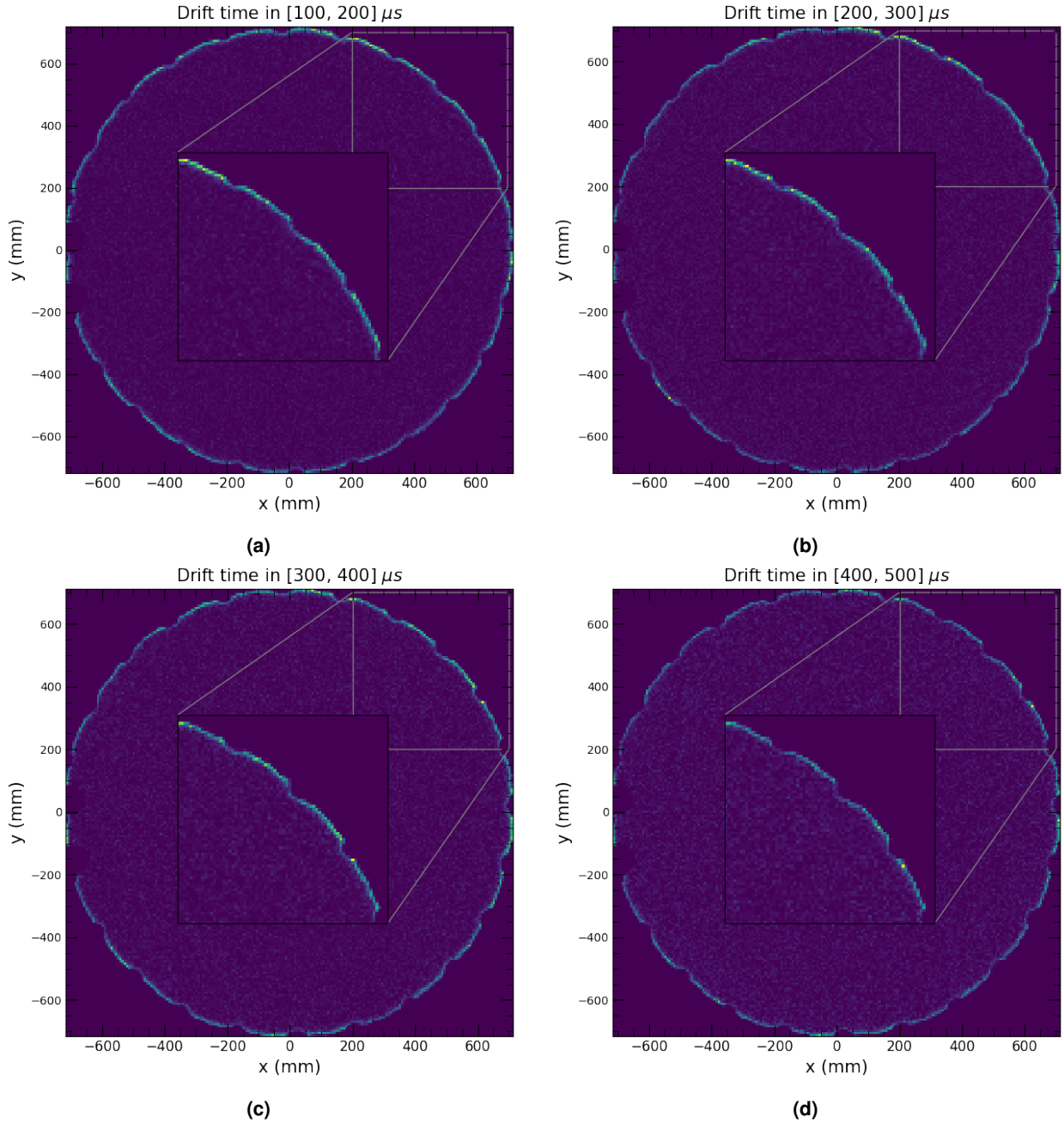

Figure A.2: Histogram of the position reconstruction for ^{131m}Xe events at different drift time.

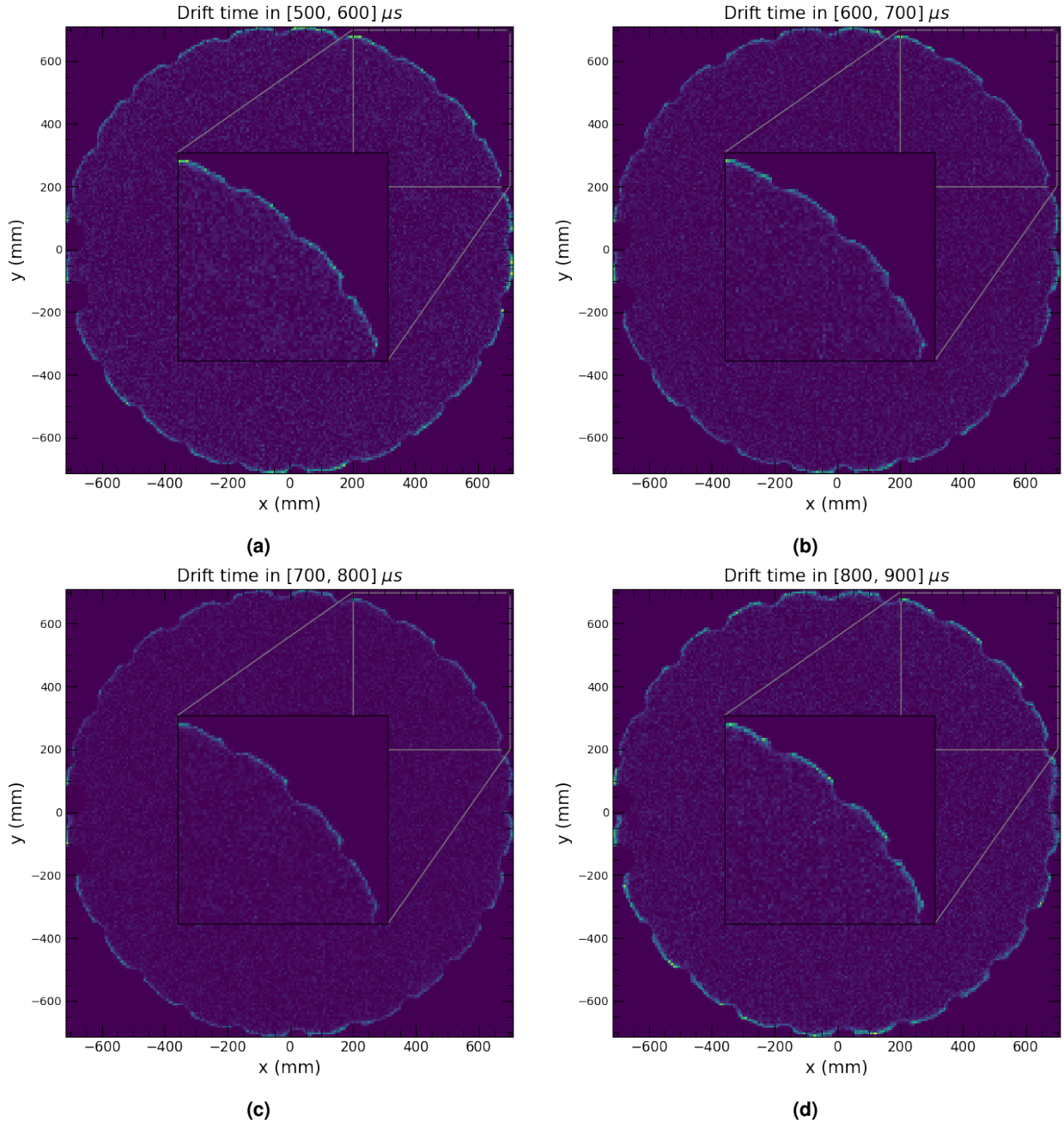

Figure A.3: Histogram of the position reconstruction for ^{131m}Xe events at different drift time.

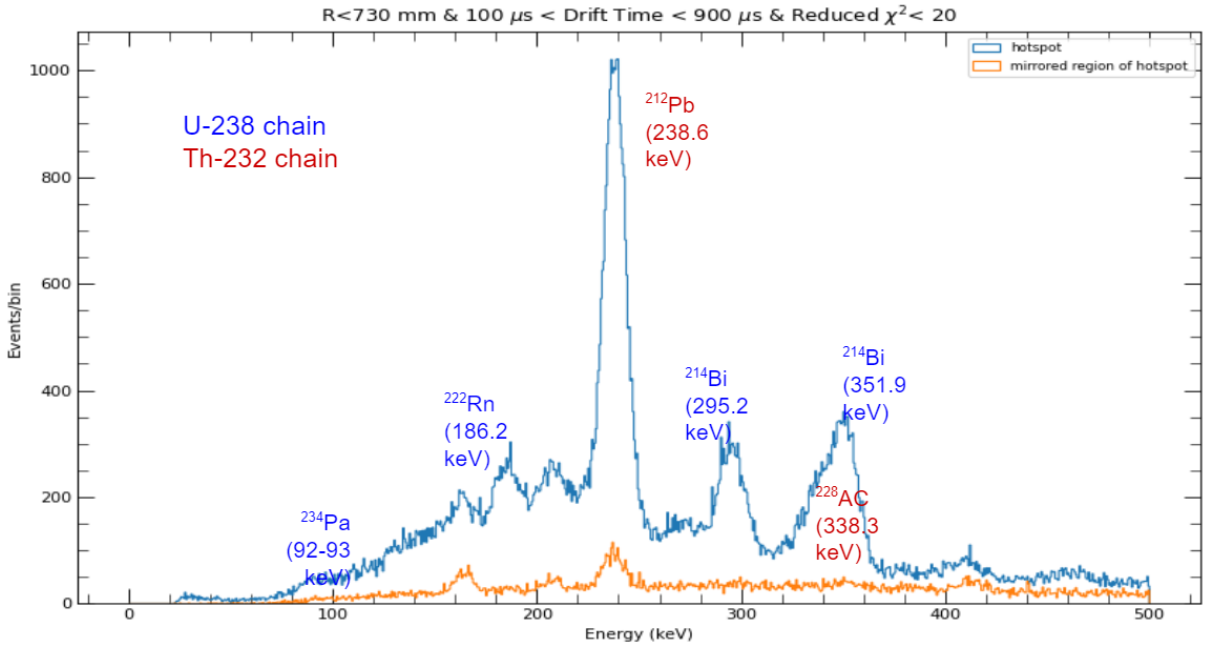

Figure A.4: Energy spectrum of the region located at (-700 mm, 40 mm) compared with the region located a (700 mm, 40 mm).

Appendix B

Energy reconstruction

Figure B.1 provides a continuous monitoring of the electron lifetime over the first science run by using events produced by ^{222}Rn α-particles.

Figure B.2 and B.3 provides, for completeness, the fits in S2 vs S1 space for the doke plot presented in section 5.6.3.

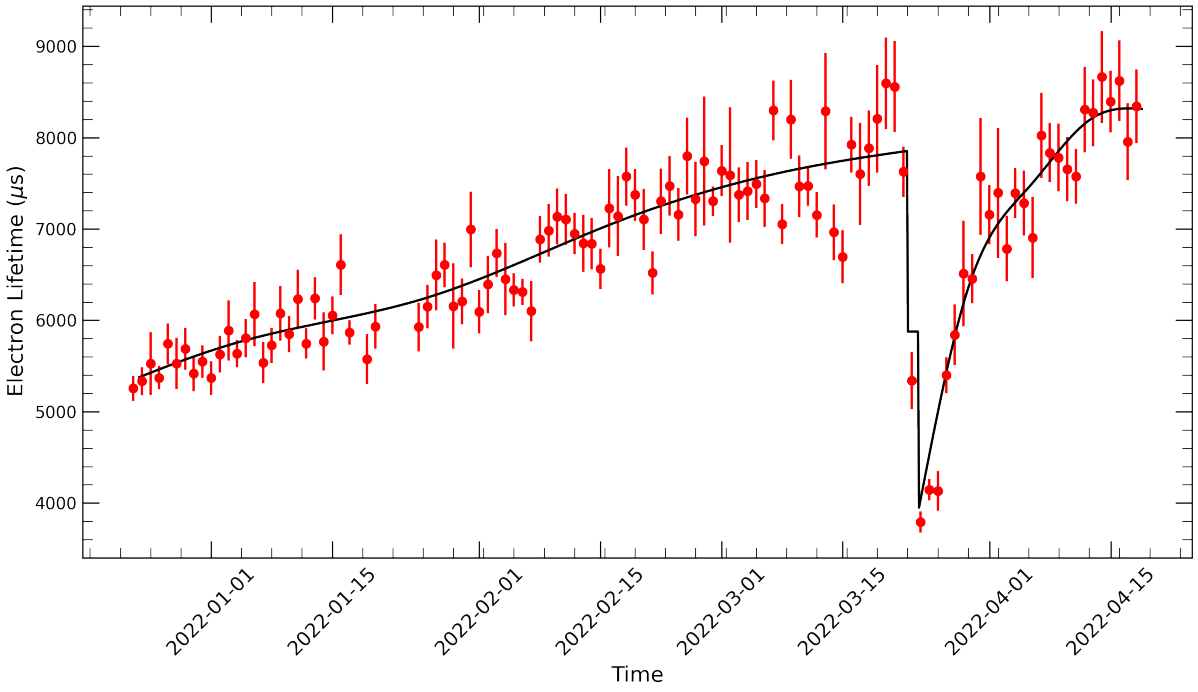

Figure B.1: Electron lifetime measured for the full first science run of the LZ detector with ^{222}Rn 5.5MeV α. The plotted lines consist of the union of two splines to better accommodate an abrupt variation in lifetime occurring towards the end of March. This discontinuity was caused by an accidental stop of the circulation.

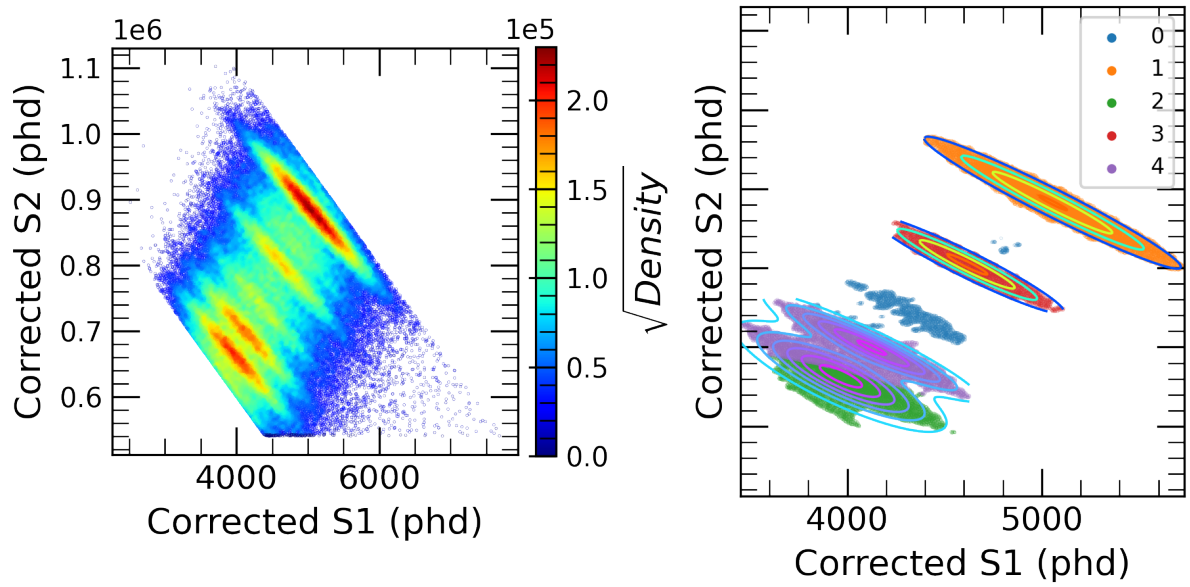

Figure B.2: Results of the 2D Gaussian fits for the Doke plot for ^{214}Bi (1120.3 keV),^{60}Co (1173.2 keV),^{60}Co (1332.5 keV),^{40}K (1460.8 keV).

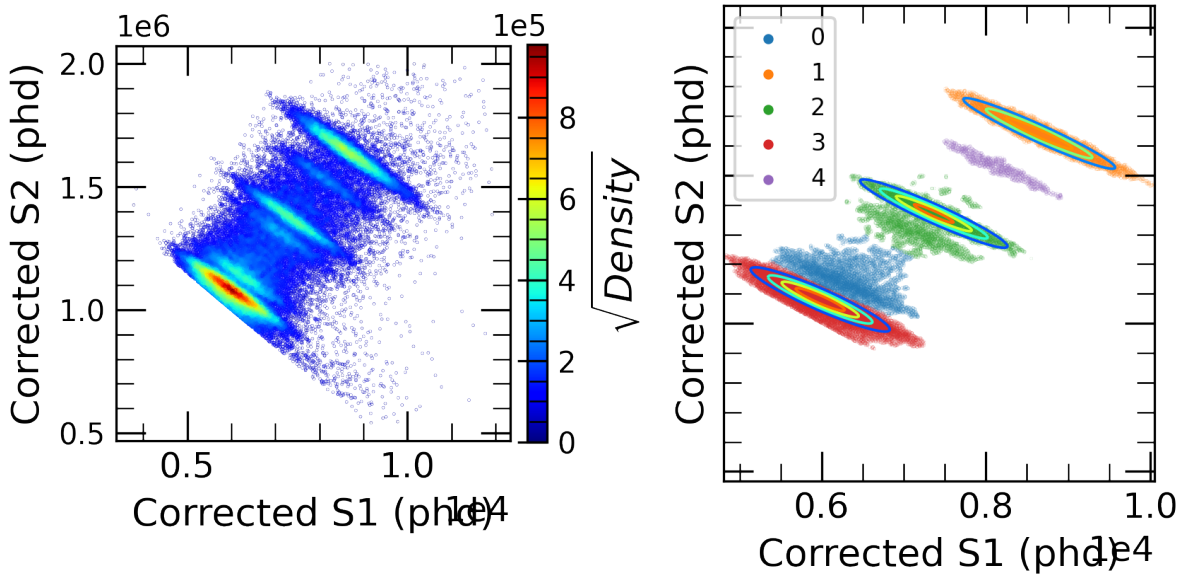

Figure B.3: Results of the 2D Gaussian fits for the Doke plot for ^{214}Bi (1765 keV),^{214}Bi (2204 keV),^{208}Tl (2614 keV).